Modelling the influence of infrared preheating and temperature uniformity in forming of powder-impregnated thermoplastic composites

Théo Baumard

Université Fédérale

Toulouse Midi-Pyrénées

THÈSE

en vue de l'obtention du

DOCTORAT DE L'UNIVERSITÉ DE TOULOUSE

délivré par

IMT – École Nationale Supérieure des Mines d'Albi-Carmaux

Cotutelle internationale avec Queen's University Belfast, Royaume-Uni

---

présentée et soutenue par

Théo BAUMARD

le 24 juin 2019

Modelling the influence of infrared preheating and temperature uniformity in forming of powder-impregnated thermoplastic composites

---

École doctorale et discipline ou spécialité :

MEGEP : Génie mécanique, mécanique des matériaux

Unité de recherche :

Institut Clément Ader, UMR CNRS 5312, IMT Mines Albi

Directeur(s) de Thèse :

Fabrice SCHMIDT, Professeur, IMT Mines Albi

Gary MENARY, Reader, Queen's University of Belfast

Autres membres du jury :

Steven LE CORRE, Professeur, Université de Nantes *(Rapporteur)*

Conchúr Ó BRÁDAIGH, Professor, University of Edinburgh *(Rapporteur)*

Brian FALZON, Professor, Queen's University of Belfast *(Examinateur)*

Biqiong CHEN, Professor, Queen's University of Belfast *(Présidente)*

Olivier DE ALMEIDA, Maître-Assistant, IMT Mines Albi *(Examinateur)*

Peter MARTIN, Reader, Queen's University of Belfast *(Examinateur)*

Modelling the influence of infrared preheating and temperature uniformity in forming of powder-impregnated thermoplastic composites

Théo Baumard
Dipl. Ing., M.Eng.

A thesis submitted in partial fulfilment of the requirements for the degree of
Doctor of Philosophy

Supervised by:
Prof. Fabrice Schmidt (IMT Mines Albi)
Dr. Gary Menary

Cosupervisors:
Dr. Olivier De Almeida (IMT Mines Albi)
Prof. Yannick Le Maoult (IMT Mines Albi)
Dr. Peter Martin

School of Mechanical and Aerospace Engineering
Queen's University Belfast
June 2019

QUEEN'S UNIVERSITY BELFAST

Thesis Deposit Form

To be completed by Student

Degree:	Doctor of Philosophy
Full Name:	Théo Baumard

Thesis title:
Modelling the influence of infrared preheating and temperature uniformity in forming of powder-impregnated thermoplastic composites

Summary: (max. 300 words)
Non-isothermal thermoforming of thermoplastic composites, in which a preconsolidated blank is heated above the melting temperature of the matrix before being formed in a press, is a process well adapted to the high production rates of automotive structural parts, allowing for cycle times <1min. Numerical tools to predict the apparition of manufacturing-induced defects based on the process parameters used are of an obvious industrial interest to avoid relying on a cost and time intensive trial-and-error approach.

This thesis focused on the development of a comprehensive simulation of the forming of powder-impregnated PA66/glass composites, modelling explicitly the infrared preheating step to investigate the effect of temperature homogeneity on shape defects.

The thermophysical and optical properties of the material were characterized experimentally at two levels of consolidation, and as a function of temperature when relevant. The structure of the non-consolidated material leads to a less uniform heating, compared to preconsolidated blanks. A finite element model based on the radiosity method to compute the radiative heat transfer was used to simulate the preheating step; this approach was validated against experimental results from a custom-built infrared oven. The model has been used to investigate the effect of blank sag on temperature distribution, and an optimization method to determine the oven parameters based on a desired temperature field has been presented.

The mechanical behaviour of the woven composite during forming was modelled with a hypoelastic continuum approach, implemented in Abaqus/Explicit. The model parameters were determined from experimental tensile tests and in-plane shear tests at various temperatures and shear rates. Non-isothermal simulations of the forming of hemispherical parts were conducted, using the temperature field predicted from the preheating simulation as an input, and showed good agreement with that observed on parts formed on a lab-scale thermoforming setup.

To be completed by Examiner

EXAMINER CERTIFICATION OF SUBMITTED WORK

I hereby certify that this is the final accepted copy of the submitted work and that all required amendments have been completed and submitted within the required deadline.

Name of Examiner: BRIAN G. FALZON

Signature of Examiner:

Date: 29-10-19

Remerciements

En premier lieu, je remercie vivement mes directeurs de thèse Fabrice Schmidt et Gary Menary, ainsi qu'Olivier de Almeida, pour leur encadrement au cours de ces quatre ans (et quelques mois...). Fabrice, merci de m'avoir donné l'opportunité de travailler sur ce sujet un peu loin de l'injection-soufflage et d'avoir partagé ton enthousiasme pour la modélisation. Gary, merci pour la confiance que tu m'as témoignée et pour tous tes conseils sur la simulation numérique. Olivier, merci pour ta disponibilité (dont j'aurais sûrement pu plus profiter !), ton dynamisme, et ton appui précieux sur les parties expérimentales. Merci à tous les trois de m'avoir guidé en me laissant la liberté d'explorer mes idées, et d'avoir su me remotiver dans les moments de creux.

Je souhaite également remercier Yannick Le Maoult et Peter Martin d'avoir suivi d'un peu plus loin, mais toujours avec un grand intérêt, la progression de mes travaux, et pour les précieux conseils, notamment sur le sujet des transferts radiatifs. Je suis très reconnaissant envers Solvay d'avoir fourni les matériaux d'étude et financé une partie de cette thèse, et en particulier envers Jérôme Bikard d'avoir apporté un point de vue industriel toujours pertinent aux réunions d'avancement.

Je tiens à remercier les professeurs Steven Le Corre, Conchúr Ó Brádaigh et Brian Falzon d'avoir accepté d'être examinateurs de cette thèse, et pour les échanges enrichissants sur ce projet et plus généralement sur la simulation de la mise en forme des composites pendant la *viva voce*. Merci également au professeur Biqiong Chen d'avoir présidé cette soutenance.

Je remercie également l'équipe de support technique des deux laboratoires pour leur aide avec la partie expérimentale de ces travaux, et en particulier à Jean-My, Rémi, Fabrice, Karim et Vincent côté francais, et Dan, Troy, Bronagh, Paula et Wez côté irlandais pour la conception des pilotes de chauffage infrarouge et pour les essais de traction de biais ; merci également à Aurélien et Adrien pour la préparation et l'envoi des échantillons à Belfast, à Denis Marty du centre Rapsodee pour les mesures Hot Disk, et à Tristan Mangeard de l'ICA

Toulouse pour les essais de tomographie. Un grand merci à Esther, Cathy et Olwyn pour avoir grandement facilité la partie administrative de cette cotutelle, ce qui n'était clairement pas une mince affaire. Je remercie également l'ensemble du personnel des deux laboratoires pour leur accueil chaleureux.

Merci à mon escouade de stagiaires : Neale, François, Sarah, Logendra, Ryan et Krishna pour leur motivation et leur contribution à cette thèse même si elle n'apparaît pas forcément explicitement dans ce manuscrit, pour m'avoir rendu j'espère plus pédagogue, et pour m'avoir donné une autre vision du cubisme.

Bien entendu, un grand merci à l'ensemble des doctorants et postdoctorants que j'ai pu croiser pendant cette thèse, en commencant par les collègues du bureau des connards : Rémi, Manu, Patou, Quentin, Lilian, Mr. Copin, Ludo, Phuong, Jenny, Paul, pour les pauses café toujours studieuses et le partage des joies simples de l'origami ; au groupe de recherche de Gary : David, Narendran, Surendra, Huidong, James, Shiyong, Ross, Josh, Stephen, Claire, pour l'excellente ambiance et l'entraide, à Katie pour les discussions sur la politique britannique et la dissection des moutons, à Aurélien, Charline, Raffa, Lilia, Abdel, Sinan, David, Georg, Ali, et à tous les autres, sans qui cette thèse aurait été très différente.

Plus personnellement, je remercie mes amis de Descartes, de Centrale, de Montréal, aux musiciens parisiens, à ceux des sessions toulousaines et du Maddens, aux grimpeurs de Puygouzon et Belfast, pour les parenthèses toujours bienvenues dans le travail. Enfin, merci à mes parents pour leur soutien sans faille tout le long de cette thèse, à mon frère pour ses excellents conseils typographiques, et à Céline d'avoir partagé cette aventure avec moi même depuis l'autre bout du monde.

Contents

List of Figures

List of Tables

List of Symbols

Latin letters

a	$\mathrm{W\,m^{-1}\,K^{-4/3}}$	Parameter of the polymer matrix thermal conductivity model
a_{1-3}	Pa	Shear stiffness parameters
A	-	Temperature scaling factor
Bi	-	Biot number
C_p	$\mathrm{J\,K^{-1}\,kg^{-1}}$	Specific heat capacity
D	$\mathrm{rad\,s^{-1}}$	Cowper-Symonds parameter
$\mathbf{D}$	-	Strain rate tensor
$E_{\mathrm{app.}}$	Pa	Apparent tensile modulus at high strain
E_a	$\mathrm{J\,mol^{-1}}$	Flow activation energy
F	N	Axial force (bias extension test)
$F_{i\rightarrow j}$	-	View factor between surfaces A_i and A_j
F_{sh}	$\mathrm{N\,m^{-1}}$	Normalized shear force (bias extension test)
$\mathbf{F}$	-	Deformation gradient tensor
G	$\mathrm{W\,m^{-2}}$	Irradiation
G_{12}	Pa	Shear modulus
H	-	Heaviside step function
h_c	$\mathrm{W\,m^{-2}\,K^{-1}}$	Convective heat transfer coefficient
h_r	$\mathrm{W\,m^{-2}\,K^{-1}}$	Radiative heat transfer coefficient

J	$\mathrm{W\,m^{-2}}$	Radiosity
k	-	Parameter related to the sharpness of the decrimping/tension transition
L	$\mathrm{W\,sr^{-1}\,m^{-2}}$	Radiance
Nu	-	Nusselt number
P	-	Cowper-Symonds parameter
$\mathbf{Q}$	-	Rotation tensor
R	$\mathrm{J\,mol^{-1}\,K^{-1}}$	Universal gas constant
Ra	-	Rayleigh number
$\mathbf{R}$	-	Rotation tensor from polar decomposition of the deformation gradient
T	K	Temperature
T_0	K	Reference temperature
T_c	K	Crystallization temperature
T_g	K	Glass transition temperature
T_{lamp}	K	Halogen lamp filament temperature
T_m	K	Melting temperature

Greek letters

α	-	Absorptivity
δ_c	m	Deflection of the center of the blank
δ_{ij}	-	Kronecker delta
ϵ	-	Emissivity
ϵ_0	-	Transition strain between decrimping and tension
η	Pa s	Dynamic viscosity
γ	rad	Shear angle between yarns
κ	$\mathrm{W\,m^{-1}\,K^{-1}}$	Thermal conductivity
λ	m	Wavelength
ρ	$\mathrm{kg/m^3}$	Density
ρ	-	Reflectivity
$\boldsymbol{\sigma}$	$\mathrm{N\,m^{-2}}$	Cauchy stress tensor
σ_{SB}	$\mathrm{Wm^2\ K^{-4}}$	Stefan-Boltzmann constant
τ	-	Transmissivity
ζ	$\mathrm{m^{-1}}$	Blank curvature

Exponents

$\square^{0}$	-	Property considered for the black body
$\square^{\cap}$	-	Hemispherical quantity
$\square^{\nabla}$	-	Objective derivative
$\square^{\intercal}$	-	Transpose

Indices

$\square_{f}$	-	Indicates property of the fibers
$\square_{in\text{-}plane}$	-	Indicates property in the plane of the warp and weft directions of the fabric
$\square_{\lambda}$	-	Spectral property
$\square_{m}$	-	Indicates property of the matrix
$\square_{out\text{-}plane}$	-	Indicates property out-of-plane of the warp and weft directions of the fabric
$\square_{yarn}$	-	Indicates property of the yarns

Chapter

1

General introduction

1.1 Use of thermoplastic composites in the automotive industry

1.1.1 Emission regulations: a driver for weight reduction

Automotive original equipment manufacturers (OEM) have to comply with increasingly stringent emission standards (Fig. 1.1), with the introduction of Euro 5 & 6 norms in the European Union [Williams+2016] or CAFE regulations in the USA [Bento+2015]. While the targets have been met so far, the further 15% reduction of CO_2 emissions by 2025 compared to the 2021 target, as well as the implementation of a standard testing procedure more representative of real driving conditions (the Worldwide harmonized Light vehicles Test Procedure, or WLTP, replacing the New European Driving Cycle introduced in the 1970s), means that significant efforts are still required to improve the fuel efficiency of motor vehicles.

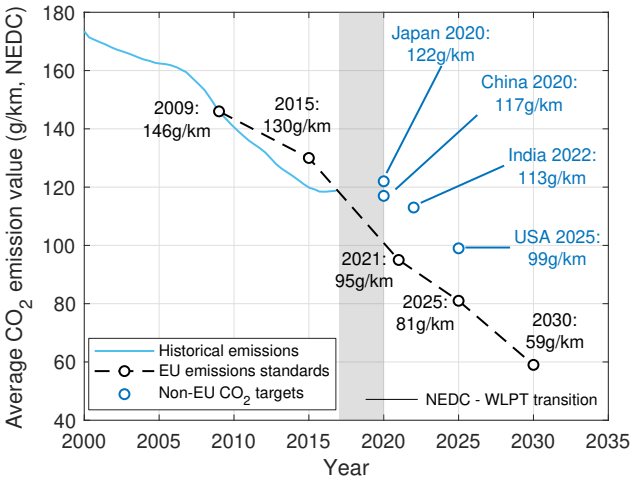

Figure 1.1 – Passenger cars CO_2 emissions: EU trend and future targets (data from [Mock2019])

In addition to improving the aerodynamics and road resistance of the vehicles developed, OEMs have been focusing research work on two complementary areas to reach these goals [Redelbach+2012]:

- Modifications of the powertrain (hybridization, use of electric motors, alternative fuels...).
- Structural weight reduction, with the use of advanced materials: high to ultra-high-strength steels, aluminium alloys, or composite materials.

The vehicle weight is a key factor, as a 100 kg reduction in weight can lead to a 10 g km^{-1} reduction in emitted CO_2 [Wilson2017]. The weight of safety and comfort features in passenger cars has however been steadily increasing [Amiot2014; Cheah2010], which makes the use of lighter materials in structural parts all the more important.

1.1.2 Towards structural composite parts in high volume applications

Despite their lightweighting potential, fibre reinforced polymer composites have historically been used in the automotive industry mostly for semi-structural or cosmetic parts (exposed carbon), with structural parts limited to low-volume markets such as luxury or sports cars [Beardmore+1986; Taggart+1987]. The use of long glass fibre semiproducts based on thermoset (sheet and bulk molding compounds: SMC/BMC), or thermoplastic matrix (glass mat or long fibre reinforced thermoplastic: GMT/LFRT) has been favoured for body panels applications [Renault2001].

Improvements in manufacturing processes used as well as reductions in materials costs have allowed continuous fibre reinforced polymer composites to make their way in body-in-white structural parts of passenger cars [Holmes2017; Ishikawa+2018]. Composite parts have been successfully developed for prototype and commercial models, a few recent examples being the floorpan and B-pillars of the Renault EOLAB concept car manufactured from glass/PA66 [Liraut+2015], or the body-in-white (BIW) of BMW i3 and i8 which make extensive use of carbon/epoxy parts [Starke2016]; additional demonstrator parts developed for load-bearing applications are presented in Fig. 1.2.

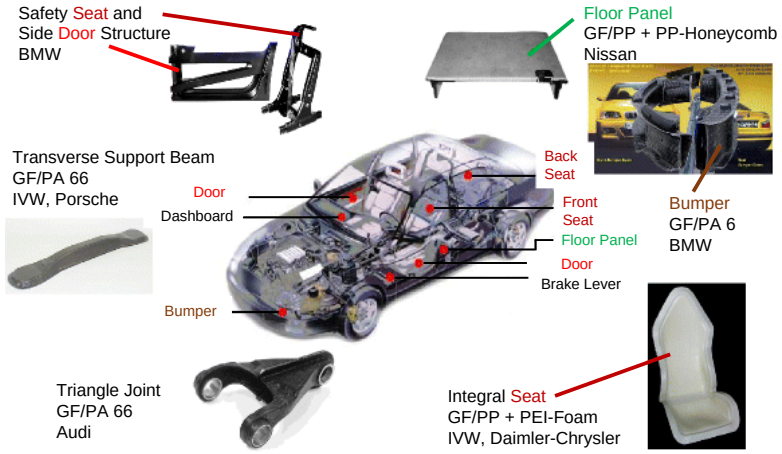

Figure 1.2 – Fibre-reinforced composites in load bearing automobile structures [Friedrich+2012]

Thermoplastic composites show several advantages compared to thermoset for automotive applications: they present increased toughness and fatigue resistance (which makes them better suited to crash-relevant structural parts), as well as faster processing times as no curing time is needed (although higher processing temperatures are required) [Friedrich+2012; Mathijsen2016].

The assembly of thermoplastic composite parts in a BIW structure is facilitated as welding processes can be used for joining parts. Overmoulding (injection moulding following forming of the part) can be used for function integration [Bouwman+2016], while the absence of cross-linking of the polymer chains permits recycling [Yang+2012]. Their widespread usage

is still hindered by the cost of the raw materials, and by the relatively low maturity of the manufacturing processes and associated design and numerical validation tools used [Renault2015]. Process optimization to reach the cycle times required for mass production (<2 min) remains a challenge.

1.2 Forming of thermoplastic composite parts

1.2.1 Thermoplastic composite semiproducts

Woven fabric-reinforced thermoplastic composites (in which warp and weft reinforcement yarns are interlaced in a repeating pattern and impregnated with a thermoplastic matrix) present a good trade-off between formability, mechanical properties, and cost, when compared to GMTs and unidirectional laminates [Brooks2007].

Thermoplastic polymers present a high melt viscosity, and resin transfer moulding (RTM) processes as used in manufacturing of thermoset composites parts require significant adaptation in terms of injection pressure [Bourban+2001]. While recent research work has focused on the development of low viscosity thermoplastic resins [Cazaux2016; Faraj+2016] or reactive RTM [Vicard+2017; Wakeman+2006], those technologies are not in widespread use. To reduce the flow distance of the matrix during processing, different types of semiproducts (or semipregs) in which the reinforcement is partially impregnated have been developed [Vaidya+2008]. Common forms (schematized in Fig. 1.3) are commingled fabrics, in which polymer filaments are dispersed in reinforcement yarns, and powder-impregnated tows or fabric where the matrix is deposited as droplets either within the yarns or at the surface of the fabric.

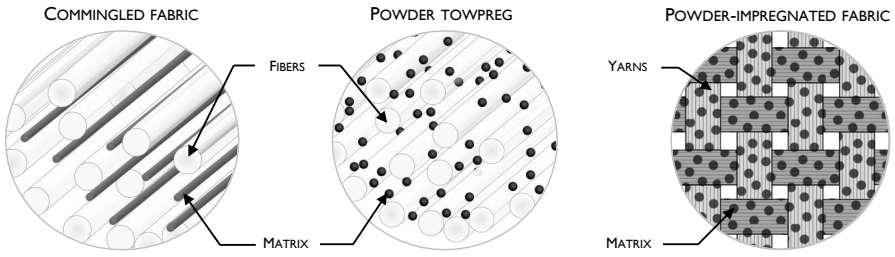

Figure 1.3 – Thermoplastic semiproducts (semipregs)

These semiproducts are usually processed through thermocompression or double belt press/-calendering to obtain fully impregnated, flat laminates (also called organosheets) that can be subsequently shaped with a variety of forming processes.

1.2.2 Thermoforming processes

The basic principles of thermoplastic composite forming processes consists in heating a preconsolidated laminate to a temperature above the semicrystalline matrix melting point

(or above the glass transition temperature in the case of an amorphous matrix), before applying pressure to deform the blank into the required shape in a mould. Isothermal and non-isothermal processes can be used: in the isothermal approach, both the blank and the tool are heated to the forming temperature, and pressure is applied while the temperature is held constant. The pressure is maintained during cooling. This results in parts with low void content, but the necessity of heating and cooling the tools limits the achievable cycle time [Brooks2007].

In non-isothermal processes, the blank is preheated in a separate infrared oven before being transferred to the forming tool, which is at a temperature below the crystallization temperature of the matrix. Forming and cooling of the blank occur simultaneously. As the tool temperature is not cycled, much shorter processing times can be achieved (<1 min) [Akkerman2018; Land+2015]. Specific forming processes are distinguished based on the means used to apply pressure on the blank (gas/fluid pressure, vacuum, mechanical contact) and the tooling materials (rigid versus rubber die forming); a few examples are shown in Fig. 1.4.

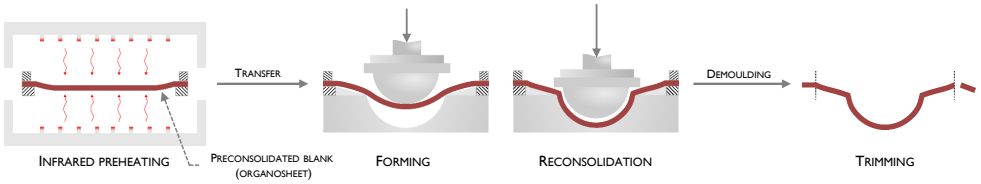

(a) Stamp forming

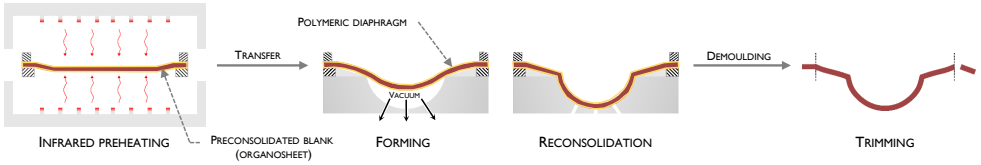

(b) Diaphragm forming

Figure 1.4 – Examples of non-isothermal composite thermoforming processes

1.2.3 Virtual manufacturing for process optimization

Non-isothermal thermoforming processes are well adapted to manufacturing high-volume parts, with cycle times compatible with the requirements of the automotive industry. As the structural performances of the parts depend heavily on the processing history (through resulting fibre orientation, crystallinity, ...), process optimization is primordial to ensure that parts are produced without defects, and with acceptable time and energy efficiency. In order to avoid the costs associated with experimental trial-and-error procedures, numerical simulation is increasingly used as a predictive tool to optimize process parameters [Akkerman2018; Lee+2001].

Significant efforts have focused on proposing numerical models to simulate the complex mechanical behaviour of textile reinforcements during forming, from the microscale (considering each fibre individually) to the macroscale (assuming the material as continuous). Most of the studies have been limited to dry fabric draping, or isothermal forming processes, and the influence of temperature on the mechanical behaviour of the woven composite has only been considered recently. The infrared ovens used in the preheating step of industrial forming processes can lead to significant temperature gradients in the blanks, which in turn affect the forming behaviour. While models aiming at predicting the temperature evolution during infrared heating have been proposed, no simulation tools have been developed to evaluate the influence of the quality of the preheating on forming-induced defects.

1.3 Research objectives

The work presented in this thesis has been conducted as part of a collaboration between Institut Clément Ader (ICA) at IMT Mines Albi, and the School of Mechanical and Aerospace Engineering (SMAE) of Queen's University Belfast, with support from Solvay (Saint-Fons).

The main goal of this project is to propose validated numerical tools to simulate the effect of the temperature field of a thermoplastic composite blank on the defects generated during forming. Given the sequential nature of the preheating and forming steps, two sub-objectives have been defined. The first one consists in developing a model to simulate the transient temperature distribution in a composite blank during the infrared preheating step: this allows evaluating the temperature homogeneity before forming for a given oven configuration.

The second objective consists in simulating the temperature-dependent, mechanical behaviour of woven thermoplastic composites during forming to predict macroscale shape defects. The temperature field resulting from the preheating simulation is used as an input for the forming simulation: a loose coupling will be considered between the numerical tools.

A secondary goal is to investigate the feasibility of forming parts directly from non-consolidated powder-impregnated blanks. This would allow to reduce the cost of the preforms by removing the need for a preconsolidation step; the structure of the non-consolidated fabrics leads however to specific challenges during heating, forming, and reconsolidation, part of which are addressed in this work through experimental characterization and modelling.

1.4 Thesis outline

Following this introduction, a review of the literature dedicated to the simulation of composite forming processes is presented in **Chapter 2**. The review is subdivided in three parts: the first one compiles experimental studies showing the impact of the preheating step on forming, and introduces the different approaches developed to model the heat transfer in an infrared oven. The second part reviews the extensive literature on models of the mechanical behaviour of woven composites in forming conditions. The third part of the literature review then presents the existing work on experimental forming of unconsolidated thermoplastic composites.

Chapter 3 presents the development of a modelling approach to describe the evolution of temperature in a composite blank subject to radiative heat transfer. The structure of the PA66/glass composite considered is described, and the optical and thermophysical properties are characterized experimentally at two levels of consolidation. The numerical simulation tool is validated against a 1-lamp heating setup.

An instrumented, modulable lab-scale infrared oven is developed in **Chapter 4**, to evaluate the capabilities of the model in simulating test cases closer to the industrial heating process. The influence of the oven configuration on the surface gradients on the blank is investigated experimentally, and the different test cases replicated with the numerical model. The influence of the blank sag on temperature homogeneity is addressed numerically. An optimization procedure to determine the oven parameters based on a desired temperature field is proposed.

Chapter 5 introduces an hypoelastic approach to model the mechanical behaviour of woven thermoplastic composites at the macroscale. Model parameters are identified as a function of the preconsolidation level from experimental tensile and in-plane shear tests, the latter at different temperatures and shear rates.

Finally, **Chapter 6** is dedicated to non-isothermal forming of PA66/glass composites. An experimental forming setup is developed using an hemispherical punch, and parts are manufactured with different preheating conditions introduced in Chapter 4. The implementation of the hypoelastic model developed in Chapter 5 in a finite element code is discussed, and forming simulations are presented with an increasing degree of complexity.

Chapter

2

Modelling and simulation of composite forming processes: literature review

2.1 Introduction

The interest of using a virtual manufacturing approach for process optimization has been introduced in Chapter 1. This chapter presents a review of the literature on the simulation

of composite forming processes, and more specifically on thermoforming of woven fabric reinforced composites.

The first step of these processes consists in heating the composite blank to a temperature that allows deformation. The modelling and simulation of heat transfer during this preheating phase is discussed in section 2.2. The review is focused on infrared heating which is the heating mode used in the following study. The second step involves the physical forming of the blank over a tool to reach the required shape. This topic has been the subject of intensive research, and the different mechanical models and approaches developed to describe the forming behaviour of dry fabric and fabric-reinforced polymers are critically reviewed in section 2.3.

2.2 Modelling of the preheating phase

2.2.1 Industrial heating systems

The preheating of the composite blank to the required processing temperature (either above the glass transition temperature T_g for an amorphous matrix, or above the crystalline melting temperature T_m for a semi-crystalline matrix) can be carried out using different approaches based on the three modes of heat transfer.

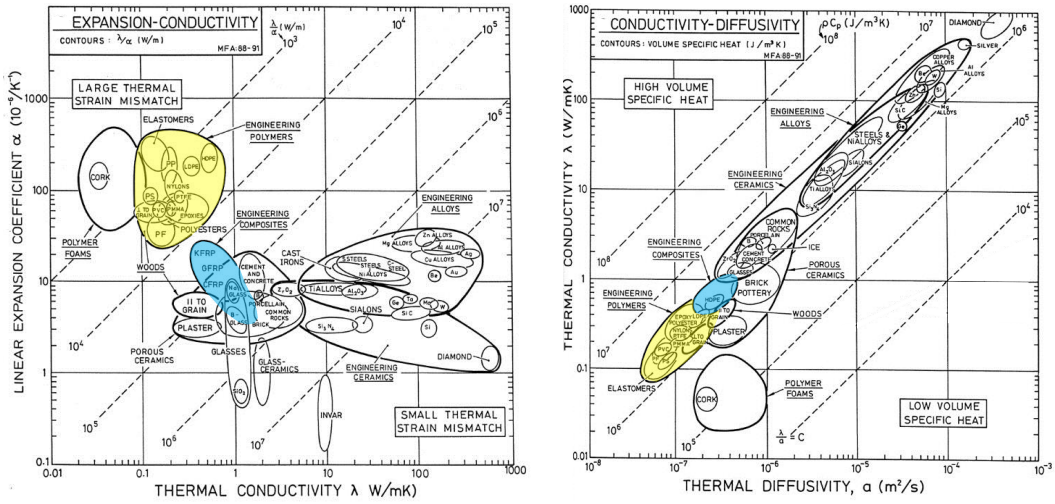

Figure 2.1 – Thermal properties of engineering materials at room temperature [Ashby1992]: (left) expansion coefficient vs. thermal conductivity, (right) thermal conductivity vs thermal diffusivity. Polymers and fibre-reinforced composites are highlighted in yellow and blue respectively.

Contact heating consists of heating a blank by conduction against hot plates. The through-thickness thermal conductivity of typical engineering polymers and fibre-reinforced polymers is between $0.1\,\mathrm{W\,m^{-1}\,K^{-1}}$ and $1\,\mathrm{W\,m^{-1}\,K^{-1}}$ (see Fig. 2.1): this makes the industrial applications usually limited to thermoforming of thin polymer sheets [Throne2008]. The quality of the contact between the heated plates and the composite sheet has a major

impact on the temperature distribution, as air pockets modify the interfacial thermal contact resistances. The pressure applied to ensure the contact has to be monitored to avoid undesirable flow of the matrix. Additionally, adhesion of the matrix to the hot platens can occur when processing semi-crystalline composite above their melting point [Sweeney+1995]. Contact heating has been used by Friedrich and Hou [Friedrich+1997; Hou+1991; Hou1996] to preheat carbon- and glass-reinforced polypropylene laminates with thicknesses up to 3 mm; adhesion with the platens is avoided through the use of polyimide diaphragms.

Convective ovens are used when heating large or thick laminates, or when the heating time is not a critical factor. The power density achievable depends both on the airflow speed, and temperature; convective transfer is not competitive with radiative heat transfer when high power densities are required (Fig. 2.2a). This type of heating is thus seldom used in high production rate environments such as the automotive industry. However, the good temperature homogeneity achieved makes it interesting in laboratory scale thermoforming setups. It can also be used in heating non-consolidated laminates (Fig 2.2b), as the loosely compacted plies are permeable to the hot air [TrudelBoucher+2006].

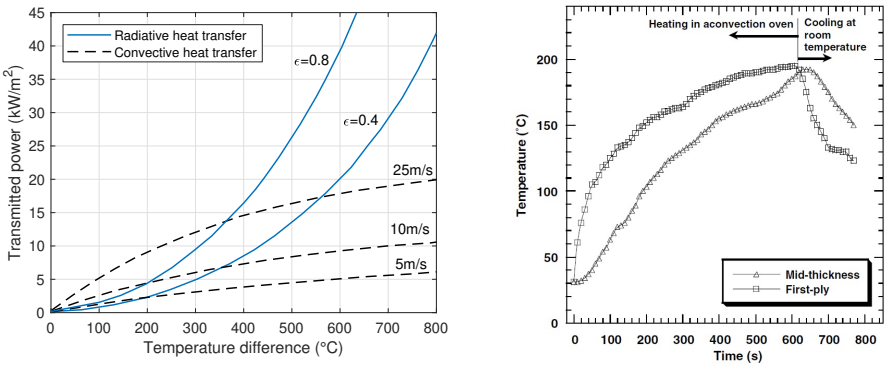

(a) **(b)**

Figure 2.2 – a: transferable power by convection and infrared radiation for different air flow speeds and emissivity [Muhlbauer+2007], b: temperature profiles during convective heating of six plies of GF/PP commingled fabric, [TrudelBoucher+2006]

Radiative heating is the most commonly used method for heating thermoplastic composites; it relies on the absorption of electromagnetic radiation by the media to be heated. The physics of radiative heat transfer will be introduced in section 2.2.3.1. Several technologies exists depending on the wavelength used for heating, from short-wave infrared lasers in automated tape placement [StokesGriffin+2015] to microwave ovens [Mishra+2016]. Infrared ovens are classically used in thermoplastic composites forming [Brooks2007], and the principal heating elements available will be presented here. The simplest heaters used are flat panel heaters: a nichrome wire is embedded in ceramic and in contact with a metal or quartz glass panel. Energy from the wire radiates to the backside of the heater panel, which itself reradiates to the thermoplastic sheet. Those heaters have a slow response time, and high thermal inertia, making them unsuitable for applications where accurate temperature control is needed [Knights1996].

Figure 2.3 – Left: ceramic heating elements, right: tungsten halogen lamps and heating modules [Ceramicx2015]

Quartz heaters (Fig. 2.3) are composed of a resistive wire made of nichrome or tungsten inside of a cylindrical quartz tube, filled with nitrogen or halogen (in which case the denomination "halogen heater" is used), that protects the filament from oxidation. These emitters have a fast response time that allows precise control of the emitted power, and zoning. A comparison of the different technologies in terms of inertia conducted by Bédard and Brunet [Bédard+1996; Bédard1998] (see Fig. 2.4) show start-up time constants up to 100 times faster for tungsten halogen lamps when compared to quartz tubes and ceramic heaters.

An infrared oven is composed of a number of infrared heaters, grouped in modules or banks. They can be backed with a metallic reflector to increase the radiated energy going towards the blank. The heaters can be controlled using dimmers, either independently or by zones. The spacing between heaters is usually fixed, while the distance between the heaters and the blank can often be adjusted using shims.

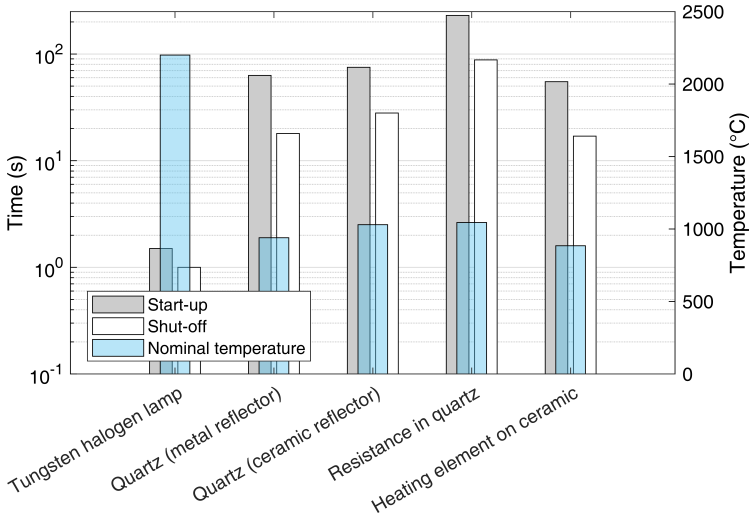

Figure 2.4 – Start-up and shut-off time constant (63% of final state) and nominal temperature (red) for various industrial infrared sources. Data from [Bédard1998].

Processes using a combination of different heating modes have been developed recently. For example, the Quilted Stratum Process [Wedhorn+2017] preheats multi-thickness preforms using conduction platens to heat the blank to below the melting point of the matrix, followed

by infrared heating to bring the blank to the forming temperature, in a similar fashion to work presented by Mahlke et al. [Mahlke+1989].

2.2.2 Influence of temperature on forming

The processing temperature has an important impact on the quality of a formed thermoplastic composite part, via its influence on the polymeric matrix. The mechanical behaviour of the composite blank during the forming stage depends on the viscosity of the resin: the matrix acts as a lubricant that reduces the yarn/yarn and fibre/fibre friction during the deformation, but conversely the high viscosities associated with thermoplastic matrices can prevent the reorganization of the yarns [Bersee+1991]. The viscosity of thermoplastic polymer melts decreases with an increase of temperature [Wang+1995], and is often modelled by an Arrhenius-type law:

$$\eta = Be^{E_a/RT} \tag{2.2.1}$$

Where η is the viscosity, B a pre-exponential factor depending on the polymer, E_a the flow activation energy, R the universal gas constant and T the absolute temperature. This thermo-dependence indicates that increasing the temperature facilitates the forming operation.

Several studies have investigated experimentally the effect of the temperature on the forming of thermoplastic composites. The influence of the mould temperature was investigated by Cakmak and Dutta [Cakmak+1991] for the forming of unidirectional carbon/PEEK laminates. Low mould temperatures were shown to promote wrinkling (Fig. 2.5), and the authors proposed an optimal temperature of 400 °C for this material, i.e. an isothermal process similar to thermocompression. The cycling of the tool temperature needed for the demoulding of the part leads to long process times.

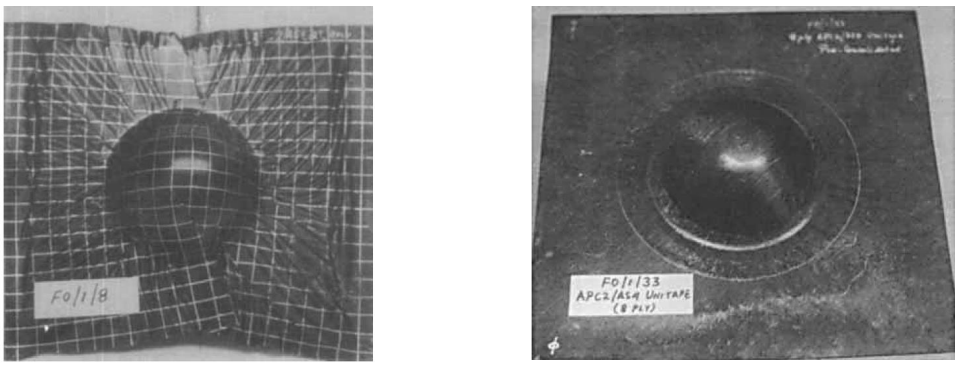

(a) (b)

Figure 2.5 – Forming of carbon/PEEK unidirectional laminates: (a) mould at room temperature, (b) mould at 400 °C [Cakmak+1991].

Similar results are presented by Bhattacharyya et al. [Bhattacharyya+2003] on woodfibre mats/polypropylene laminates. The blanks were preheated in a convective oven and formed

in a heated mould with temperatures between the glass transition and the melt temperature of the resin (Fig. 2.6). Wrinkles were reported for low mould temperatures, while the higher temperatures resulted in fibre failure. Friedrich and Hou [Friedrich+1998] have studied the effect of the preheating temperature on the forming of unidirectional glass fibre-polypropylene single-curvature parts: increasing the temperature was shown to alleviate out-of-plane fibre buckling and in-plane wrinkling by reducing the yield shear stress of the matrix, allowing for interply shear and slip. The diminution of wrinkles with increasing temperature (and decreasing matrix viscosity) on C-shaped diaphragm formed laminates was also presented by Bian et al. [Bian+2013]. Gröschel et al. [Gröschel+2017] studied the gas pressure diaphragm forming of PA6/glass laminates at various blank and blankholder temperature, and show a significant influence of the blankholder/mould temperature on the draw-in as presented in Fig 2.7, with hemispherical parts formed at lower temperatures exhibiting lower drawing ratio and necessitating higher forming pressures.

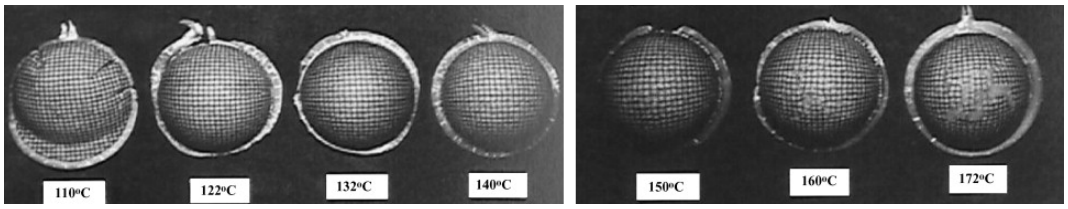

Figure 2.6 – Hemispherical forming of woodfibre/PP laminates at different temperatures [Bhattacharyya+2003].

Most recent studies report the effect of temperature on specific modes of deformation of woven thermoplastic composites, rather than on the quality of thermoformed parts. Temperature is shown to have a significant impact on in-plane shear [GuzmanMaldonado+2015; Harrison+2004; Lebrun+2003; Machado+2016b] and bending [Liang+2014; Ropers+2016] which are the principal modes of deformation in forming (see 2.3.1.2), as well as on inter-ply friction which is dependent on the matrix viscosity [Haanappel+2014].

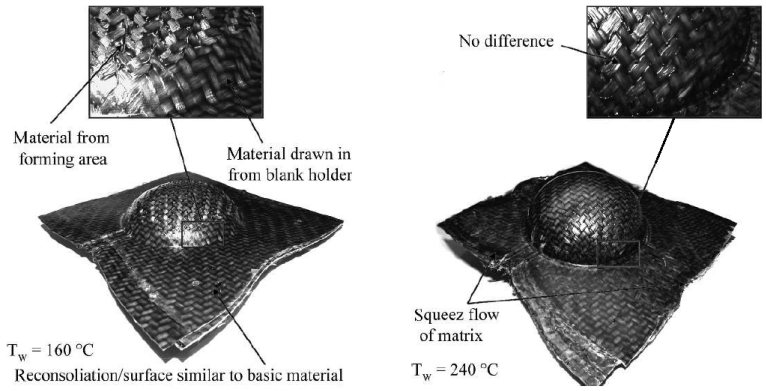

Figure 2.7 – Diaphragm forming of glass/PA6 laminates at blankholder temperatures of 160 °C and 240 °C showing different draw-in [Gröschel+2017].

The temperature at the end of the preheating stage is usually assumed to be homogeneous in the blank, and temperature gradients are seldom described. Chen et al. [Chen+2000] report a significant sensitivity of the deformation to non-uniform heating, with a 20 °C gradient leading to an imbalanced draw-in.

Localized heating was used in Hwang et al. [Hwang+2002] to form single curvature V-shaped parts. The unidirectional carbon/PA6 laminate was heated with an infrared strip heater on a controlled width before being formed. An increase in the processing temperature is shown to reduce the spring-in of the part, and fibre buckling in the radius. While locally heated parts show more fibre wrinkling compared to entirely heated parts, the local heating is faster and more energy efficient. No equivalent study has been conducted on local heating of woven composites, or on double curvature shapes, where shear and draw-in are preponderant.

2.2.3 Optimization of heat transfer in composite forming processes

The experimental studies presented in the previous section show the importance of controlling the temperature of the blank during the preheating and forming stages. The development of numerical simulations and optimization methods for the preheating stage requires a good understanding of the interaction of infrared radiation with composites materials; the principles of radiative heat transfer are presented in section 2.2.3.1. The modelling approaches proposed in the literature are introduced in section 2.2.3.2.

2.2.3.1 Principles of radiative heat transfer

The radiative flux emitted by a physical body depends both on its temperature, and surface roughness. To quantify the emissive power of a real body, elementary notions have to be introduced.

The spectral radiance in a point $P(\overrightarrow{r})$ in space for a wavelength λ in the direction $\overrightarrow{\Omega}$ is written as $L_\lambda(T, \overrightarrow{r}, \overrightarrow{\Omega})$. It corresponds to the flux density $d^2\Phi_\lambda$ radiated through a surface dA oriented along the unit surface normal $\overrightarrow{n}$, by unit angle solid $d\Omega$ around $\overrightarrow{\Omega}$:

$$L_\lambda(T, \overrightarrow{r}, \overrightarrow{\Omega}) = \frac{d^2\Phi_\lambda(\overrightarrow{r})}{(\overrightarrow{\Omega} \cdot \overrightarrow{n}) d\Omega dA} \tag{2.2.2}$$

To describe the radiative emission of real bodies, an ideal reference called the black body is employed. It absorbs and emits the entirety of the radiative energy at a given temperature, for every wavelength and in every direction. The spectral, hemispherical radiance of the black body is defined by Planck's law:

$$L^0_\lambda(T) = \frac{c_1 \lambda^{-5}}{e^{\frac{c_2}{\lambda T}} - 1} \ (W.m^{-3}.sr^{-1}) \tag{2.2.3}$$

Where $c_1 = 3.742 \times 10^{-16}\,\mathrm{Wm}^2$ and $c_2 = 1.439 \times 10^{-2}\,\mathrm{m\,K}$ are the first and second radiation constant respectively. The integration of Planck's law over the wavelength spectrum yields

Stefan-Boltzmann law:

$$L^0(T) = \int_0^\infty L^0_\lambda(T)d\lambda = \frac{\sigma_{SB}T^4}{\pi} \tag{2.2.4}$$

Where $\sigma_{SB} = 5.670 \times 10^{-8}\,\mathrm{Wm^2K^{-4}}$ is Stefan-Boltzmann constant. This equation shows that the power radiated by a black body is directly proportional to the fourth power of its temperature. Derivation of equation 2.2.3 leads to a relation between the wavelength of maximum radiative emission λ_m and the black body temperature called Wien's displacement law:

$$\lambda_m T = 2897.8\ (\mu m.K) \tag{2.2.5}$$

The product $\lambda_m T$ is constant; this means that the higher the source temperature is, the shorter the wavelength of maximum emission will be. This is a key point when selecting an infrared source for heating applications, as the material will need to absorb energy at the characteristic wavelength of the emitter. The spectral radiance of a black body at temperatures representative of the processing range of thermoplastic composites and of industrial infrared sources is presented in Fig. 2.8. This figure clearly shows the shift of the maximum of emission towards the short wavelengths as the temperature increases: for example, a typical tungsten-halogen lamp at a nominal temperature of 2400 K has a peak emission at 1.2 µm, while a body at room temperature (300 K) has a peak emission at 9.7 µm, in the mid-infrared spectrum. Integration of the curves described by Planck's law additionally shows that 95.6% of the energy radiated is in the spectral range $[0.5\lambda_m,\ 5\lambda_m]$.

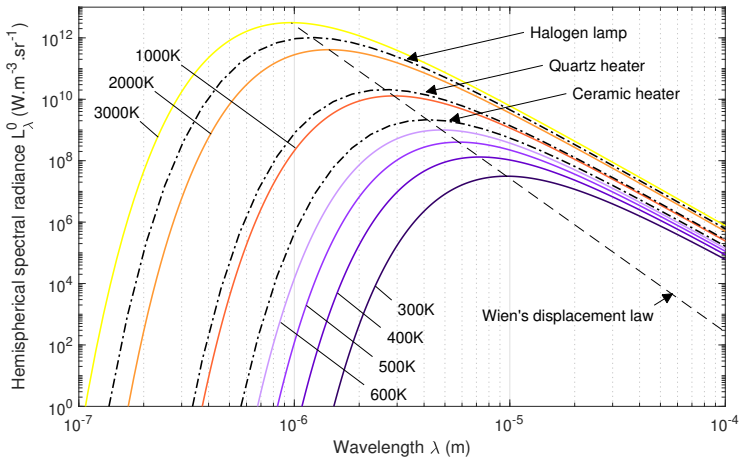

Figure 2.8 – Spectral radiance of the black body for various temperatures

The radiative emission of a real body can be described by its spectral directional emissivity $\epsilon_\lambda(\overrightarrow{\Omega}, T)$. This quantity describes the amount of energy radiated by a real body in direction $\overrightarrow{\Omega}$, for a wavelength λ and at a temperature T, compared to the energy radiated by the reference black body at the same temperature:

$$\epsilon_\lambda(\overrightarrow{\Omega}, T) = \frac{L_\lambda(\overrightarrow{\Omega}, T)}{L^0_\lambda(T)} \tag{2.2.6}$$

The hemispherical spectral emissivity $\epsilon_\lambda^\cap(T)$ and the total emissivity $\epsilon^\cap(T)$ are obtained by integrating equation 2.2.6 over an hemisphere, and over the wavelength spectrum respectively. If the spectral emissivity does not depend on the direction, the body is called *Lambertian*; if the directional emissivity does not depend on the wavelength, the body is called *grey*.

Surface interaction: When incident radiation impacts a surface, the energy can be reflected, absorbed, or transmitted through the media (Fig. 2.9). Three adimensional spectral parameters are used to describe this phenomenon: reflectance $\rho_\lambda^\cap$ is the ratio of reflected over incident energy; absorbance α_λ is the ratio of absorbed over incident energy, and transmittance τ_λ is the ratio of transmitted over incident energy.

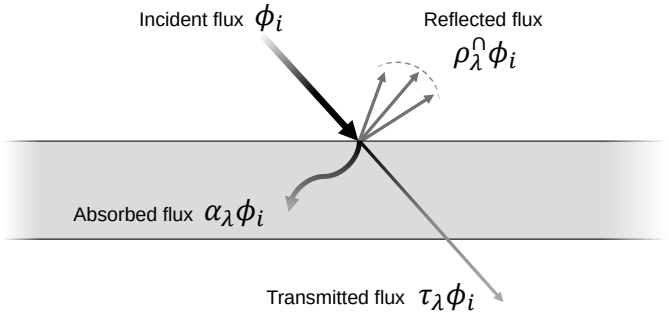

Figure 2.9 – Incident flux on a real body

The energy balance allows to relate these parameters (Kirchhoff's law):

$$\alpha_\lambda + \rho_\lambda^\cap + \tau_\lambda = 1 \tag{2.2.7}$$

An opaque material does not transmit the incident radiation: in this case, $\tau_\lambda = 0$ and the equation can be further simplified to $\alpha_\lambda + \rho_\lambda^\cap = 1$. At thermal equilibrium, the absorbed and emitted flux are equal, and therefore $\alpha_\lambda = \epsilon_\lambda$.

Reflection: The way the incident radiation is reflected depends on the surface roughness of the material. The two ideal cases of reflection are presented in Fig. 2.10: a *specular* surface reflects the incident flux in a direction symetrical to the surface normal, following Snell-Descartes law. Reflection can be considered specular when the surface roughness σ is small compared to the wavelength ($\frac{\sigma}{\lambda} \ll 1$).

Diffuse reflection corresponds to the scattering of the incident ray in multiple directions. An ideal diffuse reflection is called *Lambertian*: the radiation is reflected uniformly in all directions, and for all angles of incidence. The reflection can be considered diffuse when the surface roughness is large compared to the wavelength. In the general case, reflection of an incident flux can depend both of the angle of incidence, and the angle of observation. The distribution function describing the reflectance for all angles of incidence and observation is called the Bidirectional Reflectance Distribution Function (BRDF), and can be determined using Fourier-transform infrared spectroscopy. For an opaque material, the determination of the spectral emissivity depends solely on the knowledge of the reflectance.

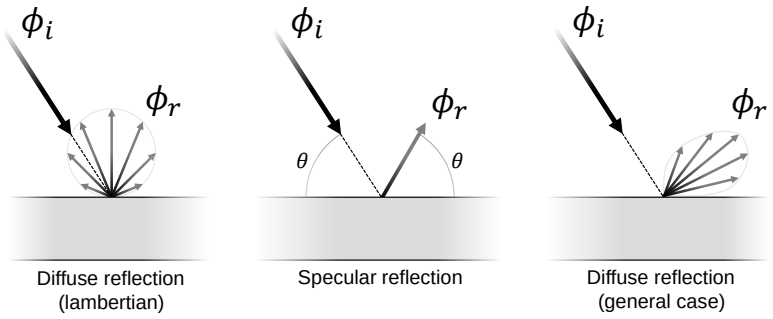

Figure 2.10 – Types of reflection

View factor: The view factor between two surfaces is defined as the fraction of energy exiting a Lambertian, isothermal and opaque surface A_i by emission or reflection, intercepted by a surface A_j. This dimensionless quantity is noted $F_{i\to j}$, and depends only on the geometry of the problem. The view factor is bounded to $0 \leq F_{i\to j} \leq 1$ by definition.

The case of two infinitesimal surfaces in arbitrary positions and orientations is presented in Fig. 2.11. The view factor $dF_{i\to j}$ representing the fraction of energy exiting dA_i and intercepted by dA_j can be expressed analytically as:

$$dF_{i\to j} = \frac{\cos\theta_i \cos\theta_j}{\pi r^2} dA_j \tag{2.2.8}$$

This quantity does not depend on the area of the emitting surface. For finite surfaces, the view factor $F_{i\to j}$ is the *average* over the surface A_i of the sum over A_j of the infinitesimal view factors $dF_{i\to j}$:

$$F_{i\to j} = \frac{1}{A_i} \int_{A_i} \int_{A_j} \frac{\cos\theta_i \cos\theta_j}{\pi r^2} dA_j dA_i \tag{2.2.9}$$

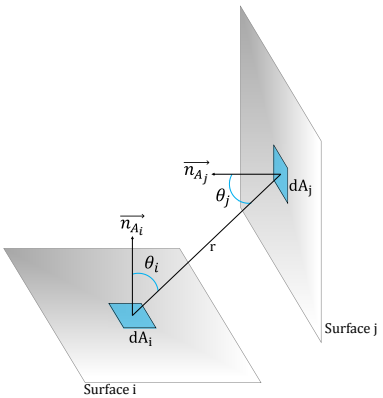

Figure 2.11 – View factor between two infinitesimal surfaces

When all surfaces considered in an enclosure are isothermal, opaque and Lambertian, the additional relations can be applied:

- Closeness: summing up all view factors from surface A_i in an enclosure, $\sum_j F_{i\to j} = 1$ as all emitted radiation must be absorbed
- Reciprocity: $A_i F_{i\to j} = A_j F_{j\to i}$
- Summation: $F_{i\to j+k} = F_{i\to j} + F_{i\to k}$

Direct integration of equation 2.2.9, either by analytical surface integration or transformation of the surface integrals to contour integral using Stokes' theorem as proposed by Sparrow and Cess [Sparrow+1978] is complex in non-trivial cases; a catalog of analytical view factors is compiled by Howell [Howell+2011]. The most common methods for the numerical resolution of the double integral are:

- **Unit sphere method.** This method initially developped by Nusselt [Modest2013] allows for the evaluation of the inner integral of equation 2.2.9, i.e. the view factor of an infinitesimal surface to a finite surface [Vueghs+2006]. It consists in placing an hemisphere of unit radius centered on the infinitesimal surface; the conical projection of the finite surface on the hemisphere is orthogonally projected on the base plane containing the infinitesimal surface, as shown in Fig. 2.12. The view factor is the fraction of the circle occupied by the projection.

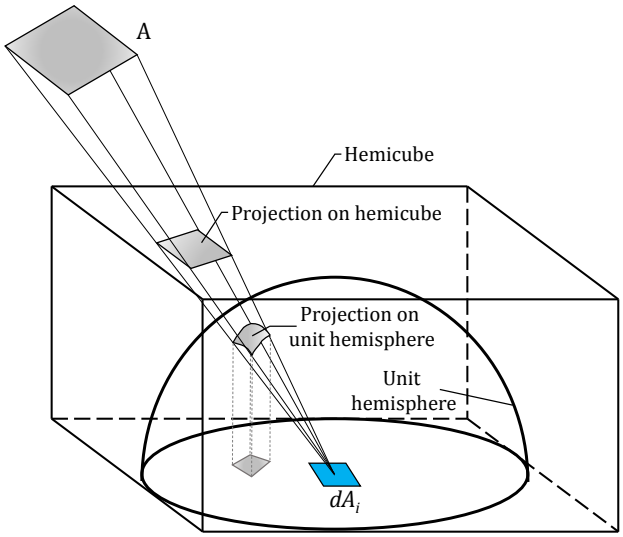

Figure 2.12 – Comparison between unit sphere and hemicube methods

- **Hemicube method.** The hemicube method [Cohen+1985] is a modification of the unit sphere method, where the finite surface considered is projected on a cube centered on the infinitesimal surface. The cube is discretized in a number of square cells associated

with a precomputed elemental view factor. For these methods, the evaluation of the outer integral in 2.2.9 is often conducted by averaging the view factor $F_{di\to j}$ for different points sampled on A_i.

- **Monte-Carlo method.** This statistical method consists in generating rays emitted from a source surface at angles defined by a probability density function. The view factor is then evaluated as the ratio of rays impacting the considered receiving surface, over the total number of rays emitted [Hoff+1989]. As this method is based on statistical sampling, the precision of the prediction is a function of the number of rays considered.

Radiative transfer equation: In a semi-transparent body, the energy balance of the emitted, absorbed, and diffused energy leads to the radiative transfer equation (RTE) which describes the mechanisms of radiative heat transfer in a participating media:

$$\frac{dL_\lambda(s,\overrightarrow{\Omega})}{ds} = -\beta_\lambda L_\lambda(s,\overrightarrow{\Omega}) + \kappa_\lambda L^0_\lambda(s,\overrightarrow{\Omega}) + \frac{D_\lambda}{4\pi}\int_{\Omega=4\pi}\Phi(\overrightarrow{\Omega'}\to\overrightarrow{\Omega})L_\lambda(s,\overrightarrow{\Omega'})d\Omega' \quad (2.2.10)$$

Where κ_λ is the absorption coefficient, D_λ the diffusion coefficient, $\beta_\lambda = \kappa_\lambda + D_\lambda$ is the spectral attenuation coefficient and $\Phi(\overrightarrow{\Omega'}\to\overrightarrow{\Omega})$ is a phase function representing the probability density of an incident ray propagating in direction $\overrightarrow{\Omega'}$ to be diffused in the direction $\overrightarrow{\Omega}$. This equation describes the change of radiation along ds as the sum of the losses by absorption and diffusion, and the gain by self-emission and inward diffusion.

Heat equation The evolution of temperature in a volume element heated by radiative heat transfer is described by the heat equation, which expresses the conservation of energy:

$$\rho C_p\frac{\partial T}{\partial t} = -\nabla\cdot(-\kappa\nabla T + q_r) \quad (2.2.11)$$

Where ρ is the density, C_p the specific heat capacity, κ the thermal conductivity (a second order tensor in the case of composite materials), and q_r the radiative source term expressed as a function of radiance:

$$q_r = \int_0^\infty\int_{4\pi} L_\lambda(s,\overrightarrow{\Omega})\overrightarrow{s}\,d\Omega d\lambda \quad (2.2.12)$$

In the case of opaque materials, the radiative source term expressed in Eq. 2.2.12 is reduced to a surfacic heat flux that can be considered as a boundary condition.

2.2.3.2 Modelling approaches

Given the complexity of the radiative transfer equation in the general case, research on modelling infrared heating is highly dependent on the progress in computer performances, and is therefore quite recent. Some of the earliest work on radiative transfer models for thermoforming is presented by Brinken and Potente [Brinken+1980]. An energy flow diagram adapted to the thermoforming heating phase of various neat thermoplastics is presented. The temperature inside the thermoplastic sheet is calculated considering one-dimensional

conduction through-the-thickness, with boundary flux conditions being correlated from thermocouple measurements. This simple model doesn't take into account the losses due to the view factor between the heater element and the sheet, nor those due to the flux reflected by the sheet.

Several models to describe the temperature evolution of a composite blank during the preheating operation have been developed in the frame of a BRITE/EURAM funded project [BRITEEURAM1992]. Monaghan et al. proposed an analytical model for the preheating stage of diaphragm forming conducted inside an autoclave [Monaghan+1991]. The analysis is based on experimental determination of convective transfer coefficients, and a view factor radiosity method for the computation of the radiative heat transfer: the cylindrical interior of the autoclave is discretized as a 10-surfaces parallelepiped and the view factors are determined from analytical correlations for flat plates, assuming that all surfaces are isothermal, opaque, diffuse and grey. Comparisons between the model and experimental data show a good agreement for the heating of thermally thin brass plates at high and low emissivities, where radiation represents 30–50% of the total heat transfer.

This model has been further developed to include one-dimensional conduction for the heating of a stack of carbon/PEEK unidirectional composite [Sweeney+1995], with the heat flux calculated by the radiosity enclosure method being used as a boundary condition. The effect of the heater bank-to-plate distance, power density and one- or two-sided heating on the through-the-thickness temperature distribution and preheating time was investigated to propose optimal preheating parameters as a function of laminate thickness.

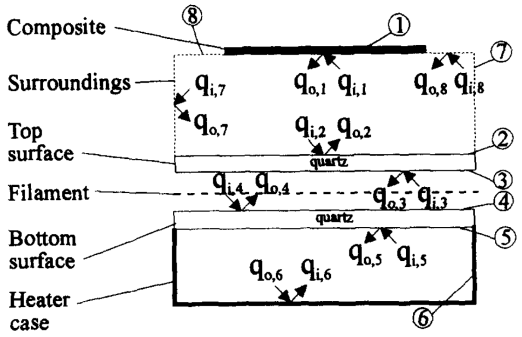

Figure 2.13 – Enclosures considered for analysis of heat transfer between quartz heaters and composite panel [Brogan+1996]

Brogan et al. [Brogan+1996] extended the approach by modelling the interaction between the heater filament and quartz, removing the need for the determination of effective heater temperatures and emissivities; the enclosures considered are presented in Fig. 2.13. The heat flux received by the composite panel was assumed uniform, and the heater bank treated as one combined heater i.e. no zoning was considered.

Discretization of the blank to consider two-dimensional conduction by finite differences was conducted by Cunningham et al. [Cunningham+1997; Cunningham+1998]. Transient temperature fields during infrared preheating and transfer from the oven to the forming

station are modelled, showing an overestimation of the steady-state temperature, and an underestimation of the temperature gradients during the transient phase (Fig. 2.14).

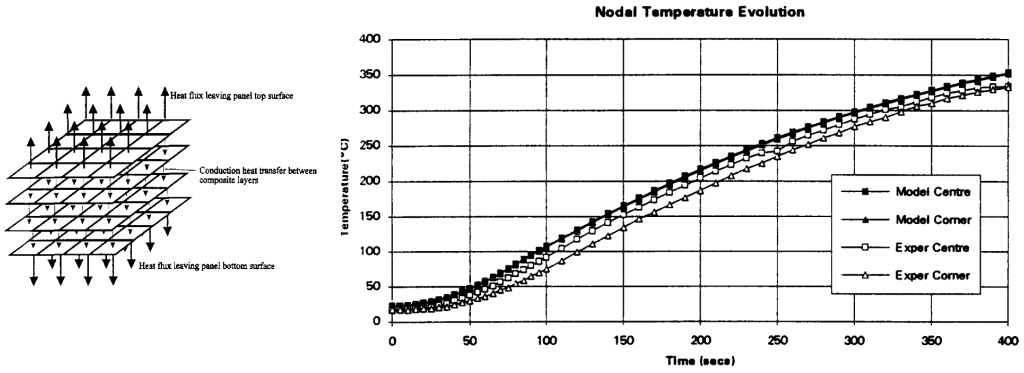

Figure 2.14 – Discretization of the blank and experimental and modelled evolution of temperature during infrared heating of carbon/PEEK unidirectional laminate [Cunningham+1998]

Finite element analysis with a radiosity method was used by Labeas et al. to investigate the heating phase of the diaphragm forming process of carbon/PEI plates [Labeas+2008]. The finite element model used is presented in Fig. 2.15: the halogen lamps are modelled explicitly, with the filament temperature calculated as a function of the electrical power from the energy balance proposed in [Pettersson+2000]. An optimization procedure to minimize temperature gradients in the blank as a function of the blank thickness and the process parameters (number of lamps, power and distance of the heaters to the blank) is conducted with a zero-order method, showing strong dependence between the process variables. A thermomechanical simulation of the forming phase is also proposed to optimize the mould temperature. Only tension modes are considered, which is not representative of the behaviour of woven composites (see section 2.3).

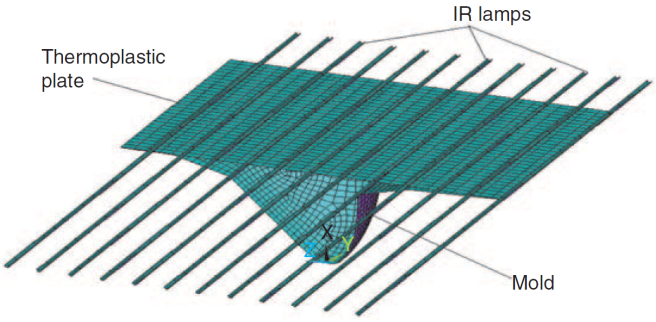

Figure 2.15 – FE model of infrared preheating in diaphragm forming [Labeas+2008]

A finer description of the halogen sources is proposed in Monteix et al. [Monteix2001]. The coiled filament is modelled as a cylinder of equivalent diameter to represent the actual

geometry of the emissive surface of the coil:

$$d_{w_{eq}} = \frac{d_w}{2}\left(\pi + \frac{e_w}{d_w}(2-\pi)\right) \tag{2.2.13}$$

Where d_w and e_w are the diameter and width of a single coil as represented in Fig. 2.16. The halogen lamp temperatures are calculated assuming an isotropic source, with a uniform temperature. The participation of the quartz tube is shown to be less than 2% of the total radiant emittance and can be neglected, given the relative temperature of the tube and the filament.

A numerical model using a control volume method has been developed by Schmidt et al. [Schmidt+2003] to simulate the heating stage of the thermoforming of thermoplastic sheets. The sheet and lamp are discretized in volume elements, and calculations of the surface integrals that appear in the view factors definition is done using Stokes theorem, i.e. by transforming those integrals in equivalent contour integrals as in [Rao+1996]. The model takes into account the spectral properties of the filament and material. The radiative source term inside of the sheet is computed considering a one-dimensional exponential flux attenuation given by Beer-Lambert's law. Reflection is not taken into account, which is a limiting point of this approach.

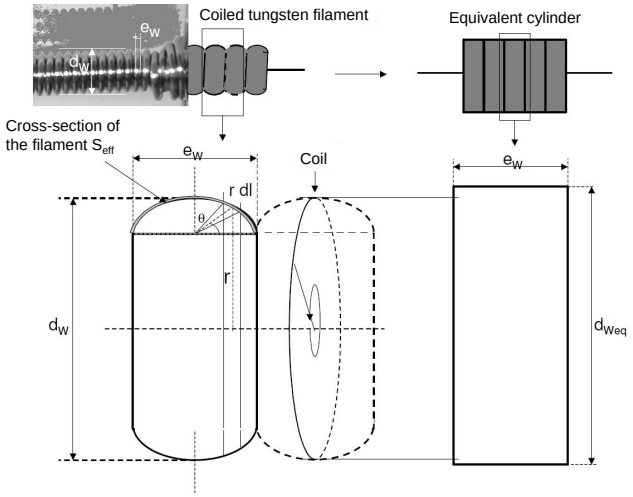

Figure 2.16 – Equivalent diameter of a coiled filament [Monteix2001]

A more physical numerical solver is proposed by Andrieu [Andrieu+2004; Andrieu2005], using the ray tracing framework presented in [Cai1992] for the calculation of view factors. This method consists in discretizing the flux emitted in every material point by arrays which directions depend on the emitter properties. This method takes into account the optical phenomenon including specular and diffuse reflection, and can treat three dimensional problems: complex reflector shapes can be modelled. The accuracy is limited by the number of rays [Maxwell+1986] which can greatly increase the computation time. The absorption in the polymers is treated with the Rosseland approximation, so the propagation of radiation inside the polymer is considered as an equivalent "radiative" thermal conductivity. This

method has been further developed in work from Champin and Bordival [Bordival+2010; Champin2007], with the absorption modelled with the Beer-Lambert law. Most of these approaches were developed to describe the heating of semi-transparent PET preforms for blow-moulding applications.

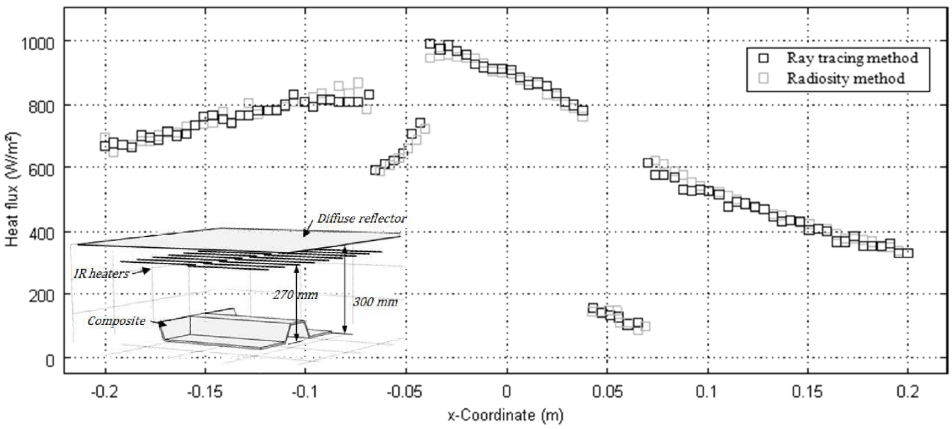

Figure 2.17 – Comparison between simulated heat flux from radiosity and ray-tracing methods [Nakouzi+2011]

Nakouzi [Nakouzi+2011; Nakouzi+2012] compared the software developed by Cosson [Cosson+2010], based on ray tracing (RAY-HEAT), with a radiosity method implemented in commercial finite element software COMSOL Multiphysics, for the curing phase of RTM manufactured thermoset composite parts. The precision of the former is limited by the number of rays emitted and the emission polar diagram, and the refinement of the mesh respectively. Although the radiosity method can only be applied to diffuse and opaque surfaces, the shorter computation time and versatility makes it interesting on an industrial standpoint. This approach was also used in [El Bakali+2013] for studying the thermoforming of composites.

Improved ray tracing based methods have been proposed to tackle complex radiative heat transfer problems for which the radiosity method is not adapted (semi-transparent participating flow, etc.), making use of the embarrassingly parallel nature of the ray generation and GPU acceleration to limit the computational time [Mazumder+2000; Silvestri+2019; Tanaka+2015]. Given the rather simple geometry of the enclosure considered during thermoforming, and the difficulties associated with the implementation of these advanced ray tracing algorithms, the radiosity method has been used in this work.

2.3 Thermomechanical modelling of the forming phase

2.3.1 Mechanical behaviour of woven fabrics and characterization methods

2.3.1.1 A multiscale problem

Composite materials are composed of a discrete reinforcement distributed in a continuous matrix. In the case of woven reinforcements, individual fibres are bundled in yarns, and yarns are woven to form a fabric. Different scales of observation can therefore be defined (Fig. 2.18):

- The microscopic scale is the scale of the fibres. Typical reinforcing fibres have diameters ranging between 5 and 15 µm for glass, 5 and 8 µm for PAN-based carbon fibres [Bunsell2011]. Each fibre is considered individually.
- The mesoscopic scale is the scale of the yarns (usual width from 0.5 to 5 mm). Each yarn is considered as an homogenized continuous medium. Representative volume elements, or unit cells, of the fabric are defined at this scale.
- The macroscopic scale corresponds to the scale of the woven fabric (from several centimetres to a few metres for large parts). At this scale, the fabric is treated as a continuous surface.

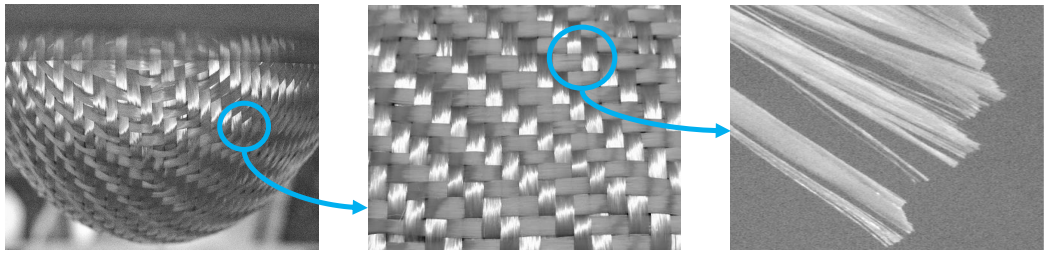

Figure 2.18 – Different scales of a composite reinforcement

The behaviour of the woven fabric at the macroscopic scale, which is the focus of this work, depends on the interaction between the constitutive elements at the smaller scales. An hypothesis on the mesoscopic behaviour is classically made to ensure the validity of the macroscopic approach: the absence of sliding between the warp and weft yarns at their crossover point is assumed (although second-gradient models proposed recently [Barbagallo+2016] allow for the prediction of sliding in a macroscale continuum approach, by introducing fictive elongation of the yarns). This nonsliding condition has been shown to be valid experimentally [Boisse+2005] far from the free edges of the fabric. Modelling approaches that can describe

the inter-yarn sliding are presented in Section 2.3.2.2. The next section introduces the principal modes of deformation at the macroscale during the forming of woven reinforcements, namely tension, in-plane shear and bending [Boisse+2011].

2.3.1.2 Macroscopic modes of deformation

Tension: In a woven fabric, the yarns are not perfectly straight as a certain amount of waviness, or *crimp*, is introduced by the weaving process. This is quantified by the ratio of a yarn apparent length in a fabric over its real length. This crimp leads to a non-linear tensile behaviour: as the warp or weft direction of the fabric is put under tension, the other direction being free, the yarns first straighten in the loading direction (this decrimping phenomenon is schematized in Fig. 2.19) before stretching [Cavallaro+2007].

The non-linearity is maximal when the fabric is under uniaxial tension, as the crimp in the loaded direction varies from its maximum value to zero. In the general case, both directions of the fabric are loaded, and the biaxial tensile behaviour of the fabric can be described for different strain ratios $k = \epsilon_{\text{orth}}/\epsilon_{\text{obs}}$, where ϵ_{obs} is the strain in the observation direction, ϵ_{orth} the strain in the orthogonal direction (i.e., $k = 0$ corresponds to uniaxial tension, $k = 1$ to equibiaxial tension).

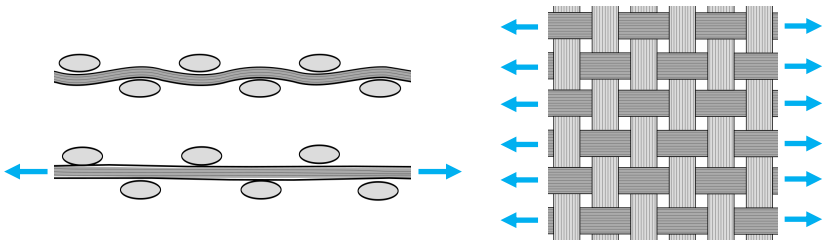

Figure 2.19 – Decrimping during uniaxial tension (plain weave)

Several researchers have investigated the biaxial tensile behaviour of woven dry fabrics [BuetGautier+2001; Gasser+2000; Kawabata+1973; Willems+2008]. The experimental setup and results in the case of a 2×2 twill carbon fabric are shown in Fig. 2.20. The two stages corresponding to the straightening and stretching of the yarns are clearly visible. The non-linearity observed at small loads on a single yarn is associated with misalignment at the microscopic scale of the fibres that compose the yarn.

In contrast with the amount of literature on the tensile behaviour of dry fabrics, only a few articles report on the tensile behaviour of thermoplastic composites at high temperatures, as the testing procedure (alignment of the yarns and clamping) is further complicated by the impregnation of the fabric with molten polymer. Abbassi et al. [Abbassi+2011] have conducted uniaxial and biaxial test results on a 5-harness satin carbon/PPS fabric at 320 °C; the authors however neglect the non-linear portion of the load-extension curve in the following analysis (the tensile behaviour of the fabric at high temperature is modelled by a constant elastic modulus).

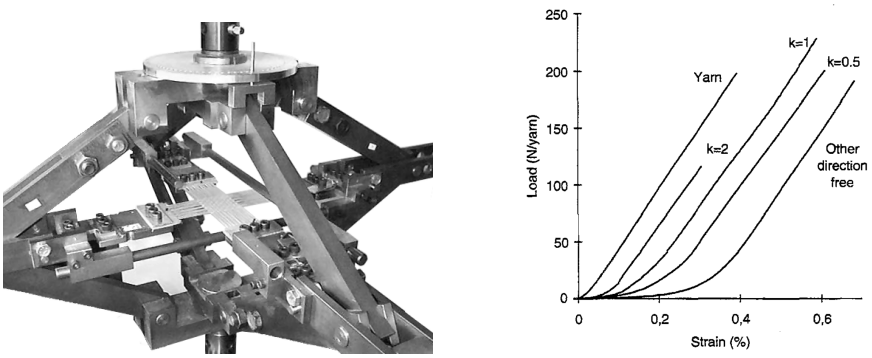

(a) Biaxial tensile device

(b) Biaxial tests on a 2×2 twill carbon fabric with different strain ratios

Figure 2.20 – Biaxial tensile behaviour of a woven fabric [BuetGautier+2001]

Uniaxial tests on glass/PEI samples at 330 °C are presented in [Suemasu+1994]. Two satin weaves (4- and 8-harness) are tested; the higher crimp ratio of the 4H fabric leads to a higher threshold strain between the straightening and stretching phase. Wang et al. [Wang+2014] present the influence of temperature on the tensile behaviour of single stretch broken carbon yarns commingled with PEEK and PPS. The results show a negligible influence of the temperature on the load/displacement curves (see Fig. 2.21a), with the exception of tests conducted above 380 °C on the PEEK-based yarns, where the diminution in viscosity allows slippage between the fibres which leads to a plateau with strains of up to 10% before failure. This behaviour is specific to stretch-broken yarns, and is not expected when yarns made of continuous fibres are used. Relaxation tests at the matrix melting temperature indicates that the viscous effect of the resin can be neglected in the tensile behaviour (Fig. 2.21b).

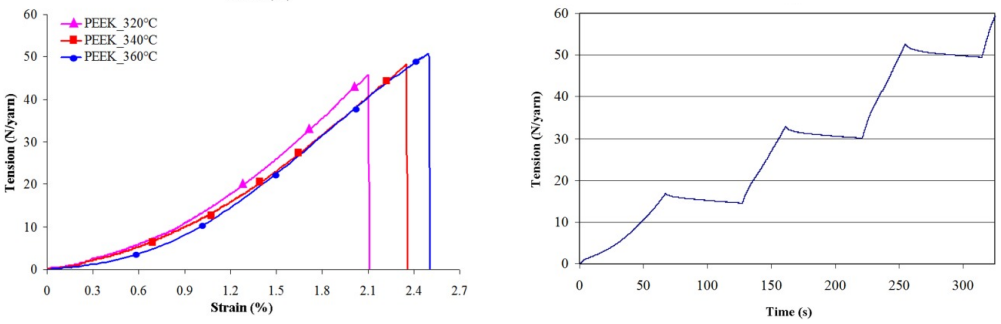

(a) Tensile tests on stretch-broken carbon/PEEK yarn

(b) Relaxation test on carbon/PPS yarn at 290 °C

Figure 2.21 – Determination of the tensile behaviour of stretch-broken commingled yarns at high temperatures [Wang+2014]

In-plane shear: In-plane shear at the macroscopic scale corresponds to the rotation of the yarns around their crossover point. Assuming the no-sliding condition between warp and weft yarns hold, the in-plane shear corresponds to trellising deformation. As the shear stiffness is

small compared to the tensile stiffness of the yarns, this is the main mode of deformation that allows the fabric to conform to double-curvature surfaces without buckling [Wang+1998].

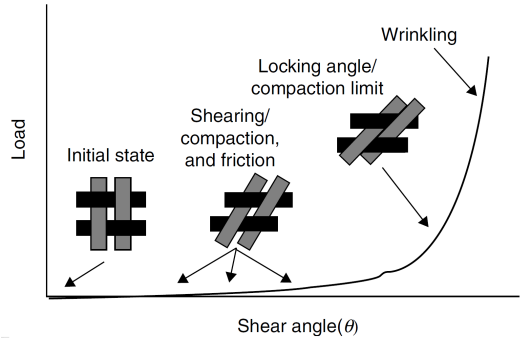

Figure 2.22 – Typical woven fabric shear behaviour [Sherwood+2012]

The typical shear behaviour of a woven fabric is presented in Fig. 2.22, where the shear angle represents the change in angle between the warp and weft yarns. The load versus shear angle curve is non-linear, and different zones can be defined. At small shear angles, the yarns are free to rotate around their crossover point (Fig. 2.23a). The observed load is small, and is associated with the dynamic friction between the moving yarns. As the shear angle increases, the yarns gradually come into lateral contact, and transverse compaction is observed (Fig. 2.23b).

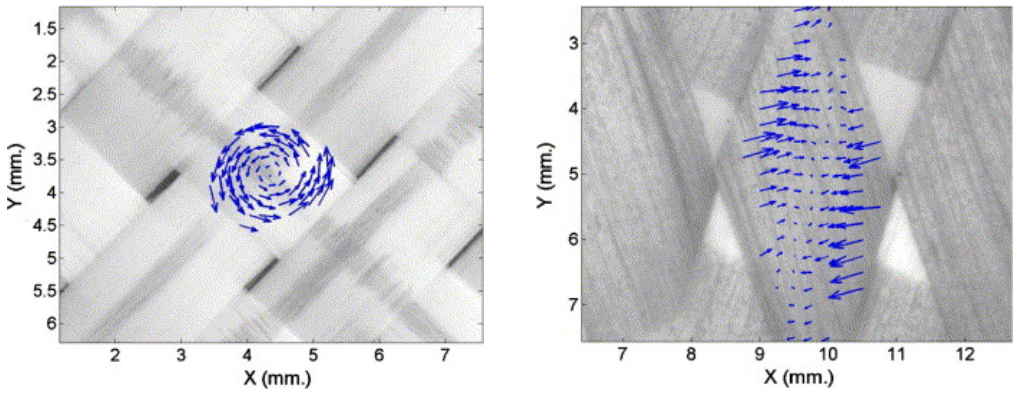

(a) Displacement field before locking angle **(b)** Displacement field after locking angle

Figure 2.23 – Displacement field in a yarn during fabric shearing [Dumont2003]

The angle of contact depends on the fabric, and can be estimated from geometric considerations, provided the width and spacing of the yarns are known [Prodromou+1997; Skelton1976]. The transverse compaction is associated with an increase of the observed shear force, which becomes large after the compaction limit of the yarns is reached. Out-of-plane wrinkling is frequently observed after this point as the energy associated with the transverse compaction of the yarns becomes higher than the energy associated with flexion modes. The *locking angle* of a fabric is usually defined as the shear angle corresponding to the onset of wrinkling [Long+2001; Sharma+2003], although it is sometimes associated with the transition between

the yarn rotation and yarn compaction zones. This parameter can be used as an indicator of the presence of wrinkles when simulating the draping of a woven reinforcement.

The two experimental tests that have been developed to investigate the in-plane shear behaviour of woven fabrics are the picture frame and bias extension test.

The picture frame test consists of clamping a square sample of woven fabric in a hinged rhombus frame. The yarn directions are initially parallel to the sides of the frame. One joint of the frame is fixed, and a tensile load is applied to the opposite joint along the diagonal with a universal testing machine (see Fig. 2.24). This leads to a state of pure shear in the sample [McGuinness+1998].

The theoretical shear angle depends only on the imposed displacement d and geometry of the sample (with L_c the initial side length):

$$\gamma(d) = \frac{\pi}{2} - 2\arccos\left(\frac{\sqrt{2}}{2} + \frac{d}{2L_c}\right) \tag{2.3.1}$$

This test has been widely used to study the in-plane shear behaviour of dry fabrics (notably in the benchmark study reported by Cao et al. [Cao+2008]) and thermoplastic composites at high temperatures [Harrison+2004; Lebrun+2003; McGuinness+1998], in which case the experimental rig is placed inside an environmental chamber. While the post-processing of the test results is straightforward thanks to the pure shear kinematics, the setup is complex, as a small misalignment of the sample can lead to high spurious loads because of the large tensile stiffness of the yarns [Chang+2003; Milani+2007].

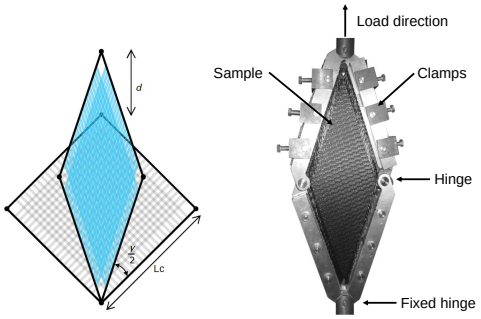

Figure 2.24 – Kinematics and experimental setup of the picture frame test [Guzman-Maldonado2016]

Ensuring an homogeneous temperature during testing can also prove difficult: the dwell time ensuring that the sample and clamping system equilibrate with the oven temperature are not always compatible with the thermal oxidation of the polymer [ElMazry+2013], and cold regions can often be observed close to the flanges [Harrison+2004]. The effect of temperature gradients can be mitigated by modifying the geometry of the samples (square vs. cross shaped), introducing slits or removing matrix and cross-direction yarns in the flanges [Dangora+2015].

In the bias-extension test, a rectangular sample of aspect ratio > 2 with yarns oriented at ± 45 deg is subjected to tensile loading in a universal test frame. The kinematics of the test are presented in Fig. 2.25.

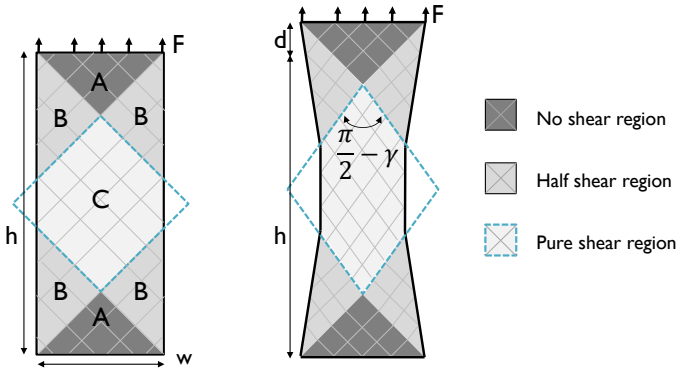

Figure 2.25 – Kinematics of the bias extension test

As the yarns in the central region of the sample are not clamped, and assuming no slippage between the warp and weft yarns, three distinct zones can be defined [Boisse+2016; Cao+2008]:

- Zone A: a non-sheared zone closest to the extremities of the sample, where all yarns have one end clamped
- Zone B: a half-sheared zone (shear angle $\gamma/2$), where the yarns in one of the fabric direction are free on both ends while the yarns in the other direction are clamped on one end
- Zone C: a central zone under pure shear (shear angle γ), where the yarns are free on both ends.

As none of the yarns are clamped on both ends, the tension is negligible; this test is thus less sensitive to misalignment of the yarns during setup, compared to the picture frame test. It is also less sensitive to temperature gradients, since the zones closest to the grips do not contribute to the recorded force. As for equation 2.3.1, a theoretical expression of evolution of the shear angle during the bias-extension test can be obtained from geometrical considerations (equation 2.3.2).

$$\gamma(d) = \frac{\pi}{2} - 2\arccos\left(\frac{\sqrt{2}}{2}\left(1 + \frac{d}{h-w}\right)\right) \tag{2.3.2}$$

This expression is however not valid for large displacements, where sliding between the yarns cannot be neglected [Zhu+2007], and optical measurements methods need to be used in this case. A normalised force, independent of the sample dimensions, can be derived from energetic considerations by equating the power of the axial force F with the power of the

shear torque in zones B and C [Härtel+2014; Launay+2008]:

$$F_{sh}(\gamma) = \frac{1}{(2h-3w)\cos\gamma}\left(\left(\frac{h}{w}-1\right)F\left(\cos\frac{\gamma}{2}-\sin\frac{\gamma}{2}\right)-wF_{sh}\left(\frac{\gamma}{2}\right)\cos\frac{\gamma}{2}\right) \tag{2.3.3}$$

This equation is recursive, as the normalised shear force at a shear angle γ depends on the normalised shear force at the half shear angle $\gamma/2$. It is solved incrementally, assuming linearity of the expression for small shear angles:

$$\lim_{\gamma\to 0} F_{sh}\left(\frac{\gamma}{2}\right) = \frac{1}{2}F_{sh}(\gamma) \tag{2.3.4}$$

Bias-extension tests have been conducted by several research groups to investigate the temperature and rate-dependent behaviour of preconsolidated thermoplastic composites [GuzmanMaldonado+2015; GuzmanMaldonado+2016; Harrison+2004; Machado+2016b] or commingled fabrics [Lebrun+2003; Zhu+2007]. A decrease of the shear stiffness is reported with an increase in temperature (see Fig. 2.26), as the viscosity of the matrix decreases and facilitates the relative movement of the yarns. This confirms the interest of taking into account the temperature of the blank during the forming simulation.

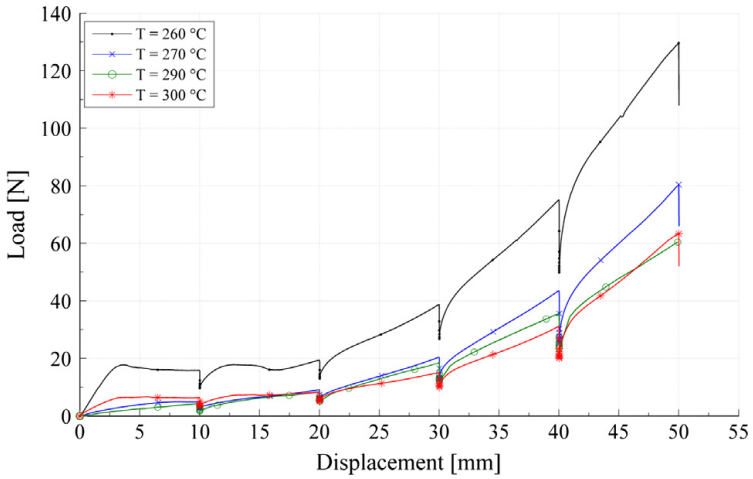

Figure 2.26 – Bias-extension tests on satin 8H glass/PA66 composites at different temperatures [GuzmanMaldonado+2015]

The influence of the shear rate on the shear behaviour is not as widely reported as that of temperature; results presented by Machado et al. [Machado+2016a] and Haanappel et al. [Haanappel+2014] show a slight increase of the shear stiffness with increased shear rate.

Bending: The bending stiffness of dry woven reinforcements is small, and as such it is usually neglected in process simulation [Chen+2015; Lin+2007; ten Thije+2007], as the apparition of wrinkles is controlled by the in-plane shear behaviour. The flexural behaviour of woven reinforcements has however been shown to affect the number and shape of the wrinkles, as presented in Fig. 2.27.

The experimental characterization methods and simulation approaches to take into account the bending stiffness of fabric reinforcements has been reviewed by Boisse et al. [Boisse+2018].

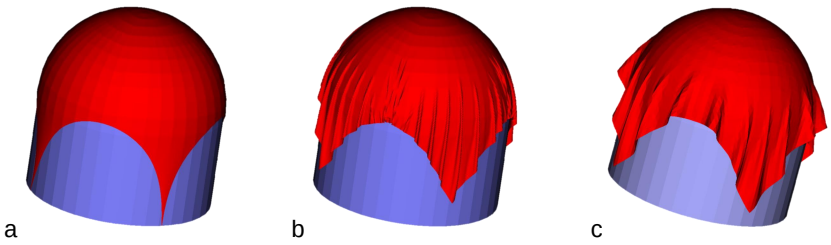

Figure 2.27 – Draping on an hemisphere with (a) tensile stiffness only, (b) tensile and in-plane shear stiffness, (c) tensile, in-plane shear and bending stiffness [Boisse+2011]

Only a small number of references discuss the influence of temperature on the bending behaviour of thermoplastic composites; Liang et al. [Liang+2014] and Guzman-Maldonado et al. [GuzmanMaldonado+2016] used a cantilever-type setup in an environmental chamber (Fig. 2.28a) to investigate the flexural properties of PEEK and PPS carbon satin, and PA66 glass satin respectively. A decrease of the bending stiffness with increasing temperature is observed, until a limit is reached after which the resin is melted and the bending stiffness is attributed entirely to the reinforcing fabric. The analysis has been conducted by increasing the temperature from 20 °C to a temperature above the melting point of the considered material; the effect of supercooling (the difference between the melt temperature and the crystallization temperature), which is relevant to the thermoforming process as the blank is cooled from the melt in the mould, is therefore not considered.

A modified Kawabata test mounted on a rheometer (Fig. 2.28b) was used for the characterization of unidirectional carbon/PEEK [Sachs+2014] and 2×2 twill glass/PA6 composites [Ropers+2016; Ropers+2017]. The temperature dependence reported is high, with a difference of approximately one order of magnitude on the bending moment between tests conducted at room temperature and at the melt temperature of the PA6.

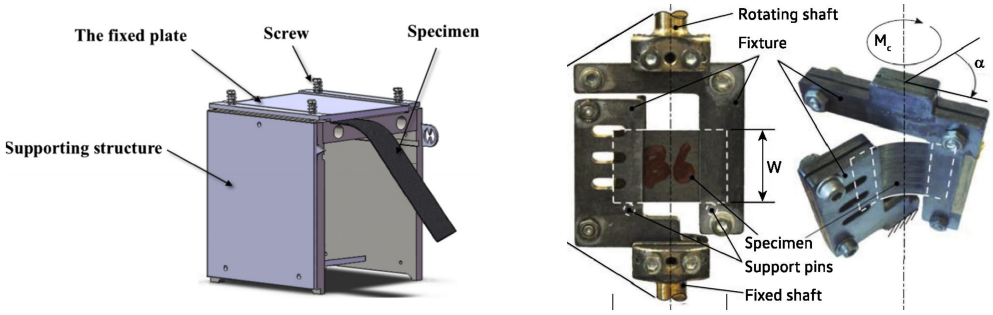

(a) Cantilever bending test [Liang+2014] **(b)** Kawabata bending test [Ropers+2016]

Figure 2.28 – Experimental methods for the characterization of the bending behaviour of thermoplastic composites

Tension-shear couplings: Couplings between different modes of deformation are usually neglected in forming simulation. The nature of woven reinforcements and the interactions between the warp and weft yarns can however lead to tension-shear couplings, where the shear

response of woven fabric depends on membrane tension. At the mesoscale, this is due to an increase in the compression contact forces at the crossover points from tension in the yarns, which in turn affects the shear behaviour. This has been first shown experimentally using a biaxial bias-extension setup [Sharma+2003]. While this study reported only a minor influence of the biaxial tests on the shear stiffness, other researchers [Harrison+2012; Willems+2008] present an increase of measured shear force by a factor 30 to 40 with an increase in transverse loads from 5 to 100 N .

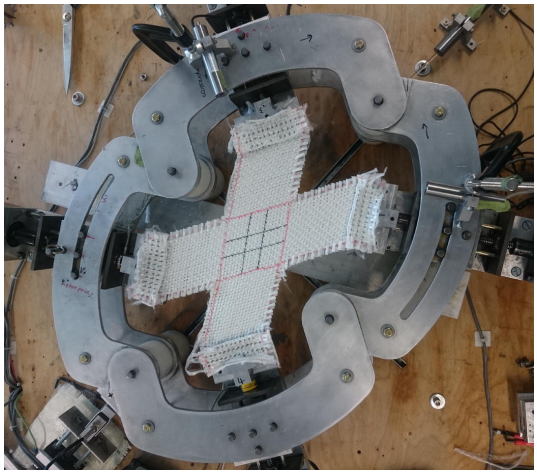

Figure 2.29 – Biaxial picture frame test [Kashani+2016]

The proper determination of coupling factors requires complex testing frames to control the tensioning of the fabric. Using a modified biaxial picture frame test, Nosrat-Nezami et al. [NosratNezami+2014] have derived coupling factors for different fabric architectures, showing that a higher filament count and lower weave density (twill weave compared to plain weave) increases the tension-shear coupling effect. Kashani et al. [Kashani+2016; Kashani+2017] developed the setup presented in Fig. 2.29 to investigate couplings in a commingled glass/PP plain weave. Results suggested that the effect of yarn tensioning on shear should not be neglected in process simulation, while tension-tension couplings and shear-tension couplings have a less significant influence on the material behaviour. The materials used in the literature are either dry fabrics or commingled prepregs; as such, no results on the effect of temperature on coupling factors for woven thermoplastic materials are reported.

2.3.2 Modelling the behaviour of woven fabrics

As presented in section 2.3.1.1, the mechanical behaviour of a woven composite can be considered at different scales. Forming models have been extensively researched in the literature, and have recently been reviewed by Gereke et al. [Gereke+2013] and Bussetta and Correia [Bussetta+2018]. The main modelling approaches developed at each scale will be presented in this section, with an emphasis on simulations conducted at the macroscale.

2.3.2.1 At the microscale

Simulation approaches at the microscale aim at modelling the behaviour of woven fabrics from their simplest constituents, i.e. the fibres. Individual fibres can be described as three-dimensional beams with an orthotropic linear behaviour. These approaches have been derived from models developed for steel cables [Nawrocki+2000] and adapted to woven fabrics [Durville2002; Durville2009], braided structures [Vu+2015; Zhou+2004] and more recently 3D interlock fabrics [Daelemans+2016; Durville+2018].

The difficulty associated with the microscale approach lies in the extremely high number of contact-friction interactions between the fibres: usual commercial tows contain from 3000 to 12 000 fibres. To reduce the computational cost, larger *virtual fibres* that represent a bundle of fibres are used (see Fig. 2.30: 48 virtual fibres are modelled per tow, resulting in approximately 100 000 contact elements). The simulations are limited to a few unit cells, and are used to predict the microstructure of a woven fabric based on simple input properties (yarn stiffness, weave style) or the mechanical behaviour of the reinforcement without the need of complex constitutive laws.

While considering the microscale leads to a fine description of the behaviour, the simulation of the forming of an industrial part of large dimensions is not possible at this stage.

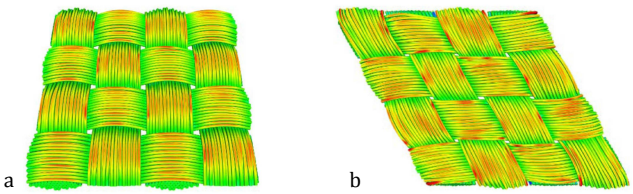

Figure 2.30 – Initial (a) and sheared (b) configuration of a plain-weave fabric (48 virtual fibres per tow) [Durville2010]

2.3.2.2 At the mesoscale

Models at the mesoscale consider yarns as a continuous media. They are used principally to obtain homogenized properties at the macroscale (mechanical behaviour [Jauffrès+2009], fabric permeability [Loix+2008; Zeng+2014] or thermal properties [Dasgupta+1996; Li+2011]), when experimental characterization is complex.

These approaches are based on a simplification of the real geometry of the representative unit cell of a fabric. In Kawabata et al. [Kawabata+1973], yarns are modelled by linear bar elements (Fig. 2.31) with elastic tensile behaviour, and the interactions between yarns are approximated by spring elements at the intersection points. While this model can predict the biaxial tension behaviour of fabrics, it is not adapted for the determination of the shear behaviour, and a more precise description of the yarn geometry is needed, either modelled from the characteristics of the fabric or obtained experimentally.

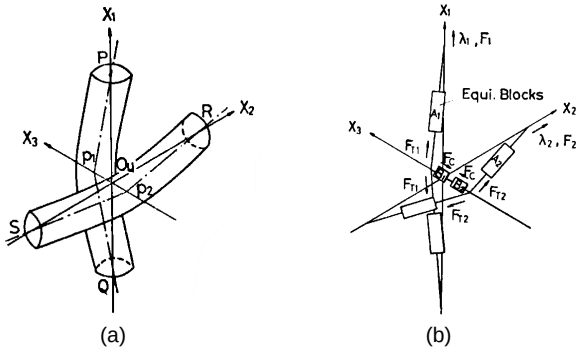

Figure 2.31 – Unit structure (a) and equivalent model (b) of a plain-weave fabric [Kawabata+1973]

Characterization of the unit cell geometry: Micro-computed tomography (or μCT) [Maire+2001] is the most commonly used technique for the experimental characterization of the mesoscale geometry of a woven fabric. Three-dimensional volumetric data can be obtained from X-rays cross-sections of a fabric sample, with resolution (voxel size) in the micrometer range. The yarns and matrix phase are segmented and reconstructed using various image analysis techniques [Latil+2011; Naouar+2014], and meshed models can be generated for finite element analysis. This method has been adapted recently for the in-situ characterization of the mesostructure and fibre distribution in yarns during shear tests for dry fabrics [Badel+2008b] and preconsolidated composites at high temperatures [Gassoumi+2017].

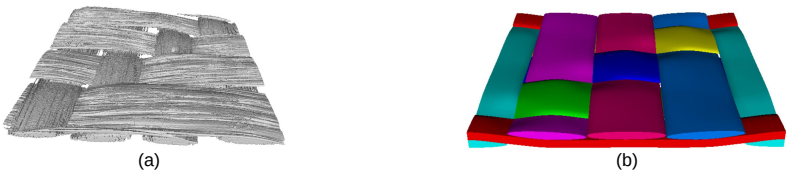

Figure 2.32 – μCT reconstruction (a) and TexGen model (b) of a Chomarat 4H satin glass fabric [Sherburn2007]

Alternatively, various softwares have been developed to model the mesoscale geometry of a reinforcement. *WiseTex* [Lomov+2000; Verpoest+2005] derives the geometry of the unit cell by minimising the deformation energy of the yarns, taking into account tension, compression, bending, torsion and friction. This relies on extensive mechanical characterisation of the yarn behaviour which can prove complex. *TexGen*, developed at the University of Nottingham [Lin+2011; Sherburn2007], is based solely on geometrical considerations: yarns paths are generated with periodic Bezier splines from the fabric parameters (yarn spacing, fabric thickness...) and volume elements are created by propagating a cross-section surface along the yarn path. The resulting geometry shows good agreement with experimental measurements, as is presented in Fig. 2.32. The architecture defined at the mesoscale can be subsequently

used in finite element analysis using a suitable material model to describe the behaviour of the yarns.

Mechanical models: The yarn is usually considered as a transversely isotropic material. Its mechanical behaviour has been modelled through hyperelastic [Charmetant+2011] or hypoelastic [Badel+2008a; Gasser+2000] laws, taking into account elongation, yarn compression and in-plane shear. Periodic boundary conditions have to be applied to the boundaries of the representative unit cell. The results of a virtual shear test on a plain weave fabric modelled at the mesoscale is shown in Fig. 2.33a.

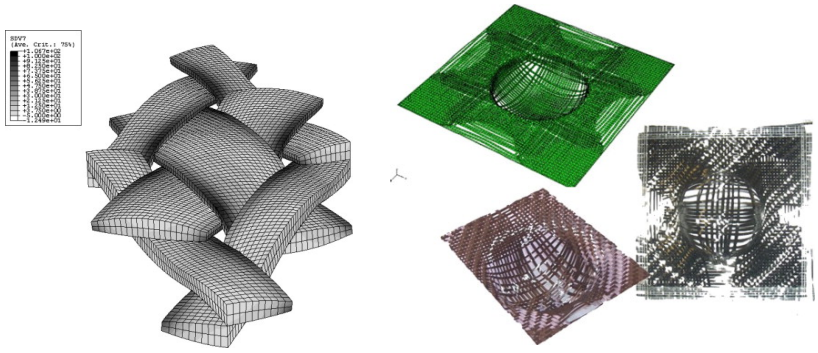

(a) Sheared unit cell [Badel+2008a] **(b)** Forming simulation showing yarn sliding [Gatouillat+2013]

Figure 2.33 – Simulations at the mesoscopic scale

The mesoscale modelling of woven structures at a scale larger than the unit cell is common in simulations of ballistic impact, where yarn pull-off, tensile elongation and rupture are the principal modes of energy absorption [Duan+2006; Nilakantan+2010]; simpler geometrical models based on coarse volume meshes or planar elements are used. Applications to woven composite forming are more recent: Gatouillat et al. [Gatouillat+2013] used a simplified geometry to successfully predict the loss of cohesion of the woven network during hemispherical forming when high blankholder loads are used. Mesoscale approaches are more frequently used to model the draping of non-crimp fabrics (NCF), although simplification of the yarn geometry is required [Creech+2006; Tavana+2012]. While these approaches allow for a finer prediction of the deformation of the fabrics during draping, the number of contact pairs associated with the discrete description of the yarns leads to an increased computational time compared to continuous approaches [Thompson+2018b].

2.3.2.3 At the macroscale

Two categories of models developed at the macroscale can be considered: kinematic approaches, and mechanical models.

Kinematic approaches: The models developed to simulate the draping of woven fabrics on curved surfaces were initially based on kinematic assumptions. The fishnet algorithm [Mack+1956] describes the fabric as a set of pin-jointed bars. The main assumptions made are the inextensibility of the bars, free rotation at the pin joints and the absence of sliding

between the fabric and the forming tool. The intersection points are generated by propagation from an initial point, with constant yarn spacing and a contact constraint between the new intersection point and the forming tool. As analytical equations for two-dimensional surfaces are accessible for simple geometries only, numerical methods are often used (Fig. 2.34). The accuracy of the algorithm can be increased by constraining the path between two intersection points to a geodesic curve [Heisey+1988].

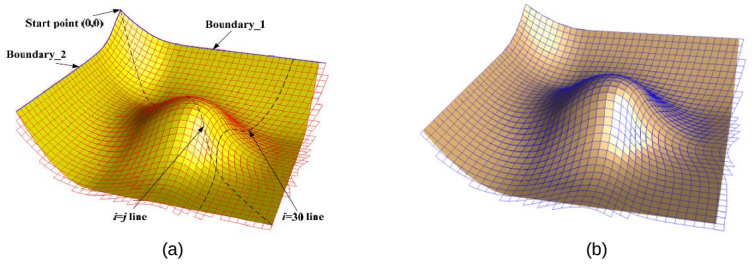

Figure 2.34 – Draping of a non-developable surface (a) fishnet algorithm, (b) PAM-QUIKFORM simulation [Yang+2014]

Alternatively, energy-based approaches have been proposed [Weeën1991], where elements are generated by minimizing the elastic energy to obtain intersection points: the inextensibility constraint on the fabric is lifted. These kinematic methods, while computationally efficient, do not give information on shear-induced defects such as wrinkles. The influence of the material weave style, yarn properties, or processing parameters such as blankholder load, cannot be determined. The applications are limited to the evaluation of the drapability of non-developable surfaces.

Mechanical models: Mechanical models developed at the macroscale consider the laminate as an homogenized continuous material, which is a valid hypothesis if the non-sliding between warp and weft yarns is respected (Section 2.3.1.1). Various constitutive laws have been developed in large deformations assumptions within hyperelastic frameworks [Charmetant+2011; GuzmanMaldonado+2015], in which the stress-strain relationship derives from a strain energy density function, or hypoelastic frameworks [Khan+2010; Machado+2016a; Peng+2005] (with the stress-strain relationship expressed in terms of rate), and implemented in finite element softwares. The tracking of the anisotropy directions during forming is necessary to obtain realistic results. The general expression of a hypoelastic law is presented in Eq. 2.3.5:

$$\boldsymbol{\sigma}^{\nabla} = \mathbf{C} : \mathbf{D} \tag{2.3.5}$$

Where $\boldsymbol{\sigma}$ is the Cauchy stress tensor, $\mathbf{C}$ is a fourth-order constitutive tensor and $\mathbf{D}$ is the strain rate tensor. $^{\nabla}$ represents an objective derivation operator, independent of the reference frame. This allows avoiding the apparition of spurious stresses from rigid body rotations. The objective derivative of the stress tensor can be expressed as in Eq. 2.3.6:

$$\boldsymbol{\sigma}^{\nabla} = \mathbf{Q}\left(\frac{d}{dt}(\mathbf{Q}^{\intercal}\boldsymbol{\sigma}\mathbf{Q})\right)\mathbf{Q}^{\intercal} \tag{2.3.6}$$

Where **Q** is an *adequate* rotation tensor. Badel et al. have shown that classical objective derivatives used in finite element softwares, such as the Green-Naghdi derivative where **Q** is the rotation of the polar decomposition of the deformation gradient tensor, or the Jaumann derivative based on the material spin, are not objective in the case of woven materials where the orientation of the principal directions can change during deformation, and that a derivative based on the rotation of the yarns has to be used [Badel+2008a]. The objective nature of the derivation allows for a simpler expression of the material constitutive law, as it can be expressed in a frame fixed with the yarns, however the numerical implementation is more complex.

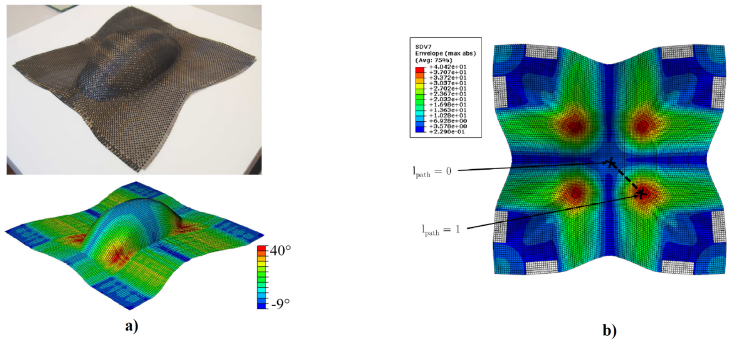

Figure 2.35 – (a) Experimental layup and simulated shear angle field on a hemi-ellipsoid mould [Pierce+2014], (b) hemispherical forming simulation of a glass/PP twill fabric [Machado+2016a]

Pierce et al. [Pierce+2014] implemented this hypoelastic approach to model the draping of a dry carbon plain weave fabric in the frame of a global simulation of the liquid composite moulding process. Non-linear elastic tensile and shear properties were determined experimentally; bending of the yarns was neglected. Comparison between the predicted shear angle field and experimental results is presented in Fig. 2.35. This non-orthogonal approach has been used in a variety of configurations and validated on hemispherical tests [Machado+2016a; Machado+2016b; Peng+2005] and double-dome geometries [Khan+2010].

Different approaches have been proposed to take into account the matrix behaviour and coupling the effect of temperature in the forming simulation: in Cao et al. [Cao+2003], two subroutines and a switch based on contact conditions with the cold die were used to describe the behaviour of a commingled glass-polypropylene laminate at low and high temperature. As forming is a short operation, isothermal conditions are often assumed as a simplifying hypothesis [Haanappel+2014; Harrison+2013; Liang+2014; Machado+2016a; Wang+2012], with material properties characterized experimentally at high temperatures.

Guzman-Maldonado et al. [GuzmanMaldonado+2015; GuzmanMaldonado+2016] used an hyperelastic approach to describe the forming of a glass fibre/polyamide-6.6 prepreg, with a viscoelastic model for the shear behaviour of the matrix. The relaxation time, and shear strain energy were considered as linearly depending on the temperature, and fitted using an optimization algorithm. This assumption was validated experimentally for the 260–300 °C range only, and the effect of lower temperature as can be found during the cooling phase was

not investigated. A weak coupling between the mechanical deformation and the heat transfer problem was used, with the temperature field and strain field being updated sequentially. Thermo- and shear-dependent thermal properties were used for the PA66/glass satin fabric considered. The simulated evolution of the temperature during the forming of an industrial part is represented in Fig. 2.36.

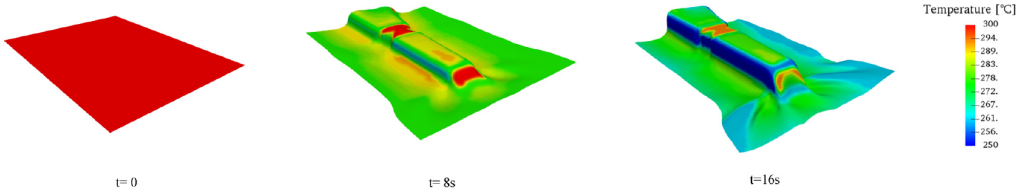

Figure 2.36 – In-plane temperature distribution during forming [GuzmanMaldonado+2016]

Machado et al. [Machado+2016b] proposed an expression of the shear modulus based on a phenomenological multiplicative decoupling between the effects of temperature and shear rate, and conducted transient simulations taking into account heat losses from conduction with the tool and convection. The thermal properties of the materials were considered constant. In the literature reviewed, the blank temperature was always assumed to be uniform at the beginning of the forming stage.

2.4 Forming of non-consolidated preimpregnated fabrics

The thermoforming of thermoplastic composites is usually conducted with blanks that have been manufactured through autoclave or press consolidation. The preconsolidation step is time and energy consuming, and the resulting blanks prove to be expensive for high volume applications [Renault2015].

Additionally, the preheating stage is, with the exception of contact heating methods and diaphragm forming, conducted without the application of pressure. This can lead to deconsolidation of the blank, through thermal expansion of entrapped dissolved moisture and decompaction of the fibre bed from release of frozen-in stresses [Donadei+2018; Slange+2018; Ye+2005]. The deconsolidation of a thermocompressed laminate is presented in Fig. 2.37.

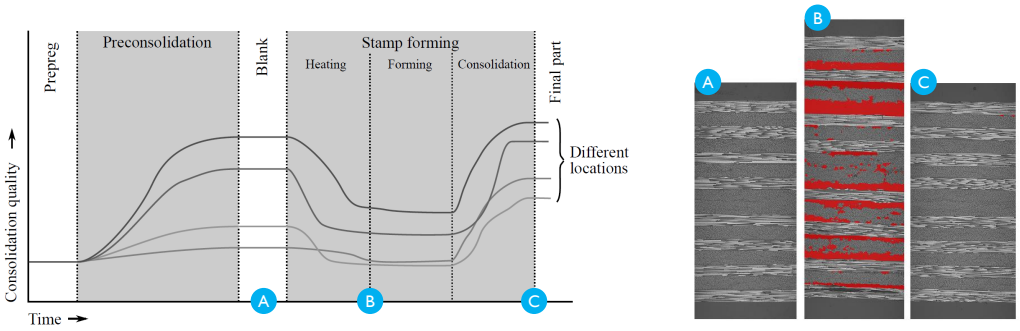

Figure 2.37 – Schematic representation of the evolution of consolidation quality during processing and micrographs of a unidirectional carbon/PEEK laminate after press forming consolidation, infrared heating and stamp forming (voids in red) [Slange+2016]

Consequently, the use of non-consolidated preimpregnated fabrics as blanks for the thermoforming process appears as an interesting alternative and a cheaper precursor, provided simultaneous forming and consolidation can be achieved [Bourban+2001]. Isothermal forming from a stack of non-consolidated plies manufactured by tape layup was shown possible by Cakmak and Dutta [Cakmak+1991]. Experimental studies on the direct forming of non-consolidated thermoplastic prepregs are presented in the following sections for the principal types of semi-products available.

2.4.1 Commingled fabrics

Fabrics manufactured from commingled yarns presents a number of advantages compared to other semi-products such as powder towpregs or powder coated fabrics. The degree of commingling results in short polymer flow distances for impregnation, which reduces the consolidation times; in addition, they present a drapability at room temperature similar to that of a dry fabric [Bernet+2001; Svensson+1998].

The mechanisms controlling the consolidation of these semipregs have been extensively studied, with various fibre/matrix combinations. The main parameters influencing the

quality of the impregnation are the degree of commingling [Van West+1991; Ye+1995] (which describe the homogeneity of the repartition of the polymer fibres in the yarn), pressure [Patou+2018] and temperature [Bernet+1999] (see Fig. 2.38).

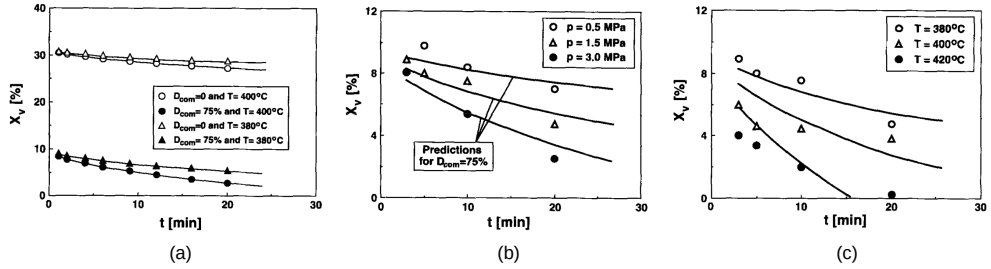

Figure 2.38 – Evolution of void content in a commingled AS4/APC2 composite as a function of: (a) commingling quality, (b) pressure and (c) temperature [Ye+1995]

The direct stamp forming of commingled fabrics is associated with short consolidation times. Bernet et al. obtained CF/PA12 laminates with high void contents (>8%), and suggested that a preconsolidation to void contents lower than 4% was sufficient to obtain laminates with acceptable residual voids [Bernet+2001]. A parametric study was conducted by Wakeman et al. [Wakeman+1998] on the forming of flat laminates from glass/polypropylene twill fabric, and concluded that the preheating temperature was the most influential parameter on the consolidation quality, with optimal parameters allowing for the manufacturing of laminates with approximately 1% void content with press times shorter than one minute.

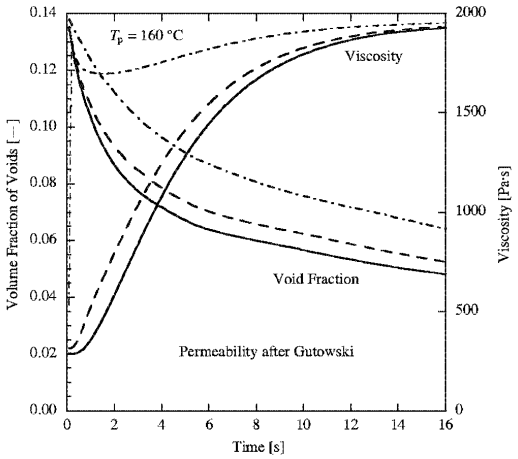

Figure 2.39 – Modelled evolution of void content and viscosity during the consolidation of commingled fabrics [Thomann2003]

Thomann [Thomann+2004; Thomann2003] developed a model to predict the evolution of void content during the stamp forming of commingled composites by coupling a one-dimensional heat transfer model with an impregnation model, taking into account thermodependent viscosity and thermal conductivity. The results show that void content lower than 5% can be achieved using highly commingled yarns and thermally insulated moulds (Fig. 2.39). The

quality of the prediction is however affected by the model used to describe the permeability of the fibre bed.

The influence of process parameters on the mechanical properties of flat laminates thermoformed from commingled carbon/PA12 fabrics at different levels of pre-consolidation is presented in [Wakeman+2006]. In accordance with previous results, preheating temperature, tool temperature and preconsolidation quality are the most influential parameters, while the tool speed, pressure and consolidation time are not found to be significant. The evolution of compressive strength with the process parameters is presented in Fig. 2.40. The mechanical properties are significantly reduced for low preconsolidation levels.

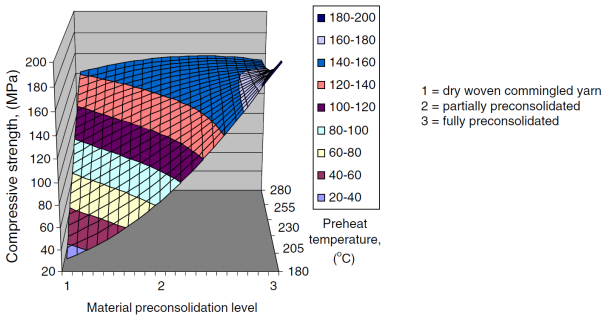

Figure 2.40 – Compressive strength versus thermoforming parameters [Wakeman+2006]

A square bowl geometry was formed in [TrudelBoucher+2006] for glass/polypropylene fabrics with different nominal weights and preconsolidation quality. While the mechanical properties of the laminate formed from the high nominal weight unconsolidated fabric were shown to be suboptimal compared to the compression moulding reference process, results for the low nominal weight fabric show very good flexural properties (Fig. 2.41).

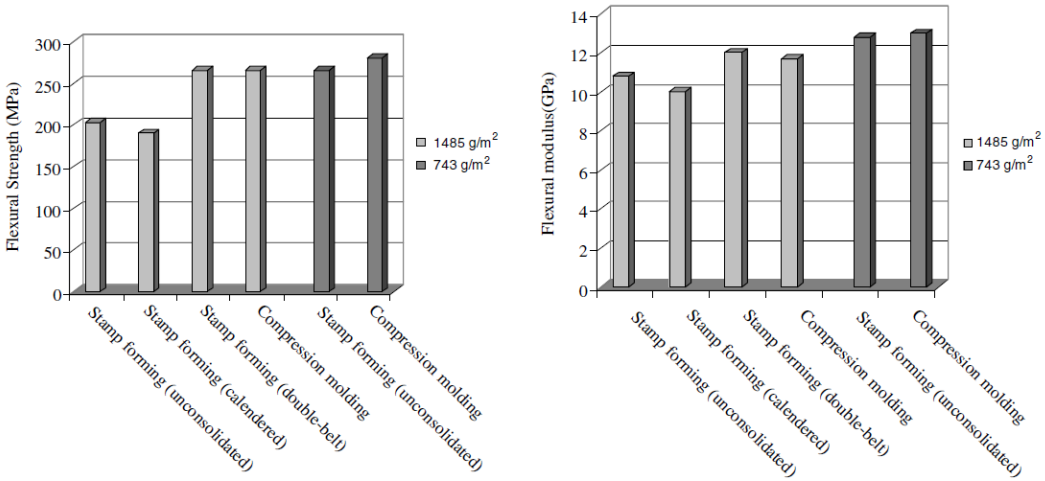

Figure 2.41 – Flexural properties of thermoformed composites from different preconsolidation levels [TrudelBoucher+2006]

The drapability of non-consolidated commingled fabrics has also been investigated at high temperature [Cao+2008; Jauffrès+2009; Lebrun+2003; Zhu+2007]. The influence of the level of preconsolidation of the shear behaviour is however not reported, and the forming quality on more complex geometries (hemisphere, double dome) is described in terms of shape defects (wrinkles etc.) rather than mechanical properties or void content.

2.4.2 Powder-impregnated fabrics

Two main categories of powder impregnated fabrics can be defined: powdered towpregs, or *Fibres Imprégnées de Thermoplastiques* (FIT) if the powder matrix slurry is deposited on the tows before the weaving process, and powder-coated fabrics if the powder is deposited after the weaving (in which case the matrix is present only at the surface of the plies, as is the case for PiPreg® materials [Porcher Industries2017]). Compared to commingled fabrics, this class of semipreg has the advantage of being easier to handle as the matrix distribution stabilizes the fabric: the thermoplastic powder effectively acts as a binder on the dry fabric, preventing fraying and displacement of the yarns during the cutting and kitting operations. The drapability at room temperature is however greatly impeded. Polymer powder is also sourced more easily than fibres, and the relative easiness of the impregnation process compared to commingling results in a usually cheaper semiproduct [Biron2007]. The literature on powder-impregnated composites is however not as developed.

The consolidation of FIT fabrics has been studied by Connor et al. [Connor1995], and modelled based on an idealized bridge geometry (Fig. 2.42). The impregnation rate is shown to be controlled mostly by the applied pressure, and resin viscosity, which is confirmed experimentally by tests on carbon/PEEK and carbon/PEI unidirectional laminates.

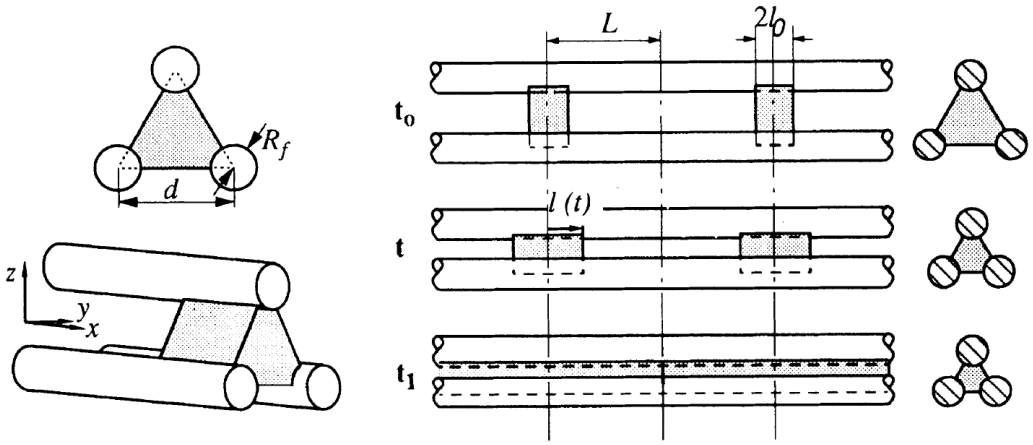

Figure 2.42 – Ideal bridge geometry for impregnation modelling [Connor1995]

The forming of more complex shapes was also investigated in [Connor+1995], where commingled fabrics and powder coated towpregs were used to form corrugated sheets with high processing rates, resulting in parts with void volume fraction <2% in both cases. Even though the commingled material required a higher processing temperature to reach this

void content, the comparison between the two precursor types is biased by variations in the viscosity of the PA12 grades used. Hemispherical shapes were also formed from FIT in [Cutolo+1992] using isothermal diaphragm forming, with cycle times of approximately one hour.

While several authors have studied experimentally the consolidation of powder-coated fabrics [De Almeida+2012; Meyer+2009; Patou+2018; SteggallMurphy+2010], showing the influence of processing temperature, pressure and dwell time, no study has been found on the feasibility of the direct forming of non-consolidated powder-coated fabrics on non-developable shapes, with a single article investigating the shear behaviour of thermoplastic PiPreg® materials at high temperatures [Wang+2012]. The influence of the preconsolidation on the drapability is not discussed.

2.5 Conclusion

The main steps involved in the manufacturing of thermoplastic composites parts by thermoforming (namely, infrared heating and mechanical forming) have been extensively studied in the literature, as a proper understanding of the physical phenomena involved is of an obvious interest for the optimization of this high volume industrial process.

Modelling approaches developed for the infrared heating step aim at simulating the temperature field in the blank during the preheating by solving the heat equation with a radiative source term, or radiative flux as a boundary condition. The characterization of temperature dependent thermal and optical properties of the heated material, as well as a fine description of the infrared lamps, is necessary. Simulations based on view factor computation for the determination of radiative heat flux are the most common, and the use of more physical approach based on ray tracing is not computationally efficient if diffuse and opaque surfaces are considered.

The main modes of deformation of a fabric during the draping on a non-developable surface are tension, in-plane shear, and bending. The associated characterization methods are not standardized, and the woven nature of the material leads to non-linear behaviours. For thermoplastic composites, the influence of the matrix viscosity on shear and bending is high, and these properties have to be characterized in the processing temperature range. Strong couplings between modes of deformation arise from interaction between yarns at the mesoscale; however, the experimental determination of coupling factors requires complex test set-ups, and shear-tension couplings are often neglected. While mechanical models have been defined at different scales, macroscale approaches are the most commonly used for draping applications as they can be easily scaled to industrial parts dimensions. The material is approximated by an homogeneous continuous media. The representation of the change in orientation of the anisotropy directions requires a specific implementation to ensure the objectivity of the formulations.

As mechanical models were originally developed for the draping of dry fabrics, the influence of temperature has only recently been introduced in forming simulation tools, even though

there is abundant literature on its effect on the formation of shape defects. Additionally, all the models reviewed assume a homogeneous temperature in the blank at the start of the forming operation, and no coupling with an infrared heating model to develop a global process simulation is proposed.

Finally, the direct forming of non-consolidated preimpregnated fabrics has been reviewed. Non-consolidated semipregs show potential as a cheaper alternative to preconsolidated blanks for high volume production, provided a good consolidation quality can be achieved; this is made easier with the development of low viscosity thermoplastic matrices. The experimental work presented in the literature is focused mainly on commingled fabrics; powdered prepregs, and specifically powder-coated fabrics, have barely been studied, and no evaluation of their shear behaviour as a function of preconsolidation quality is available.

This thesis aims at predicting the effect of the temperature distribution in the blank resulting from the infrared preheating step on shape defects generated during forming. To this end, two loosely coupled simulation tools are developed. In a first part, a numerical finite element model is introduced to solve the heat equation during the preheating of a composite blank in an infrared oven with tungsten halogen lamps, with the radiative heat transfer between the infrared sources and the blank computed using the radiosity method. In a second part, the simulated temperature field at the end of the preheating is used as a boundary condition in a finite element forming simulation based on a non-orthogonal, hypoelastic formulation. The models parameters are characterized from experimental tests on a powder-impregnated fabric, with and without preliminary consolidation. An experimental thermoforming campaign is performed in parallel to the simulations and allows for the validation of the numerical results.

Chapter

3

Thermal model for the infrared preheating stage of the thermoforming process

3.1 Introduction

The first part of this thesis is focused on the development of a modelling approach to describe the evolution of temperature in a composite blank during the infrared preheating step of the thermoforming process, as the resulting temperature distribution has been shown to have a significant influence on the subsequent forming step (section 2.2.2).

The principal assumptions made for the development of a simplified model based on the radiosity method and finite element simulation to solve the heat equation considering radiative transfers as boundary conditions are presented in section 3.2. The emission of the infrared sources (halogen lamps), the interaction of the infrared radiation with the composite blank and the heat conduction through the thickness of the blank have to be described. The lamps used are introduced in section 3.3; the filament temperature data provided by the manufacturer as well as the explicit modelling of the lamps are validated by solving the inverse problem associated with an experimental 1-lamp heating setup.

The polyamide 66/glass woven fabric used in this study is presented in section 3.4.1. The optical and thermophysical properties are characterized experimentally for the semipreg material as received, and following a preconsolidation step. Because of the anisotropic nature of the composite considered, the determination of the temperature-dependent thermal conductivity is not straightforward, and two characterization methods are proposed and compared.

Finally, in the case of a stack of non-consolidated composite, imperfect contact at the plies interfaces leads to thermal contact conductances that have to be considered; the effect on temperature gradients is discussed in section 3.4.5 based on an experimental compaction study. The validation of the simulation tool is presented for the heating of a vacuum-bagged blank by a single lamp.

3.2 Heat transfer problem

The schematic heat transfer problem is represented in Figure 3.1. The composite blank considered is heated by an array of infrared lamps at arbitrary positions in space, within an enclosure made up by the oven panels. All three modes of heat transfer have to be considered for an accurate prediction of the temperature field in the laminate: incident (from the lamps or reflections on the oven panels) and self-emitted radiation, convective losses, and conduction both in plane and through-thickness.

3.2.1 Modelling assumptions

The dimension of the lamps and composite blank are of the same order of magnitude. The incident radiation from one lamp to the laminate surface cannot be considered uniform.

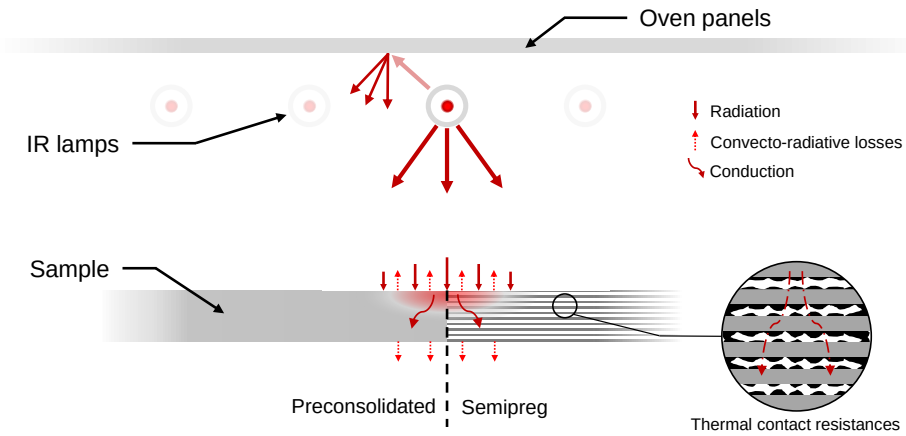

Figure 3.1 – Schematic heat transfer problem

Through-thickness conduction is not negligible when heating thick or non-consolidated preforms; a three dimensional model is thus needed. The heat equation is solved using the finite element method.

Determination of the incident radiative flux from one lamp to the blank corresponds to the derivation of a view factor between a finite rectangle and a finite cylinder of arbitrary length. An analytical view factor between a finite cylinder and rectangular surface of same length is proposed in [Leuenberger+1956]; this does not cover the case where the blank is larger than the lamps, or when the lamps are offset. Alternatively, Chung and Kermani proposed a closed form expression for the view factor between a differential strip in an arbitrary orientation and a rectangular flat surface [Chung+1989]. The extension of this expression to the view factor between a cylinder and a finite rectangle however relies on numerical integration techniques.

The choice is made in this work to model the lamps and oven panels explicitly rather than applying an analytical surface heat flux at the boundaries of the composite blank, using the approach described in [Nakouzi2012]. The radiating surfaces in the enclosure are assumed to be grey, opaque (this is verified experimentally for the composite material in section 3.4.2, and the semi-transparent quartz bulb of the lamps is neglected), Lambertian [El Bakali+2013], and separated by a non-participating media. Additionally, the temperature of the radiating surfaces of the elements within the considered enclosure is assumed uniform. These hypotheses allow the computation of radiative heat transfer using a radiosity approach (see section 2.2.3.2) in finite element software Comsol Multiphysics with Heat Transfer module [COMSOL2013a; COMSOL2013b]. This module computes the finite view factors between elements using the hemicube projection method (Section 2.2.3.1). Z-buffering is used to consider partial occlusion between objects, with a resolution of 256x256 pixels per face of the hemicube. As the elemental view factors depend only on the mesh geometry which is not updated during the simulation (as the heating and forming steps are decoupled), they are computed at the initial step and stored in memory for use in later time steps.

The constituents of the woven fibre-reinforced composites considered may have considerably different thermal properties which, in addition to the highly oriented structure of the material, leads to anisotropy. The assumption is made that the material can be considered as a continuous orthotropic media at the scale of the ply, i.e. homogenized properties are considered. As the material is heated from room temperature to above the melting point of the matrix, temperature dependent properties are considered when relevant.

3.2.2 Boundary conditions

Three distinct components are considered in the finite element model:

- **Infrared lamps:** the lamps described in section 3.3 are modelled as cylinders with a diameter corresponding to the effective emissive surface of the coiled filament (see section 2.2.3.2). The temperature T^i_{lamp} of each lamp is considered constant during the simulation, and depends on the electrical power supplied which is an input parameter. Knowledge of this temperature, and of the emissivity of the filament at this temperature $\epsilon_{\text{w}}(T)$ is sufficient to compute the radiative flux leaving the cylinder surface with a grey body assumption.

- **Oven panels:** the oven panels reflect part of the energy emitted by the lamps. The temperature evolution of the panels surfaces, resulting from the absorption of radiative energy from the lamps and convecto-radiative losses on both sides, is neglected [Nakouzi+2011]. On a point on the panels surface, the radiosity can be expressed as:

$$J_{panel} = \rho_{\text{panel}} \sum_i F_{\text{lamp}_i \to \text{panel}} G^i_{\text{lamp}} \tag{3.2.1}$$

  where ρ is the surface reflectivity, F the view factor between lamp i and the considered point, and G^i_{lamp} the irradiation from lamp i.

- **Composite blank:** the surfaces of the blank are subject to irradiation from the lamps and from the oven panels, as well as convective and radiative losses. The general expression of the heat flux at the surface of the blank is then:

$$q = G_{\text{ext}} - J_{\text{blank}} - h_c(T - T_{ext}) \tag{3.2.2}$$

  where G_{ext} is the total incoming radiative heat flux, J_{blank} the total outgoing radiative flux (reflected and emitted) and h_c a convective heat transfer coefficient.

3.3 Infrared sources

3.3.1 Short-wave tungsten halogen lamps

Two different short-wave tungsten halogen lamps are used as infrared sources in this work. A 1000 W–235 V lamp is used for the characterization of material properties in this chapter. A 500 W–235 V lamp is then used in the design of an infrared oven presented in Chapter 4. Both lamps are supplied by DIRTECH (Pierre-Percée).

The structure of the lamps is presented in Figure 3.2. The coiled tungsten filament is maintained in the center of the quartz tube by support rings. The atmosphere inside the quartz tube is composed of a mix of argon and halogen gas. This inert atmosphere prevents the oxidation of the filament, while the addition of the halogen avoids blackening of the lamp by ensuring that evaporated tungsten particles are redeposited on the coil rather than on the inner surface of the quartz tube.

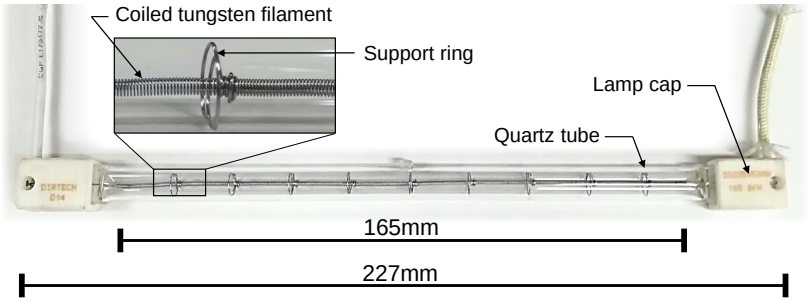

Figure 3.2 – 500W tungsten halogen lamp with detail of the coiled filament

The nominal temperature of both lamps is specified by the manufacturer at 2400 K, which corresponds to a maximum of emission at a wavelength of 1.2 µm and 95% of the energy emitted between 0.6–6 µm, from equation 2.2.5. The actual temperature of the filament can be controlled using a dimmer to change the electrical power supplied to the lamp.

Computation of the radiosity of the lamps requires knowledge of the emissivity of the tungsten filament, which depends on temperature. Monteix [Monteix2001] used a combination of experimental results at wavelength between 0.24–2.6 µm [Siegel+1992] and the Hagen-Rubens model relating the emissivity as a function of electrical conductivity at higher wavelengths [Desvignes1997] to describe the temperature dependence of the spectral emissivity of pure tungsten.

A thermodependent Lorentz-Drude model to describe the reflectivity as a function of the electric permittivity of tungsten was recently proposed by Minissale et al. [Minissale+2017]. The total emissivity predicted by these two models is plotted in Figure 3.3, along with temperature dependent experimental results presented in the literature [Brodu+2015; Matsumoto+1999; Rudkin+1962]. The approach proposed by Monteix shows a good agreement with experimental data reported by Matsumoto et al. at temperatures higher than 1800 K, while the model presented in Minissale et al. allows for a good representation of the sharp

decrease in emissivity observed at lower temperatures in the experiments of Brodu et al. The dispersion between the experimental measurements could be explained by variation in surface roughness of the samples tested as suggested by Brodu. The performances of the model at low temperatures cannot be compared directly, given the smaller wavelength integration range in Monteix. Considering the nominal temperature of the lamps, and the increasing deviation of the model proposed by Minissale at temperatures higher than 1500 K, the approach of Monteix et al. is used in the rest of the study.

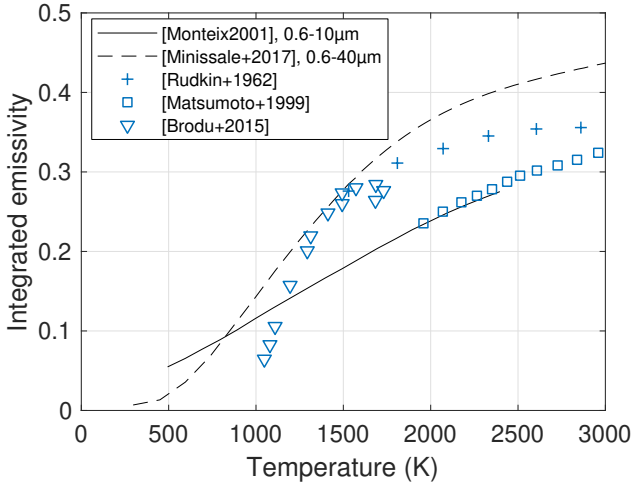

Figure 3.3 – Integrated tungsten emissivity as a function of temperature

3.3.2 Filament temperature

An expression relating the filament temperature to the input voltage is provided by the manufacturer, based on the rerating equations derived by Fink [Fink+1978]:

$$\frac{T_f}{T_N} = \left(\frac{V}{V_N}\right)^{0.42} \tag{3.3.1}$$

where T_N and V_N are the nominal filament temperature and voltage respectively. The development of an experimental 1-lamp heating setup, with the aim of verifying this expression and validating the approach used to model the lamps, is presented in the next section.

3.3.2.1 Experimental setup

The effect of the input voltage and electrical power on the filament temperature is observed using the setup schematized in Figure 3.4. A material sample is heated on its front face by the considered infrared source, and a two-dimensional temperature field is recorded on the back face by a SC325 FLIR infrared camera, operating in the 7.5–13.5 µm range. The three elements are mounted on separate guiding rails that allow precise relative positioning.

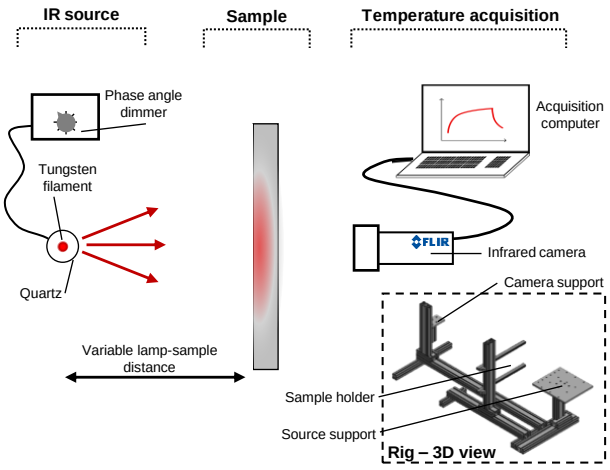

Figure 3.4 – Schematized 1-lamp heating test setup

To characterize the 1000 W source, a 300x300x1.4 mm plate of opaque black acrylonitrile butadiene styrene (ABS) is used as the reference sample. The thermal and optical properties of this material have been characterized experimentally by Andrieu [Andrieu2005], and are presented in Table 3.1.

Table 3.1 – ABS sample properties [Andrieu2005]

Sample dimensions (mm)	$300 \times 300 \times 1.4$
Density (kg/m^3)	1050
Specific heat (J g^{-1} K^{-1})	1.30 at 50 °C, 1.55 at 75 °C (interpolated)
Thermal conductivity (W m^{-1} K^{-1})	0.15
Integrated emissivity 0.6–6 µm (-)	0.94
Integrated emissivity 7.5–13.5 µm (-)	0.96

The evolution of the temperature on the back surface of the ABS sample is measured during a heating phase in which the electrical power supplied to the infrared lamp is increased by increments of 20% using the phase angle dimmer (Figure 3.5). The increments are held for a time sufficient to ensure that a steady state is achieved in the plate. The heating tests are conducted at two different lamp-plate distances (20 cm and 25 cm), and repeated twice per condition. The evolution of temperature during cooling to ambient temperature is also recorded.

3.3.2.2 Inverse analysis

The filament temperature is obtained from the described experimental tests by inverse analysis. While solving a *forward* (direct) problem consists in predicting the effect of a system on its surroundings based on known characteristics, inverse analysis is a class of optimization problem which consists in inferring the characteristics of a system from observable effects.

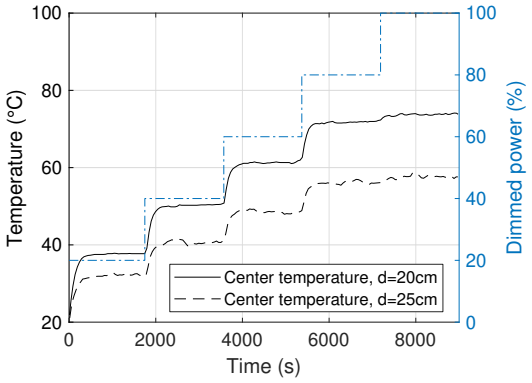

Figure 3.5 – Evolution of temperature at the center of the backface with varying lamp input power

A two-steps procedure is used to determine the convective transfer coefficient on the plate (assumed constant) and the filament temperature. The cooling of the plate from the steady state at nominal lamp power to ambient temperature by convection is first simulated, neglecting through-thickness gradient at the initial time (i.e, the experimental two-dimensional temperature field measured on the back face is assumed constant through the thickness as a boundary condition). The convective transfer coefficient is determined as the value that minimizes the difference (in the least square sense) between the experimental and simulated temperature evolution in a set of discrete points on the backface of the plate:

$$\min_{h_c} \sum_i \int_t \left(T_{i,sim}(t) - T_{i,exp}(t)\right)^2 dt \tag{3.3.2}$$

where $T_{i,exp}$ and $T_{i,sim}$ are the experimental and simulated temperature on point i, respectively. The optimization problem is solved with the Nelder-Mead algorithm (simplex method) and leads to a spatially averaged heat transfer coefficient $h_c = 4\,\mathrm{W\,m^{-2}\,K^{-1}}$. The value is close to that obtained using empirical correlations for a vertical plate [Churchill+1973]: $Nu = 0.59Ra^{0.25}$, which leads to $h_{\mathrm{c,corr}} = 4.2\,\mathrm{W\,m^{-2}\,K^{-1}}$. The hypothesis of neglecting the through-thickness temperature gradient can be verified a posteriori by computing the dimensionless Biot number that describes the ratio of heat transfer inside and at the surface of a media:

$$Bi = \frac{(h_c + h_r)L_c}{\kappa} \tag{3.3.3}$$

where L_c is a characteristic length (the thickness of the plate) and $h_r = \epsilon\sigma(T + T_{\mathrm{amp}})(T^2 + T_{\mathrm{amp}}^2)$ the radiative transfer coefficient. In this case, $Bi = 0.082$: the plate can be considered as thermally thin.

The filament temperature is then determined at every percentage of input power tested through the simulation of the steady-state temperature field in the plate subject to radiative

heating from the infrared source, and convecto-radiative losses (Figure 3.6a). The filament temperature is defined as minimizing the difference between the experimental and simulated temperature on a horizontal profile at the center of the backface (a horizontal profile is chosen to minimize the effect of the buoyancy driven convective flow on the minimization results):

$$\min_{T_{filament}} \int_s \left(T_{sim}(s) - T_{exp}(s)\right)^2 ds \tag{3.3.4}$$

The optimized simulated temperature profile is presented in Figure 3.6b in the case d=20 cm and P=60%.

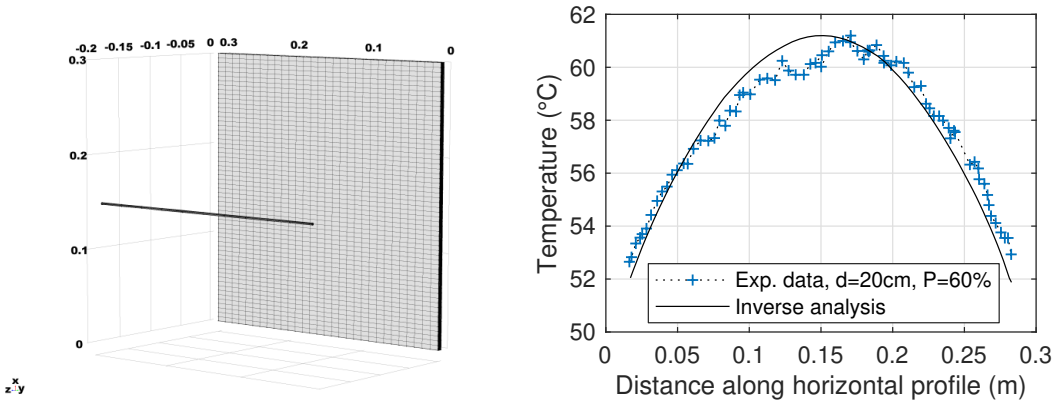

(a) Meshed COMSOL model: lamp 8×16 quad elements, blank $30 \times 60 \times 4$ hex elements

(b) Experimental and optimized simulated temperature profile, d=20 cm, P=60%

Figure 3.6 – Model and simulated results to determine the filament temperature

The filament temperature obtained from the inverse analysis approach are presented in Figure 3.7, along with the equation given by the manufacturer. The error bars presented correspond to the standard deviation from the two different distances and two repeats per distance considered. An excellent agreement is observed, with the exception of the lower input power considered, for which the temperature obtained by simulation is 50 °C below the theoretical prediction.

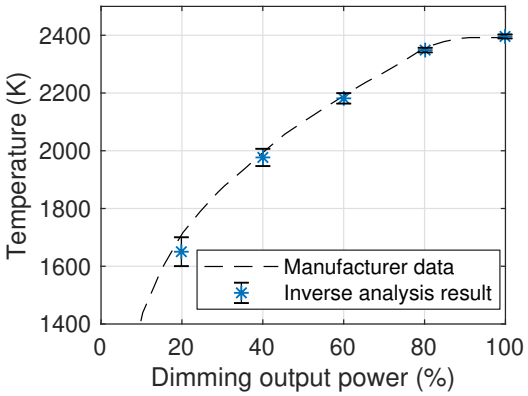

Figure 3.7 – Filament temperature as a function of input power: manufacturer data and inverse analysis results

3.4 Characterization of the thermal properties of powder-impregnated composites

3.4.1 Presentation of the material

3.4.1.1 Powder-impregnated glass/polyamide 66 twill fabric

The material used in this study is a woven glass/polyamide 66 composite developed by Solvay (not commercially available). It is supplied as a 2×2 twill E-glass fabric, powder-coated on both sides with PA66. Figure 3.8 shows the weave of the glass fabric as well as the surface of the semipreg. The balanced glass fabric presents an areal weight of $600\,\mathrm{g\,m^{-2}}$. The semipreg has an areal weight of $960\,\mathrm{g\,m^{-2}}$, with an homogeneous resin repartition on both sides of the fabric; the expected fibre volume fraction after consolidation is between 50–52%.

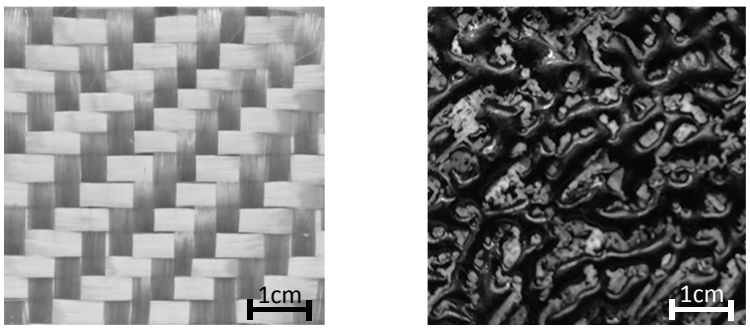

Figure 3.8 – Left: twill 2/2 glass fabric, right: powder-impregnated fabric

The specific PA66 grade used in this study (XA1481) is part of a new generation of low viscosity polyamides developed by Solvay for Resin Transfer Moulding (RTM) and processing at low pressures [Faraj+2016]. DSC measurements on the polymer at a rate of $10\,^{\circ}\mathrm{C\,min^{-1}}$ are presented in Fig. 3.9 between 30 °C and 300 °C.

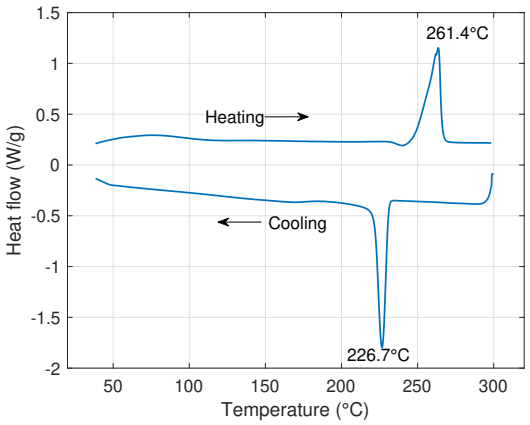

Figure 3.9 – DSC thermogram of PA66-XA1481, heating and cooling at $\pm 10\,°C\,min^{-1}$ (endo up)

Peaks corresponding to first-order transitions are clearly visible, and characteristic temperatures can be defined (relative to the heating/cooling rate): the melting temperature T_m at 261 °C and the crystallization temperature T_c at 227 °C. The glass transition is not apparent on the curves; data provided by the manufacturer specifies T_g at 69 °C.

The viscosity of the PA66 matrix has been measured experimentally from tests on a Haake Mars Rheometer with a plate-plate geometry. Temperature sweeps from 270 °C to 300 °C (Figure 3.10a) and cooling from 300 °C to 260 °C (Figure 3.10b) were conducted at 20 °C/min, at a strain of 1% and strain rate of $10\,s^{-1}$. Results shown in Fig. 3.10a confirms that the polymer has not entirely melted at 270 °C as expected from the DSC analysis. The viscosity decreases continuously as the temperature increases. The measured dynamic viscosity η at 280 °C is between 30–40 Pa s when cooling from the amorphous melt, compared to melt viscosities above 250 Pa s in typical PA66 grades [Orange+2014].

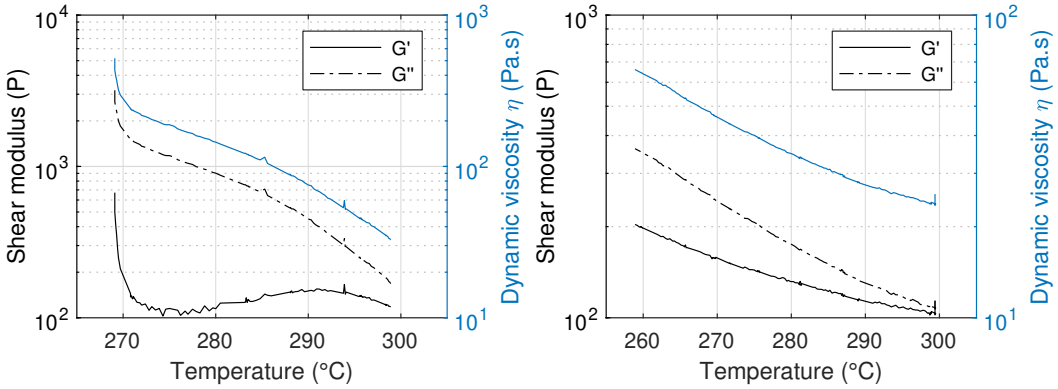

(a) Heating from 260 °C to 300 °C

(b) Cooling from 300 °C to 260 °C

Figure 3.10 – Shear moduli and dynamic viscosity of the PA6.6 matrix as a function of temperature, heating to or cooling from the melt

The hysteresis observed between the behaviours in figures 3.10a and 3.10b is attributed to an incomplete melting of the crystalline phase during heating.

The matrix is deposited on the fabric after the weaving operation: the thermoplastic powder is spread on both faces of the fabric and heated above the melting point to fix it to the tows. This leads to the structure observed in the surface micrograph of Figure 3.11, with the glass fabric being partially covered by a network of coalesced polyamide droplets.

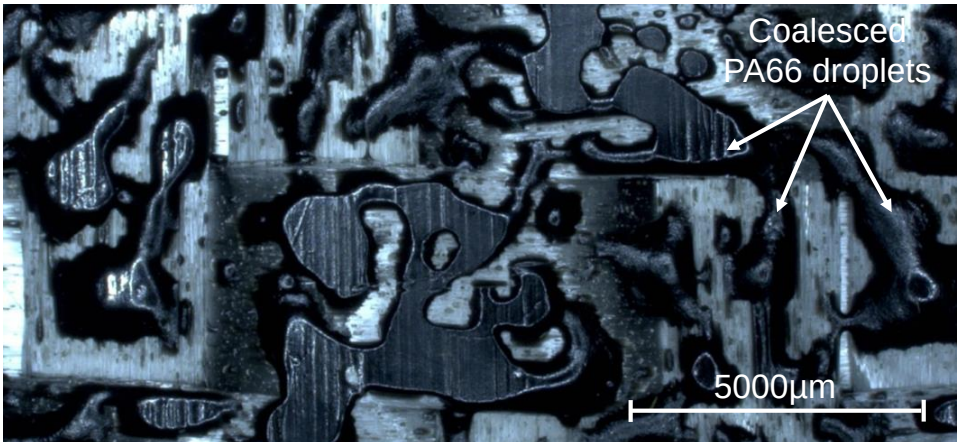

Figure 3.11 – Surface micrograph of the powder-impregnated fabric, showing the network of coalesced polyamide droplets.

The structure of the cross-section of the powder-impregnated fabric is presented in Figure 3.12. The droplets, highlighted in blue, are dispersed on the surface of the fabric and do not impregnate the yarns. The maximum thickness of the observed droplets varies from 200 to 350 µm.

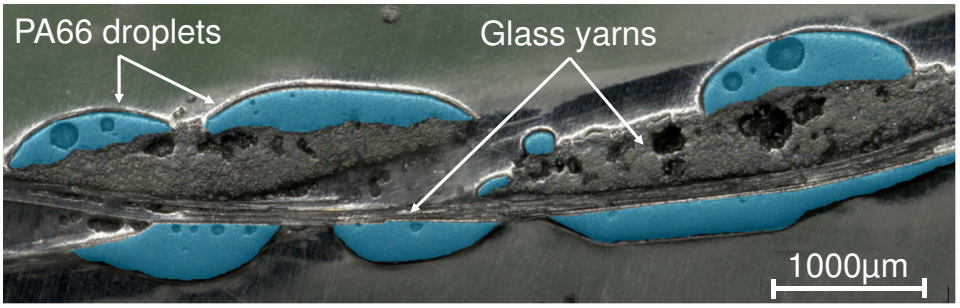

Figure 3.12 – Cross-section micrograph (x50) of the powder-impregnated fabric, showing warp and weft yarns with polyamide droplets highlighted in blue.

3.4.1.2 Fabric consolidation

To compare the properties of the powder-impregnated fabric with the blanks used in industrial processes, stacks of plies cut from the as-supplied roll of semipreg have been thermocompressed to form consolidated plates. The thermocompression press used (EDyCO: *Élaboration Dynamique de Composites Organiques*) is a pilot system developed in Institut Clément Ader [Bessard2012]. The system is presented in Figure 3.13. In contrast with standard heated press systems, the compression platens are equipped with an electromagnetic induction heating element developed by Roctool (3iTech™ technology). The use of induction to heat the platens allows for fast heat-up times, as the thermal inertia of the metallic tools ceases to be a limiting factor. With only the surfaces of the tool being heated, ramps of up to 42 °C/min and complex temperature cycles can be achieved. Cooling ramps of the same order of magnitude can be achieved, as the absence of intrusive heating elements allows cooling channels to be positioned close to the tool surface.

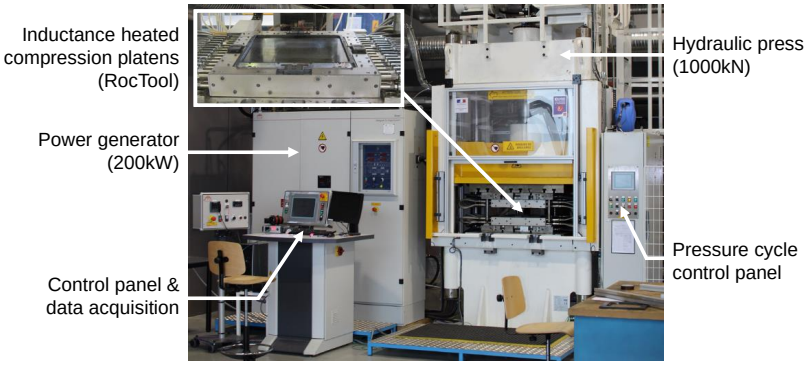

Figure 3.13 – EDyCO thermocompression press

The semipreg plies are dried as per the manufacturer recommendations (12 hours at 80 °C) in an environmental chamber before further processing. The plies are stacked in the required configuration and sandwiched between single-layer release agent-coated polyimide film to facilitate demoulding. The temperature and pressure cycle is presented in Figure 3.14.

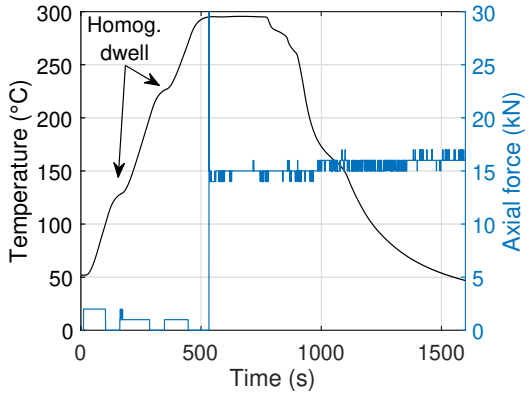

Figure 3.14 – Temperature and applied force cycle during consolidation (thermocouple on the surface of the tool)

The stack is heated to 295 °C at 30 °C/min. Homogenization dwells are done at 100 °C and 200 °C by shutting off the generator for 60 s to limit the through-thickness temperature gradients. The process temperature is held for 5 minutes, and the plate is then cooled down to below 50 °C for demoulding. A pressure of 1.75 bar is applied as the temperature reaches 295 °C and is held for the entirety of the cooling step. The low pressure is justified by the viscosity of the polyamide matrix, and prevents fibre washing. The variations observed in the applied force curve are due to the low magnitude of the force required compared to the capacity of the press.

3.4.2 Infrared optical properties

The experimental characterization of the optical properties of the materials considered is needed to describe the interaction between the halogen lamps and the surface of the blanks, and for accurate temperature measurements by infrared thermography.

Reflection at the surface of the materials is assumed to be diffuse; the hypothesis is validated with surface roughness measurements using an Altisurf© 520 white light interferometry profilometer (100 nm vertical resolution) which showed an average asperity height of approximately 280 µm for the semipreg fabric, and 40 µm for the consolidated material which is much larger than the wavelengths relevant to the halogen lamps.

3.4.2.1 Experimental setup

The optical properties of the powder-impregnated semipreg and the consolidated composite have been measured using a Bruker Vertex 70 Fourier-transform infrared (FTIR) spectrometer (Figure 3.15). This spectrometer allows measuring the transmissivity and reflectivity of samples at wavelengths in the range 0.8–25 µm and at ambient temperature. This spectral range covers both the emission spectrum of the halogen lamps (0.6–6 µm at 2400 K) and the detection range of the infrared camera used (7.5–13.5 µm).

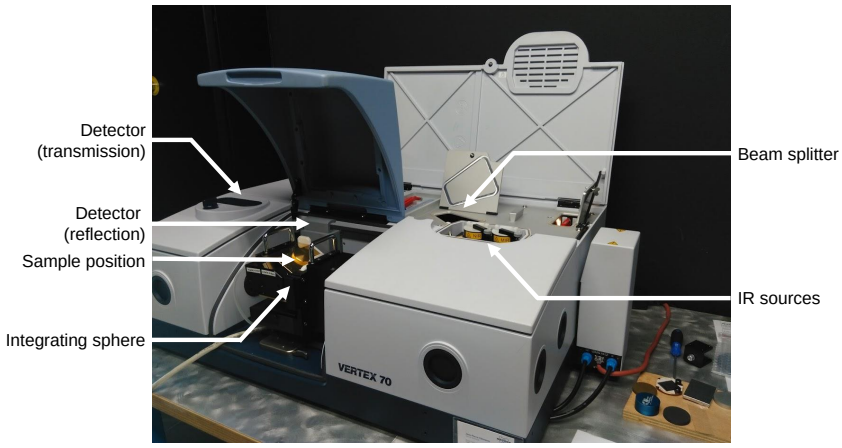

Figure 3.15 – Brucker VERTEX70 FTIR spectrometer

Two different detectors are used to cover the spectral range:

- InGaAs in the NIR range, from 0.8 to 2.5 µm
- DLaTGS in the MIR range, from 1.5 to 25 µm

The detectors present data on an overlapping range, but with a lower precision as the wavelength is closer to the bounds of the spectral interval presented. The results from both detectors have been aggregated with a cut-off wavelength set at 2 µm to avoid noise induced by the lower gain of the detectors at the edge of their useful range.

Definition of a representative surface area: as discussed in section 3.4.1.1, the semipreg fabric presents an heterogeneous surface aspect, with the distinct constituents of the composite visible. To ensure that the optical properties measured are *effective* properties, a minimum surface area size representative of the material has to be defined. This consists in finding the minimum observation area size for which the apparent coverage of PA66 on the glass fabric is equivalent to the average coverage.

This is done through image analysis: samples of the semipreg fabric (dimensions approximately 20x10 mm) are observed with an optical microscope. The resulting surface micrographs are converted to black and white from thresholding of the grey level histogram with Otsu's method [Otsu1979], so that black and white pixels represent the PA66 and glass fibres respectively. Observation zones with increasing area are defined on the image (Figure 3.16a). The percentage of the surface covered by the polyamide droplets corresponds to the ratio of black pixels over the total pixel count. The evolution of surface coverage with the size of the observation area is presented in Figure 3.16b for the 4 samples considered.

The analysis shows that 83% of the fabric surface is covered with polyamide. In addition, for observation areas larger than 100 mm^2, the apparent surface coverage is within 2% of the average value. A sample size of 100 mm^2 is therefore sufficient to ensure that effective surface properties are measured, and not affected by the dispersion in polyamide droplets size.

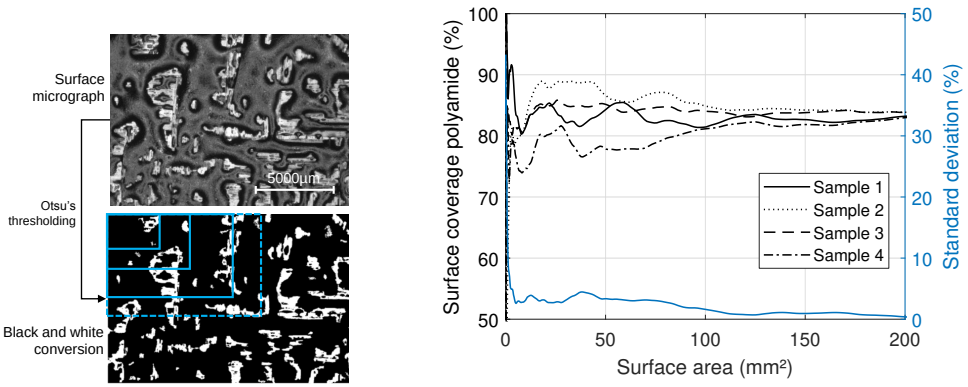

(a) Thresholding and observation area

(b) Evolution of apparent surface coverage of PA66 with observation area size

Figure 3.16 – Determination of representative surface area

3.4.2.2 Transmissivity

Spectral measurements of the transmissivity of a single ply of semipreg fabric and consolidated composite are presented in Fig. 3.17. No significant difference in the apparent transmission behaviour is observed, with less than 0.2% of the incident radiation being transmitted for wavelengths above 0.8 µm. This is an expected result as carbon black, which acts as an infrared absorbing pigment [Chen+2011], is used as a filler in the PA66 matrix considered. Additionally, while bulk E-glass is highly transmitting in the NIR range, the packed structure of woven glass fabrics promote absorption through scattering [Bian+2015]. As the ply is the smallest thickness considered at the macroscopic scale, the materials are considered opaque, with the infrared radiation being absorbed at the surface of the plies.

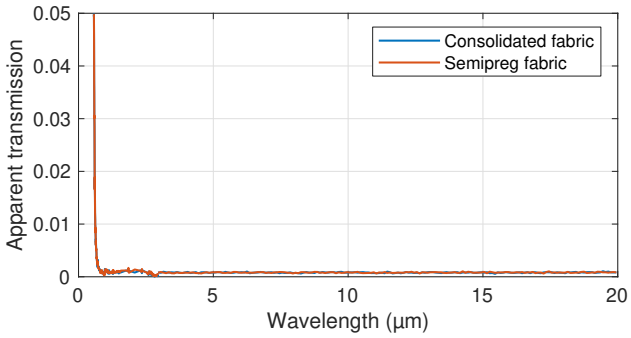

Figure 3.17 – Apparent transmission of the semipreg and consolidated fabric

Consequently, absorptivity and reflectivity are directly correlated, and measuring the reflectivity is sufficient to characterize the emissivity of the material, as per equation 3.4.1.

$$\tau = 0 \rightarrow \epsilon = 1 - \rho \tag{3.4.1}$$

3.4.2.3 Reflectivity

The spectral hemispherical reflectivity of the materials is measured using an integrating sphere attachment mounted on the spectrometer. The operating principle is schematized in Figure 3.18. The light emitted by a broadband infrared source passes through a Michelson interferometer and is reflected onto the sample. The sample reflects part of the radiation on the surface of the integrating sphere, which is coated with a Lambertian material (Infragold®). The geometry of the sphere results in the detector receiving the flux reflected by the sample in all directions of the hemisphere (spatial integration). The analysis is repeated for different positions of the mobile mirror of the interferometer. Fourier transform is used to decompose the interferogram obtained in reflectivity/wavelength data.

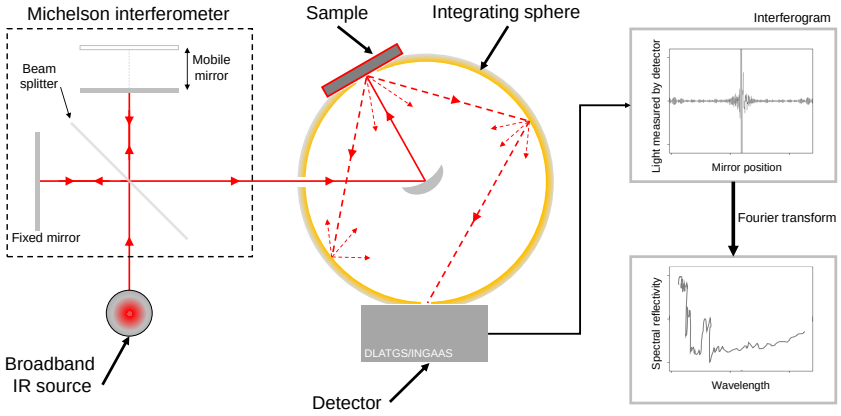

Figure 3.18 – Schematic diagram of FTIR hemispherical reflectivity measurement

The sampling area on the integrating sphere is 280 mm^2 which is sufficient to ensure that the measurement is not affected by the distribution of the polyamide on the surface in the case of the semipreg fabric. The average hemispherical spectral reflectivity measured for both materials is presented in Figure 3.19 in the range 0.8–20 µm.

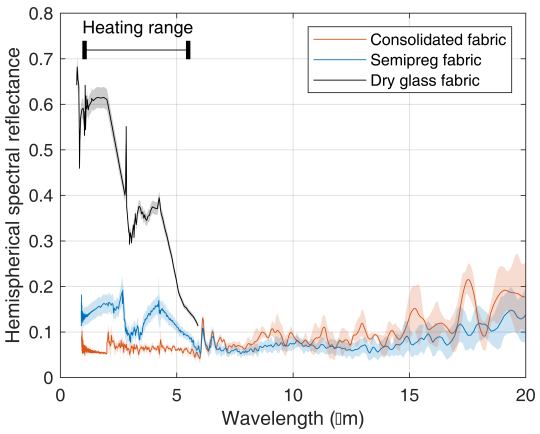

Figure 3.19 – Spectral hemispherical reflectance of the semipreg and consolidated composite, and dry twill glass fabric. Shaded patch represents standard deviation.

The reflectivity of the consolidated composite shows little variation with the wavelength: between 5 and 10% for wavelengths between 0.8 and 15 µm. The reflectivity of the semipreg material is significantly higher in the NIR and low-MIR range, with a reflectivity up to 20% at 2.7 µm. This difference is attributed to the visible glass fibres on the surface, as can be seen from results on the dry glass fabric (in black) exhibiting a high reflectivity in the NIR range. As this spectral range corresponds to the maximum of emission of the halogen lamps at nominal temperature, the difference in reflectivity suggests that the radiative heat transfer will be less effective for the semipreg as less radiation will be absorbed.

The implementation of radiative heat transfer in Comsol does not allow taking directly into account the spectral dependency of material parameters. Instead, the spectral reflectivity is

integrated over the considered wavelength range as per equation 3.4.2.

$$\rho^{\cap}(T) = \frac{\int_{\Delta\lambda} \rho_\lambda L^0_\lambda(T) d\lambda}{\int_{\Delta\lambda} L^0_\lambda(T) d\lambda} \tag{3.4.2}$$

where $\rho^{\cap}$ is the total hemispherical reflectivity, and L^0_λ is the spectral radiance of the blackbody. This quantity corresponds to the fraction of energy emitted by an ideal source at temperature T reflected on the surface of the material. The total hemispherical reflectivity integrated over the range [0.8–20 µm] is plotted in Figure 3.20a as a function of the temperature. At a source temperature of 2400 K, the semipreg shows an average reflectivity of 0.14; the consolidated composite a reflectivity of 0.07. Consequently, 86% and 93% of the incoming radiation will be absorbed by the surface.

Figure 3.20b presents the reflectivity integrated over the spectral range of the infrared camera used (7.5–13.5 µm) as a function of the surface temperature expected during processing. The variation with temperature is negligible; the surface emissivity of the material for the temperature measurement is considered constant and equal to 0.92 and 0.93 for the consolidated composite and semipreg fabric respectively.

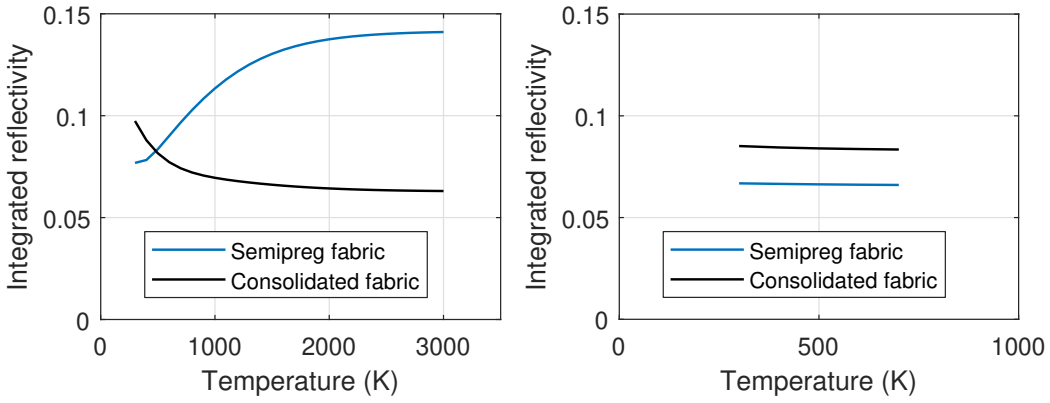

(a) Integrated reflectivity **(b)** Integrated reflectivity, $\Delta\lambda$ = [7.5–13.5 µm]

Figure 3.20 – Total hemispherical reflectivity

The optical properties have been measured at ambient temperature; the temperature dependence of the spectral reflectivity is assumed to be negligible. This hypothesis is supported by the (scarce) literature on thermodependence of optical properties of thermoplastic composites; measurements of directional-directional reflectance at 1.08 µm reported by Grouve [Grouve2012] on carbon/PPS samples show a negligible increase of the reflectivity at the glass transition and melt temperature of the thermoplastic matrix; more recently, Le Louët et al. [Le Louët+2017] showed no significant variation of normal-normal and normal-hemispherical reflectivity of a carbon/PEEK composite at 0.98 µm, for temperatures between 20 °C and 450 °C.

3.4.3 Thermophysical properties

The characterization of the thermophysical properties (density, heat capacity and thermal conductivity) is needed to describe the evolution of temperature distribution through the thickness of the blanks. The glass fibres and PA66 matrix have different thermal properties; because of the microstructure of the materials considered, properties at the microscale present strong local variations.

An equivalent, homogenized material is considered in the heat transfer model; local variations are neglected, and homogenized thermal properties have to be characterized. The anisotropy resulting from the architecture of the fibrous reinforcement is however taken into account when relevant (namely, in the description of the thermal conductivity).

3.4.3.1 Density

The density of the matrix and reinforcement fibres is provided by the manufacturer: 1140 kg/m^3 for the PA66 and 2600 kg/m^3 for the E-glass. The density of the consolidated composite is measured by hydrostatic weighing, using the setup presented in Figure 3.21.

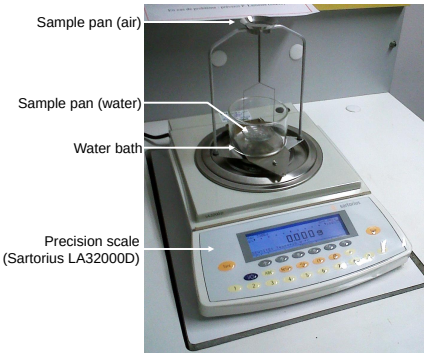

Figure 3.21 – Hydrostatic weighing measurement setup

The measurement is conducted as per ISO 1183-1 [ISO2012]. The sample is weighed in air and water; the density is determined as in Eq. 3.4.3, with ρ_{water} the density of water, m_{air} and m_{water} the apparent mass of the sample in air and water respectively.

$$\rho = \rho_{\text{water}} \frac{m_{\text{air}}}{m_{\text{air}} - m_{\text{water}}} \tag{3.4.3}$$

The density of the consolidated composite is measured at 1885±10 kg/m^3 following this procedure. The semipreg material is highly porous; an apparent (rather than bulk) density is considered, dividing the areal weight of the fabric (960 g m^{-2}) by its apparent thickness, measured under a load of 4 kPa as described in ASTM D1777-96 [ASTM2007]. The resulting density measured for the semipreg is 915±30 kg/m^3.

3.4.3.2 Specific heat capacity

The specific heat capacity is the amount of energy needed to increase the temperature of a mass of material by 1 K. This quantity is measured by Differential Scanning Calorimetry

(DSC), with a power compensation Perkin-Elmer 8500. This type of DSC is composed of two furnaces: one containing a reference (empty pan), the other the sample (a few milligrams in mass). The furnaces are calibrated so that their temperature is identical during the thermal cycle; the difference in power required to maintain the two furnaces at the same temperature is directly related to the heat flux absorbed or dissipated by the sample.

The proprietary StepScan method [Cassel+2010] is used; this modulated temperature DSC technique consists in applying a succession of heating ramps at a constant rate ($5\,\mathrm{K\,min^{-1}}$) and isothermal hold steps to the sample. The specific heat C_p is computed from the measured heat flux $\frac{dq}{dt}$ as a function of temperature, with m the sample mass and H the enthalpy (eq. 3.4.4).

$$C_p = \frac{1}{m\frac{dT}{dt}}\frac{dH}{dt} \tag{3.4.4}$$

The measurement is conducted in an inert nitrogen atmosphere, between 20 °C and 320 °C. The results are presented in Figure 3.22. The glass transition temperature (69 °C for the PA66 considered [Solvay2012]) is not accompanied with a marked change of slope. The large increase in measured specific heat observed from 220 °C corresponds to the melting of the crystalline phase of the polymer (enthalpy of fusion); the width of the peak depends on the crystal size distribution.

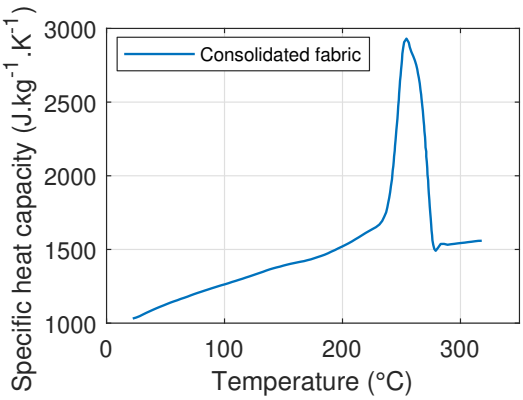

Figure 3.22 – Apparent specific heat capacity as a function of temperature

This apparent specific heat capacity (i.e., including the latent heat of melting), is used in the Comsol model interpolated from the experimental data. An alternative approach would be to model the melting of the crystalline phase as a separate kinetic phenomena, coupled with the temperature evolution through the inclusion of a source/sink term in the heat equation; while this would allow for a more precise description of the heat transfer within the blank, a much more extensive characterization program would be needed.

3.4.4 Thermal conductivity

The numerical simulation of the heat transfer in the blank requires the determination of the thermal conductivity tensor of the composite used. Because of the novelty of the PA66/glass

system considered, no data was available in the literature and the conductivity was thus characterized experimentally. The determination of the effective thermal conductivity of composite materials has been the topic of extensive research from the early work of Rayleigh and Maxwell [Rayleigh1892] on effective properties of heterogeneous media. The methods developed can be classified in two categories:

- **Homogenization:** in which the thermal conductivity of the composite is derived from the knowledge of the thermal conductivity of its constituents, and the volume fraction or a description of the microstructure. Initial work focused on the development of closed-form solutions based on ideal inclusions embedded in a continuous matrix with and without interfacial resistances, and showed that the effective properties depend on the particle volume fraction but also on particle size [Benveniste1987; Hasselman+1987]. Given the complexity of the actual microstructure of woven composites, numerical homogenization schemes are often used, with the geometry of the composite described with finite elements [Dasgupta+1992; Dasgupta+1996].
- **Inverse methods:** as described in section 3.3.2.2, inverse methods consist in using the response of a system (here, a sample of composite material) to infer its properties. In practice, a sample is subjected to a known heat flux (or temperature gradient). The resulting temperature elevation (or heat flux) is measured, and the thermal conductivity or diffusivity is computed by solving the heat equation. Various experimental set-ups have been developed, based on contact [Jannot+2010; Thomas+2010] or non-contact [Hay+2004; PechMay+2016] heating.

The thermo-dependent thermal conductivity of the glass/PA66 composite considered is obtained using these two different approaches; results are compared, and the pros and cons associated with each method are discussed in this section.

3.4.4.1 Homogenization approach

The first approach presented consists in a two-scale homogenization procedure. The thermal conductivity of the polyamide matrix and the glass fibres are characterized first; a phenomenological model describing the temperature dependence of the thermoplastic matrix is proposed. In a second step, the thermal conductivity of the yarn is derived from that of the constituents based on the Maxwell theory. Finally, the effective thermal conductivity of the composite is evaluated at the macroscale from an approximation of the fabric architecture using a numerical homogenization scheme.

Thermal conductivity of the constituents: The thermal conductivity of polymers is known to be temperature dependent [Choy1977], as the crystalline phase presents a higher conductivity than the amorphous phase. Recent experimental results presented by Faraj [Faraj2016] on PA66 using guarded hot plate show a slight decrease of the thermal conductivity between 30 °C and 145 °C. The behaviour at higher temperatures is not described, and the specific grade of polyamide used is not provided.

A piecewise-defined function has been proposed by Thomann [Thomann2003] to describe the temperature dependence of PA6 and PA12 samples: the behaviour is described by a cubic root function until the melt temperature is reached; the conductivity of the amorphous melt is then considered constant. A similar approach is used here, with the thermal conductivity of the semi-crystalline material characterized experimentally.

The conductivity of the PA66-XA1481 matrix used has been measured between 20 °C and 180 °C in the RAPSODEE center of IMT Mines Albi, using a Hot Disk® TPS 2500S instrument, based on the Transient Plane Source method [Gustafsson1991]. A plane sensor made of a Kapton-insulated conductive nickel spiral is sandwiched between samples of thickness 5 mm manufactured by injection from PA66 pellets (see Fig. 3.23).

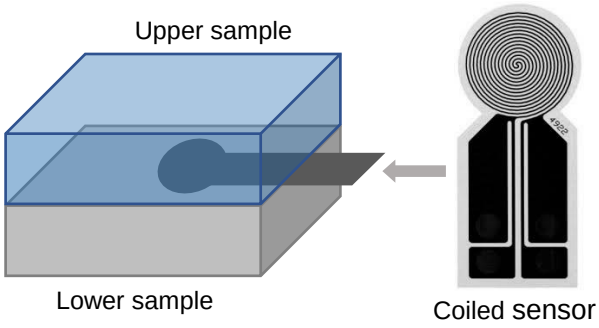

Figure 3.23 – Schematic of the Transient Plane Source test

A constant electrical power passes through the sensor; the heat generated by Joule effect is dissipated in the samples. The evolution of the sensor temperature is monitored, and its average is related to the material thermal properties and the test parameters by Eq. 3.4.5 [Log+1995], where P_0 is the total power, r the radius of the sensor, κ the thermal conductivity of the sample, and D is a term depending on the geometry of the conductive nickel wire, and the thermal diffusivity of the material.

$$\langle \Delta T(\tau) \rangle = P_0 \left(\pi^{3/2} r \kappa \right)^{-1} D(\tau) \tag{3.4.5}$$

The results show a decrease of the thermal conductivity from 0.38 to 0.31 $\mathrm{W\,m^{-1}\,K^{-1}}$ in the temperature range considered. The thermal conductivity of the amorphous melt is assumed constant and taken from the literature at 0.15 $\mathrm{W\,m^{-1}\,K^{-1}}$ [Brandrup+1998]. A cubic-root function is fitted on the experimental results, and the thermal conductivity is defined piecewise by Eq. 3.4.6.

$$\kappa_m(T) = \begin{cases} a(T_c - T)^{1/3} + \kappa_{m,\mathrm{melt}} & \text{if } T \leq T_c \\ \kappa_{m,\mathrm{melt}} & \text{if } T > T_c \end{cases} \quad (\mathrm{W\,m^{-1}\,K^{-1}}) \tag{3.4.6}$$

with $a = 3.7 \times 10^{-2}\,\mathrm{W\,m^{-1}\,K^{-4/3}}$ and $\kappa_{m,\mathrm{melt}} = 0.15\,\mathrm{W\,m^{-1}\,K^{-1}}$. The threshold temperature T_c can represent the melting temperature T_m if the phase transition is approached by

heating, or the crystallization temperature if the phase transition is approached by cooling from the melt (the hysteresis due to supercooling can be considered). The model is presented along with experimental results and data from the literature in Figure 3.24. The experimental thermal conductivity is in good agreement with results presented in [Brandrup+1998], and presents the same temperature dependency as that reported by Faraj [Faraj2016]. The model presents an excellent fit to the experimental data in the temperature range tested experimentally. The non-differentiability of the model due to the sharp transition at $T = T_c$ was not shown to be an issue in the numerical implementation; smoothness could easily be ensured through multiplication with a sigmoid function.

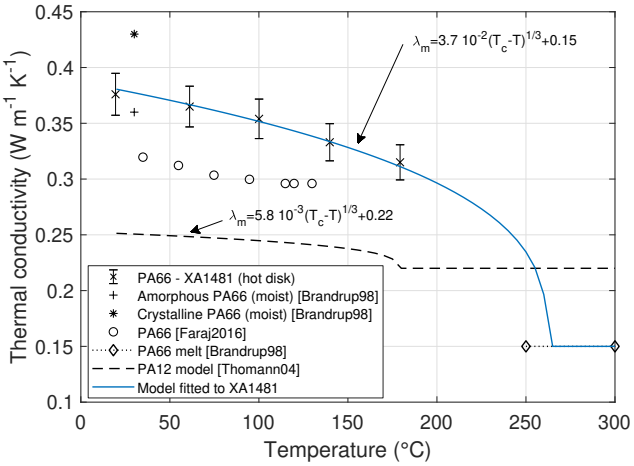

Figure 3.24 – Thermal conductivity of PA66 as a function of temperature during heating

The fibres are treated as an isotropic media, which is a validated hypothesis for E-glass [Kalaprasad+2000; Kawabata+2002].The thermal conductivity of the glass fibres κ_f is assumed to be constant with regards to temperature, and equal to $1\,\mathrm{W\,m^{-1}\,K^{-1}}$ [Thomas+2012].

$$\boldsymbol{\kappa}_\mathrm{f} = \kappa_\mathrm{f}\,\mathbf{I} \tag{3.4.7}$$

Yarn thermal conductivity: The longitudinal conductivity of the yarns is determined by a parallel model expression, depending on the fibre volume fraction v_f in the yarn:

$$\kappa_{yarn}^{long.} = \kappa_f v_f + \kappa_m(1 - v_f) \tag{3.4.8}$$

The transverse conductivity is evaluated using the approach developed by Hasselman et al. [Hasselman+1987] for the effective conductivity of unidirectional composites considered as an isotropic matrix reinforced with dilute concentrations of cylindrical fibres. Perfect contact between the fibres and the matrix is assumed (e.g., the interfacial contact resistance is neglected), which leads to the following expression:

$$\kappa_{yarn}^{transv.} = \kappa_m \frac{\left(\frac{\kappa_f}{\kappa_m} - 1\right) v_f + \left(1 + \frac{k_f}{k_m}\right)}{\left(1 - \frac{\kappa_f}{\kappa_m}\right) v_f + \left(1 + \frac{k_f}{k_m}\right)} \tag{3.4.9}$$

The average fibre volume fraction in the yarn is evaluated from micrographic analysis, on polished cross-section cuts (see Appendix A.1): $v_f = 0.668 \pm 0.015$. The homogenized properties of the yarn are presented in Figure 3.25 as a function of the thermal conductivity of the matrix. The longitudinal thermal conductivity of the yarn is higher than its transverse conductivity, and the difference is increased at lower values of κ_m, i.e. at higher temperatures considering the thermodependence presented in Fig. 3.24. The transverse conductivity is also more sensitive to variations of κ_m. A higher fibre volume fraction v_f leads to an increased thermal conductivity, with a relative influence increasing with the difference in the conductivity of the constituents.

Macroscale thermal conductivity: Evaluating the thermal conductivity at the macroscale requires a model of the mesostructure of the material. The flowchart of Figure 3.26 presents the steps taken to generate the mesostructure from experimental measurements.

First, a 3D model of a consolidated sample is generated using X-ray microtomography (µCT), with a voxel size of 20 µm (1). The fibres and matrix phase are separated using the grey-level histogram data (2). The resulting black-and-white slices are post-processed to separate the individual yarns (3) using an image analysis script developed in MATLAB, based on k-means clustering [Hartigan+1979]. Ellipses are fitted on the yarns to retrieve the section parameters; the values are confirmed with independent measurements using micrographic analysis (4) on polished cross-section cuts. The yarns present an average width of 5080±300 µm and an average thickness of 280±40 µm (Figure 3.27). The stack of black-and-white slices obtained from µCT is further processed to observe the undulation of the yarns: the centroid of the individual clustered yarns are defined on each slice; the centroids are then connected

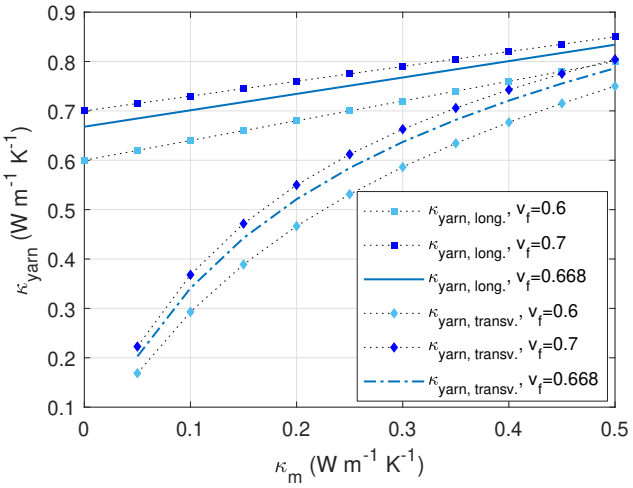

Figure 3.25 – Principal thermal conductivity of the yarn as a function of thermal conductivity of the matrix

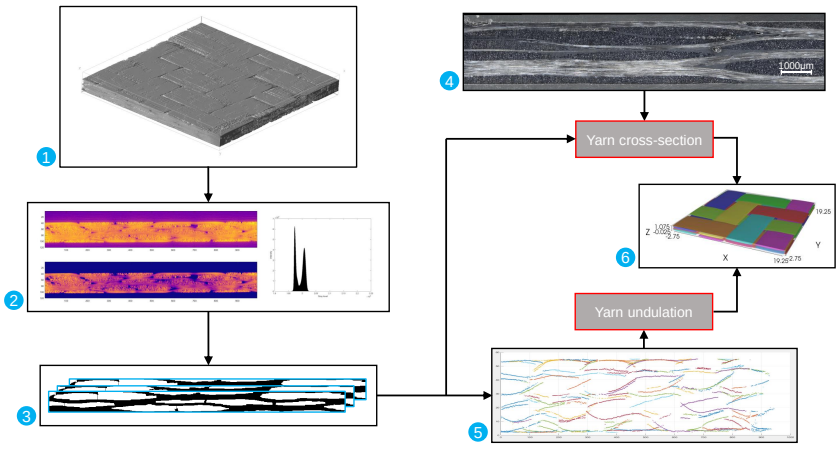

Figure 3.26 – Flowchart for the generation of the mesoscale model

slice-by-slice using a distance criterion, to reconstruct the yarn path (5) (the reconstruction is further detailed in Appendix A.2).

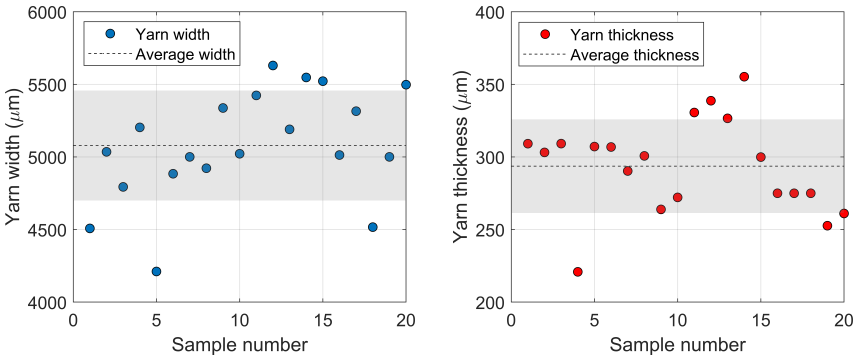

Figure 3.27 – Average yarn dimensions

The geometrical data are finally used to generate an idealized model at the mesoscale, based on the real mesostructure of the consolidated samples, using TexGen (6).Two plies are generated, to evaluate the influence of the ply offset on the results. The individual yarns with orientation vectors and the continuous matrix phase are represented. The TexGen model is discretized in voxels and imported in Abaqus; the voxels are mapped to DC3D8 linear heat transfer brick elements. The effective thermal conductivity tensor at the macroscale is evaluated by applying boundary conditions to generate a temperature gradient $\Delta T = 1\,\mathrm{K}$ between two opposite faces of the parallelepipedic geometry, all other faces being insulated. The analysis is repeated for different values of matrix thermal conductivity κ_m. The normalized steady state heat flux in the matrix and fibrous (yarns) phase is presented in Figure 3.28 for the simulations in the three principal directions. The heat is mostly transferred through the yarns, as expected from their higher thermal conductivity.

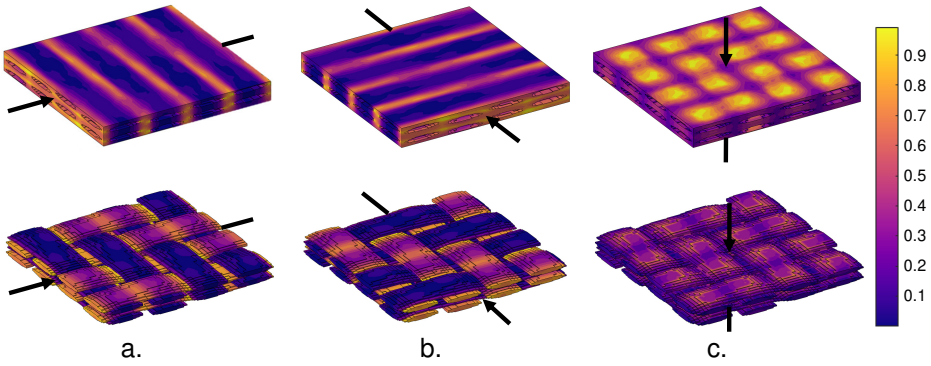

Figure 3.28 – Normalized steady-state heat flux during thermal simulation in the matrix (top) and fibrous (bottom) phase. a: temperature gradient along x, b: temperature gradient along y, c: temperature gradient along z

The diagonal terms of the thermal conductivity tensor are computed from the steady state average of the heat flux per unit area ϕ_i, multiplied by the distance e between the two

considered faces and divided by ΔT (eq. 3.4.10). The operation is repeated on every couple of faces to obtain the full tensor.

$$\kappa_i = \frac{e}{S\Delta T} \iint_S \phi_i \mathrm{d}S \ , \quad i = \{xx, yy, zz\} \tag{3.4.10}$$

As expected from the balanced structure of the fabric, the in-plane conductivities κ_{xx} and κ_{yy} are found equal, and no significant difference in thermal conductivity due to the offset between plies is observed. The simulated in-plane and out-of-plane conductivities are presented as a function of the thermal conductivity of the matrix in Figure 3.29a. A second-order polynomial can be fitted on the curves (eqs 3.4.11 and 3.4.12).

$$\kappa_{\text{in-plane}}(T) = -0.4192\kappa_m^2 + 1.0546\kappa_m + 0.2647 \tag{3.4.11}$$

$$\kappa_{\text{out-plane}}(T) = -0.8278\kappa_m^2 + 1.6037\kappa_m + 0.0572 \tag{3.4.12}$$

The effective thermal conductivity at the macroscale can then be expressed as a function of temperature, substituting the explicit temperature dependent expression of the matrix thermal conductivity (equation 3.4.6) as per eqs. 3.4.13 and 3.4.14.

$$\kappa_{\text{in-plane}}(T) = \begin{bmatrix} 1 \\ H(T_c - T) \times a(T_c - T)^{1/3} + \kappa_{m,\text{melt}} \\ (H(T_c - T) \times a(T_c - T)^{1/3} + \kappa_{m,\text{melt}})^2 \end{bmatrix} \cdot \begin{bmatrix} 0.2647 \\ 1.0546 \\ -0.4192 \end{bmatrix} \tag{3.4.13}$$

$$\kappa_{\text{in-plane}}(T) = \begin{bmatrix} 1 \\ H(T_c - T) \times a(T_c - T)^{1/3} + \kappa_{m,\text{melt}} \\ (H(T_c - T) \times a(T_c - T)^{1/3} + \kappa_{m,\text{melt}})^2 \end{bmatrix} \cdot \begin{bmatrix} 0.0572 \\ 1.6037 \\ -0.8278 \end{bmatrix} \tag{3.4.14}$$

The condensed form expressed using Einstein summation convention in eqs. 3.4.15 and 3.4.16 shows the thermal conductivity as a combination of parameters related to the conductivity of the matrix, and implicit architecture parameters related to the meso- and microstructure of the material.

$$\kappa_{\text{in-plane}}(T) = \underbrace{\left(H(T_c - T) \times a(T_c - T)^{1/3} + \kappa_{m,\text{melt}}\right)^{i-1}}_{\text{matrix conductivity}} \overrightarrow{e_i} \cdot \underbrace{[0.2647 \ 1.0546 \ -0.4192]}_{\text{implicit architecture parameters}} \ (\overrightarrow{e_i}) \tag{3.4.15}$$

$$\kappa_{\text{out-plane}}(T) = \underbrace{\left(H(T_c - T) \times a(T_c - T)^{1/3} + \kappa_{m,\text{melt}}\right)^{i-1}}_{\text{matrix conductivity}} \overrightarrow{e_i} \cdot \underbrace{[0.0572 \ 1.6037 \ -0.8278]}_{\text{implicit architecture parameters}} \ (\overrightarrow{e_i}) \tag{3.4.16}$$

where H is the Heaviside step function, and the vectors $\overrightarrow{e_i}$ form an orthonormal basis. The results are presented as a function of temperature in Figure 3.29b. The in-plane thermal conductivity decreases from $0.6\,\mathrm{W\,m^{-1}\,K^{-1}}$ at room temperature to $0.42\,\mathrm{W\,m^{-1}\,K^{-1}}$ above the melting temperature of the matrix, while the out-of-plane conductivity varies between $0.55\,\mathrm{W\,m^{-1}\,K^{-1}}$ and $0.28\,\mathrm{W\,m^{-1}\,K^{-1}}$ over the same range of temperature.

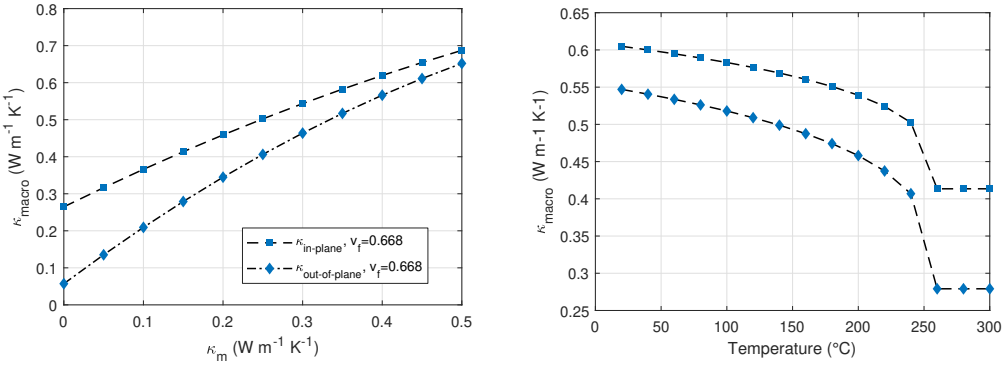

(a) As a function of matrix conductivity

(b) As a function of temperature

Figure 3.29 – Macroscale thermal conductivity

3.4.4.2 Non-contact IR thermography

The approach described in the previous section to determine the thermal conductivity tensor of the composite requires significant efforts for the characterization of the properties of the constituents and of the architecture of the composite at the meso- and macroscale. An alternative non-contact thermal conductivity measurement method, based on the experimental heating setup introduced in section 3.3.2 is presented here.

A plate-like sample is heated on its front face with an halogen lamp, positioned at a set distance from the plate. The temperature on the backface of the plate is measured using an infrared camera; the full-field data is used in an inverse analysis procedure to determine the principal thermal conductivities of the sample.

This method has been used in previous work conducted at ICA to evaluate the thermal conductivities of unidirectional [Akué Asséko+2015] and woven composites [El Bakali+2013], based on measurements at the steady-state and using automotive lamps as a heat source [Dauphin+2012]. This work is extended here to allow transient optimization (as a way of increasing the sensitivity of the measurement) and using cylindrical halogen lamps as described in section 3.3.1, to limit the influence of the shape of the quartz bulb on the incident heat flux.

Experimental setup: A consolidated plate manufactured from 8 plies of 300×300mm PA66/glass with a layup $[0/90]_{2S}$ is heated with an halogen lamp (operating under a reduced voltage at temperature of 2050 K) positioned 15 cm from the plate. The temperature of the backface is measured with a FLIR SC325 infrared camera (see Fig. 3.4 for a schematic of the setup). The sample is heated for 1800 s and allowed to cool with the lamp turned off for

1800 s. The temperature evolution averaged on three test repeats is presented in Fig. 3.30, along with the temperature field measured on the backface at steady state.

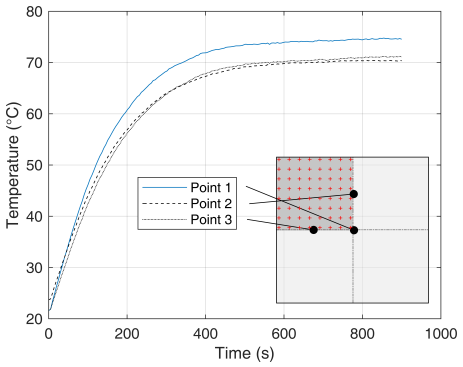

(a) Evolution of temperature on the backface during the heating phase

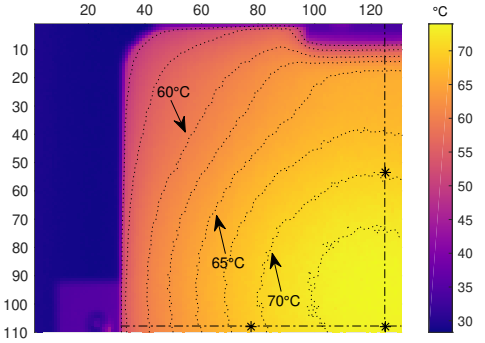

(b) Thermogram of the backface after 900 s; dashed lines represent isotemperature contours

Figure 3.30 – Experimental temperature measurement

The thermogram shows that while the isotemperature contours are symmetrical relative to the vertical median line of the plate, they present a slight upward shift and are not symmetrical relative to the horizontal median. This is attributed to the formation of a convective plume on the vertical sample. The influence of the mica sample holder (opaque to the infrared wavelengths) is visible in Fig. 3.30b (top right); the temperature field is perturbed only on a short distance, as the thermal conductivity of the sample is low.

Inverse analysis: The inverse analysis consists in finding the thermal conductivity tensor $\boldsymbol{\kappa}$ that minimizes the least square difference between the measured and simulated temperature on the backface of the sample.

$$\min_{\boldsymbol{\kappa}} \int_0^{t_f} \left(T_{\text{sim}}(t,\kappa) - T_{\text{exp}}(t)\right)^2 dt \tag{3.4.17}$$

A quarter of the plate is considered for the optimization, with a 8×8 grid of control points on which the objective function is evaluated (+ in Fig. 3.30a). The built-in optimization solver proposed in Comsol is not adapted to solve transient optimization problems; a coupling with Matlab through a LiveLink™ module is used, as described in Fig. 3.31. The minimization problem is solved with an interior-point algorithm using *fmincon*, as information on gradients are unavailable (black-box optimization).

At each evaluation of the objective function in Matlab, a transient heat transfer simulation is run in Comsol. The simulated temperature evolution at the control points is extracted and compared to the experimental data; the values of the minimization parameters are updated accordingly, and the procedure is repeated until the optimality tolerance condition is verified or the maximum number of objective function evaluations is reached.

Non-thermodependent conductivity: In a first step, the optimization is conducted assuming a constant thermal conductivity in the temperature range observed during the test.

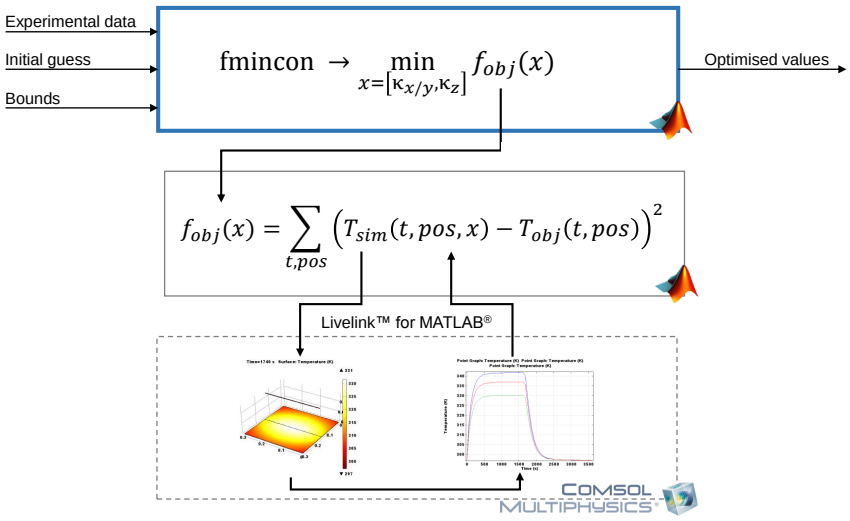

Figure 3.31 – Flowchart of the transient optimization

The in-plane conductivities are assumed to be equal, and the optimization parameters are reduced to $[\kappa_{\text{in-plane}}, \kappa_{\text{out-plane}}]$.

The parameters used in the simulation and for the optimization solver are presented in Table 3.2 along with the optimized conductivity obtained.

Table 3.2 – Simulation and optimization solver parameters

Simulation parameters	
Sample dimensions $l \times w \times t$	300x300x4.05 mm
Density ρ	$1885 \pm 10\,\mathrm{kg/m^3}$
Specific heat C_p	Interpolated from Sect. 3.4.3.2
Emissivity ϵ	0.93
Lamp temperature T_{lamp}	2050 K
Convection coefficient h_c	$5.2\,\mathrm{W\,m^{-2}\,K^{-1}}$ [Churchill+1973]
Optimization parameters	
Initial in-plane conductivity $\kappa^{\text{init}}_{\text{in-plane}}$	$0.5\,\mathrm{W\,m^{-1}\,K^{-1}}$
Initial out-of-plane conductivity $\kappa^{\text{init}}_{\text{out-plane}}$	$0.5\,\mathrm{W\,m^{-1}\,K^{-1}}$
Conductivity bounds	$[0.1\text{–}1]\mathrm{W\,m^{-1}\,K^{-1}}$
Optimized values	
In-plane conductivity $\kappa_{\text{in-plane}}$	$0.57 \pm 0.03\,\mathrm{W\,m^{-1}\,K^{-1}}$
Out-of-plane conductivity $\kappa_{\text{out-plane}}$	$0.49 \pm 0.07\,\mathrm{W\,m^{-1}\,K^{-1}}$

The macroscale conductivity values obtained from the optimization procedure have the same order of magnitude as the one obtained using the homogenization approach, at temperatures <100 °C, and the out-of-plane conductivity is found as expected to be lower than the in-plane conductivity. The dispersion on the out-of-plane thermal conductivity corresponding to the different experimental tests is high (15%); a potential explanation is the fact that the Biot number of the system is less than 1 ($Bi \approx 0.1$), which suggests small temperature

gradients through the thickness of the sample. The use of a thicker sample would increase the sensitivity on the out-of-plane conductivity.

Thermodependent conductivity: In a second step, a simplified linear temperature dependence of the matrix thermal conductivity is considered, assuming that the architecture parameters determined in section 3.4.4.1 are known. The in-plane and out-of-plane effective conductivities of the composite can be written as in eqs. 3.4.20 and 3.4.21.

$$\kappa_{\text{in-plane}}(T) = \begin{bmatrix} 1 \\ \kappa_{\text{m,slope}} \cdot T + \kappa_{\text{m,zero}} \\ (\kappa_{\text{m,slope}} \cdot T + \kappa_{\text{m,zero}})^2 \end{bmatrix} \cdot \begin{bmatrix} 0.2647 \\ 1.0546 \\ -0.4192 \end{bmatrix} \tag{3.4.18}$$

$$\kappa_{\text{out-plane}}(T) = \begin{bmatrix} 1 \\ \kappa_{\text{m,slope}} \cdot T + \kappa_{\text{m,zero}} \\ (\kappa_{\text{m,slope}} \cdot T + \kappa_{\text{m,zero}})^2 \end{bmatrix} \cdot \begin{bmatrix} 0.0572 \\ 1.6037 \\ -0.8278 \end{bmatrix} \tag{3.4.19}$$

$$\kappa_{\text{in-plane}}(T) = (\kappa_{\text{m,slope}} \cdot T + \kappa_{\text{m,zero}})^{i-1} \overrightarrow{e_i} \cdot [0.2647\ 1.0546\ -0.4192]_{(\overrightarrow{e_i})} \tag{3.4.20}$$

$$\kappa_{\text{out-plane}}(T) = (\kappa_{\text{m,slope}} \cdot T + \kappa_{\text{m,zero}})^{i-1} \overrightarrow{e_i} \cdot [0.0572\ 1.6037\ -0.8278]_{(\overrightarrow{e_i})} \tag{3.4.21}$$

The optimization parameters are $\kappa_{\text{m,slope}}$ and $\kappa_{\text{m,zero}}$. The modelled macroscale in-plane and out-of-plane conductivities are related, which helps mitigating the low sensitivity on the out-of-plane conductivity (although this comes at the cost of additional experiments needed to characterize the structure of the laminate).

The optimization procedure is conducted on two input data sets: a. a 'perfect' input set, generated by simulating the heating of a plate with temperature dependent thermal conductivity (as computed using the homogenization approach) to validate the implementation, and b. the experimental data set. The optimization descent path associated with both data sets is presented in Fig. 3.32, with the response surface computed by evaluating the objective function on a grid in the parameter space ($\kappa_{\text{m,slope}}$,$\kappa_{\text{m,zero}}$). The response surface associated with the perfect input data presents a smooth, steep valley with a clearly defined global minimum (the spikes that can be observed in the graph are due to the grid used to define the response surface not being parallel to the valley). The response surface of the experimental input data presents a much shallower valley, which is expected because of the noise inherent to the experimental measurement; the direction is preserved, however no clear global minimum can be observed.

The predicted slope and intercept of the linear model are presented in Table 3.3. The validation data is within 2% of the parameters obtained by a direct fit on the matrix conductivity defined by eq. 3.4.6 between [20–200 °C].

The effective thermal conductivity as a function of temperature is presented in Fig. 3.33 for the two approaches considered: homogenization, and inverse analysis from non-contact

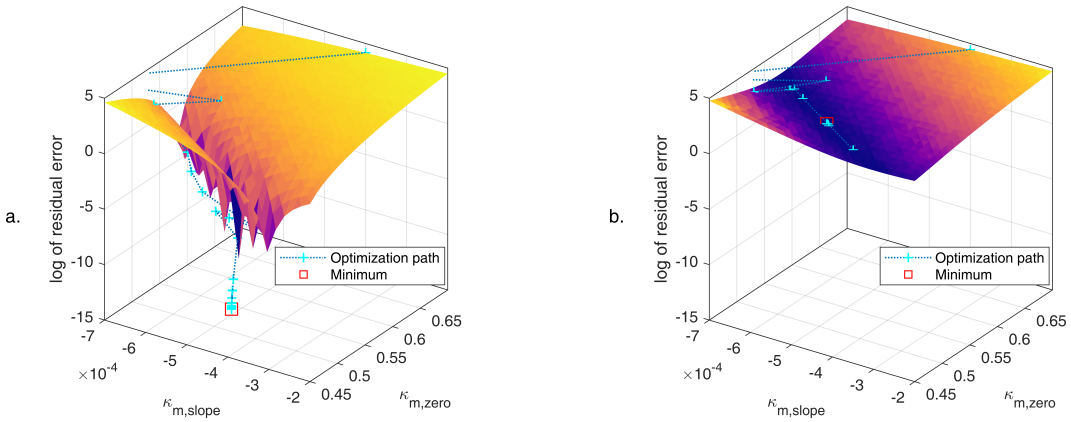

Figure 3.32 – Response surface of the optimization. a. 'perfect' validation data, b. experimental data

Table 3.3 – Linear temperature-dependent model optimized parameters

Data set	$\kappa_{m,slope}$ ($W\,m^{-1}\,K^{-2}$)	$\kappa_{m,zero}$ ($W\,m^{-1}\,K^{-1}$)
Fit on eq. 3.4.6 [20–200 °C]	-4.6196×10^{-4}	0.52
Validation data	-4.6211×10^{-4}	0.5209
Experimental data	-4.603×10^{-4}	0.5112

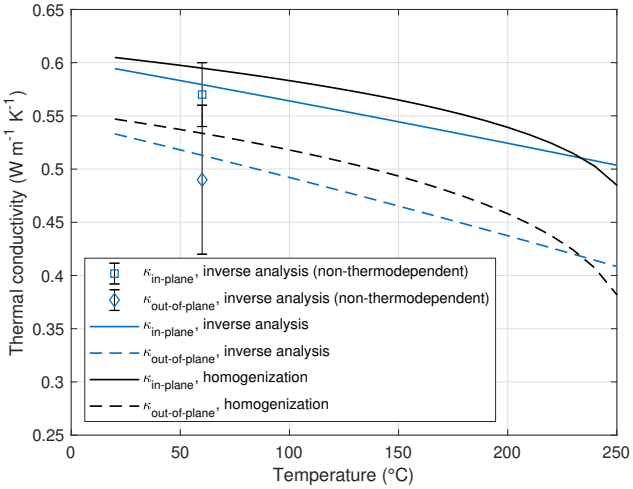

Figure 3.33 – Effective thermal conductivity as a function of temperature from homogenization and non-contact measurement

experimental measurements. The homogenization method predicts slightly higher values than the inverse analysis, although the model is within the experimental margin of error.

Those two methods present different pros and cons. While the homogenization method requires significant work to accurately model the micro- and mesostructure of the laminate, the temperature dependence is easily implemented via the properties of the constituents. The inverse analysis approach is based on a fast experiment and does not require extensive post-processing; however, the non-negligible temperature variations during the test have to be considered by supposing the form of the temperature dependence; the absence of further information on the material behaviour or structure leads to an increase of the complexity of the research space. Improving the accuracy of the measurement would require a better control of the boundary conditions: either by conducting the test in a controlled atmosphere (convection and temperature), or by using a different source (laser [El Rassy+2019], ...).

3.4.5 Ply/ply thermal contact conductance and effective thermal conductivity of an unconsolidated stack

Modelling the heat conduction in a stack of non-consolidated semipreg plies is more complex than for a consolidated laminate. The individual plies are at the mesoscopic scale composed of three distinct layers (an isotropic resin-rich layer, an orthotropic glass fabric and a second resin-rich layer) and are highly porous (in this case, the air volume fraction in a single semipreg ply v_{air} is approximately 52%), and the effect of thermal contact resistances at the ply/ply interfaces has to be accounted for.

In addition, both the thermal conductivity of the semipreg plies, and the thermal contact resistances are expected to depend on pressure (via the compaction of the fibre bed and potential increase of the number of contact points between plies) and temperature, as the matrix conductivity is itself temperature-dependent, and an increase in temperature can cause softening and an increase of the contact points. While these effects have been described independently for dry glass and carbon woven fabrics [ElHage+2018] and for unidirectional carbon/PEEK semipregs [Cassidy+1994], no data is available in the literature in the case of powder-impregnated woven fabrics.

The influence of pressure and temperature on the effective thermal conductivity of an unconsolidated stack has been studied using the setup schematized in Fig. 3.34. A stack of 40 plies of PA66/glass semipreg with dimensions 300×300 mm is placed between the compression platens of the EDyCO press (see section 3.4.1.2). The stack is instrumented with fine gauge K-type thermocouples (diameter 75 µm), with a pair of thermocouples positioned at the center of the interfaces between every ten plies as shown. A compression load is applied on the stack (0 kN, with the top platen in contact with the stack, 10 kN and 30 kN). At every pressure level, the temperature of the platens is increased by increments of 50 °C up to 200 °C (with the exceptions of the test at 0 kN where the maximum temperature was set to 150 °C), and the evolution of temperature through the thickness of the stack is monitored. The stack is allowed to cool down to room temperature between every test, and the tests are

conducted from lowest to highest pressure as to avoid effects due to inelastic compression of the glass fibre network.

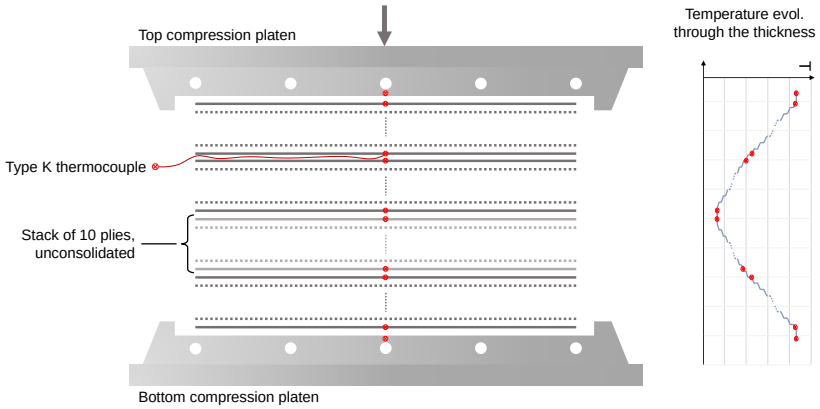

Figure 3.34 – Unconsolidated stack and position of thermocouples

The evolution of temperature through the thickness of the stack for the different pressure levels is presented in Fig. 3.35a, b and c. The results of an additional test with a vacuum-bagged stack (with top platen in contact) is presented in Fig. 3.35d. Measurements corresponding to thermocouples below the symmetry line of the stack are drawn with solid lines, measurements above with dashed lines. Symmetric measurements are plotted using the same colour. Data is missing from the thermocouples associated with ply 31 in all tests and ply 20 in vacuum-bag test; at least one thermocouple is present on all the monitored interfaces. The brutal signal increase observed for thermocouples 10, 11, 21 and 30 in test d at $t > 3600\,\mathrm{s}$ is due to melting of the insulated connections: the data is discarded accordingly. As expected from the temperature boundary conditions imposed by the heated platens, the temperature evolution is symmetrical. The increase in the applied load (mechanical or from the pressure difference in the vacuum bag) leads to reduced temperature gradients through the thickness of the stack.

The following hypothesis are made for the quantitative processing of the experimental data:

- The dimensions of the stack are assumed large enough to neglect edge effects; the problem is reduced to a one-dimensional heat transfer problem
- The thermal contact conductance h_c depends only on compaction level. The thermal conductance is defined as per eq. 3.4.22, where $\Phi_{+/-}$ is the heat flux across the interface and T_+ and T_- are the temperatures on each side of the interface.

$$\Phi_{+/-} = h_c(T_+ - T_-) \tag{3.4.22}$$

- The out-of-plane thermal conductivity is computed from the rule of mixture as per equation 3.4.23, where $v_{\text{semipreg.}}$ is the volume fraction of the solid phase (48% at 0 kN), $\kappa^{\text{cons.}}_{\text{out-plane}}$ is the temperature dependent thermal conductivity of the consolidated

material from equation 3.4.16 and κ_{air} is the temperature dependent conductivity of dry air [Kadoya+1985].

$$\kappa_{\text{out-plane}}^{\text{semipreg}} = v_{\text{semipreg}} \kappa_{\text{out-plane}}^{\text{cons.}}(T) + (1 - v_{\text{semipreg}}) \kappa_{\text{air}}(T) \tag{3.4.23}$$

The parallel model gives a high bound for the thermal conductivity of the semipreg, as this assumes perfect percolation; the thermal conductance predicted will consequently be a low bound of the real value.

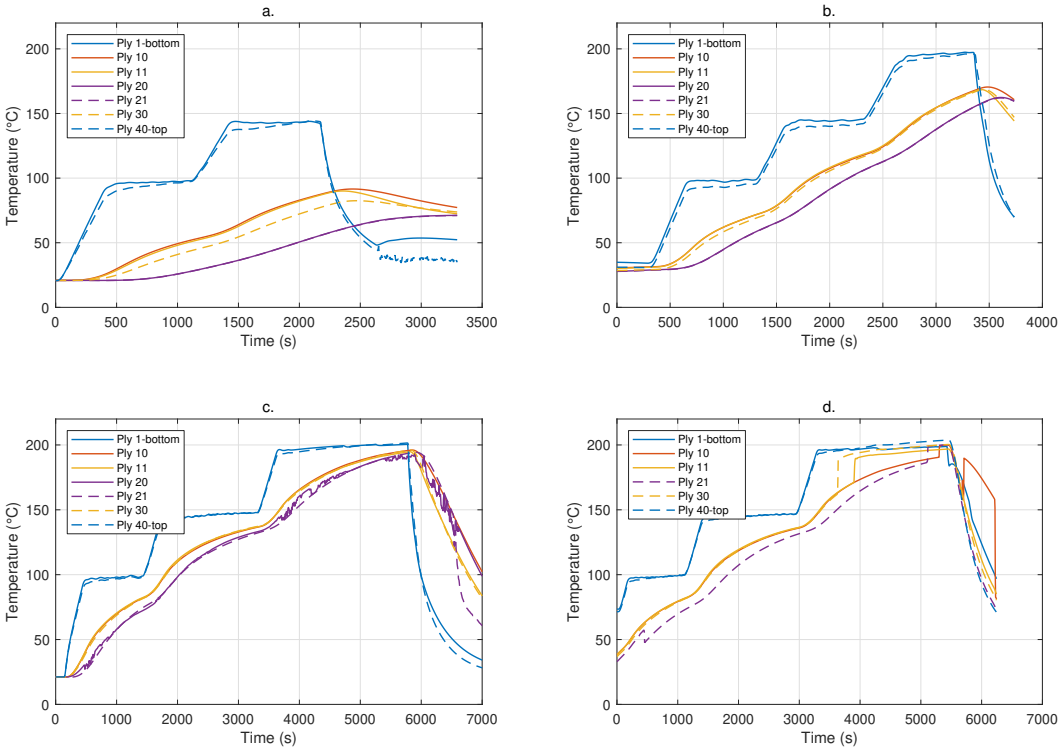

Figure 3.35 – Temperature evolution in an unconsolidated stack under different applied loads: a. 0 kN, b. 10 kN / 0.11 MPa, c. 30 kN / 0.33 MPa, d. vacuum-bagged stack (0.1 MPa)

These simplifiying assumptions, and notably the decoupling of the temperature and compaction effects help ensuring the uniqueness of the solution. Given the temperature range investigated during the experimental tests, the thermal conductance modelling is valid only for temperatures below the melt temperature of the PA66 matrix. The one-dimensional problem is modelled in Comsol as 40 plies of 5 line elements with a constant contact conductance between the plies. The temperature evolution at the top and bottom surfaces of the stack measured during the test is averaged and applied as a time-dependent boundary condition on the finite element model. As the microthermocouples are positioned inside the vacuum bag in test d., the influence of the Capran film used is neglected. The value of the thermal contact conductance is obtained by minimizing the least square difference between the experimental and simulated temperature at plies 10/11 and 20/21.

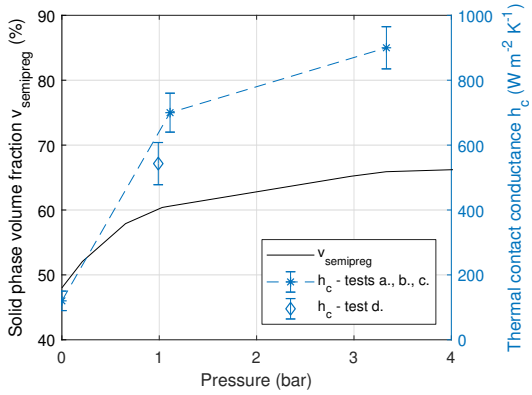

Figure 3.36 – Thermal contact conductance and solid phase volume fraction as a function of pressure

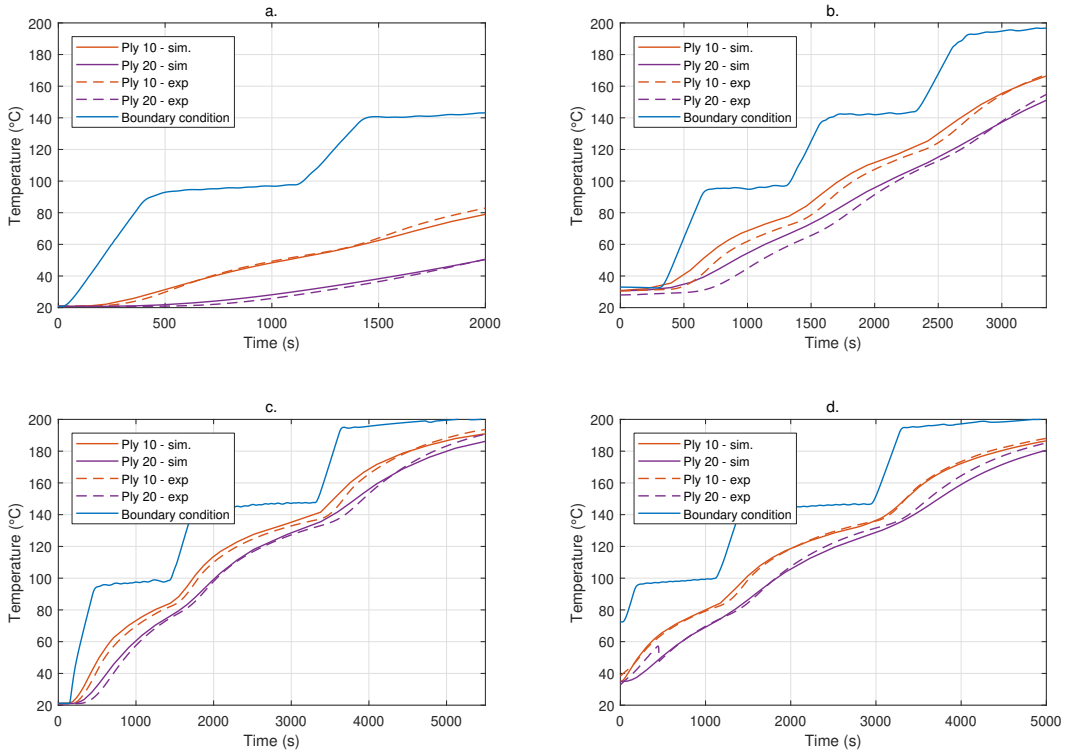

Figure 3.37 – Simulated (solid line) and experimental (dashed line) temperature at plies 10 and 20: a. 0 kN, b. 10 kN / 0.11 MPa, c. 30 kN / 0.33 MPa, d. vacuum-bagged stack (0.1 MPa)

The optimized values of thermal contact conductance are presented as a function of applied pressure in Fig. 3.36, along with the volume fraction of the solid phase, calculated from the thickness of the stack at ambient temperature. The error bars corresponds to a confidence interval in which the value of thermal conductance leads to a residual error within 5% of the minimal error obtained. The relation between the pressure and predicted contact conductance is non linear, with a sharp increase from $120\,\mathrm{W\,m^{-2}\,K^{-1}}$ to $700\,\mathrm{W\,m^{-2}\,K^{-1}}$ as the pressure increases to 1.1 bar; h_c further increases to $900\,\mathrm{W\,m^{-2}\,K^{-1}}$ at a pressure of 3.3 bar. The change in thermal contact conductance appears to be correlated to the change in semipreg volume fraction as the pressure increases. The plateau observed on additional volume fraction measurements at higher pressures is attributed to the compression limit of the dry woven fabric layer [Chen+2006a], as the temperature is not high enough to melt the PA66 matrix and impregnate the yarns.

The compaction level has an influence both on the effective thermal conductivity of the plies and on the thermal contact conductances. A higher compressive load on the stack leads to a densification of the plies and an increase of the number of fibre/fibre contacts via nesting: the higher percolation level increases the thermal conductivity. Additionally, deformation of the contact points at the ply-ply interfaces increases the contact surface and thus the thermal conductance. The compaction of the stack is reversible in the pressure range considered: the deformation of the polyamide droplets is assumed to remain elastic.

The thermal contact conductance determined from test d. (vacuum-bag with a compaction pressure of 990 mbar) is slightly lower than the conductance determined from test b. at a similar compaction pressure. This phenomenon is expected as the thermal conductivity of air is reduced at low absolute pressures (provided that gaseous conduction remains in the collisional, rather than ballistic, regime [Carminati2006]). Heat transfer by gaseous conduction through the interstitial air is thus reduced; the reduction of effective conductivity and thermal conductance has been reported for a variety of isotropic porous materials [Spagnol+2009] and delaminated composites [Donaldson+2005].

The simulated temperature evolution are presented in Fig. 3.37. A good agreement with the experimental data is observed, and the simple decoupled model used is able to represent the effect of temperature and pressure. The maximum error is observed for the test at 10 kN, where the simulation predicts higher temperatures by up to 8 °C in the transient state with low temperature boundary condition.

3.5 Model validation: 1-lamp setup

The model presented in this chapter is validated using the 1-lamp heating setup introduced in section 3.3.2. A vacuum-bagged stack composed of 6 plies of non-consolidated semipreg with layup $[0]_6$ is used as the sample; the experimental setup can be seen in Figure 3.38.

The lamp is set at at dimming output power of 60%, corresponding to a filament temperature of 2190 K, and positioned 20 cm from the sample. The temperature evolution of the backface is measured during the heating phase. The lamp and stack assembly are modelled in Comsol,

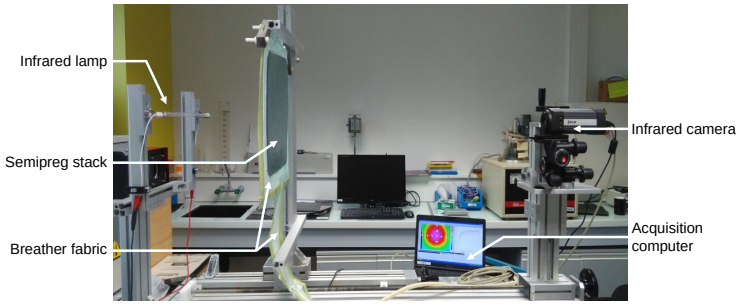

Figure 3.38 – 1-lamp heating setup with vacuum-bagged semipreg stack sample

with properties as defined from sections 3.3 and 3.4. The polyamide film used as the vacuum bag is not modelled explicitly, but its contribution to the emissivity of the sample is considered using the transmittance as characterized by Nakouzi [Nakouzi2012]. The contact conductance between the plies is taken as $550\,\mathrm{W\,m^{-2}\,K^{-1}}$. The average convection coefficient is set to $5.4\,\mathrm{W\,m^{-2}\,K^{-1}}$, from curve fitting of the cooling profiles. The experimental and simulated thermograms obtained in the steady state are presented in Figure 3.39a and 3.39b. The isovalues contours on the simulated temperature field form ellipses with the major axis aligned with the infrared lamp, while those isotemperature curves are stretched upwards in the experimental thermogram.

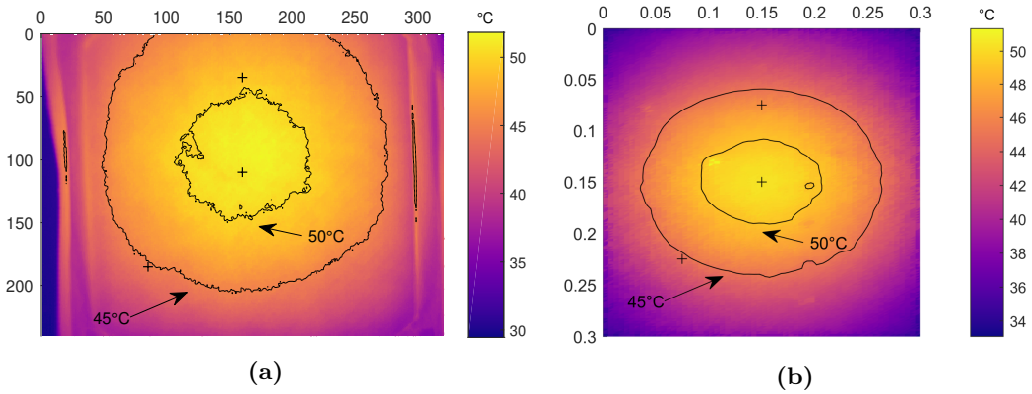

(a) **(b)**

Figure 3.39 – Backface thermogram, a: experimental measurement, b: simulation

The experimental and simulated temperature evolution on the center point of the backface (point 1) are plotted in Fig. 3.40, along with the temperature of the center point of the top half (point 2) and the center point of the bottom left quarter (point 3) of the backface.

The agreement between the experimental and simulated temperature is excellent, with the exception of point 2 for which the simulated temperature is underestimated by approximately 5%. The discrepancy is probably due to the convection state around the vertical plate: while the presence of a convective plume would lead to a higher convective transfer coefficient on the top part of the plate, the air flow also gets progressively warmer as it rises. These competing effects could explain the upward shift of the hot spot observed experimentally.

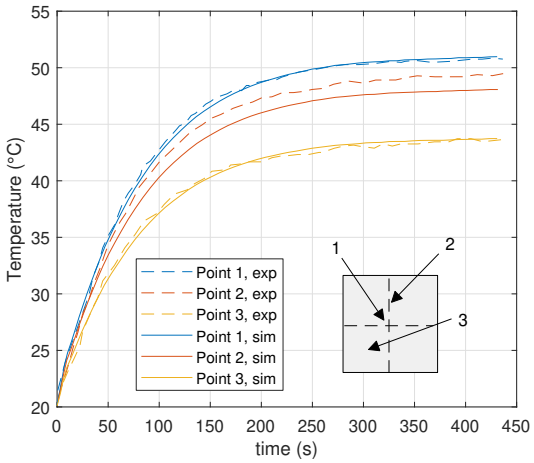

Figure 3.40 – Comparison between experimental and simulated temperature evolution on selected points

3.6 Conclusion

The simulation of the temperature field during the infrared preheating of a composite blank requires knowledge of the interaction between the infrared sources and the material surface, as well as of the properties that control heat transfer in the plane and through the thickness of the blank.

This chapter introduced the modelling assumptions made to simulate the three-dimensional temperature field in the composite blank; notably, the lamps are explicitly modelled as radiating cylinders, and the temperature of the filament has been characterized experimentally as a function of the electrical input power.

The optical properties of the consolidated and non-consolidated PA66/glass composite considered have been studied; the material is shown to be opaque at the scale of the ply, and the diffuse reflectivity has been characterized as a function of wavelength, showing the influence of the apparent glass fibres at the surface of the semipreg.

Effective thermophysical properties of the material have been characterized; two approaches for determining the thermal conductivity, from numerical homogenization or inverse analysis are compared, and non-contact infrared thermography coupled with transient optimization show a good potential as a fast measurement method. The effective thermal conductivity and thermal contact conductances in a stack of non-consolidated semipreg have been characterized and show a non-linear dependence on pressure.

The material characterization and finite element model implemented in Comsol have been validated against a 1-lamp heating setup. The development of a lab-scale infrared oven and its optimization using the model introduced in this chapter is presented in Chapter 4.

Chapter

4

Preheating of a composite blank in an infrared oven: experimental study, simulation and temperature optimization

4.1 Introduction

This chapter presents in a first part the validation of the model introduced in chapter 3 in conditions replicating the industrial thermoforming process, in which a blank of thermoplastic composite is brought to processing temperature in a radiative oven. An instrumented, modulable infrared heating oven has been developed for this purpose and is presented in section 4.2. This setup is used in section 4.3 to generate a database of experimental temperature distributions for various blanks and lamps configurations.

The experimental tests cases are replicated numerically to investigate the performances of the model. The influence of the blank sag during heating on the homogeneity of the temperature distribution is addressed numerically in section 4.5.

The temperature distribution within the blank is shown to depend non-linearly on the temperature and position of the lamps within the oven. Both gradient-based and derivative-free optimization methods are coupled to the numerical model to allow the determination of optimized oven parameters based on a required temperature field.

4.2 Development of a lab-scale infrared oven

The further validation of the model presented in Chapter 3 in a range of temperature more representative of the industrial conditions, as well as the experimental study of the entire thermoforming process (preheating and forming), required the development of a custom lab-scale infrared oven that could be adapted to an existing forming press system (presented in chapter 6). The setup, with schematic shown in Fig. 4.1, allows to investigate the influence of various lamp configurations on the resulting temperature field in blanks of dimensions $330 \times 330\,\text{mm}$.

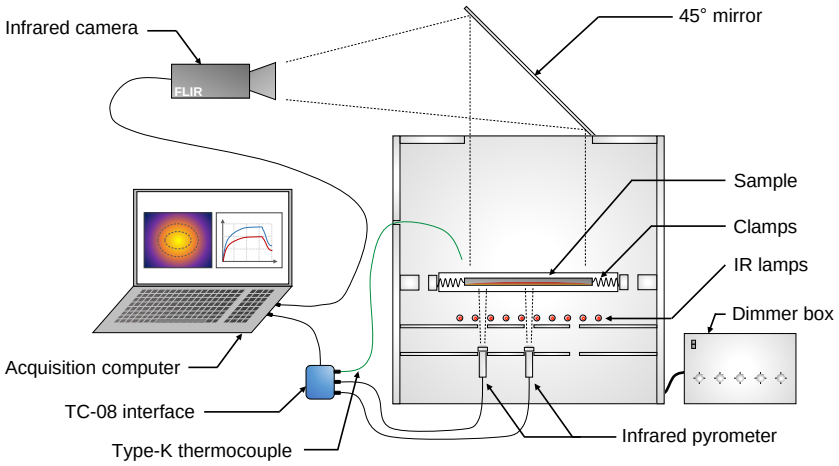

Figure 4.1 – Infrared preheating setup: oven and temperature acquisition

The system is based on a drawer-style oven design [Andrieu2005], and is composed of an aluminum profile frame with aluminium panels supporting an array of 10 tungsten halogen

lamps of 500 W–235 V as described in section 3.3.1. The composite blank is clamped using crocodile clips and mounted on a sliding frame with extension springs. The sliding frame enables an easy loading of the sample, and a fast transfer to the press with minimal actions required from the operator.

A side view of the oven is presented in Fig. 4.2. The one-sided heating design was selected to allow for a full-field temperature measurement on the back face of the blank, with a 45° polished aluminium mirror.

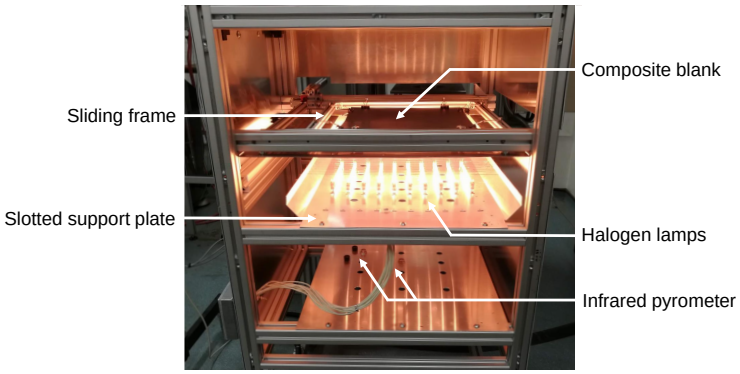

Figure 4.2 – Infrared oven (side panel removed)

4.2.1 Lamp configurations

The oven was designed to enable the modification of the geometric configuration of the lamp array. Fig. 4.3 presents a schematic top view of the lamps, with the dimensions of the composite blank superimposed.

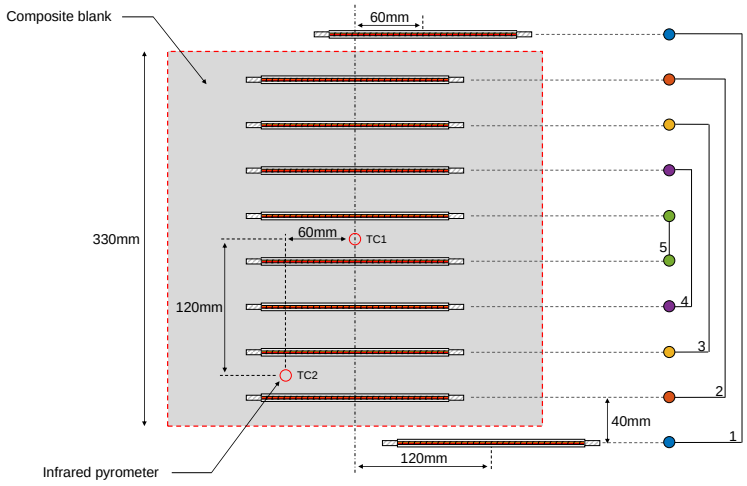

Figure 4.3 – Schematic top view of the lamp array

The inter-lamps spacing is fixed at 40 mm, and a series of pilot holes allows to reposition and offset each lamp individually by 60 mm or 120 mm along their axis, either side of the

median line. The choice of having a set of discrete admissible positions, rather than using slots to slide the lamps, ensures a good repeatability of the test configurations. In addition to the geometric configuration, the distance between the lamps and the blank can be modified between 140–200 mm by adjusting the position of the lamps support plate with the blank remaining at a fixed height.

The input power of the lamps can be adjusted via a phase angle dimmer. Given the limited number of outputs available from the dimming control box, the lamps are connected in five pairs symmetrically from the center of the array (see color coding on the right of Fig. 4.3), with the pairs being numbered in increasing order from the outer edges to the center: i.e., lamp pair 1 is comprised of the lamps farthest from the center of the blank, while lamp pair 5 is comprised of the lamps closest from the center, and each lamp in a pair has the same input voltage.

4.2.2 Temperature acquisition

Temperature measurements are taken on both sides of the composite blank. A FLIR SC640 infrared camera (Fig. 4.4a) is used to measure the temperature field on the back face of the blank through its reflection on an aluminium plate with an integrated reflectivity ρ_{mirror} measured at 0.88 in the spectral range $7.5 - 13\,\mu\text{m}$. Because of the lamp support plate, the same approach is not feasible on the front face being heated; a set of two Calex PM-HA-201-CT pyrometers (Fig. 4.4b) is used instead for spot measurements.

The pyrometers are positioned as shown in Fig. 4.3 (normal to the center, and between lamp pairs 2 and 3). Holes in the lamp support plate enables the pyrometers to view the blank but not the lamps. The distance between the sensors and the blank is set to 300 mm, which leads to a measured spot diameter of 26.9 mm with a 20:1 linear field of view. The main technical specifications of the sensors are provided in Table 4.1.

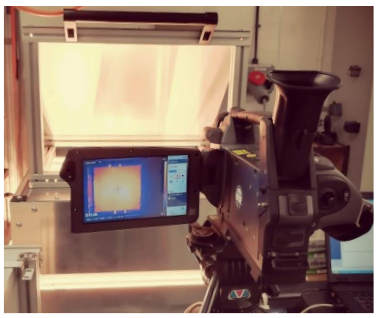

(a)

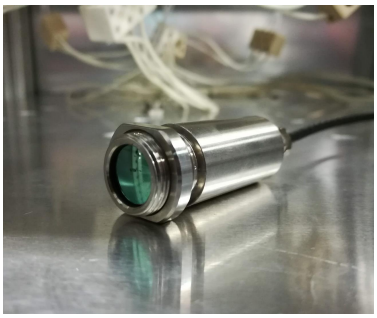

(b)

Figure 4.4 – Temperature acquisition: a. infrared camera, b. infrared pyrometer

In addition to the non-contact sensors used to measure the blank temperature, a type K thermocouple is placed 1 cm above the blank to monitor the air temperature in the oven. Aluminium foil tape is used to shield the thermocouple from radiation.

Table 4.1 – Specifications of the temperature sensors

Specifications	**FLIR SC640** [FLIR2010]	**Calex PM-HA-201-CT** [Calex2015]
Field of view	24° × 18°	5.8° (20:1)
Resolution	640 × 480 px	Spot
Spectral range	7.5–13 µm	8–14 µm

4.3 Experimental heating tests

4.3.1 Experimental setup

4.3.1.1 Lamp configurations

Four distinct lamp configurations (schematized in Fig. 4.5) are used:

- Configuration a. (LCa): all lamps centered relative to the blank
- Configuration b. (LCb): all lamps offset alternately by ±120 mm from the center of the blank (equivalent to two arrays of five lamps with 80 mm spacing)
- Configuration c. (LCc): all lamps offset alternately by ±60 mm from the center of the blank
- Configuration d. (LCd): lamp pair 1 centered, lamp pairs 2 and 3 offset by ±60 mm and pairs 4 and 5 offset by ±120 mm (the lamp offset decreases with the distance from the center)

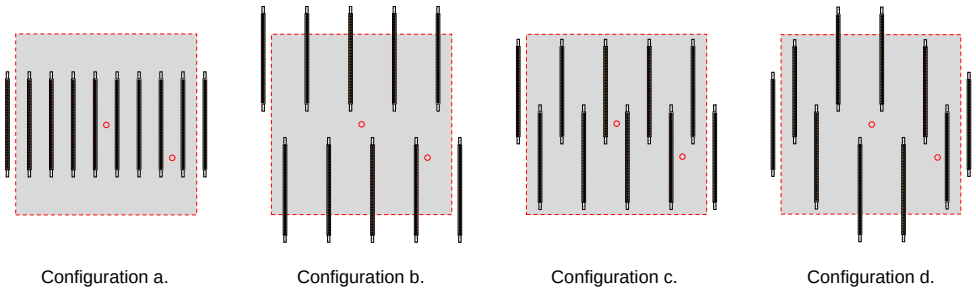

Figure 4.5 – Lamp configurations; press side on the left

These configurations result in different radiance distributions on the surface of the blank, and are used to generate a database of experimental temperature fields against which the simulation tool can be validated.

4.3.1.2 Test conditions and processing

Heating tests are performed on preconsolidated and unconsolidated blanks of dimensions 330 × 330 mm, manufactured from the PA66/glass fabric described in 3.4.1. The blank is

loaded in the oven and aligned with the center of the lamp panels. The lamps are turned on and the blank is heated for 120 s; the blank is then transferred out of the oven and allowed to cool down to room temperature. The surface temperature is recorded during the heating and cooling phase as described in section 4.2.2.

The oven parameters (lamps configurations, distance between the blank and the lamps, and percentage of nominal power) and blank parameters (layup, consolidated or semipreg) are varied according to Table 4.2. A one-factor-at-a-time (OFAT) approach is used instead of a fractional design of experiments, as the aim is to create validation test cases rather than systematically investigating the effects of the parameters or optimizing experimentally the temperature field. Test cases 1–4 and 5–8 are conducted varying the lamp configuration, for all lamps at 100% and 50% of nominal power respectively; the lamp-plate distance is varied in test cases 9–10, and different blank configurations are used in test cases 11–14. A minimum of two tests are conducted per test condition. To ensure a good repeatability of test case 14 (stack of 4 plies of unconsolidated semipreg), the blank is vacuum-bagged with partial vacuum of 500 mbar, as the dispersion associated with other approaches (manual tufting and spot welding) was not deemed acceptable.

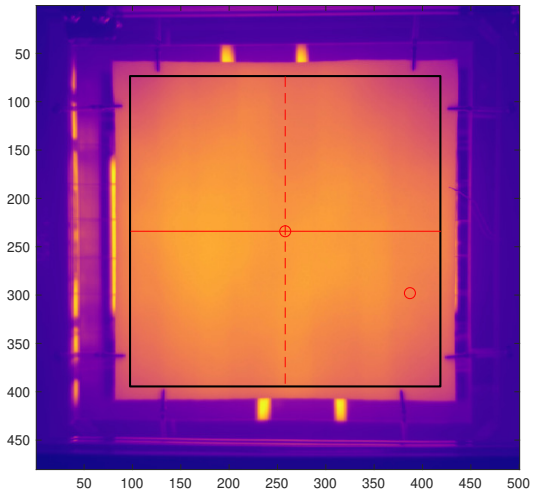

Figure 4.6 – Processed thermogram; the 300 × 300 mm region of interest is shown in black, with position of infrared thermocouples denoted by ○

An example of an experimental thermogram of the back face of the blank obtained with the infrared camera is shown in Fig. 4.6. To allow the observed temperature distribution to be compared between tests, a MATLAB script is developed to define a region of interest (ROI) of 300 × 300 mm on the blank (black rectangle in the figure). Using a ROI of reduced dimensions rather than the entire blank ensures that the temperature distribution measured is not affected by the clamps or by dispersion in the dimensions of the blanks, as the position of the region of interest is derived from reference points on the fixed aluminium frame rather than from the corners of the blank.

Table 4.2 – Heating test parameters

	Oven parameters			**Blank parameters**	
Test n°	Lamp configuration	Lamp–blank distance (mm)	% nominal power	Consolidation	Layup
1	LCa	140	100%	CS	[0°]
2	LCb	140	100%	CS	[0°]
3	LCc	140	100%	CS	[0°]
4	LCd	140	100%	CS	[0°]
5	LCa	140	50%	CS	[0°]
6	LCb	140	50%	CS	[0°]
7	LCc	140	50%	CS	[0°]
8	LCd	140	50%	CS	[0°]
9	LCa	170	100%	CS	[0°]
10	LCb	170	100%	CS	[0°]
11	LCa	140	100%	CS	[45°]
12	LCa	140	100%	SP	[0°]
13	LCa	140	100%	CS	$[0/90°]_s$
14	LCa	140	100%	SP	$[0/90°]_s$

4.3.2 Experimental results

The temperature evolution measured from the thermocouples is presented in Fig. 4.7 for the repeats of test 1 (lamp configuration LCa, all lamps at nominal power). TC1 (solid line) and TC2 (dashed line) correspond respectively to spot measurements at the center and in the lower left quadrant of the backface as per Fig. 4.3. Measurements conducted using the infrared thermocouples (blue lines) are compared with thermogram data from the infrared camera by averaging the pixels within a 13.5 mm radius of the center of each spot (red lines).

No significant difference is observed between measurements from the top or the bottom of the blank, which suggests negligible temperature gradients through-the-thickness for this test case (test case 14, with a non-consolidated blank leads to gradients through the thickness above 40 °C). A good repeatability of the measurements is shown, with a dispersion <3% on 3 tests. The heating rates achieved show the interest of infrared heating when short cycle times are needed, with the center of the one-ply consolidated blank reaching T_m in less than 30 s. The evolution of the ambient air temperature recorded by the shielded thermocouple is presented in addition to the spot measurements: a maximum temperature of (78 ± 7) °C is shown. The fluctuations observed at longer times ($t > 80$ s) on both the K-type thermocouple and the non-contact measurements are attributed to variation of the air temperature of the room where the experimental setup is installed (draught, ...).

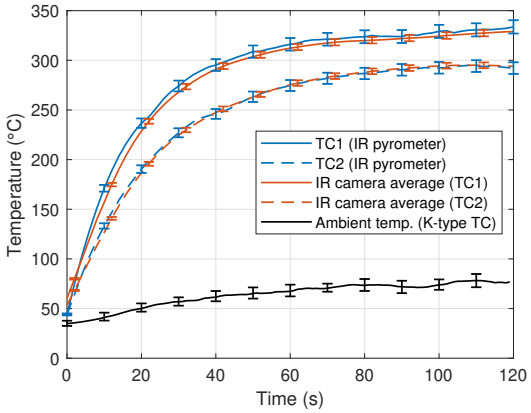

Figure 4.7 – Temperature evolution for test conditions 1

Sagging was observed on blanks manufactured from the preconsolidated fabric, as the temperature reached the melting point of the polyamide matrix (see Fig. 4.8). This phenomenon is widely reported in the literature related to the experimental forming of thermoplastic composites [Haanappel+2012; Haanappel+2014; Harrison+2013], although it is rarely addressed as compensation strategies require the design of complex blankholders [Vanclooster2010]. No quantitative measurements of the deflection were made, as the structure of the oven prevented direct viewing of the sample from the side. Sagging was less apparent in blanks assembled from non-consolidated fabric. The influence of sag on the temperature distribution is discussed in section 4.5.

Figure 4.8 – Blank after preheating exhibiting sag; edges outlined in red

4.3.2.1 Temperature distribution

The thermograms of the ROI obtained from the infrared camera after 120 s of heating are presented for the 4 distinct lamp configurations in Fig. 4.9 (with parameters set as per test conditions 1, 8, 11 and 13). The y–axis of the plots corresponds to the direction of the lamps, with thermocouple TC2 located in the lower right quadrant. To facilitate comparison between the resulting temperature fields, isotemperature contours are represented with dashed lines at fixed temperatures between 240 °C and 320 °C in steps of 20 °C.

Significant differences are observed in terms of spatial distribution of temperature between the different lamp configurations tested. Configuration LCa (all lamps centered) leads to a temperature field with elliptical isocontours, with the minor axis parallel to the lamps direction and major axis aligned with the center of the lamps. This configuration results in the highest temperatures ($T_{\max} = 334\,°C$). In contrast, configuration LCb leads to the lowest maximal temperature observed $T_{\max} = 271\,°C$, with the isothermal contours following the outline of the offset lamps. Configurations LCc and LCd present intermediate results both in terms of maximum temperature, and shape of the contours.

To complement the information given by the surface plot of the thermogram data, a quantitative representation of the temperature distribution on the surface of the blank is needed. Histograms graphical representation are not particularly suited to the comparison of a large number of results (as the graphs would become cluttered). As an alternative, the temperature distributions are represented using their empirical distribution function, as defined per equation 4.3.1 (where n is the number of pixels in the observation, and $\mathbf{1}_A$ an indicator function of event A).

$$\hat{F}_n(T) = \frac{1}{n}\sum_{1}^{n} \mathbf{1}_{T_i \leq T} \tag{4.3.1}$$

The comparison between the two graphical representations is presented in Fig. 4.10 for the four different lamp configurations tested. The distribution function also has the advantage of being independent of the histogram bin selection.

The empirical distribution functions of the temperature field for configurations LCa to LCd with a blank of 1 ply of consolidated PA66/glass fabric are presented in Fig. 4.11a–d, with

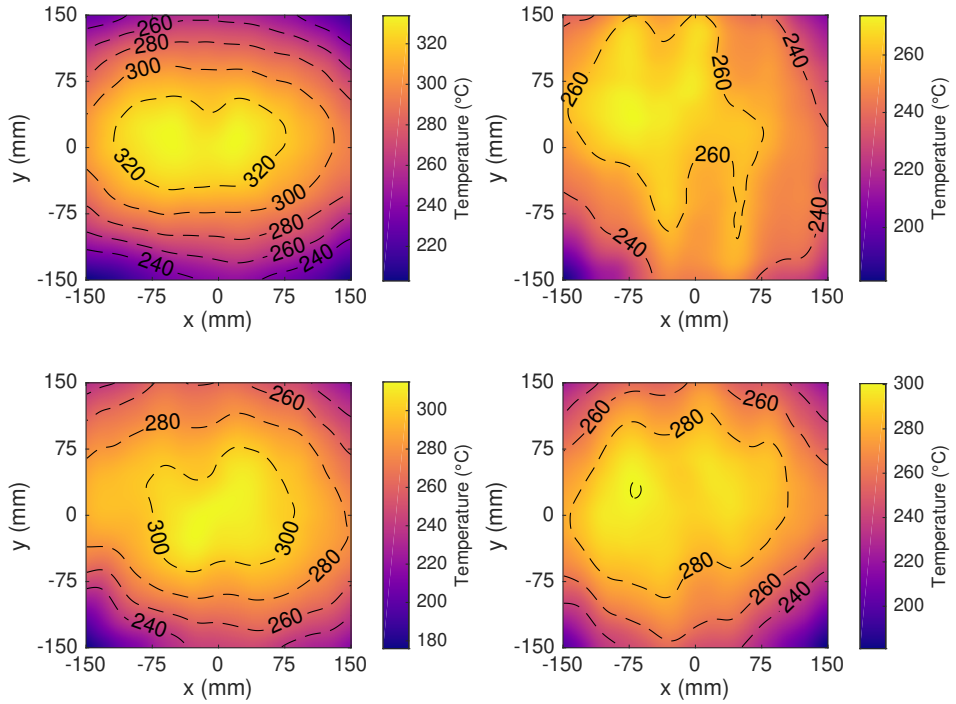

Figure 4.9 – Thermogram on the ROI (lamps at 100% nominal power, distance 140 mm, 1 ply CS). Left-to-right, top-to-bottom: lamp configurations LCa to LCd (tests 1 to 4).

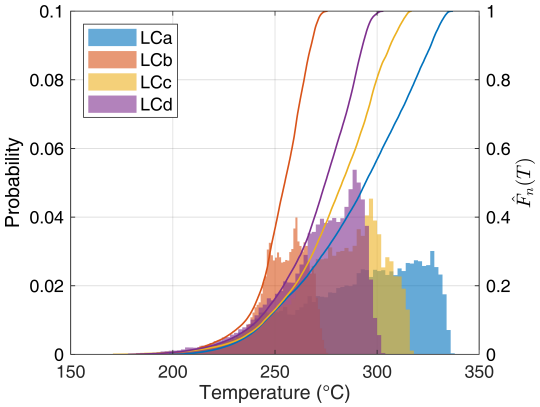

Figure 4.10 – Comparison between normalized histogram (left axis) and empirical distribution function (solid lines, right axis) for the four studied configurations; lamps at nominal power

lamps at 50% and 100% of nominal power at different times. The curves are sigmoid-shaped, and their apparent slope gives an indication on the homogeneity of temperature, with a steeper slope corresponding to a smaller temperature gradient on the surface. Increasing the heating duration ($t = 30\,\mathrm{s}$ to $t = 120\,\mathrm{s}$) results in a shift of the distribution function towards the higher temperatures. Increasing the lamps temperature also results in higher temperatures without a significant modification of the shape of the distribution function.

With all other parameters constant, the lamp configurations LCa and LCc lead to the highest temperatures (334 °C and 315 °C respectively after 120 s), but also the largest temperature gradients, with colder regions around the clamps at temperatures around 200 °C. Configurations LCb and LCd, result in lower temperatures but a more homogeneous distribution of temperature on the surface of the blank. Temperature gradients of 135 °C for configuration LCa and 71 °C for configuration LCb are observed, with 90% of the surface in a 78 °C (respectively 41 °C) temperature range.

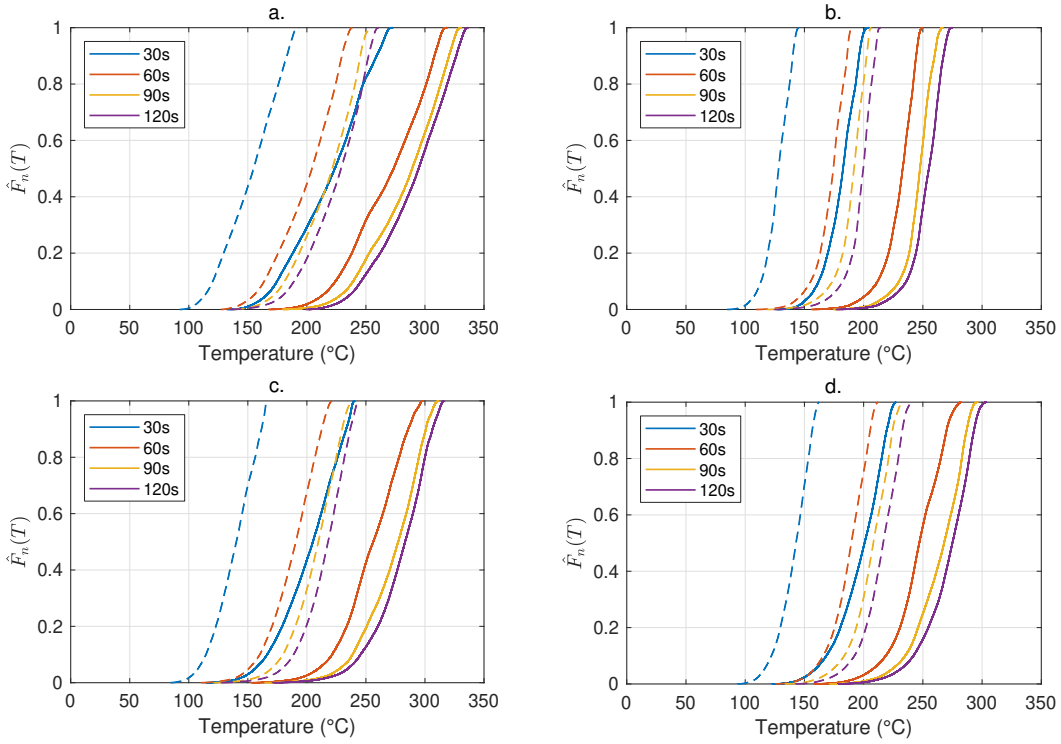

Figure 4.11 – Empirical temperature distribution function for different heating times (lamp-plate distance 14 cm, solid lines: 100% nominal power, dashed lines: 50% nominal power). Left-to-right, top-to-bottom: lamp configurations LCa to LCd (tests 1 to 8).

4.4 Finite element simulation of the heating step

4.4.1 Oven geometry

A simplified geometry of the oven described in section 4.2 is modelled in finite element software Comsol Multiphysics. The simplification of the geometry serves two purposes: a practical one first, as the direct import of the existing SolidWorks CAD (computer-aided design) model of the oven in Comsol is not possible without a specific interface module; second, a minimization of the computational time by reducing the level of details considered in the heat transfer simulation. Preliminary results showed that neglecting the contribution of the oven components situated above the panel shielding the sliding frame leads to a difference of 0.2% (less than 1 °C) on the maximum predicted temperature, while reducing the CPU time by 35%. As the oven geometry does not present symmetry planes (with the exception of lamp configuration LCa), the entire bottom section between the lamp support plate and the blank is modelled.

The simplified geometry is presented in Fig. 4.12. The blank is modelled as a parallelepipedic sheet at a distance $d_{l\leftrightarrow b}$ of the lamps array. The halogen lamps are modelled as in section 3.3: only the tungsten filament is represented as a cylinder of equivalent diameter 2.145 mm and length 165 mm.

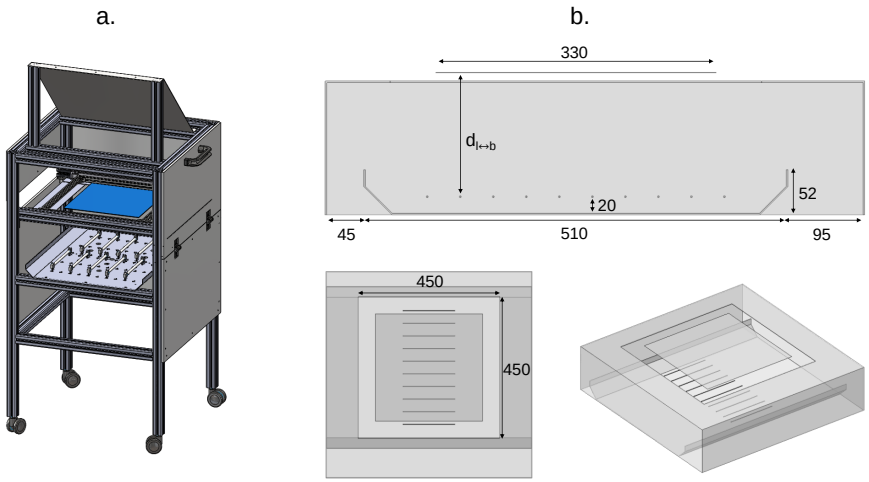

Figure 4.12 – Modelling of the oven; a. SolidWorks CAD, b. simplified geometry (all dimensions in mm)

4.4.2 Boundary conditions

The oven enclosure (comprising the lamps, blank, and reflecting panels) is composed of surfaces that are assumed Lambertian, opaque and grey. Additionally, the surface temperature distribution is uniform on the finite elements, and the ambient air is considered as a non-participating media (i.e., perfectly transparent to infrared radiation). These conditions allow

for the surface-to-surface radiation to be solved using the radiosity method, as introduced in section 2.2.3.1. As shadowing has to be accounted for, the view factors are computed with the hemicube method rather than direct integration of equation 2.2.9. A resolution of 256 is used (each face of the hemicube is discretized in 256×256 pixels). The model geometry is not modified during the analysis; consequently, the view factors are computed once per study.

Halogen lamps: The percentage of nominal power associated with each individual lamp is an input parameter of the simulation. The temperature of the filament is derived from this value using the relations presented in section 3.3.2.2. The emissivity of tungsten ϵ_W is assumed to be temperature dependent as presented in Fig. 3.3. The radiosity in a point $\boldsymbol{x}$ of the surface is then defined as per equation 4.4.1.

$$J_{\text{lamp}}(\boldsymbol{x}) = \epsilon_W(T_{\text{fil}})\sigma T_{\text{fil}}^4(P_{\%}) + (1 - \epsilon_W(T_{\text{fil}}))G(\boldsymbol{x}) \tag{4.4.1}$$

where G is the irradiance (incoming radiative flux), and σ the Stefan-Boltzmann constant.

Composite blank: The temperature of the composite blank is solved for from the 3D heat equation 4.4.2, with the material properties characterized in section 3.4. The terms of the diagonal conductivity tensor are considered temperature-dependent as per equations 3.4.15 and 3.4.16. As the material is opaque, no volumic source term exists, and the contributions of convection and radiation are considered as heat fluxes on the boundaries of the blank.

$$\rho C_p \frac{\partial T}{\partial t} = \nabla \cdot (\boldsymbol{\kappa} \nabla T) \tag{4.4.2}$$

Natural convection is considered on both sides of the blank. The convective heat flux can be expressed as $q_{\text{conv}} = h(T - T_{\text{amb}})$, where the convective transfer coefficient h is computed as per equation 4.4.3, using empirical correlations presented in [Incropera+2006] for horizontal hot surfaces facing up and down.

$$h = \begin{cases} \frac{\kappa_{\text{air}}}{L} 0.54 \text{Ra}^{1/4} & \text{(upside)} \\ \frac{\kappa_{\text{air}}}{L} 0.27 \text{Ra}^{1/4} & \text{(downside)} \end{cases} \tag{4.4.3}$$

where κ_{air} is the thermal conductivity of the ambient air, L a characteristic length defined as the area of the plate surface divided by its perimeter, and Ra is the Rayleigh number associated with the convective flow and calculated as per equation 4.4.4.

$$\text{Ra} = \frac{g\beta_{\text{air}}}{\nu_{\text{air}}\alpha_{\text{air}}}(T - T_{\text{amb}})L^3 \tag{4.4.4}$$

with g the acceleration due to gravity, β_{air} the thermal expansion coefficient, α_{air} the thermal diffusivity, ν_{air} the kinematic viscosity. T and T_{amb} are the surface temperature and fluid temperature far from the surface respectively. The air properties are evaluated at the

film temperature $(T + T_{\text{amb}})/2$, which is an approximation of the temperature inside the convection boundary layer [Incropera+2006].

The radiative heat flux on the boundaries is expressed as $q_{\text{rad}} = \epsilon(G - \sigma T^4)$, where G is the irradiance from mutually visible surfaces, and from the environment.

Oven panels: The oven panels participate to the heat transfer to the blank by reflecting part of the infrared radiation from the lamps. The reflectivity of the panels ρ_{pan} has been measured to 0.82 (integrated for a lamp at 2400 K). The value is relatively low for an aluminium reflector, and is explained by the quite rough finish of the panels and the potential effect of an oxide layer, as the surfaces are uncoated [Reynolds1961]. The radiosity on the surface of the panels is expressed as per equation 4.4.5.

$$J_{\text{pan}}(\boldsymbol{x}) = (1 - \rho_{\text{panel}})\sigma T_{\text{amb}}^4(P_{\%}) + \rho_{\text{pan}} G(\boldsymbol{x}) \tag{4.4.5}$$

4.4.3 Mesh discretization

A mesh sensitivity analysis has been conducted to find an optimum between the precision of the simulation (evaluated as the relative error on the simulated radiosity on the heated side of the blank) and the computation time of the steady-state solution (see Fig. 4.13).

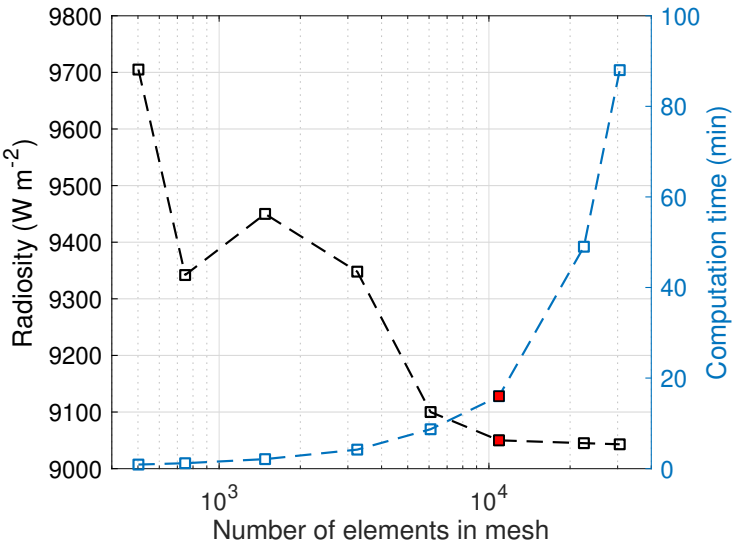

Figure 4.13 – Mesh sensitivity analysis

The blank is meshed using hexaedra elements of dimensions $10 \times 10 \times 0.25\,\text{mm}^3$ (2178 elements per ply). The oven panels are discretized using a structured mesh of quadrilateral elements ($20 \times 20\,\text{mm}$). The lamps are meshed using quad elements, with 8×16 elements per lamp. Linear shape functions are used on the quad elements to solve for the radiosity, while quadratic Lagrange shape functions are used in the blank. A cross-section view of the meshed model is presented in Fig. 4.14.

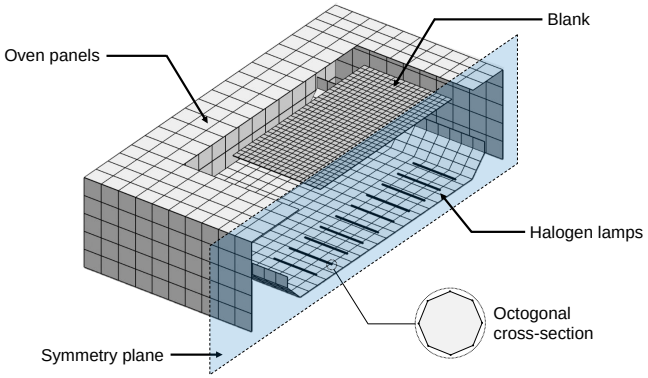

Figure 4.14 – Cross-section view of the oven mesh

4.4.4 Comparison with experimental test cases

The various test cases presented in Table 4.2 are replicated in the finite element model. The simulations are ran on a computer with a 2.8 GHz quad-core Intel Core i7 CPU. The transient evolution of the temperature of the blank is simulated for 120 s of heating.

Figure 4.15 presents the simulated field on the heated face of the blank, for lamps configurations LCa to LCd, a lamp-blank distance of 14 cm and all lamps at nominal power (tests 1 to 4). As for the experimental measurements, the heat flux density distribution is strongly affected by the position of the lamps. Configuration LCa presents a heterogeneous distribution of the radiosity, with most of the energy being deposited on the center of the blank (with a radiosity $J > 9000\,\mathrm{W\,m^{-2}}$), and isocontour lines forming ellipses oriented by the lamp array directions. The received heat flux is minimal at the edges of the blank such that $y = \pm 165\,\mathrm{mm}$ ($J < 3000\,\mathrm{W\,m^{-2}}$).

Configuration LCb, with all lamps offset by $\pm 120\,\mathrm{mm}$ from the center, shows a heat flux distribution with two maxima situated at the normal of the center of the array formed by the lamps offset by $120\,\mathrm{mm}/-120\,\mathrm{mm}$ respectively. The radiosity in this configuration is comprised between 3500 and $5800\,\mathrm{W\,m^{-2}}$, i.e. the heat flux is higher at the corners of the blank but lower at the maxima when compared to LCa. The minima are located at the corners such that $(x, y) > 0$ and $(x, y) < 0$.

Configuration LCc presents intermediate results both in terms of spatial distribution of the heat flux (with isocontour lines describing skewed ellipses) and values of the extrema ($3200\,\mathrm{W\,m^{-2}} < J < 8100\,\mathrm{W\,m^{-2}}$). The isocontour lines of configuration LCd are shaped as parallelogram with rounded corners, with heat flux minimum at the corners of the blank. The radiosity is comprised between $3100\,\mathrm{W\,m^{-2}}$ and $6700\,\mathrm{W\,m^{-2}}$.

In the absence of experimental data of irradiance in the oven, the simulation is validated by comparison with the temperature field measured on the back face of the blank. Temperature

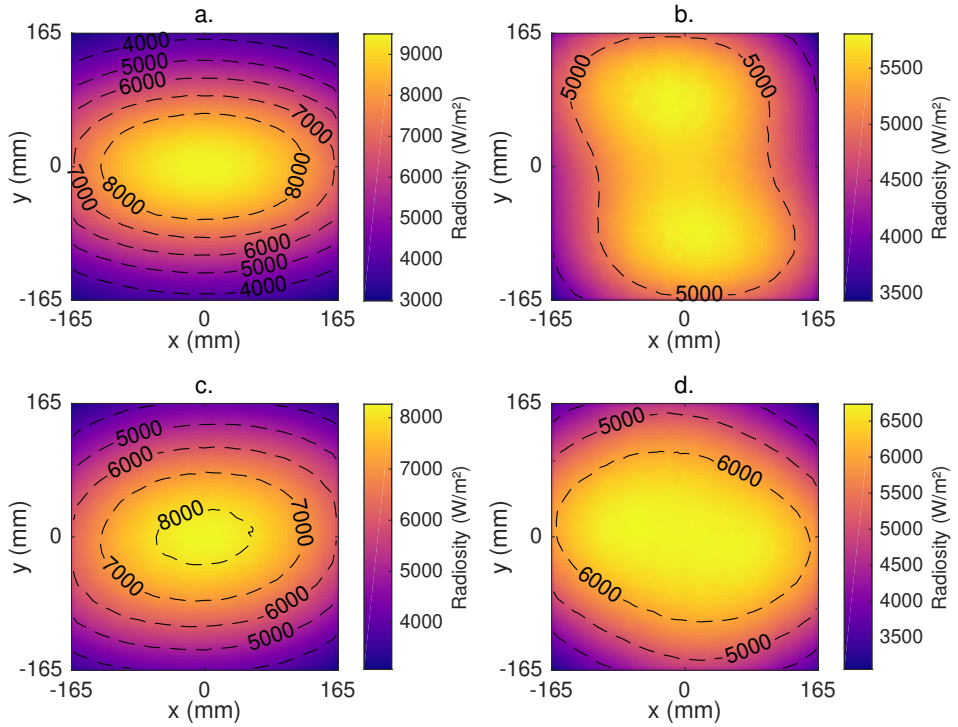

Figure 4.15 – Simulated radiosity on the heated face of the blank. The dashed lines represent the isocontours between 4000 W m^{-2} and 8000 W m^{-2}.

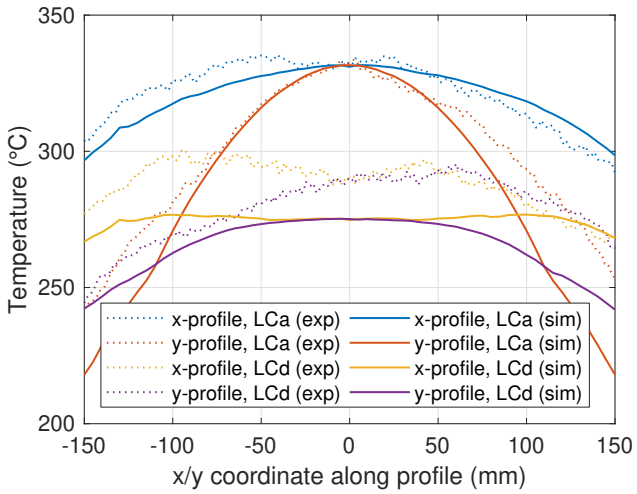

Figure 4.16 – Comparison between simulated and experimental temperature on x- and y-profiles on the back face of the blank (tests 1 and 4).

profiles along axes x and y (passing through the center of the back face) are plotted in Fig. 4.16 for test cases 1 and 4 (lamp configurations LCa and LCd).

The simulation shows a good quantitative agreement for temperature profile along x for configuration LCa, while the error on the profile along y increases from the center to the blank edges. On configuration LCd, only a qualitative agreement is obtained, with an absolute error of 10 °C in the center of the back surface. The simulated profile along x shows the same double peak feature as the experimental one, which is attributed to the variation in the lamp offset along this axis.

The relative temperature difference between the simulated and experimental temperature on the backface of the blank in the region of interest (eq. 4.4.6) is plotted in Fig. 4.17 for all test cases.

$$\Delta_{\mathrm{rel}}(x,y) = \frac{T_{\mathrm{sim}}(x,y) - T_{\mathrm{exp}}(x,y)}{|T_{\mathrm{exp}}(x,y)|} \tag{4.4.6}$$

Patterns that depend on the lamp configuration can be identified. Simulations corresponding to test cases with configuration LCa (subplots a., e., i. and k.–n. in Fig. 4.17) consistently predict lower temperatures in the zones of the ROI close to the edges at $y = \pm 165\,\mathrm{mm}$, by up to 10% ($\Delta T \approx 20\,°\mathrm{C}$), while a better agreement is observed closer to the center of the sample (i.e., the temperature in the hotter zones is correctly approximated). The simulated temperature of the centerpoint is within ±2% of the measured temperature.

The pattern of the error map on tests conducted with configuration LCb (subplots b., f., j.) presents the inverse behaviour, where the relative error in a zone close to the edges at $y = \pm 165\,\mathrm{mm}$ is smaller compared to that at the center of the back surface. In both configurations, the simulation shows a better prediction at the normal of the lamps.

Simulations with configuration LCc (c. and g.) present, similarly to configuration LCa, a good agreement with the experimental tests in the region closer to the center of the blank and an increased error closer to the edges at $y = \pm 165\,\mathrm{mm}$. The offset in this configuration is such that the lamps overlap, unlike in LCb, hence why the behaviour is similar to that of simulations with configuration LCa. Simulations with configuration LCd (d. and h.) show an increased error at the center of the blank.

A box plot of the relative temperature distribution for the various validation test cases is presented in Fig. 4.18, with dash-dotted lines showing the average experimental dispersion. The temperature prediction on the surface is within $-13\% \leq \Delta_{\mathrm{rel}} \leq 6\%$ of the measured temperature for tests 1–13, while the error on test 14 (stack of 4 unconsolidated plies) is between −3% and 8%. The temperature prediction is within ±5% of the experimental temperature for more than 75% of the surface of the ROI on tests 1–4, 7, 9–10 and 12–13, with a trend towards the underprediction of temperature. Coupled with the spatial distribution of Fig. 4.17, this box plot shows that the simulation tends to overestimate the temperature gradients in the blank.

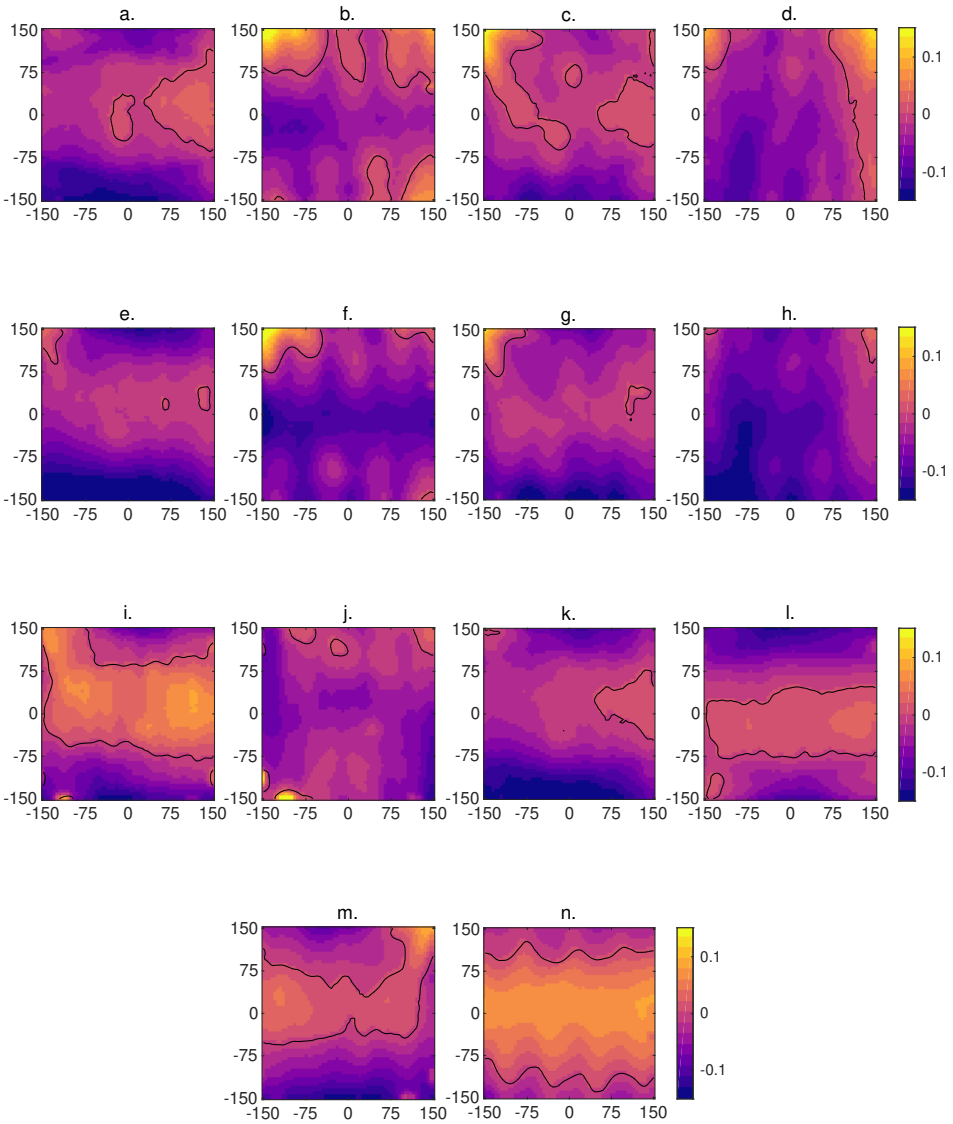

Figure 4.17 – Map of the relative temperature difference between experimental tests and simulation. Isocontours at $\Delta_{\text{rel}}(x, y) = 0$. Left-to-right, top-to-bottom: tests 1 to 14.

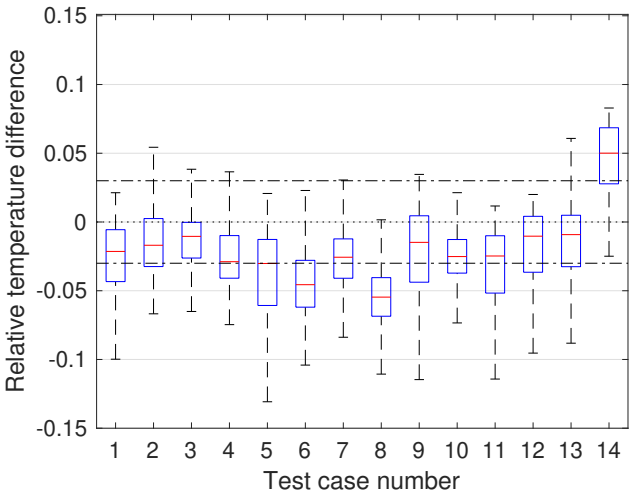

Figure 4.18 – Box plot of the relative temperature difference distribution between experimental tests and simulation

Test case 14 (Fig. 4.17n.) is the only one for which the temperature is overestimated in most ($> 75\%$) of the ROI area. This outlier can be explained by a higher experimental dispersion for this specific test case, as well as the uncertainty on the measurement of the thermal contact conductance (presented in section 3.4.5) used in the simulation.

4.4.5 Partial conclusion: model performances and limitations

The model proposed, based on the material characterization presented in chapter 3 and solving the radiative heat transfer in the oven enclosure using the radiosity method, shows correct quantitative results overall, as compared with experimental tests for various lamp configurations and different blanks lay-ups. The quality of the temperature prediction appears worse for lower lamp temperatures, and in stacks of unconsolidated plies. The relative error also increases further from the lamps.

Different factors can explain the residual error between the model and the experimental measurements. The blank geometry has been assumed fixed in the simulation, while deformation due to sagging is observed in the experiments; the influence of sag on the homogeneity of the resulting temperature field is discussed in section 4.5.

The radiosity method used in Comsol is based on the hypothesis that the surfaces in the enclosure can be considered grey, isothermal, Lambertian and opaque. The transmittance of the materials considered has been verified experimentally to be negligible, and the discretization of the surfaces in elements ensures the validity of the isothermal hypothesis.

Spectral reflectivity results presented in section 3.4.2.3 show that while it is reasonable to consider the consolidated material as a grey body, the reflectivity of the semipreg fabric

varies between 0.08 and 0.2 for wavelengths between 0.8–6 µm, which corresponds to the range of emission of a lamp at 2400 K.

The directionality of the material reflectivity could explain the increase of the error in zones further from the normal of the lamps, with studies on fibre-reinforced composites presenting an increase of the reflectivity for grazing incident angle [Grouve2012; Le Louët+2017]. Assuming the behaviour of the reflecting panels as purely Lambertian is also a strong hypothesis, as rough metallic surfaces usually exhibit a mixed diffuse/specular behaviour [Mainguy+1991]. The characterization of the bidirectional reflectance distribution function (BRDF) requires however a complex experimental setup [Ibos+2016], while its implementation in a finite element code requires the use of computationally expensive ray-tracing techniques [Peeters+2016]. The most recent release of Comsol Multiphysics (v5.4) [COMSOL2018] allows considering wavelength-dependent optical properties (by defining an arbitrary number of spectral bands in which the properties are assumed constant), and computation of radiosity through ray-tracing. The potential interest of using these features could not be tested during this study.

4.5 Influence of blank sag

As mentioned in section 4.3.1.2, the influence of blank sag is rarely discussed in the literature concerned with forming of composite materials. More studies are investigating the sagging of unreinforced polymer sheets during thermoforming, as the deflections reached are more important due to the polymer flowing under its own weight [Baek+2013; Giacomin+2010].

The influence of sag on the heat flux distribution on the surface of a polymer sheet heated by radiation has been studied analytically by Vodak et al. and Michaud et al. [Michaud+2011; Vodak+2011], modelling the polymer as a Newtonian fluid. Results show an increase of the heterogeneity of the heat flux with the deformation of the initially flat sheet. The assumption used in these articles of a 2D problem (semi-infinite sheet in a semi-infinite oven) is not valid considering the dimensions of the blank used in this study.

Consequently, a parametric study is proposed in this work to evaluate the influence of the blank sag on the resulting temperature field, with the 3D oven model presented in section 4.4.1. Extending the approach of Vodak and Michaud where the sheet is deforming cylindrically, the geometry of the sagging blank is idealized as the intersection of a hollow sphere with the same thickness as the undeformed blank, and a semi-infinite square box with side dimensions of 330 mm × 330 mm (the projected area is conserved). The geometry can be described by the curvature ζ of the sphere ($\zeta = 1/R$).

The z-coordinate of the grips (visible in Fig. 4.8) is assumed fixed (i.e, the deflection is zero at the grips). The deflection of the center of the blank can be derived from the curvature and blank parameters (blank width w_{blank} and distance between the corners and the grips $d_{\text{corner}\leftrightarrow\text{grip}}$) as per equation 4.5.1.

$$\delta_{\text{c}} = \frac{1}{\zeta} - \sqrt{\frac{1}{\zeta^2} - \left(\frac{w_{\text{blank}}^2}{4} + \left(\frac{w_{\text{blank}}}{2} - d_{\text{corner}\leftrightarrow\text{grip}} \right)^2 \right)} \tag{4.5.1}$$

In the absence of experimental measurements of the deflection of the blank, an upper bound of the curvature of $2\,\mathrm{m}^{-1}$ is used, considering the fact that the blank did not snag on the shielding panel during transfer. The mesh of the undeformed ($\zeta = 0\,\mathrm{m}^{-1}$) and deformed ($\zeta = 2\,\mathrm{m}^{-1}$) blanks is presented in Fig. 4.19, with the position of the grips highlighted in red.

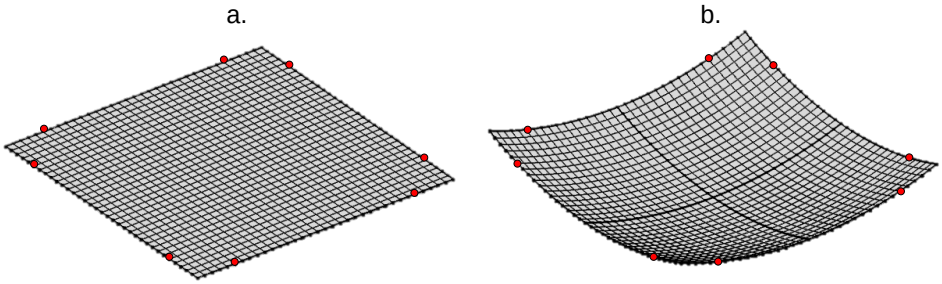

Figure 4.19 – Comparison between undeformed (a., $\zeta = 0\,\mathrm{m}^{-1}$) and deformed mesh (b., $\zeta = 2\,\mathrm{m}^{-1}$).

Steady-state simulations have been conducted by replicating test cases 1 and 2 (configurations LCa and LCb), for values of ζ varying between $0\,\mathrm{m}^{-1}$ and $2\,\mathrm{m}^{-1}$ (with a step of $0.4\,\mathrm{m}^{-1}$). The temperature field on the back face of the blank is presented in Fig. 4.20 for the highest curvature simulated, along with the spatial distribution of the relative temperature difference:

$$\Delta_{\mathrm{rel}}(x,y) = \frac{T_{\zeta=2}(x,y) - T_{\zeta=0}(x,y)}{T_{\zeta=0}(x,y)} \tag{4.5.2}$$

The position of the hot and cold spots on the blank is not significantly affected by the curvature of the blank in the range considered. This was expected for configuration LCa, as the temperature maximum is reached at the center of the back surface which is the point of maximum deflection. A larger curvature of the blank could lead to occlusion zones in the blank not in line-of-sight of the radiative sources.

The relative temperature difference map shows that sagging leads to both a temperature increase at the location of the hot spots of the blank, as well as a temperature decrease in the corners. The maximum temperature is increased by 16.8% (from 334 °C to 390 °C) and 10.3% (from 262 °C to 289 °C) for configurations LCa and LCb respectively, while the minimum temperature is decreased by 26.3% and 21.5% respectively. The influence of curvature appears to be mitigated by the position of the lamps, with configurations with a larger offset between the center of the blank and the lamps resulting in lower temperature differences.

In both cases, sagging of the blank increases the heterogeneity of the temperature field at the surface. This is clearly shown in Fig. 4.21a, which presents the empirical temperature distribution function on the back surface of the blank for the different values of curvature simulated. The increasing deflection leads to a marked decrease of the slope. Figure 4.21b shows the relative difference in temperature in spots TC1 and TC2 of the heated face of the blank, as a function of curvature. The temperature in TC2 shows minimal variations as the curvature increases, regardless of the lamp configuration. This highlights the limitations of relying solely on spot measurement for process monitoring of infrared heating.

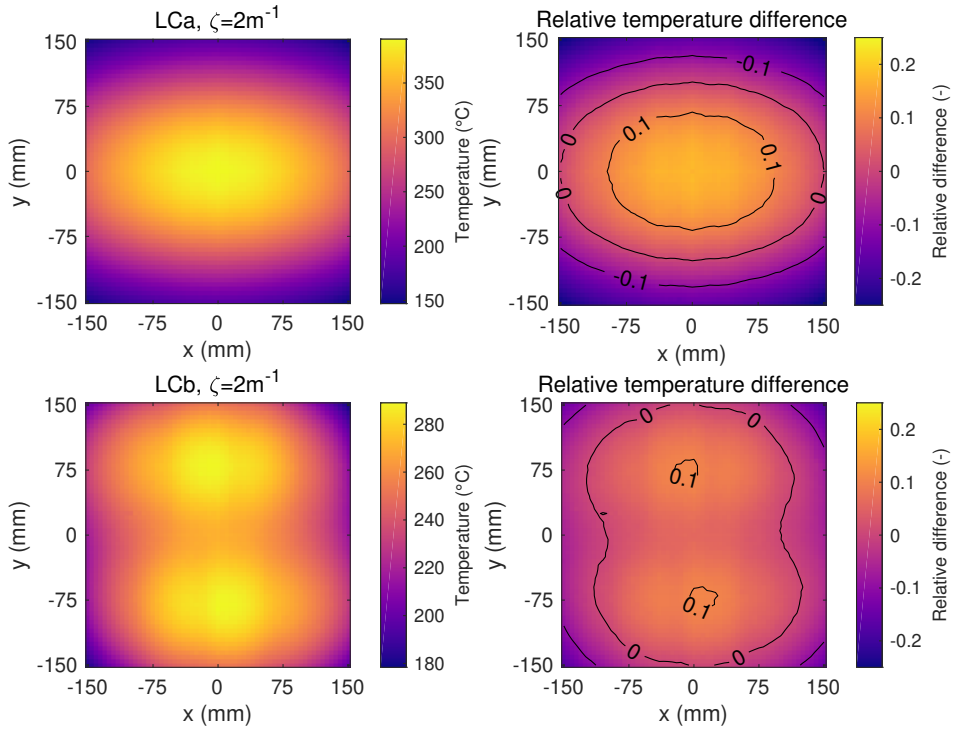

Figure 4.20 – Simulated temperature field for $\zeta = 2\,\mathrm{m}^{-1}$ (deformed mesh, configurations LCa and LCb), and map of relative temperature difference between simulations with deformed and undeformed mesh (isocontours at $\Delta_{\mathrm{rel}} = 0$ and $\Delta_{\mathrm{rel}} = \pm 10\%$).

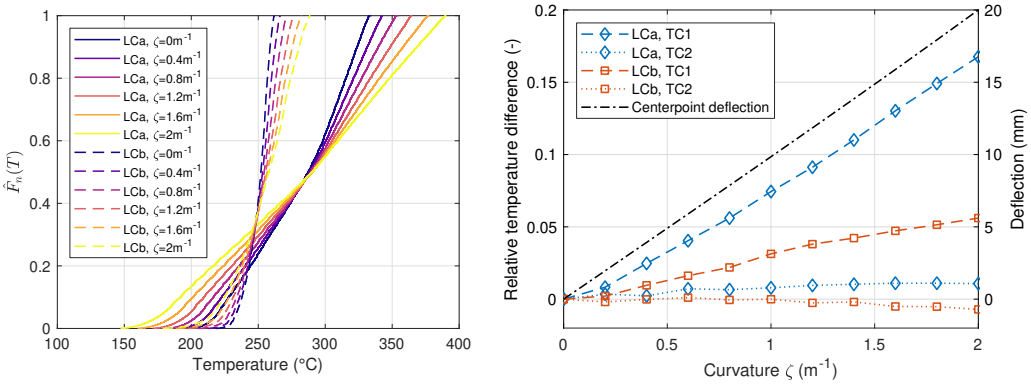

(a) **(b)**

Figure 4.21 – Influence of sagging on a. temperature distribution and b. temperature at spots TC1 and TC2

The analysis is conducted assuming no variation of the blank curvature during the heating phase, while experimentally the blank remains taut below the melting point of the matrix. The simple modelling approach proposed here thus overestimates the influence of sag on the temperature field; the results presented for the steady-state still indicate that this phenomenon should not be neglected. To simulate the transient temperature evolution in the blank, coupling with the thermomechanical bending and tensile behaviour of the fabric would have to be considered; updating the view factors during the time integration scheme would also be required to take into account the evolution of the blank geometry due to sagging.

In the case presented here, taking into account sag (for arbitrary defined levels of curvature) further increases the error between the experimental temperature measured in section 4.3.2.1 and the simulation for configuration LCa, while only a minor improvement of the agreement is observed for configurations LCb to LCd. The temperature field resulting from tests with configuration LCa is highly heterogeneous, which could lead to the blank deforming in a more complex way than is modelled. As no experimental data was available to fit the curvature parameter, the blank was assumed to be taut in all subsequent simulations.

4.6 Optimization of the temperature field

The previous sections have introduced how the model developed performs in simulating the temperature field on the blank from the knowledge of the oven parameters and blank layup. This section investigates the inverse problem by coupling the model with an optimization algorithm to determine the oven parameters required to achieve a desired temperature distribution in the blank (homogeneous or tailored [Hwang+2002]), based on the required processing range of the material considered. The approach is similar to that presented in section 3.3.2.2 for the determination of the filament temperature, although the number of parameters considered is greatly increased; the optimization strategy must be adapted accordingly to ensure a reasonable computational time.

4.6.1 Optimization problem

The optimization variables considered in this section are the temperature of the lamps (characterized by the percentage of nominal power P_i), and the offset associated with each lamp pair $x_{\text{offset,i}}$. The optimization problem can be posed as per equation 4.6.1.

$$\begin{aligned} &\underset{P_i,\ x_{\text{offset,i}}}{\text{minimize}} && T(\mathbf{x}, P_i, x_{\text{offset,i}}) - T_{\text{prescribed}}(\mathbf{x}),\ \mathbf{x} \subset \text{blank} \\ &\text{subject to} && f(P_i,\ x_{\text{offset,i}}) \leq 0. \end{aligned} \tag{4.6.1}$$

The sensitivity of the temperature to the variables P_i (equation 4.6.2) is computed for 17 points distributed in the midplane of the blank, for the two lamp configurations LCa and

LCb. The results are presented in Fig. 4.22 (interpolated on the Delaunay triangulation of the set of points).

$$\left|\frac{\partial T}{\partial P_i}\right|_{\mathbf{x}}, \quad i = 1 \dots 5 \tag{4.6.2}$$

While the individual lamp pairs have different regions of influence (with lighter colored zones associated with a stronger dependence to the relevant temperature of the lamp pair), a strong overlap between these regions can be observed as all lamps are directly visible from any point on the bottom surface of the blank. The lamp configuration also has a large impact. This suggests a high degree of coupling between the optimization variables.

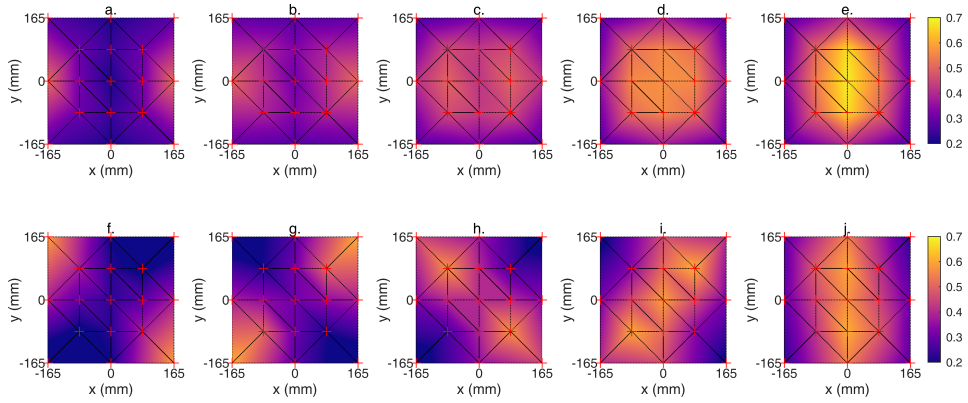

Figure 4.22 – Sensitivity of the temperature field to the lamp power. Left-to-right: lamp pairs P1 to P5, top: LCa, bottom: LCb

4.6.2 Algorithms and temperature optimization

The optimization strategy depends strongly on the complexity of the problem to be solved. The case in which the geometry of the oven is fixed, and the optimization variables are reduced to the lamps power parameters P_i, is considered first. This is for instance the approach used in [Nakouzi+2012], where the temperature distribution in a thermoset composite is optimized with the SNOPT algorithm (Sparse Nonlinear OPTimizer).

The test case considered consists in determining the lamp parameters required to heat a blank of 1 ply of preconsolidated PA66/glass, to a temperature $T_{\text{prescribed}} = 295\,°\text{C}$ in the plane $x = 0$ (passing through the center of the blank, and normal to the direction of the lamps). The constraints are $20 \leq P_i \leq 100$. The objective function is set as a least-square minimization of the steady-state temperature field, and solved using the GCMMA algorithm [Svanberg2002] in Comsol. Configurations LCa, LCb and LCc are considered. The optimized parameters are obtained after 5 iterations (CPU time 750 s), and are presented in Table 4.3.

Temperature profiles at the midplane of the blank along axis x are presented in Fig. 4.23 before and after the optimization (dashed and solid lines). The temperature gradient along x is reduced, and both configurations LCa and LCc present similar temperature profiles

Table 4.3 – Optimized lamp parameters

Configuration	P1	P2	P3	P4	P5
Initial	50	50	50	50	50
LCa	100	100	70.4	53.9	28.2
LCb	100	100	100	100	94.2
LCc	100	100	92.1	73.56	23.5

with an average at 295 °C. The optimization of configuration LCb was not successful, as the offset between the lamps is such that the temperature within the blank cannot reached the prescribed value.

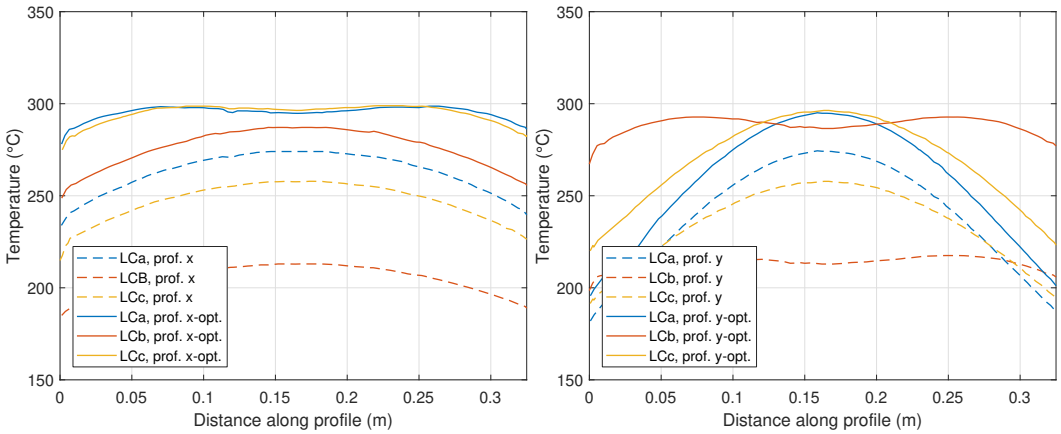

(a) **(b)**

Figure 4.23 – Lamp power optimization for configurations LCa, LCb and LCc. Dashed lines: initial midplane temperature profile along x ($P_i = 50\%$), solid lines: temperature profile along x, optimized parameters, dash-dotted lines: temperature profile along y, optimized parameters.

A second type of optimization problem is one in which the oven geometry is not fixed, i.e. where the offset of the lamps is considered as a parameter. The introduction of a geometric parameter can lead to discontinuities in the objective function, and derivative-free algorithms have to be used in lieu of gradient-based methods. The second test case considered consists in determining both the lamp power and offset required to heat a 1-ply blank to 295 °C. Given the number of parameters considered, evolution-based algorithms (particle swarm, genetic algorithms, ...) would require too high a number of objective function evaluation per generation, and a coupled approach is used: the Monte-Carlo method is first applied to sample the response space, and the Nelder-Mead simplex method is used to refine the solution around the best guesses of the random sampling.

While the lamp offset is constrained in the actual oven to a set of discrete positions (0, 6 or 12 cm), the variable is considered continuous in the Monte-Carlo step as to avoid under-sampling. The position is adjusted to the closest admissible value before the refinement step.

The optimized parameters are presented in Table 4.4 (CPU time: 9 h, with 500 evaluations of the objective function and 10 best guesses refined).

Table 4.4 – Optimized lamp power and configuration

Lamp % of nom. power					**Lamp offset (cm)**				
P1	P2	P3	P4	P5	$x_{\text{off},1}$	$x_{\text{off},2}$	$x_{\text{off},3}$	$x_{\text{off},4}$	$x_{\text{off},5}$
55.8	84.5	89.8	82.4	72.17	6	12	6	0	12

Figure 4.24 presents the interactions between the lamp power parameters P_1 to P_5 as the approximated response surface from the Monte-Carlo sampling, with the optimized minimum shown in cyan. The plots correspond to the Voronoi tessellation associated with the projection of the sampling points of the Monte-Carlo analysis in the P_i/P_j plane (which is why local discontinuities can be observed, as points whose projections appear close in the plane can be far apart in the research space). Darker regions represent lower values of the objective function. Relatively high lamp temperatures are required to reach the desired blank temperature, as can be seen from the location of the darker region in the upper right quadrant of the subplots. A compensation between the lamps can also be admissible, with a lamp at a high temperature compensating for a lamp at a lower temperature, with darker bands visible along the top and right edges of the subplots. The position of the minimum close to the boundaries of the design space suggests that the oven might be underpowered for the objective considered.

The temperature field on the backface of the blank obtained from the optimization is presented in Fig. 4.25, along with a comparison of the empirical distribution functions associated with the different lamp configurations studied. The optimized configuration leads to reduced gradients compared to LCc and LCa, and higher peak temperatures compared to LCb and LCd. This configuration, along with configuration LCa, will be used in Chapter 6 to investigated the influence of the homogeneity of the temperature field in the blank on forming defects.

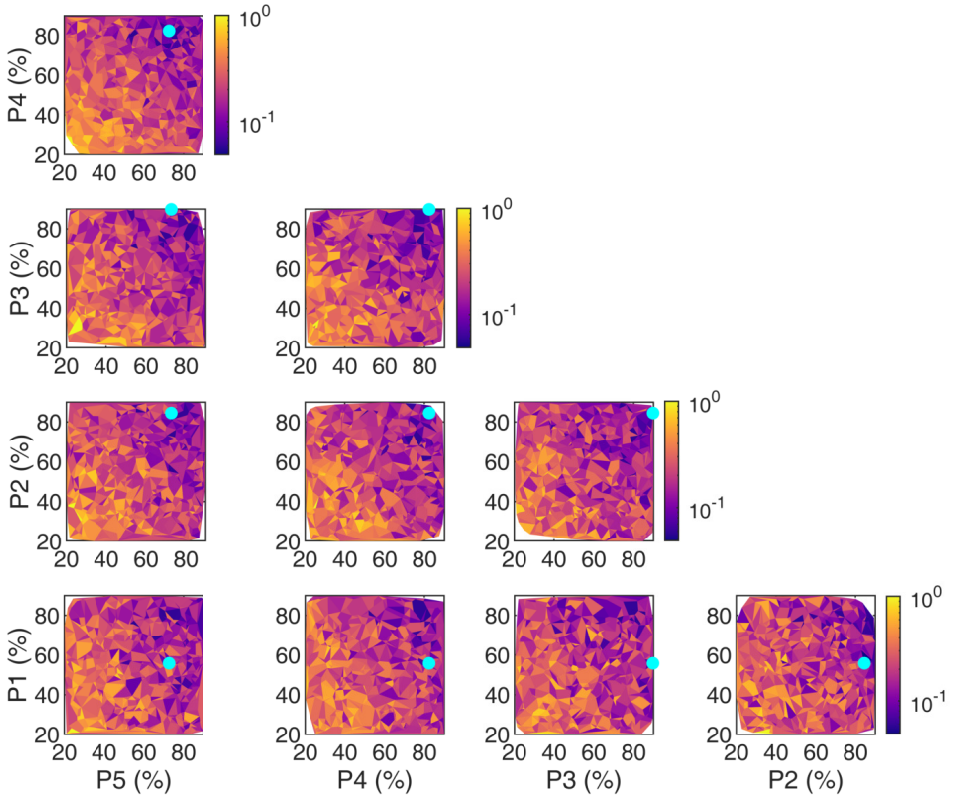

Figure 4.24 – Two-way interactions between the lamp power parameters P1 to P5, minimum of the Monte-Carlo optimization represented with ○

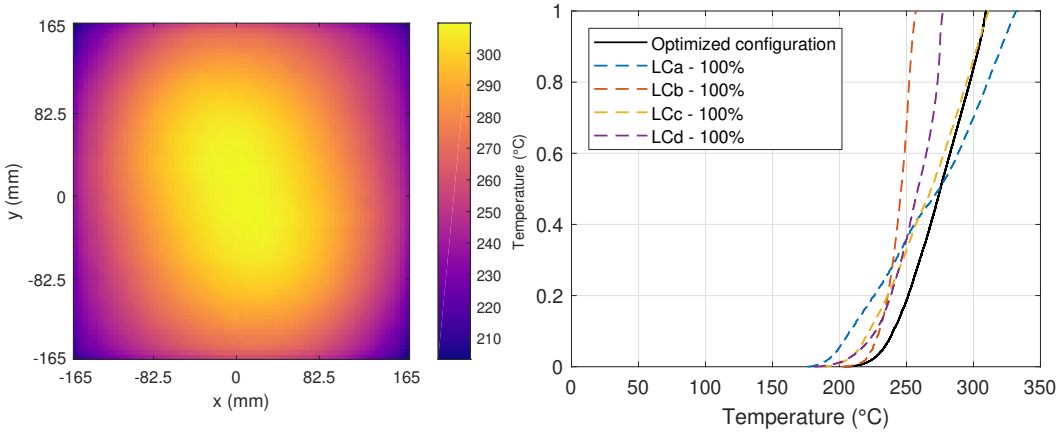

(a) **(b)**

Figure 4.25 – a. Temperature field on the backface of the blank, b. comparison of the empirical distribution function

4.7 Conclusion

An instrumented infrared oven with control over the lamp configurations and power has been developed, and is able to generate a variety of temperature fields on a blank of controlled dimensions. The model introduced in chapter 3, based on the homogenization of thermal properties and the radiosity method to solve the radiative heat transfer, has been validated against experimental test cases conducted using the setup described.

The representation of the spatial distribution of the relative error shows an overall good quantitative agreement with the experiments, with an increase of the error in points further from the lamps. The numerical simulation is shown to overestimate the temperature gradients on the surface of the blank, while underestimating the average temperature. The relative error for the test cases considered is within the range $-13\% \leq \Delta_{\text{rel}} \leq 8\%$.

Sagging of the blanks was visually observed during the heating phase, as the temperature reached the melting point of the PA66 matrix. A simple numerical approach was used to investigate the effect of sag on the temperature homogeneity of a composite blank. Results show that while the sag does not affect the spatial distribution of hot and cold spots within the blank (in the range of curvatures considered), it has a large impact on the temperature, with variations of up to 20%. The effect was however neglected in subsequent simulations, due to the lack of experimental characterization.

Finally, an optimization strategy depending on the complexity of the design space was proposed; the optimization of the blank temperature was conducted using a Monte-Carlo approach followed by a refinement of the solution using the simplex method. The resulting parameters will be used in chapter 6 to investigate the influence of the temperature distribution of the blank on process-induced shape defects, both experimentally and numerically, using a temperature dependent mechanical model derived in chapter 5.

Chapter

5

Characterization and modelling of the mechanical properties of woven thermoplastic composites at high temperatures

5.1 Introduction

This chapter presents the approach used to describe the mechanical behaviour of the woven materials considered. As the aim of the study is to investigate and propose simulation tools to reproduce the influence of the preheating step on the deformation of the laminate during forming, the mechanical model must be able to reproduce the change in orientations of the yarns (quantified by the shear angle) that allows the material to conform to the shape of the tools but can also lead to wrinkles, as discussed in Chapter 2.

The theory of the non-orthogonal model is presented in section 5.2. As described in Chapter 4, the infrared preheating step can result in a non-homogeneous temperature field in the laminate, and the forming step is not an isothermal process; thermodependant mechanical properties must be characterized: the experimental identification of the model parameters (tensile and shear modulus as a function of temperature) for the semipreg and consolidated fabric is presented in sections 5.3 and 5.4.

5.2 Non-orthogonal constitutive model

5.2.1 Continuum approach

From the literature review presented in section 2.3, modelling the behaviour of the woven materials at the macroscale using finite element analysis has been deemed to be the most efficient approach in view of the goals of the project. Micro- and mesoscale models allow a finer description of the kinematics of the yarns, but they require a complex characterization of the fibrous network structure and a vastly increased computational cost.

While a continuum approach cannot represent defects resulting from loss of cohesion or yarn pull-out, first-order shape defects (wrinkles) can accurately be modelled from the evolution of shear angle in the plies. Each ply is treated as a continuous medium with homogenized material properties, using the constitutive relations defined in the following section. Modelling the ply as a continuum also allows for an easier mapping of the temperature field resulting from the infrared heating simulation.

5.2.2 Non-orthogonal model

The model used in this study to describe the behaviour of the woven thermoplastic composites considered is based on work by Peng and Cao [Peng+2005] and Khan et al. [Khan+2010]. This model has been used successfully to model the draping behaviour of dry woven fabrics [Peng+2011; Pierce+2014] and more recently the thermoforming of thermoplastic composites [Machado+2016a]. The model is based on a hypoelastic (rate-dependent) formulation:

$$\boldsymbol{\sigma}^{\nabla} = \mathbf{C} : \mathbf{D} \tag{5.2.1}$$

where $\boldsymbol{\sigma}$ and $\mathbf{D}$ are the Cauchy stress tensor and strain rate tensor respectively, and $\mathbf{C}$ is a constitutive tensor expressed in a frame fixed with the yarns. $^{\nabla}$ represents an objective derivation operator, independent of the reference frame. In the case of woven materials, the material frame does not remain orthogonal during deformation as the yarns are sheared. Most finite element codes and their implementation in commercial softwares, notably Abaqus/Explicit, use the Green-Naghdi (GN) frame, based on the rotation tensor $\mathbf{R}$ from the polar decomposition of the deformation gradient tensor $\mathbf{F}$:

$$\mathbf{R} = \mathbf{F}\mathbf{U}^{-1} \tag{5.2.2}$$

The Green-Naghdi axes in the current configuration g_α are updated from the rotation tensor $\mathbf{R}$ and the initial configuration as in equation 5.2.3.

$$g_\alpha = \mathbf{R} \cdot g_\alpha^0 \tag{5.2.3}$$

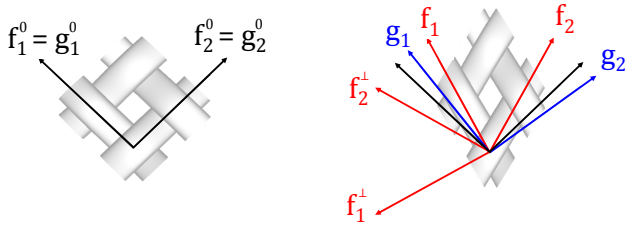

Figure 5.1 – Evolution of Green-Naghdi and material frames during shear

As this frame is based on the average material rotation and remains orthogonal during deformation, the axes do not remain coincident with the yarns directions (see Fig. 5.1). This leads to an impractical expression of the constitutive tensor $\mathbf{C}$ in this frame. The non-orthogonal approach consists in expressing equation 5.2.1 in a frame where the axes are updated from the deformation gradient tensor $\mathbf{F}$ as per equation 5.2.4. The undeformed configuration of the fibre frame is set to be coincident with the initial GN frame.

$$f_\alpha = \frac{\mathbf{F} \cdot f_\alpha^0}{\|\mathbf{F} \cdot f_\alpha^0\|} = \frac{\mathbf{F} \cdot g_\alpha^0}{\|\mathbf{F} \cdot g_\alpha^0\|} \tag{5.2.4}$$

The general expression of the constitutive law in fibre direction α neglecting the tension/shear couplings can be expressed as per equation 5.2.5, assuming plane stress conditions (bending neglected).

$$\begin{bmatrix} d\sigma_{11}^{f_\alpha} \\ d\sigma_{22}^{f_\alpha} \\ d\sigma_{12}^{f_\alpha} \end{bmatrix} = \begin{bmatrix} \delta_{\alpha 1} C_{11} & C_{12} & 0 \\ C_{12} & \delta_{\alpha 2} C_{22} & 0 \\ 0 & 0 & C_{33} \end{bmatrix}_f \begin{bmatrix} d\epsilon_{11}^{f_\alpha} \\ d\epsilon_{22}^{f_\alpha} \\ d\epsilon_{12}^{f_\alpha} \end{bmatrix} \tag{5.2.5}$$

Where $\delta_{\alpha i}$ is the Kronecker delta. If tension/tension couplings are neglected (as discussed in section 2.3.1.2), the expression can be further simplified to equation 5.2.6, where E_{11} and E_{22} are tensile moduli in the fibre directions and G_{12} is the shear modulus.

$$\begin{bmatrix} d\sigma_{11}^{f_\alpha} \\ d\sigma_{22}^{f_\alpha} \\ d\sigma_{12}^{f_\alpha} \end{bmatrix} = \begin{bmatrix} \delta_{\alpha 1} E_{11} & 0 & 0 \\ 0 & \delta_{\alpha 2} E_{22} & 0 \\ 0 & 0 & G_{12} \end{bmatrix}_f \begin{bmatrix} d\epsilon_{11}^{f_\alpha} \\ d\epsilon_{22}^{f_\alpha} \\ d\epsilon_{12}^{f_\alpha} \end{bmatrix} \tag{5.2.6}$$

The stress increments computed from equation 5.2.6 are accumulated in each fibre direction using a mid-point integration scheme to compute the stress state at time t^{n+1} knowing the stress state at time t^n:

$$[\boldsymbol{\sigma}^{n+1}]_{f_\alpha^{n+1}} = [\boldsymbol{\sigma}^n]_{f_\alpha^n} + [d\boldsymbol{\sigma}]_{f_\alpha^{n+1/2}} \tag{5.2.7}$$

The following sections (5.3 and 5.4) present the experimental characterization of the tensile and shear properties of the PA66/glass materials used in this study, while the numerical implementation of the model in finite element code Abaqus FEA is discussed in Chapter 6 along with validation on the experimental data presented here.

5.3 Tensile characterization

As discussed in section 2.3.1.2, the tensile behaviour of woven fabrics is biaxial: the behaviour in the warp direction is influenced by the load applied in the weft direction, and vice versa as the yarns are interlaced. No standard exists for the characterization of the biaxial tensile behaviour of woven composites, and testing requires the development of a complex rig to ensure an homogeneous stress field [Quaglini+2008]; as tension is not the main mode of deformation during thermoforming, and to facilitate the characterization, the tensile behaviour is assumed to be uniaxial in this study (this hypothesis is often made in forming simulations, by lack of experimental data [GuzmanMaldonado+2016; Khan+2010; Machado+2016a; Peng+2013]).

5.3.1 Experimental setup

The uniaxial tensile tests have been conducted according to the strip test standard ASTM D5035-11 [ASTM2015]. Samples with a gauge area of 25×50 mm were cut from the semipreg and preconsolidated material at 0° and 90° orientations to test the warp and weft directions. The tests were conducted using a Lloyd Instruments LS5 machine equipped with a 5 kN load cell, at a constant extension rate of $1\,\mathrm{mm\,min^{-1}}$ and at room temperature: the behaviour is assumed to depend mostly on the glass yarns and therefore considered independent of temperature (as shown experimentally in [Wang+2014]). As only the elastic behaviour is relevant to the thermoforming process, the tests were ran until reaching either a load of 5 kN, or failure of the sample, with five repeats per direction.

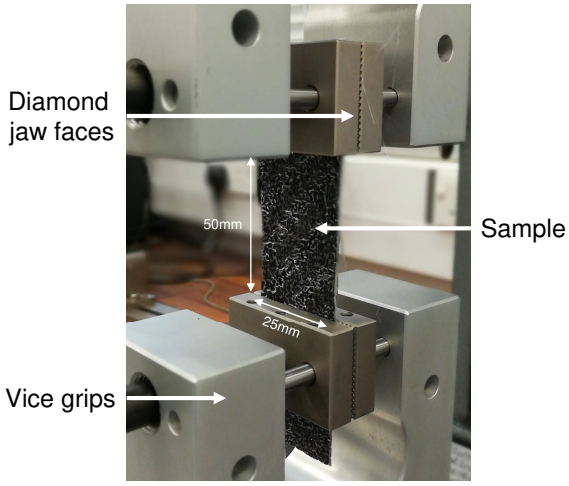

Figure 5.2 – Experimental tensile characterization setup

The experimental setup is presented in Fig. 5.2. Vice grips with diamond serrated jaw faces were used to clamp the strip samples. In addition to the PA66/glass samples, tests were conducted on the dry glass fabric. To avoid the issues associated with the fraying of the fabric (which is not stabilized by the polymer), wider strips were cut and ravelled (longitudinal yarns removed) to the gauge width as recommended by the standard (Fig. 5.3). This ravelling ensures that the gauge area is not affected by potential misalignment or sliding of the yarns induced by the cutting process.

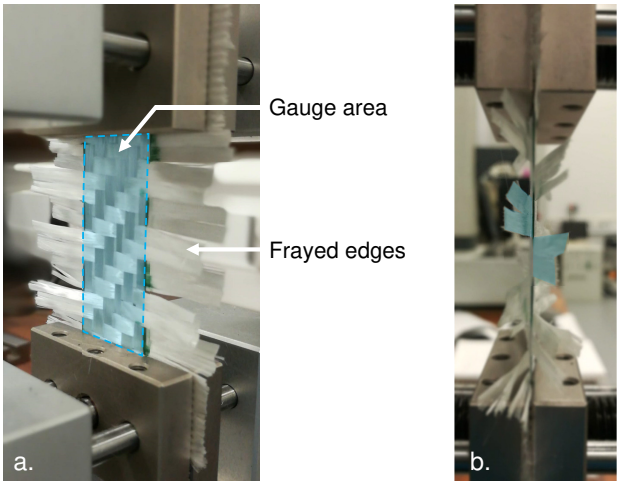

Figure 5.3 – a. dry glass fabric sample with ravelled edges and b. side view showing yarns crimping in transverse direction

5.3.2 Results

The tests on the thermoplastic composite samples (both semipreg and consolidated) showed no slippage in the clamps up to loads of 5 kN. The dry fabric samples slipped at much smaller

loads (between 50 N and 500 N), even with the addition of adhesive tape on the gripped region of the samples.

The experimental results, presented in terms of load per yarn versus nominal (Cauchy) strain are shown in Fig. 5.4 up to a strain of 0.04. Solid lines correspond to the average of the tests in the warp direction and dashed line to weft direction, with standard deviation represented with coloured patches. The results presented for the dry fabric are an average of the 4 tests presenting the highest peak load. The results on the semipreg and consolidated thermoplastic composite show a good repeatability of the tests with standard deviation <5% at a strain of 0.08.

The curves present two distinct regions: the behaviour is initially nonlinear at low strains, and linear at higher strain values. The first phase corresponds to the straightening of the yarns in the loading direction, which leads to an increased undulation of the yarns in the transverse direction (as shown in the side view of the ravelled glass fabric sample in Fig. 5.3). The second phase corresponds to the stretching of the yarns, with a higher apparent tensile modulus. No significant difference is observed between tests in the warp and weft directions; this result was expected as the fabric is balanced.

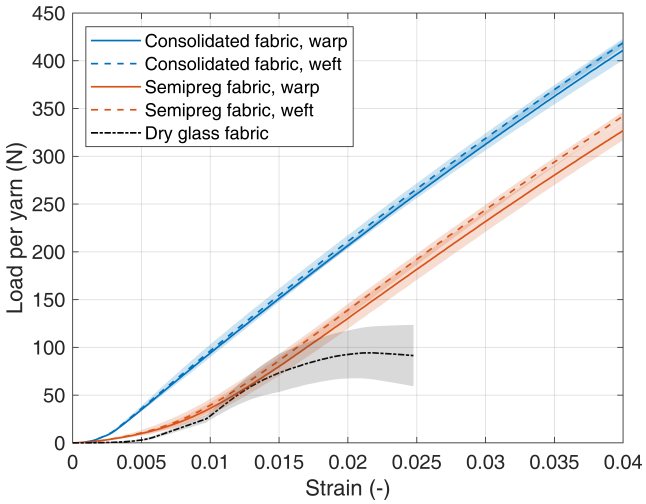

Figure 5.4 – Average load per yarn versus strain results for warp and weft directions.

The transition between the two phases happens at a lower strain for the consolidated material, compared to the semipreg. This indicates a reduced waviness in the consolidated material: a smaller extension is needed to straighten the yarns in the loading direction. The difference between the materials can be explained by the thermocompression process used to produce the consolidated samples: the compaction pressure leads to a reorganization of the fibre network, and notably a reduction of the crimp percentage of the yarns as the curvature is localized at yarn crossover points [Chen+2006b; Thompson+2018a]. In addition, the curves corresponding to the semipreg and the dry glass fabric present similar behaviour at small strains, which suggest that the powder-impregnation process does not significantly affect the mesostructure of the fabric.

Brittle failure was observed for all semipreg samples, at an average strain of 0.084 ± 0.003 and a load per yarn of 672 ± 25 N, while a single consolidated sample failed in the clamps below 5 kN. The loads associated with the forming process are unlikely to lead to tensile failure, and only the elastic behaviour is modelled in the following section.

5.3.3 Tensile model

As the mechanical model considered is developed at the macroscale, the load data obtained from the experimental tests are converted to stresses assuming the samples can be considered as homogeneous continuum. A constant rectangular cross section with thicknesses as defined in section 3.4 (1.04 mm and 0.51 mm for the semipreg and consolidated sample respectively) is used, and results obtained for the warp and weft directions are averaged (the stress-strain behaviour in the two in-plane orthotropy direction is assumed identical).

Several models have been proposed to describe the tensile modulus in forming simulations. Most authors assume the behaviour as linear, i.e. neglecting the decrimping/straightening phase at low strains [GuzmanMaldonado2016; Khan+2010; Wang+2014]. Non-linear descriptions are less common: Peng and Cao [Peng+2002] and Pierce [Pierce+2014] used polynomial functions of order 3 and 4 respectively, while a piecewise-defined function was proposed in [Peng+2005] with the tensile modulus described by a sigmoid at low strains.

The phenomenological approach proposed by Peng et al. is adapted in this study to ensure continuity of the tensile modulus. The stress/strain response of the material is described as the multiplication of a logistic function that represents the response at low strains and during the transition region and a linear function that represents the behaviour at higher strains, as per equation 5.3.1. This expression allows for a correct description of the non-linear tensile behaviour while keeping a low number of parameters.

$$\sigma_{ii} = \frac{1}{1 + e^{-k(\epsilon_{ii} - \epsilon_0)}} E_{\text{app.}} \epsilon_{ii} \tag{5.3.1}$$

The model parameters $E_{\text{app.}}$, ϵ_0 and k represent respectively the apparent tensile modulus of the material at high strains, the transition strain and a parameter describing the sharpness of the transition, the latter two being related to the crimp of the fabric. The parameters have been determined in MATLAB by curve fitting from the experimental data in a range of strain from 0 to 0.04 and are presented in Table 5.1.

Table 5.1 – Tensile model parameters

Parameter	**Consolidated material**	**Semipreg material**
k (-)	339.43	152.84
ϵ_0 (-)	3.15×10^{-3}	11.06×10^{-3}
$E_{\text{app.}}$ (GPa)	4.59	1.80

Comparison between the experimental and predicted stress as a function of strain is shown in Fig. 5.5a. The model shows an excellent agreement with the experimental data in the

quasi linear stress-strain region. Comparison of the tensile modulus obtained by numerical differentiation of the stress/strain curves is presented in Fig. 5.5b: the model predicts a stiffer response at low strains, however the deviation remains small. The lower apparent stiffness of the semipreg fabric compared to the consolidated material is due to the difference in the ply thickness measured and used subsequently in the model, the number of yarn per unit length remaining sensibly the same at both consolidation levels.

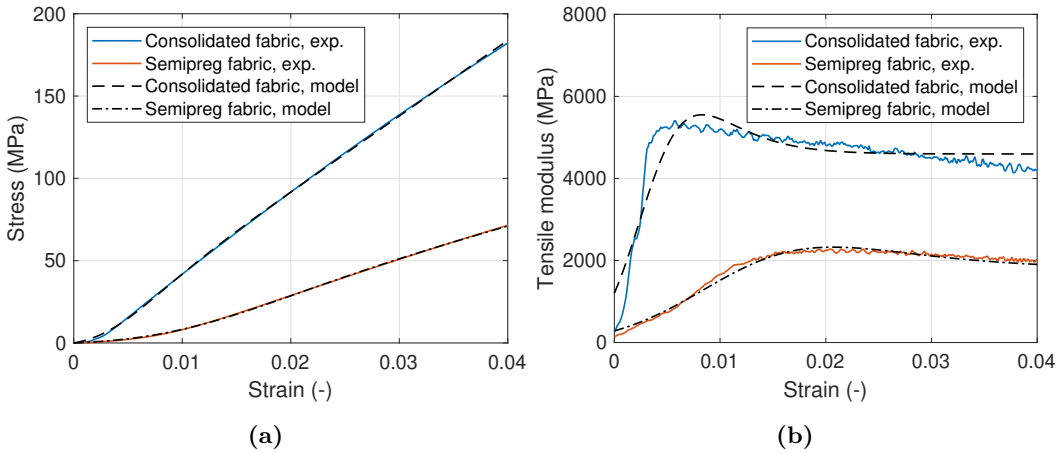

(a) **(b)**

Figure 5.5 – (a) Stress versus strain curves for experimental data (solid lines) and model (dashed lines), (b) tensile modulus versus strain

The absolute value of the relative error on stress is plotted in Fig. 5.6. The error is below 10% for strains over 0.007, and $< 2\%$ for strains between 0.01 and 0.045. The maximum relative error is observed at low strains; given the small stresses in this region, the impact on the quality of the simulation is considered negligible. In addition, the model is shown to perform correctly up to a strain of 0.08. The tensile strains obtained from the forming simulation will have to be compared to this value to ensure the validity of the model used.

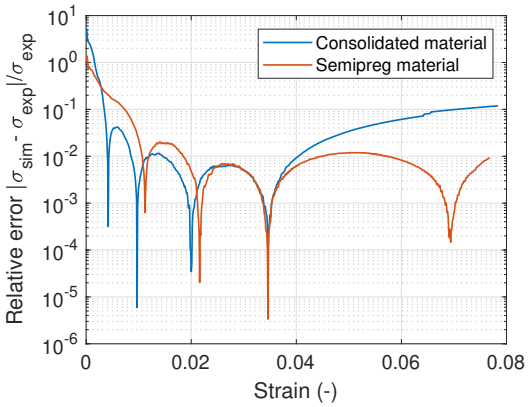

Figure 5.6 – Relative error versus strain

5.4 Shear characterization at high temperatures

This section[1] presents the experimental characterization of the shear behaviour of the woven thermoplastic composites considered. In-plane shear was shown in section 2.3.1.2 to be the main mode of deformation of the material during forming on non-developable surfaces. In contrast with the tensile behaviour of thermoplastic composites, the influence of temperature and strain rate is not negligible and needs to be characterized, especially for the semipreg material as no data is available in the literature.

Even though efforts have been made in that sense [Cao+2008], in-plane shear tests on woven fabrics are not standardized; based on the literature review conducted, bias-extension test was selected over picture frame as it is:

- less sensitive to misalignment of the sample
- less sensitive to temperature gradients induced by colder grips
- an easier design compared to the hinged mechanism used for picture frame
- narrower and easy to fit in an environmental chamber for high temperature testing.

The limitation of this test is the potential for intraply sliding at high shear, as the yarns are not clamped on both ends. The kinematics of the test are reproduced in Fig. 5.7, with the location of the different shear zones in the rectangular sample.

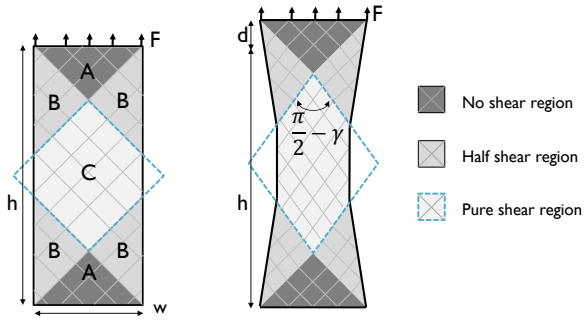

Figure 5.7 – Kinematics of the bias-extension test

5.4.1 Experimental procedure

5.4.1.1 Experimental set-up

Single ply samples of height $h = 250\,\text{mm}$ and width $w = 100\,\text{mm}$ were cut out of the semipreg and the preconsolidated plates. White lines were marked on the specimens with high-temperature paint to facilitate the post-processing of the shear angle evolution. To

[1] *Reproduced in part from:* T. Baumard, G. Menary, O. De Almeida, P. Martin, F. Schmidt, J. Bikard. Experimental characterization and modeling of the temperature and rate-dependent shear behaviour of powder-impregnated glass fibre/PA66 woven semipregs. *Composites Science and Technology* 180, pp. 23-32.

minimize the influence of moisture on the behaviour of the matrix, all specimens were dried at 80 °C for 12 hours as per the manufacturer recommendation prior to testing.

The bias-extension tests were conducted using a MTS 250 kN servo-hydraulic machine equipped with a 5 kN load cell and a MTS651 environmental chamber. The load cell was selected as the lowest capacity load cell suitable for high temperature testing; its accuracy at small loads was verified with weights between 5 N and 100 N. Results show the systematic error and random error below 5% and 10% at 5 N respectively, and below 2.5% and 5% for loads above 10 N (see Fig. 5.8).

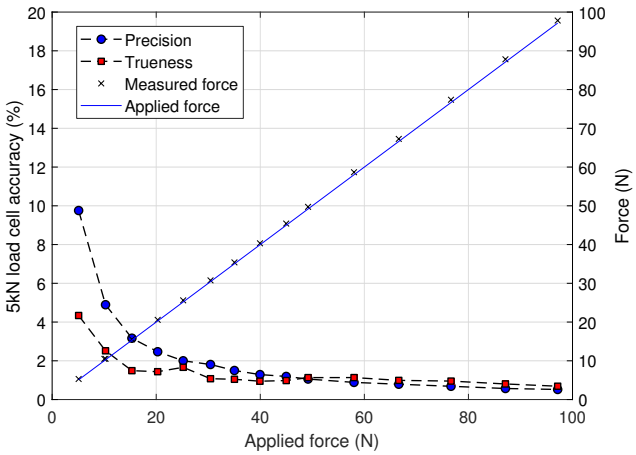

Figure 5.8 – Accuracy (precision and trueness) of the load cell.

Purpose-made grips described in Fig. 5.9 were used to prevent slippage of the samples. To ensure proper clamping of the sample above melting temperature, the grip force is introduced by a combination of set screws and compression springs. This allows a consistent gripping of the sample as the matrix melts.

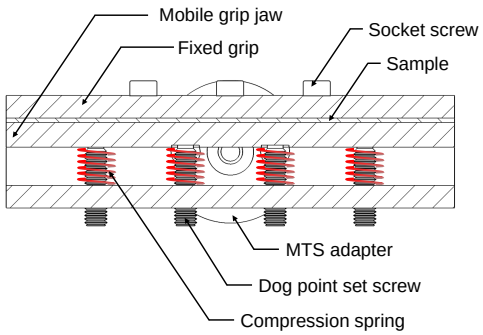

Figure 5.9 – Grips used for the bias extension tests.

To replicate the thermal history seen by the blank in the industrial thermoforming process, the samples were heated to 295 °C before being cooled down to the test temperature. The temperature homogenization steps were kept intentionally short (15 min) to limit the thermal oxidation of the PA66. Convection and grips-induced temperature gradients were evaluated

prior to testing with thermocouples distributed along the length of the sample (see Fig. 5.10). A thermal probe consisting of a type-K thermocouple held in between two plies of the material (as proposed in [Peng+2003]) was used to monitor the temperature during testing.

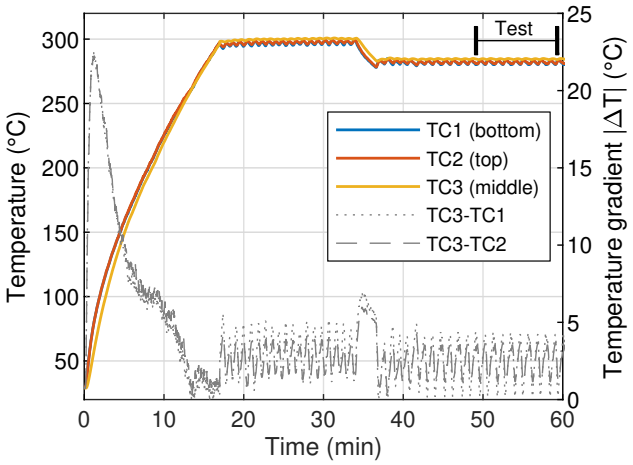

Figure 5.10 – Thermal cycle applied to the sample prior to testing. Thermocouples are located at the middle of the sample and half-height of the top and bottom non-sheared regions; dotted lines represent the absolute values of temperature gradients.

A full factorial experiment with two temperatures in the processing range (265 °C and 280 °C) and three different speeds (10, 100 and 1000 mm min^{-1}) was conducted for each material (semipreg and preconsolidated). A minimum of three samples were tested per test condition. Each test was filmed with an Allied Vision AVT Pike camera to track the evolution of shear angle during the deformation. For the sake of completeness, bias-extension tests were also conducted on the dry twill fabric at room temperature and 10 mm min^{-1}. The complete test setup is presented in Fig. 5.11.

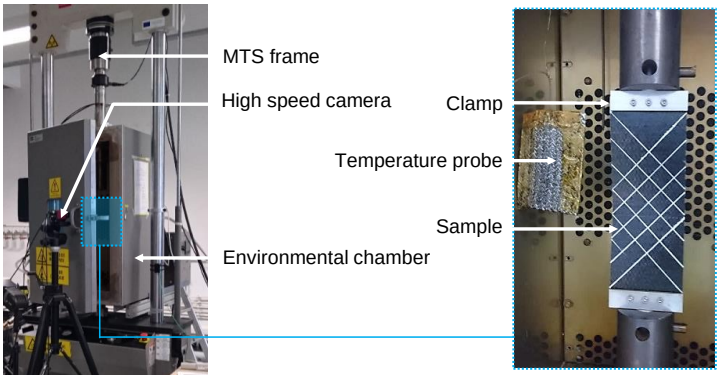

Figure 5.11 – Bias extension setup

5.4.1.2 Post-processing

As the determination of the shear angle through geometric considerations does not lead to valid results after the onset of sliding [Boisse+2016], an optical method was used. The

images obtained during the test were post-processed using routines developed in ImageJ [Schindelin+2012] and MATLAB: the shear angle is calculated as the average on three discrete measurements in the central region of the sample as shown in Figure 5.12.

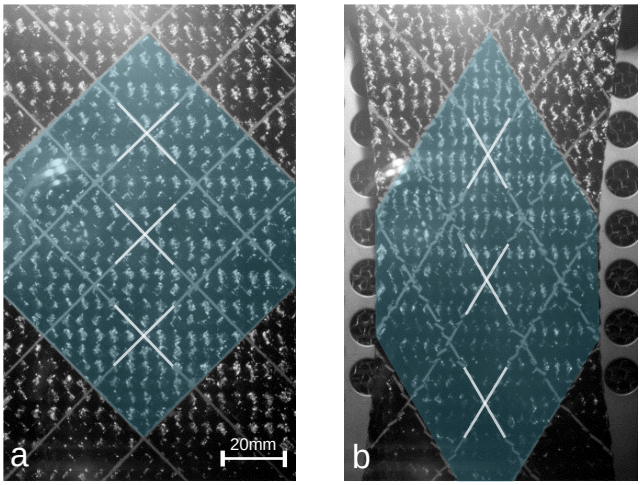

Figure 5.12 – Preconsolidated sample in (a) undeformed configuration and (b) after 30 mm of extension at 265 °C and 1000 mm min^{-1}, with location of the shear angle measurements. The central region undergoing pure shear is highlighted in blue.

Shear force was determined from axial load using the energetic approach presented by Launay et al. [Launay+2008], and subsequently reviewed in [Härtel+2014], where the power related to the displacement of the grips is equated with the power needed to shear the different regions of the sample:

$$F_{sh} = \frac{1}{(2h - 3w)\cos\gamma}\left(\left(\frac{h}{w} - 1\right)F\left(\cos\frac{\gamma}{2} - \sin\frac{\gamma}{2}\right) - wF_{sh}\left(\frac{\gamma}{2}\right)\cos\frac{\gamma}{2}\right) \tag{5.4.1}$$

where F_{sh} is the normalised shear force, F the axial force as recorded during the test, γ the shear angle and h and w the sample initial height and width, respectively. As the shear force is obtained recursively from the shear force at the half shear angle, linearity is assumed at the initial step of the computation:

$$F_{sh}\left(\frac{\gamma}{2}\right) = \frac{F_{sh}(\gamma)}{2} \tag{5.4.2}$$

The shear stress is then calculated by dividing by the initial sample thickness.

5.4.2 Results

The axial force versus extension curves obtained are presented in Figure 5.13 for all test repeats on the semipreg material at 265 °C. The mean force at each test speed is shown with solid lines, with grey surfaces representing the standard deviation. The reproducibility of the tests is good, with standard deviation increasing up to a maximum of 20% after the onset of sliding (when the specimen is failing).

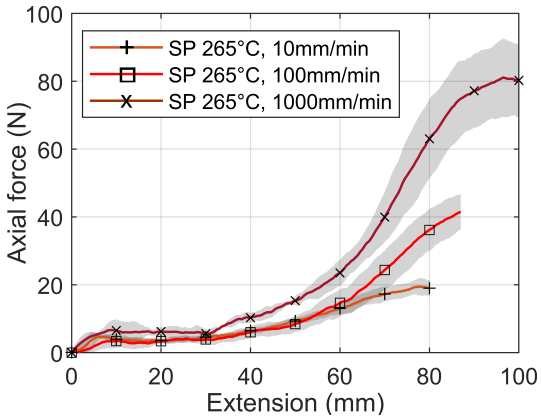

Figure 5.13 – Axial force versus extension curves; semipreg material at 265 °C.

The curves present the same features regardless of the test conditions: the sample first undergoes a realignment in the plane (as the heating cycle induces sag). No change in shear angle was observed as the material became slack from heating, which indicates that the sag was accommodated by buckling rather than shearing of the sample.As proposed by Harrison [Harrison+2004], the measured displacement data were shifted by approximately 1 mm to account for this effect. The resulting shear stress versus shear angle curves are shown in Figure 5.14a to 5.14d for the preconsolidated and semipreg material respectively.

Static friction initially prevents shearing until the applied load is sufficient ; at small shear angles, the yarns are free to rotate around their crossover points and the shear stress arises from inter-yarn friction only, as discussed in [Dumont2003] (see Fig. 2.23). As the yarns gradually come in contact, transverse compaction leads to a gradual increase in the shear stiffness. The theoretical asymptote of the curve corresponding to the compaction limit of the yarns is not reached, as intra-ply slippage mechanisms (crossover and inter-tow slip) become the primary mode of deformation to accommodate the prescribed displacement [Harrison+2004].

Intra-yarn shear was also observed during the deformation, as can be seen in Figure 5.15 where lines drawn on the undeformed sample present a loss of continuity due to the rotation of segments on yarns initially orthogonal to the lines. The low values of maximum shear stresses recorded here are attributed to the fabric coarseness (2.6 ends per cm) and weave style which reduces the waviness and affect the inter-yarn friction behaviour as reported by Dong et al. [Dong+2009].

Additional comparison between results for both the preconsolidated and semipreg composite and the dry fabric at $10\,\mathrm{mm\,min^{-1}}$ are presented in Figure 5.16: the stiffening effect of the matrix is clearly visible, with values of shear stress for the dry fabric being on average 50 % and 30 % of the semipreg and preconsolidated material respectively.

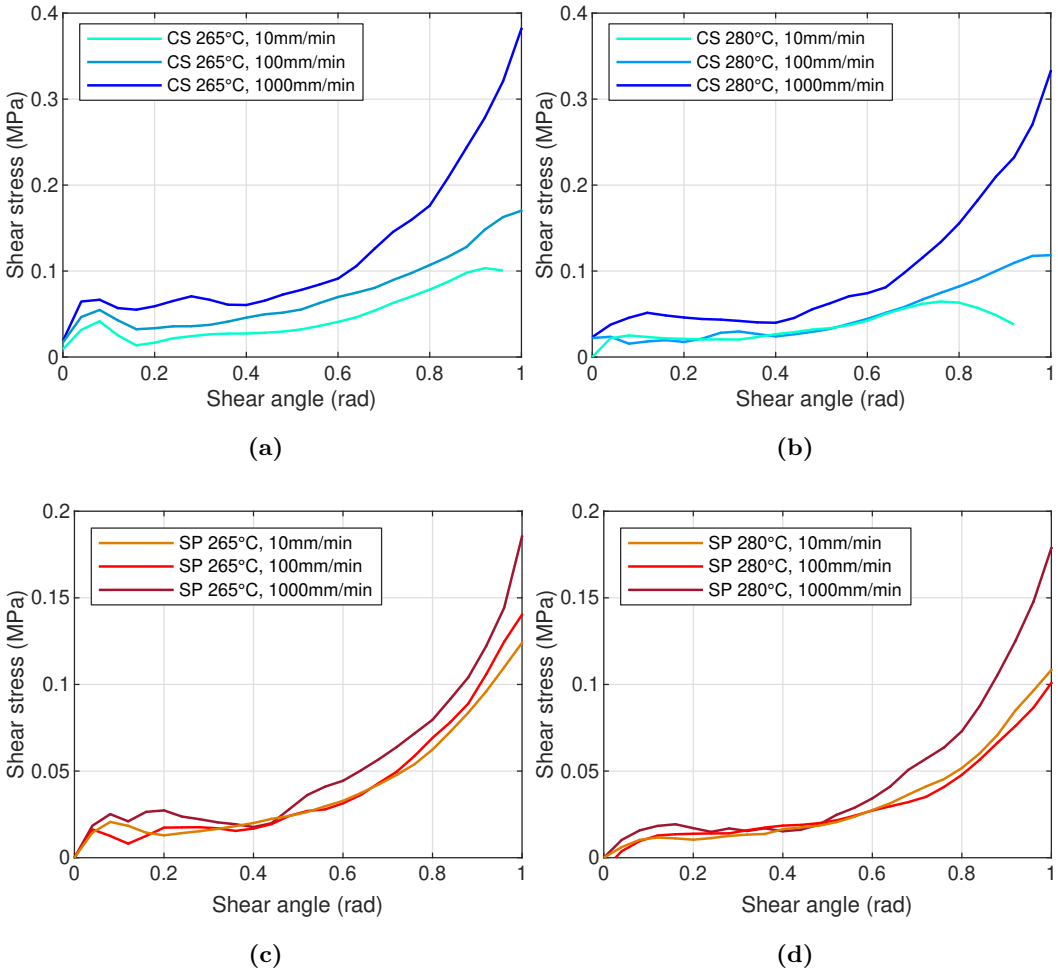

Figure 5.14 – Average shear stress versus shear angle curves for preconsolidated specimens at (a) 265 °C and (b) 280 °C, and semipreg specimens at (c) 265 °C and (d) 280 °C respectively.

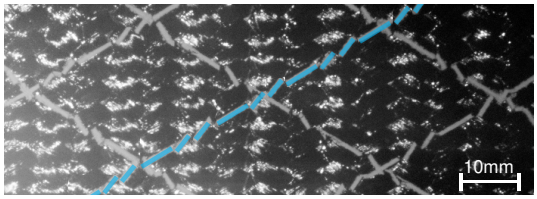

Figure 5.15 – Detail of a preconsolidated sample at 265 °C, 1000 mm min^{-1} after 30 mm of extension, with an initially continuous and straight line showing intra-yarn shear (highlighted in blue).

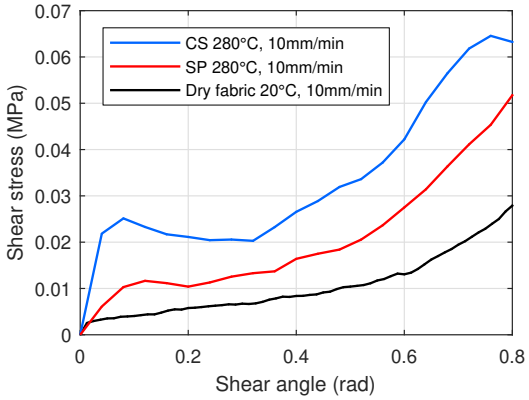

Figure 5.16 – Average shear stress versus shear angle curves for the preconsolidated (CS, blue) and semipreg (SP, red) specimens at 280 °C, and dry fabric at room temperature and 10 mm min^{-1}.

5.4.2.1 Temperature effect

The tests conducted at 280 °C and 265 °C show an increase of the measured shear stress with decreasing temperature for both the preconsolidated and semipreg material. Figure 5.17 presents the relative effect on shear stress of: (a) decreasing the temperature from 280 °C to 265 °C and (b) increasing the test speed by 1 or 2 decades, averaged for shear angles between 0.1 rad and 0.8 rad to ignore both the initial static friction and the sliding phase. The consolidated and semipreg material are denoted by blue and red bars respectively. Temperature is shown to have a significant effect on the observed behaviour, with the exception of tests conducted on the preconsolidated material at 10 mm min^{-1}, for which the only noticeable difference is the onset of sliding (see Fig. 5.14). The effect of temperature on the shear behaviour of woven composites is well documented in the literature [Dangora+2015; GuzmanMaldonado+2016; Machado+2016b], and is attributed to the increase in viscosity of the thermoplastic matrix as the material cools from the melt. A higher viscosity at lower temperatures impedes the shearing of the yarns that are either fully impregnated (in the case of the preconsolidated fabric) or sandwiched between polymer rich layers (in the case of the semipreg).

5.4.2.2 Rate effect

Strain rate dependence is not as widely reported as temperature dependence [Dangora+2015; Haanappel+2014], and as a result is not taken into account as often in modeling approaches [Boisse+2016]. The average effect on the shear stress of increasing the test speed is shown in Fig.5.17b. In the case of the preconsolidated composite (blue bars), an increase in the strain rate leads to a significant increase of the shear stress with exception of the tests conducted at 280 °C and 100 mm min^{-1}. Higher shear angles before sliding are also achieved at higher speeds as observed in Fig. 5.14. In the case of the semipreg, increasing the test speed from 10 to 100mm/min does not have a significant effect, with only tests at 1000 mm min^{-1} presenting a slight increase in the observed shear stress.

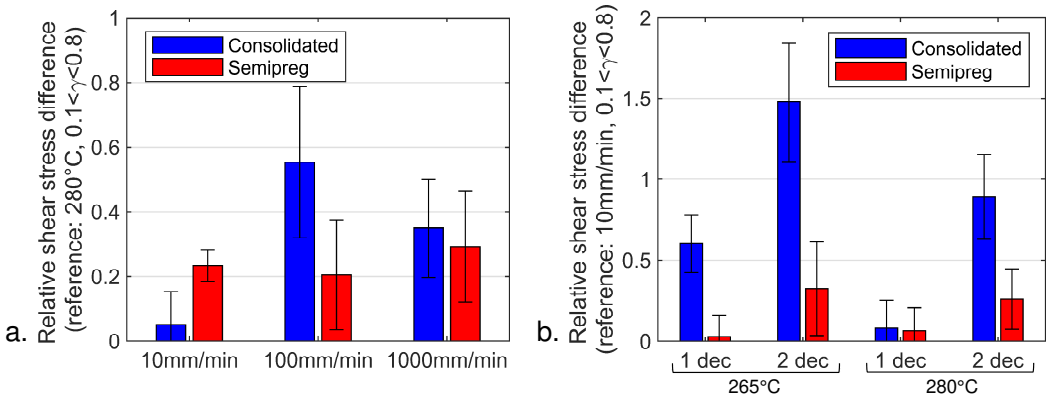

Figure 5.17 – Average relative shear stress difference resulting from: (a) reducing the temperature by 15 °C, (b) increasing the speed by 1 or 2 decades.

5.4.2.3 Intra-ply sliding behaviour

Sixteen tests were conducted up to an extension of 150 mm to observe the behaviour of the samples past the onset of sliding. In the case of semipreg samples where the matrix is located only on the top and bottom surfaces of the fabric, cross-over slip leads to a characteristic pattern of visually resin-free macroscopic zones and accumulation of resin at the boundaries of these zones (see Fig. 5.18).

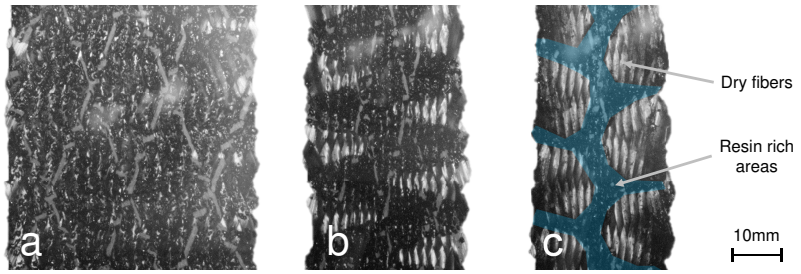

Figure 5.18 – Semipreg sample at 280 °C, 1000 mm min^{-1} after (a) 60 mm, (b) 100 mm and (c) 140 mm of extension, showing the onset of slippage and characteristic pattern of resin-rich areas highlighted in blue.

This behaviour is assumed to be due to a combination of non-coated surfaces becoming exposed and resin accretion in the region of yarn crossover opposite to the direction of sliding (see Fig. 5.19). Since the resin is distributed uniformly in the preconsolidated material, the effect is limited to semipreg samples. The initial flow distance required for the through-thickness impregnation of the yarns in the unsheared fabric is on average equal to the yarn thickness; sliding of the yarns results in a local increase of the polymer flow distance. In addition, in-plane shear affects the permeability of the fabric both in-plane [Heardman+2001; Verleye+2008] and out-of-plane [Xiao+2014]. This results in modification of the local matrix volume fraction and can lead to dry spots after the consolidation of the part which is detrimental to the resulting mechanical properties.

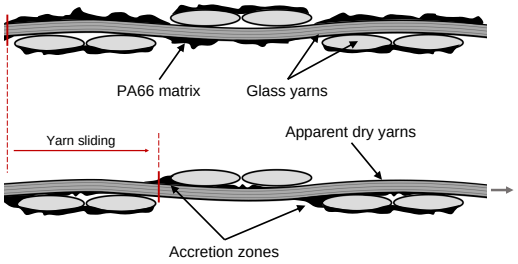

Figure 5.19 – Inter-yarn sliding and resin accretion at crossover points

5.4.3 Temperature and rate dependent model

The temperature and rate-dependence is assumed to be related only to the in-plane shear term and tension/shear couplings are neglected. The analytical expression of the shear modulus developed by Machado et al. [Machado+2016b] for preconsolidated composites is used to represent the nonlinear, temperature and rate-dependent shear behaviour, assuming a multiplicative decoupling between the different effects:

$$G_{12}(\gamma,\dot{\gamma},T) = (a_1 + 2a_2\gamma + 3a_3\gamma^2)\left(1+\left(\frac{\dot{\gamma}}{D}\right)^{\frac{1}{P}}\right)\left(e^{A\frac{T-T_0}{T_0}}\right) \tag{5.4.3}$$

where a_1, a_2 and a_3 are fit coefficients of the shear stiffness, D and P are parameters of Cowper-Symonds overstress law [Cowper+1957], and T_0 and A are the reference temperature and temperature scaling factor respectively.

The model parameters have been determined by minimizing the sum of least square errors associated with each shear stress versus shear angle/shear rate experimental curve. The specificities of the bias-extension test lead to a variable shear rate, which was therefore evaluated by numerical differentiation of the shear angle using finite differences. The optimization problem was solved using an interior-point algorithm in MATLAB [Waltz+2005]. The resulting parameters are presented in Table 5.2.

Table 5.2 – Shear modulus model parameters

Parameter	**Preconsolidated**	**Semipreg**
a_1 (MPa)	0.3351	0.3276
a_2 (MPa)	-0.9356	-0.9040
a_3 (MPa)	0.8466	0.8817
D (rad s^{-1})	2.7251×10^{-3}	5.7215×10^{-3}
P (-)	3.6578	7.4378
A (-)	-6.9429	-10.6933
T_0 (K)	495.01	499.97

Figures 5.20 and 5.21 show the superposition of the model prediction and average experimental curves in the shear angle/shear rate plane for the preconsolidated and semipreg composite respectively.

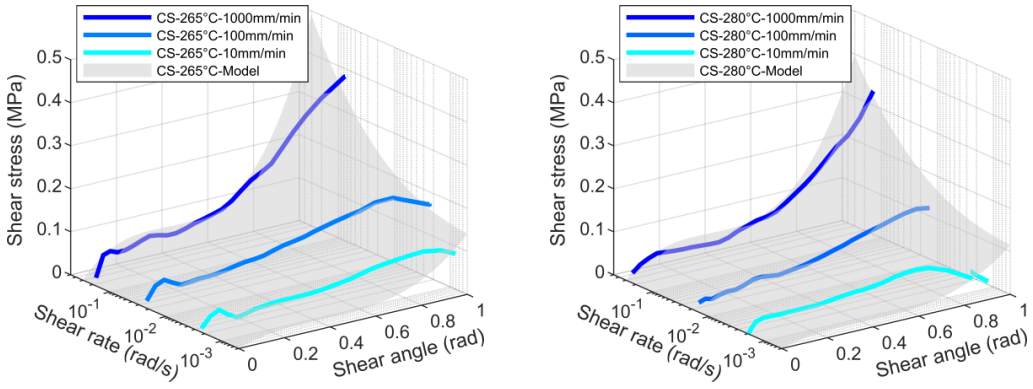

Figure 5.20 – Comparison between experimental data and model for preconsolidated specimens at 265 °C (left) and 280 °C (right). The grey surface represent the model prediction.

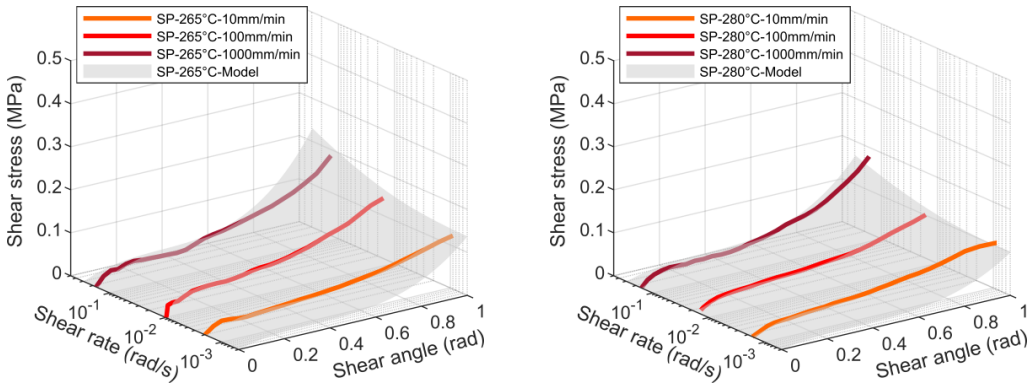

Figure 5.21 – Comparison between experimental data and model for semipreg specimens at 265 °C (left) and 280 °C (right). The grey surface represent the model prediction.

The model shows a good agreement with the experimental data at low to intermediate shear angles. At high shear angles, shear stresses are overpredicted compared to the experiments. This is due to intra-ply sliding during the experiments, resulting in lower shear stresses as the sample is fraying. This behaviour is not expected during the actual forming experiments, as the blankholders used prevent much of the intra-ply sliding: the model is expected to perform better at high shear angles in this case.

The sum of squared relative residuals for each configuration, divided by the corresponding number of data points, is presented in Figure 5.22. The model provides a good qualitative description of the behaviour in both cases, including the lower sensitivity of the semipreg to temperature and rate as can be seen in the values of the temperature scaling factor and exponent of the Cowper-Symonds law.

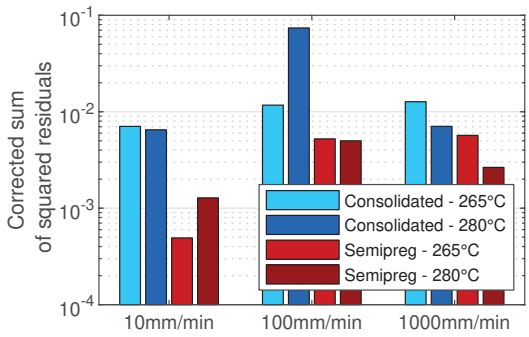

Figure 5.22 – Sum of squared relative residuals corrected by number of data points in each configuration.

5.5 Conclusion

This chapter introduced the continuum approach used to model the behaviour of woven thermoplastic composites during forming. A non-orthogonal model based on a hypoelastic formulation is presented, and is used to track the orientation of the yarns during the deformation. A simple expression for the constitutive tensor expressed in a frame fixed with the yarns is defined, considering only tensile and shear modulus terms.

The nonlinear tensile behaviour of the consolidated and semipreg PA66/glass composites is characterized at room temperature, and results show the influence of the consolidation step on the initial decrimping phase; a phenomenological model with a small number of parameters is proposed to describe this behaviour and shows a good agreement with the experimental data.

Finally, the in-plane shear behaviour is characterized using bias-extension tests at high temperature and various strain rates. Results show an increased shear stiffness at low temperatures and high strain rates in the consolidated material, while these effects are less influent on the semipreg material. In addition, the heterogeneous distribution of resin on the surface of the yarns in the case of the semipreg leads to a pattern with resin-rich regions and apparent dry yarns after intra-ply sliding at high shear angles. A model based on multiplicative decoupling of the temperature and rate effect is fitted to the experimental data.

The implementation of the tensile and shear model in finite element code Abaqus FEA is discussed in Chapter 6, along with its validation on virtual bias extension tests. The model is then applied, using the temperature fields predicted by the heat transfer model as an input, to simulate the forming of thermoplastic composite under various conditions.

Chapter

6

Forming of hemispherical PA66/glass parts: experimental and numerical study

6.1 Introduction

A non-orthogonal hypoelastic model has been introduced in the previous chapter to represent the mechanical behaviour of the thermoplastic composites studied, as a function of temperature and rate. The validation of this model requires experimental data; the first part of this chapter is dedicated to the presentation of an experimental thermoforming program: a forming rig, adapted to the existing infrared oven described in chapter 4, is designed. A grid-based post processing method is developed to measure shear angle fields, and hemispherical parts are formed with various process conditions.

In a second part, the constitutive model is implemented in the commercial finite element software Abaqus, and first validated on virtual bias extension tests. The experimental forming rig is modelled, and the forming process simulated with increasing levels of complexity, up to non-isothermal forming with a non-uniform temperature field, based on a simplified description of the temperature evolution in the blank. Finally, the finite element model is used to discuss the impact of local heating on the resulting shear in a double-curvature part.

6.2 Experimental hemispherical forming tests

6.2.1 Stamp forming setup

A press forming fixture has been developed to allow for experimental stamp forming tests at the laboratory scale with the infrared oven described in chapter 4. A hemispherical geometry has been selected, based on its frequent use in the literature to validate forming simulation tools [Boisse+2011; Cao+2003; Machado+2016a; Smith+2013] and for its dimensions better adapted to the blank sizes used (compared to the larger double dome geometry [Harrison+2013; Khan+2010]).

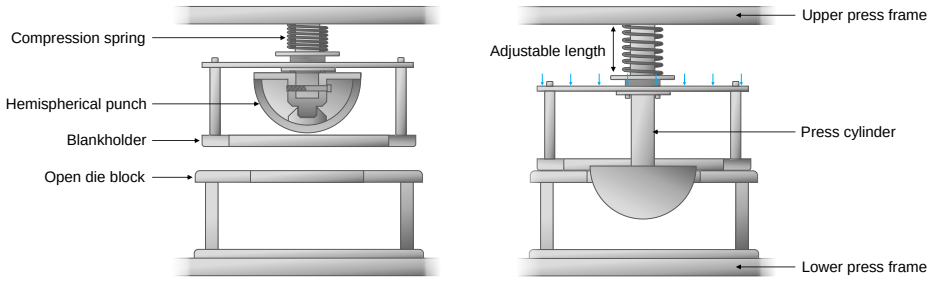

Figure 6.1 – Hemispherical test fixture (left: open, right: closed position)

The test fixture is schematized in Fig. 6.1: the assembly is composed of an hemispherical punch ($r = 75\,\mathrm{mm}$), an open die block with cylindrical opening (allowing for a 2 mm clearance with the punch) and a square blankholder. The punch and blankholder subassembly is mounted on the cylinder of a displacement controlled, electro-mechanical PROMESS 60 kN press with a precision of 0.05 mm and a maximum stroke speed of $120\,\mathrm{mm\,s^{-1}}$. The blankholder applies a clamping force on the blank with help of a compression spring (spring rate $k = 12.5\,\mathrm{N\,mm^{-1}}$).

The magnitude of the force can be modified by adjusting the length of the spring in the closed position, between 50 N and 800 N depending on the free length of the spring. The complete test setup, showing the oven at the rear of the press, and detail of the forming station is shown in Fig. 6.2.

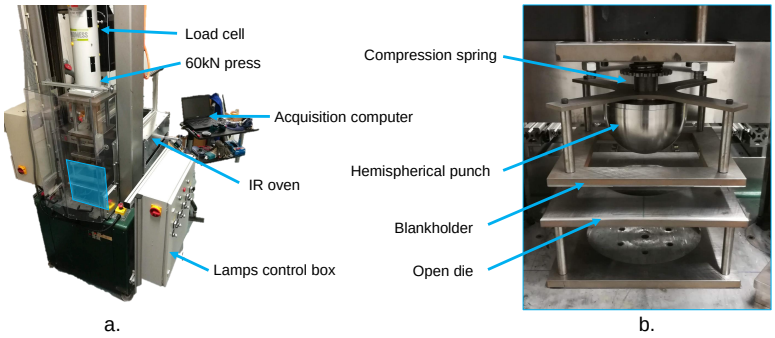

Figure 6.2 – a. Stamp forming setup, b. detail of the forming station

6.2.2 Development of a GSA-based method for shear angle measurements

6.2.2.1 Full-field measurements

In addition to the axial force measured by the press during the forming of the blank, shear angle data is needed to validate the simulation model. The dimensions of the press frame and the presence of a safety guard prevent the use of cameras to record the shear angle evolution as the sample is not clearly visible. Methods based on in-situ digital image correlation (DIC) during forming, as proposed in the literature, are not directly applicable [Bonnaire+2017; Capelle+2014]. DIC using a single pair of images (before/after forming) did not provide satisfying results, as the deformations are too large for the algorithm to track the displacement of the subsets; and while manual measurement of the shear angle on discrete spots is possible, the process is time intensive and lacks precision on parts presenting double curvature [Patou2018].

Grid-based methods are widely used in control of sheet metal and composite forming [Keeler1968; Martin+1997]. The sample surface is marked with a regular pattern (grid or evenly spaced markers); strain information can be retrieved with knowledge of the initial grid spacing either by tracking the position of the markers/grid intersection, or by measuring the change in phase between the reference and deformed configuration. These methods are able to derive strain fields even with large deformations between the configurations considered [Grédiac+2016], and are thus well suited to closed-mould processes.

In the absence of an adapted system available in the SMAE, a post-processing method based on grid strain analysis (GSA) has been developed to measure surface strains from images obtained with commercial DIC software VIC-3D [Correlated Solutions], as inspired by work presented by Shi et al. [Shi+2012] and Machado [Machado+2016a].

6.2.2.2 DIC-GSA algorithm

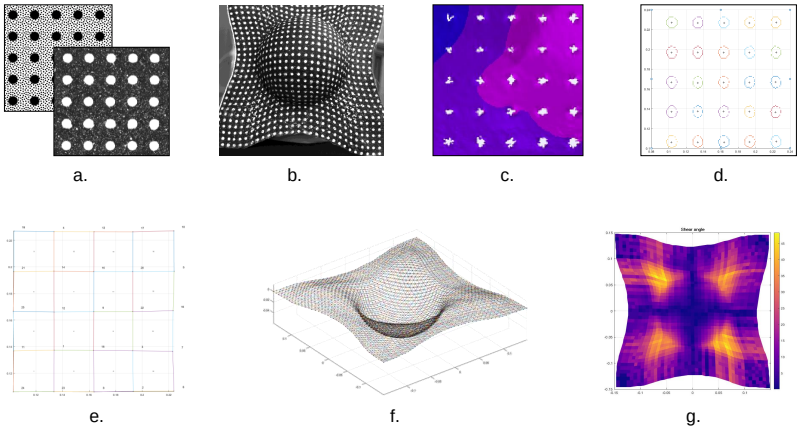

Figure 6.3 – Steps of the quantitative shear angle post-processing

The different steps of the quantitative post-processing method are presented in this section (further detail on the algorithms and procedure are presented in Appendix B):

1. Circular markers (diam. 4 mm) are first marked on the sample on a grid with spacing 10 mm using temperature resistant white paint and a laser cut stencil. The grid directions are aligned with the principal directions of the blank. The markers form the nodes of the mesh used to derive the surface strain fields. A random white speckle pattern is superimposed on the grid markers (see Fig. 6.3a.-b.): this speckle pattern allows acquisition of the blank surface coordinates by VIC-3D.
2. After forming of the part, images of the surface of interest are obtained with a set of 2 precalibrated cameras, in a 'reference' configuration, and following a small rigid body rotation ('deformed' configuration). VIC-3D is used as a 3D scanner, rather than as a strain measurement software. The random speckle pattern ensures that the position field can be resolved everywhere except in the uniformly white circular markers (provided the subset size is selected carefully). The result is a *negative* of the position of the markers (Fig. 6.3c.), i.e. the x, y, z coordinates are known for all points (pixels) on the surface of the blank, with exception of the pixels inside the markers. The coordinates matrix is exported to MATLAB which is used for all subsequent processing.
3. The coordinates of the center of the markers are determined from the coordinates of the negative in two steps:
   - The points on the boundary of the grid markers are identified using an algorithm proposed by Chalmovianský [Chalmovianský+2003]: the k-nearest neighbours of each points are computed, and the distance between the point and the centroid of the corresponding neighbourhood is measured: a small distance suggests that the point is surrounded by other points, while a large distance suggests that the distribution of nearest neighbours is skewed in one direction, i.e. the point is on a

boundary. The threshold value of the distance for which a point is considered as part of a boundary is selected manually.

- The points that belong to the same boundary are grouped using k-means clustering (the data is partitioned in k clusters that minimize the distance of the points within a cluster, and maximize the distance between the clusters). The center of the markers are computed as the centroid of the clusters (Fig. 6.3d.)

4. A mesh of quad elements is generated from a seed element using the 3D grid generation algorithm presented in [Shi+2012] (Fig 6.3e.-f.).
5. Strains are computed with the finite element method from the nodal displacements, using bilinear shape functions (Fig. 6.3g.).

The method developed allows for a reasonably fast (<30 min) and repeatable post-processing of full-field strain data on the samples, and is especially well adapted to consolidated blanks. The surface roughness of the semipreg blanks lead to a lower precision in the geometry of the markers (as the stencil did not adhere perfectly to the surface): smaller region of interests had to be considered, and paint touch ups had to be conducted in some instances.

6.2.3 Test conditions

Forming tests have been conducted on preconsolidated and unconsolidated blanks of dimension 330 × 330 mm. Circular markers were painted on the bottom surface of the blanks as per Fig 6.3a.; the blanks were preheated during 120 s in the infrared oven described in chapter 4, before being transferred to the press and stamped. The average transfer time between the oven and the press stations has been measured to 0.75 s; the average blankholder and punch closing time is 2.4 s, with a punch speed of 50 mm s^{-1} and an effective forming depth of 70 mm. A blankholder force of 200 N has been used based on values suggested in the literature [Najjar+2013; Skordos+2007; Willems+2006]. The punch is held down for 10 s, before the part is demoulded. Two oven configurations have been investigated: configuration LCa (as defined in section 4.3.1.1), with lamps operating at nominal temperature, and the optimized configuration LCopt presented in section 4.6.2. Blanks of 1-ply with a 0° and 45° orientation have been tested for the preconsolidated and semipreg fabric. The parameters of the forming tests are summarized in table 6.1 (two repeats per condition).

Table 6.1 – Forming tests parameters

Test n°	Consolidation	Orientation	Oven configuration
1	CS	0°	LCa
2	CS	45°	LCa
3	SP	0°	LCa
4	SP	45°	LCa
5	CS	0°	LCopt
6	CS	45°	LCopt
7	SP	0°	LCopt
8	SP	45°	LCopt

6.3 Experimental results

6.3.1 Description of the parts formed

A top view of the parts formed with configuration LCa (tests 1 to 4) is presented in Fig. 6.4. The grid markers are present on a quarter of the blank, in regions where high shear is expected. The influence of the paint on the heating behaviour and the deformation pattern has not been found to be significant.

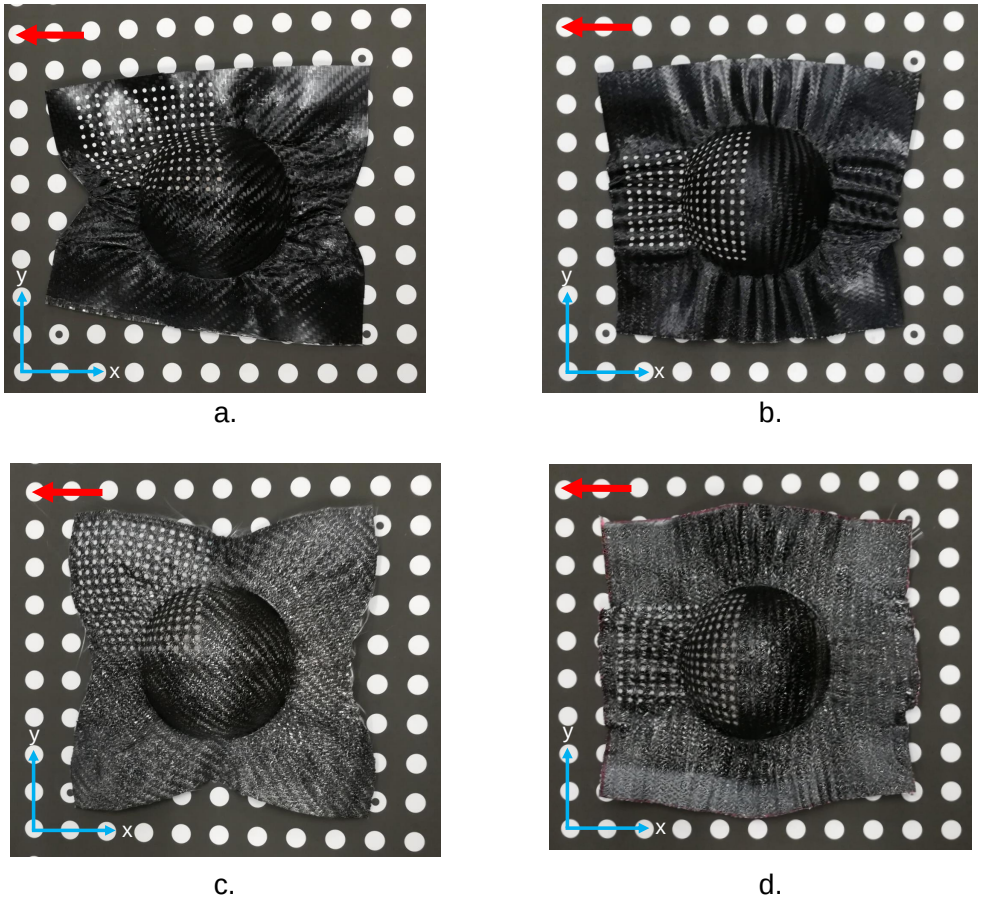

Figure 6.4 – Top view of parts formed with configuration LCa (first repeats). a.-d.: tests 1 to 4. Red arrow indicates the direction of transfer from the oven.

Large wrinkling is observed in parts formed from preconsolidated blanks. The deformation pattern is asymmetrical for the blanks formed with test condition 1: wrinkles radiating from the hemisphere (see Fig. 6.5) are localized mostly along the x-axis, while regions close to the edges initially at $y = \pm 165\,\text{mm}$ barely show any shear deformation. Wrinkles propagating along the x- and y-axes from zones with high shear angles at the base of the hemisphere are also observed in preconsolidated blanks with a 45° orientation.

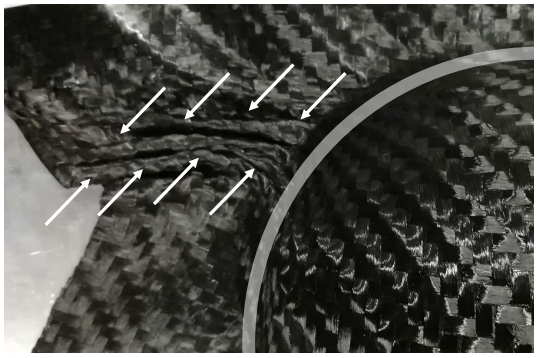

Figure 6.5 – Wrinkle propagation from high shear angle region

Parts formed from non-consolidated semipreg present lower wrinkling. Blanks at 0° show zones with high shear along the diagonals. The shear angle increases from the top of the hemisphere to a maximum at the base and decreases closer to the corners. The edges corresponding to yarns passing through the center of the blank are drawn in during forming and show limited shear deformation. More wrinkles are observed with blanks oriented at ±45°, with high shear zones located at the base of the hemisphere along the x and y-axes. The corners of the initially square blank, that contain yarns passing through the center, are drawn in.

The influence of the oven configuration is mostly visible on consolidated blanks at 0° (see Fig. 6.6). Smaller wrinkles are present on the part, and are distributed symmetrically with regards to the x and y axes. Ear-like wrinkles similar to those presented in [Liang+2014] are observed in the corners.

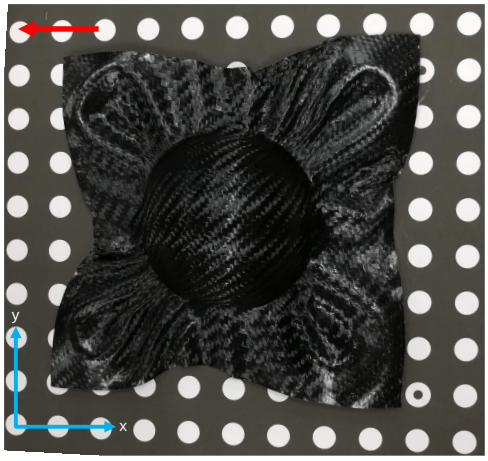

Figure 6.6 – Top view of part formed with test conditions 5. Red arrow indicates the direction of transfer from the oven.

An example of the reconstructed surface of the blank using the grid strain algorithm presented in section 6.2.2 is shown in Fig. 6.7a. The evolution of shear angle in the part is well reproduced (with exception of reconstruction errors along the diagonals due to wrinkles masking the grid nodes), with maximal shear angles observed at the base of the hemisphere

at a 45° angle of the initial yarn directions and minimal shear in the center of the hemisphere and in the corners. The maximum shear angle measured on the formed parts is presented in Table 6.2. While the experimental dispersion is quite high, lower shear angle values are observed in preconsolidated blanks compared to semipreg. As the blank cools from convection and contact with the tool, the viscosity of the matrix increases and restricts movement of the yarns. The lower shear angle, along with the larger magnitude of wrinkles observed for parts manufactured from preconsolidated blanks, suggests that shear locking happens at lower angles/higher temperatures in preconsolidated blanks, i.e. the imposed deformation is accommodated preferentially by out-of-plane bending and wrinkling rather than in-plane shear if the temperature is too low. As the in-plane shear behaviour of the semipreg is less sensitive to temperature, higher shear angles without wrinkles can be achieved. A slight increase of the maximum shear angles measured is also observed in configuration LCopt.

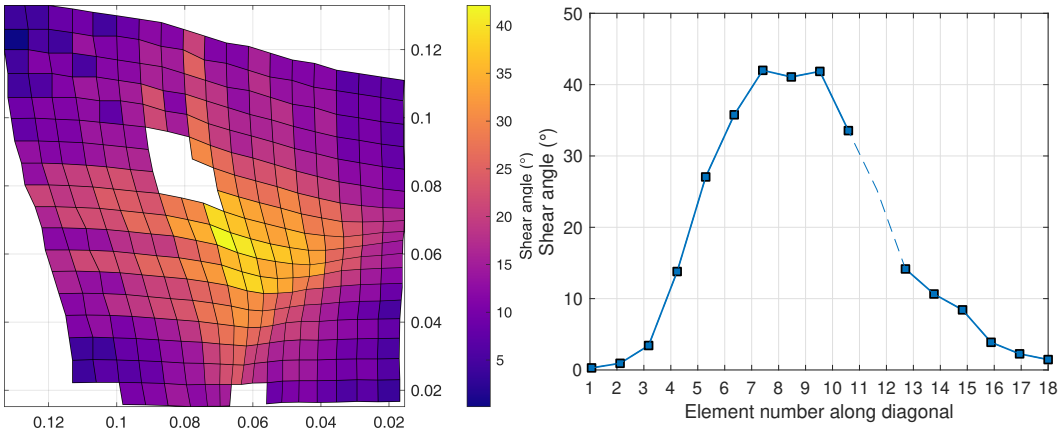

Figure 6.7 – Example of shear angle processing from GSA (test conditions 3). a. reconstruction of shear field, b. shear angle evolution along a diagonal (elt. 1: center, elt. 18: corner)

Table 6.2 – Maximum shear angle

Test	$\gamma_{12,max}$	**Test**	$\gamma_{12,max}$
1	$37.9 \pm 2.6°$	5	$39.1 \pm 2.2°$
2	$39.5°$	6	$41.3 \pm 0.3°$
3	$42.4 \pm 1.2°$	7	$42.7 \pm 0.9°$
4	40.8 ± 2.5	8	$41.6 \pm 1.0°$

6.3.2 Axial force on the punch

The axial forces recorded during forming are shown in Fig. 6.8a and 6.8b for oven configurations LCa and LCopt respectively, as a function of the position of the punch. The force is plotted as a function of the punch position relative to the die, i.e. the punch makes contact with the blank at $x = 0\,\text{mm}$ and the forming process corresponds to $x > 0$ (the quasi-linear

tensile load measured for negative x values corresponds to the force exerted by the spring on the blankholder).

The curves present the same features regardless of the test conditions: a first region associated with low compression forces between 0 mm and 20 mm, and a progressive increase of the load at larger drawing depths until 70 mm. Higher compressive loads are required to form pre-consolidated blanks, with peak forces around 1 kN, compared to 400 N for semipregs. A slight increase of the load required to form blanks at a 45° orientation is also observed.

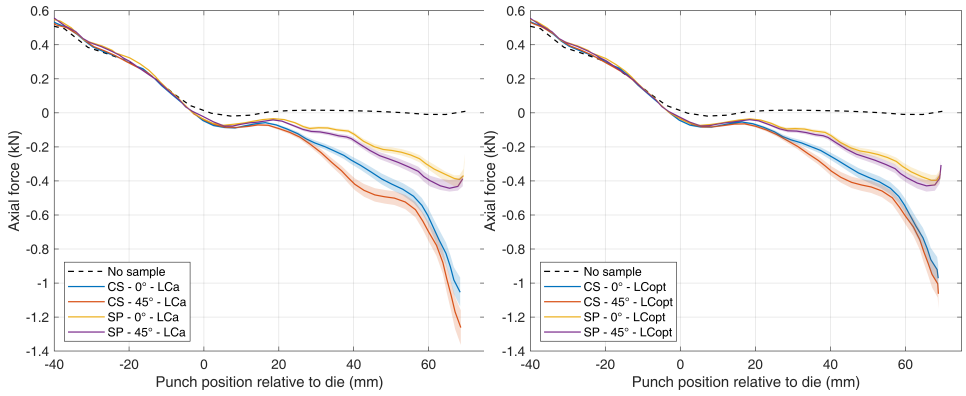

(a) **(b)**

Figure 6.8 – Axial force during forming, (a): LCa, (b): LCopt

The reaction force measured on the punch corresponds to the contributions of bending, shear, and blank/tool friction. The in-plane shear modulus has been shown in chapter 5 to increase with decreasing temperature. The bending modulus of thermoplastic woven composites also increases at temperatures lower than the melt [Boisse+2018; Liang+2014]. This is coherent with the force increase observed here, as the blanks cools down during the non-isothermal forming. The effect of temperature on tool-ply friction is less clear, with researchers reporting a decrease of the friction coefficient with increasing temperature [GorczycaCole+2007; ten Thije+2008b; Vanclooster+2010] related to the diminution of viscosity of the matrix, while other studies show an increase of the coefficient with increasing temperature [Lebrun+2004; Lee+2017; Murtagh+1995] which is attributed to a reduction of the lubricating film thickness, associated with higher shear loads, at high temperatures.

The difference in measured force between the preconsolidated and unconsolidated blanks is also coherent with the experimental results presented in chapter 5, with the semipreg showing a lower shear modulus as well as a lower temperature dependence.

Similar results in terms of influence of the fabric orientation on the axial force are presented in [Labanieh+2018] (for experimental tests on a dry carbon fabric). The difference is attributed to the length of the yarns initially under the blankholder: in a blank at ±45°, yarns being pulled in are oriented along the diagonals of the blankholder; the length under the blankholder is then $\sqrt{2}$ times that of a blank at 0/90° (see Fig. 6.9 for a schematic). The larger number of yarn crossovers under the blankholder thus leads to higher frictional forces.

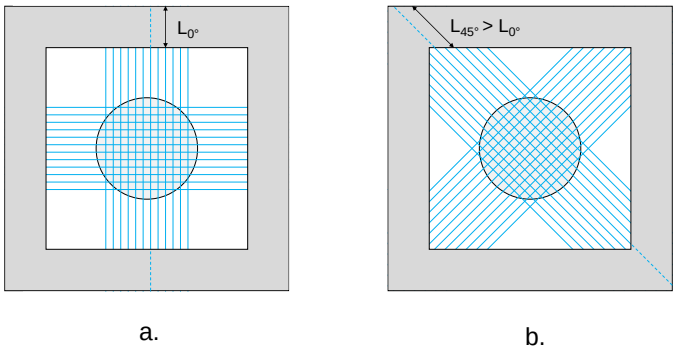

Figure 6.9 – Schematized yarn length under blankholder as a function of fabric orientation: a. 0/90°, b. ±45°

6.3.3 Mesoscale defects

In addition to the macroscale wrinkles discussed in section 6.3.1, defects are also observed at the mesoscale, and notably yarn buckling (Fig. 6.10a) and yarn sliding (Fig. 6.10b). Yarn buckling (which corresponds to out-of-plane bending) has been shown in [Ouagne+2013; Tephany+2016] to depend mainly on membrane tensions, with higher blankholder pressures leading to reduced buckling by constraining the yarns.

Yarn sliding along the hemisphere is mostly visible in semipreg blanks. As discussed in section 5.4, sliding modifies the local matrix volume fraction and could affect the resulting mechanical properties of the part. This defect is also dependent on the blankholder pressure: Labanieh et al. [Labanieh+2018] have shown experimentally that higher blankholder pressures are associated with larger intra-ply yarn sliding, as the frictional forces between yarns under the blankholder becomes higher than that of yarns crossover points not compressed. As the model developed in chapter 5 is based on a macroscale approach, these defects cannot be replicated numerically.

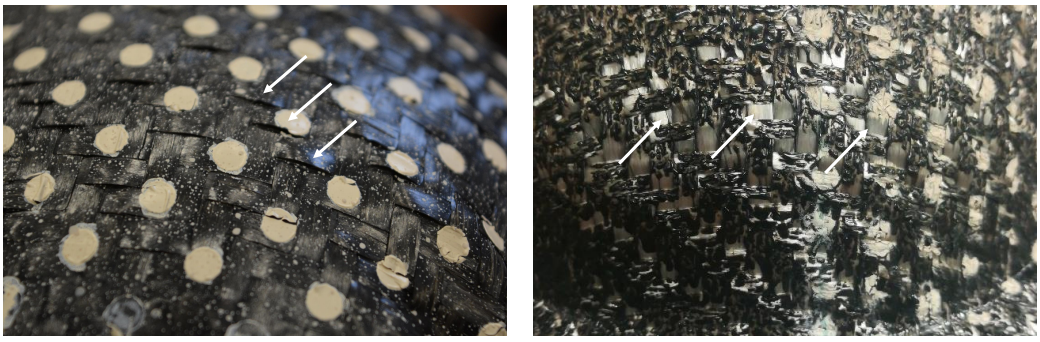

(a) **(b)**

Figure 6.10 – Mesoscale defects. (a) buckling (preconsolidated blank), (b) yarn sliding exposing dry glass fibres

6.3.4 Temperature evolution during forming

A SC-640 FLIR infrared camera operating in the wavelength range 7.5–13 µm has been used to record the evolution of temperature on the visible part of the top surface of the blank during the forming step, for tests 1 and 5 (preconsolidated and semipreg blank with configuration LCa). The surface emissivity has been set to 0.92 and 0.93 for tests 1 and 5 respectively, based on the characterization presented in section 3.4.2.3. The temperature is recorded during 18 s at 10 Hz (180 frames). The timeframes corresponding to the different phases of the forming step are presented in Fig. 6.11, where the y-axis represents the spatial average of the temperature over the field of view of the camera.

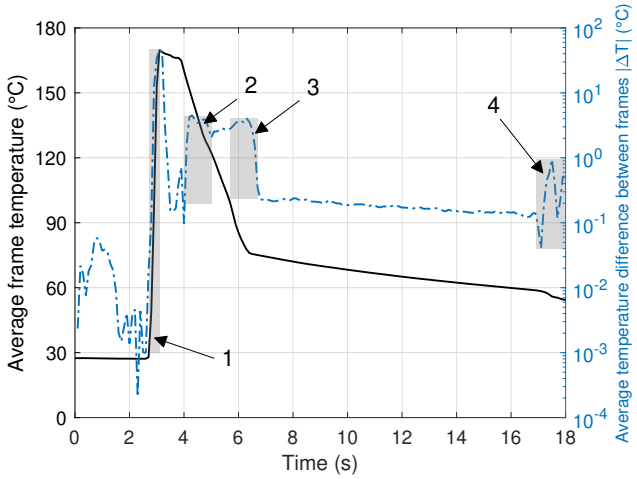

Figure 6.11 – Average temperature and temperature difference between frames, showing the different phases of the forming step. 1: transfer of the blank from IR oven, 2 and 3: downward movement of blankholder and punch, 4: demoulding

Specific frames corresponding to times before and after the main phases (before and after transfer, after blankholder contact with the blank, after punch contact with the blank and during cooling and demoulding) are presented in Fig. 6.12 and 6.13 for a preconsolidated and unconsolidated blank respectively.

The first frame after transfer (t=4 s) shows a non-uniform temperature distribution in the blank expected from configuration LCa with a higher temperature in the region closer to the symmetry line perpendicular to the lamp direction. Uneven cooling is observed as the blank is pressed against the die block by the blankholder (t=5.5 s), with cooler regions where the blank is in contact with the tool and higher temperatures in the center where the blank is cooled only by natural convection on both faces. As the punch comes in contact with the blank, and because of the quasi-inextensibility of the fibres, colder regions of the fabric initially under the blankholder are drawn towards the center (t=6.2 s). At larger depths, radial wrinkles are generated in the preconsolidated blank (t=7 s). These wrinkles become clearly visible as the blank cools down (t=14 s and t=18 s) because of loss of contact with the die. Wrinkling appears much less pronounced in the case of the unconsolidated semipreg blank.

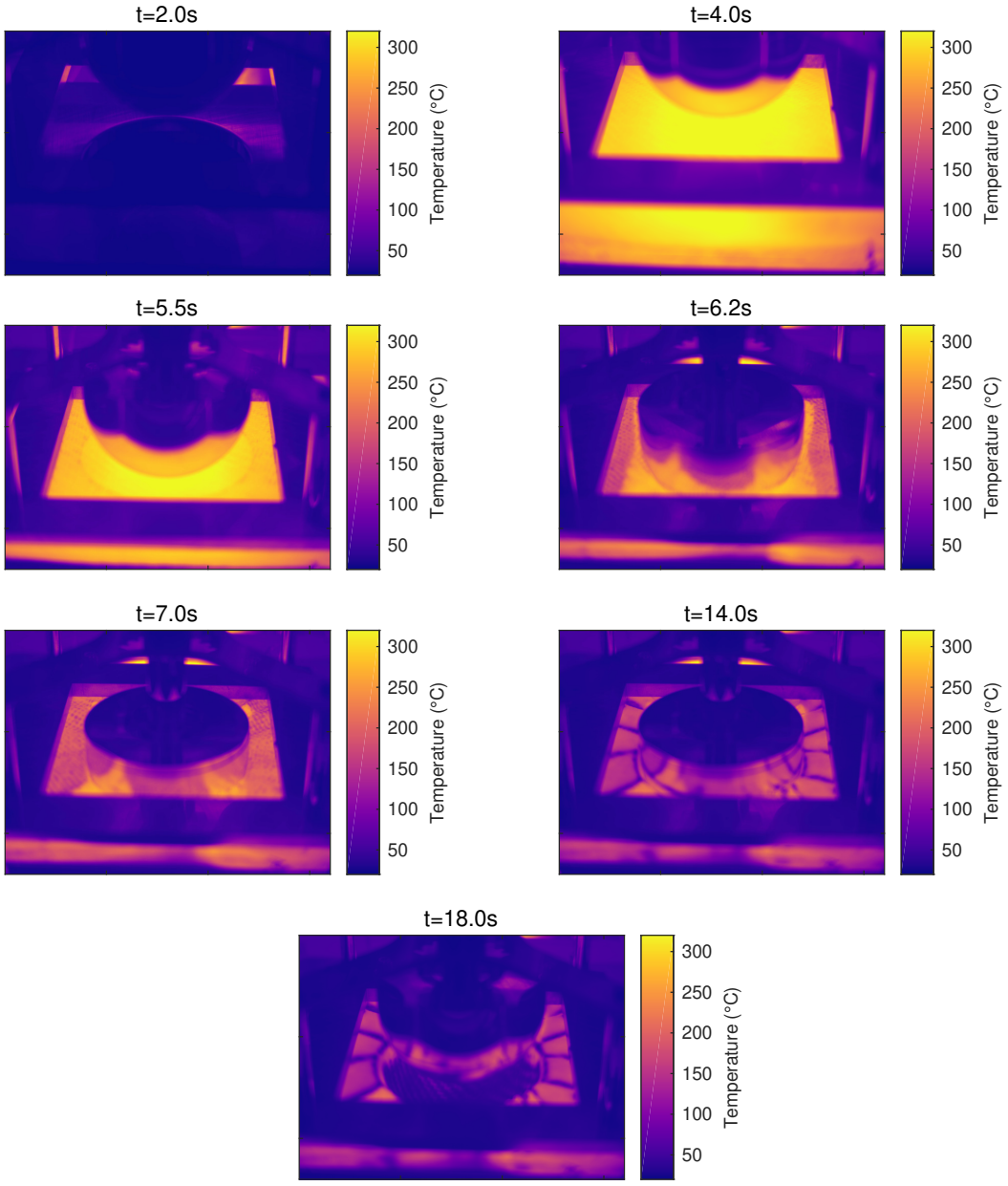

Figure 6.12 – Temperature evolution during forming, consolidated blank

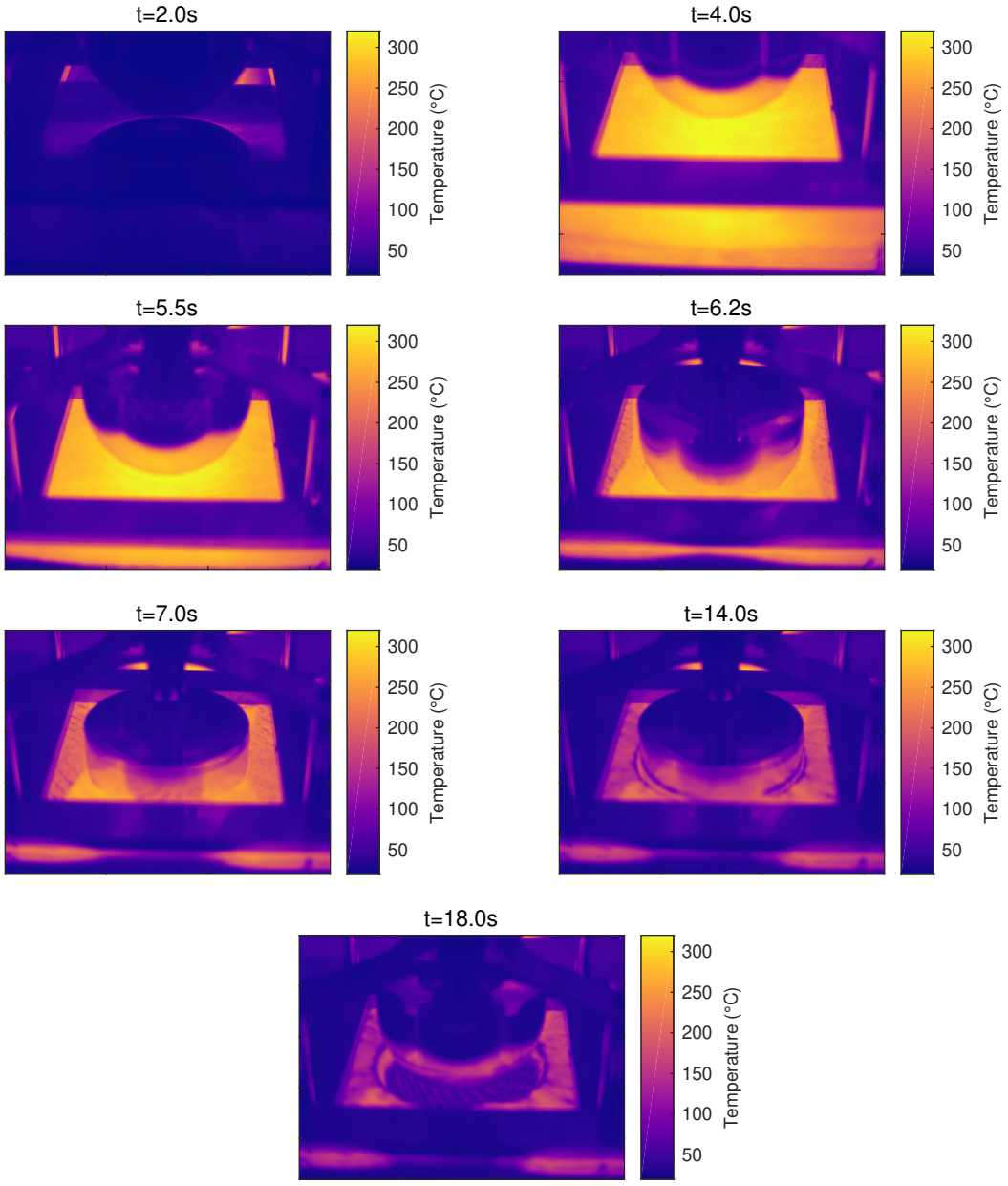

Figure 6.13 – Temperature evolution during forming, semipreg blank

The measured evolution of temperature on selected points is presented in Fig. 6.14a.-d. for the two test cases. The observation points are fixed; as the blank is deformed, the curves correspond to the Eulerian description of temperature during the phases corresponding to movement of the blankholder and punch; the Lagrangian and Eulerian descriptions are equivalent after then (for t>7 s).

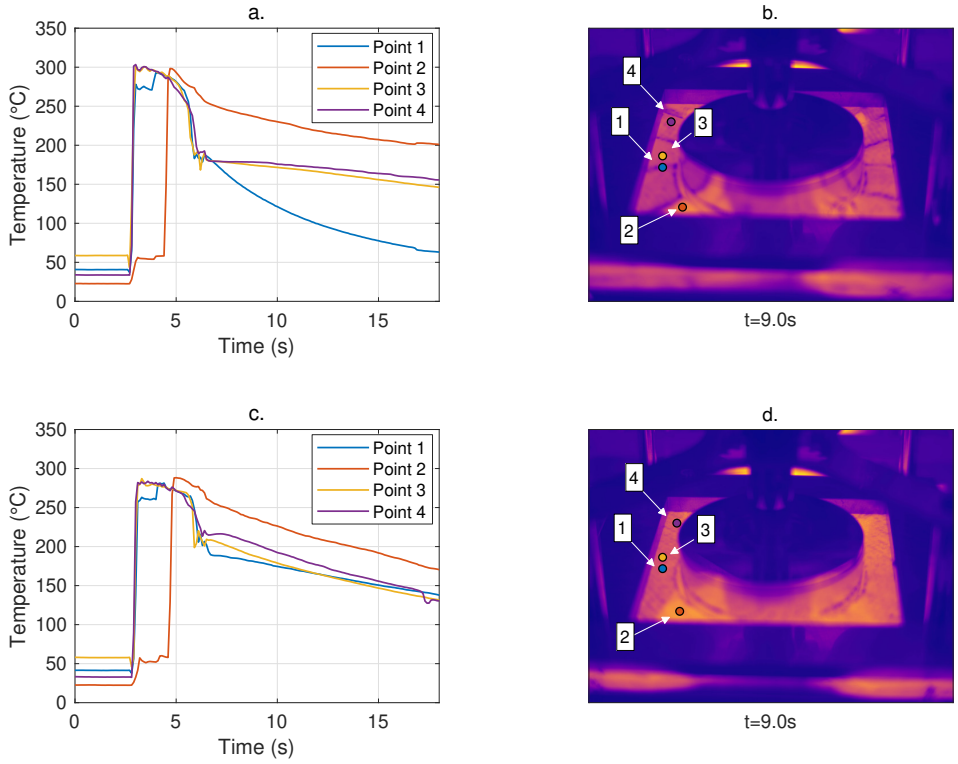

Figure 6.14 – Temperature evolution during forming, a./c.: preconsolidated and unconsolidated blank respectively, b./d.: corresponding position of observation points

The sharp temperature increase observed at t=3.2 s corresponds to the transfer of the blank from the oven to the press. The blank is initially hidden by the blankholder in its open position on points 1 and 2; the discontinuities at 3.8 s for point 1 and 4.5 s for point 2 correspond approximatively to the start and end of the blankholder closing. Points 1, 3 and 4 are in a zone in which significant fabric draw-in is observed; this is not the case for point 2 which is along the diagonal of the blank. A significant drop in temperature is observed as the fabric initially under the blankholder is drawn in, i.e. faster cooling occurs under the blankholder as the material is cooled by conduction on both sides. Temperatures as low as 190 °C are observed at the end of the forming on points 1, 3 and 4. While this is lower than the crystallization temperature of 227 °C presented in section 3.4.1.1 (see Fig. 3.9), the cooling rate during processing appears orders of magnitude higher than that of the measurement (in the range of 10–100 °C s^{-1}, compared to 10 °C min^{-1} $\approx$ 0.17 °C s^{-1}). Consequently, a lower crystallization temperature is expected; Flash DSC results on the non-isothermal crystallization kinetics of neat PA66 presented in [Rhoades+2015] show T_c between 205–175 °C for cooling ranges between 10–100 °C s^{-1}.

The part of the wrinkles that remains in contact with the mould (point 1 in Fig. 6.14a.) also cools faster than the part that looses contact with the tool. This temperature data will be used to validate the approach proposed to model the non-isothermal forming.

6.4 Finite element simulation of the forming of thermoplastic composites

The mechanical model presented in chapter 5 is implemented in Abaqus/Explicit through a VUMAT user material subroutine. The non-orthogonal approach is validated with unit tests on a single element in tension and shear; results are unaffected by rigid body movements, which shows that the derivative used based on the material rotation is indeed objective [Badel+2008b].

6.4.1 Validation of the model implementation: virtual bias extension tests

The bias extension tests conducted for the characterization of the shear behaviour of the PA66/glass are reproduced in Abaqus to validate the constitutive law used.

6.4.1.1 Mesh and element type selection

Two different meshes based on quadrilateral elements have been investigated: one in which the principal directions of the elements are aligned with that of the rectangular bias extension sample (0/90°), and another in which the principal directions are aligned with the initial yarn directions (±45°). The meshes, and corresponding simulated shear angle fields after 30 mm extension are presented in Fig. 6.15 for membrane elements with full and reduced integration.

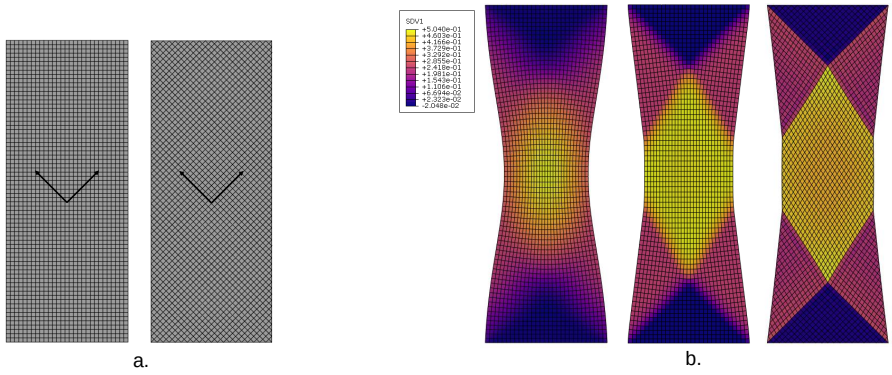

Figure 6.15 – a. Mesh aligned with sample principal directions (left) and yarn directions (right), b. Resulting shear angle field after 30 mm extension (l. to r.: M3D4 and M3D4R aligned with sample, M3D4R aligned with yarns)

While the different sheared zones expected in the bias extension test are visible in both cases, simulations conducted with the mesh aligned with the rectangular sample directions cannot reproduce the discontinuity in the shear field predicted by the theory: a smooth transition region is visible between the different sheared zones. This is accompanied with a large increase in the simulated axial force (Fig. 6.16), and while reduced integration elements perform better (especially as the mesh density is increased), a significant error is still observed.

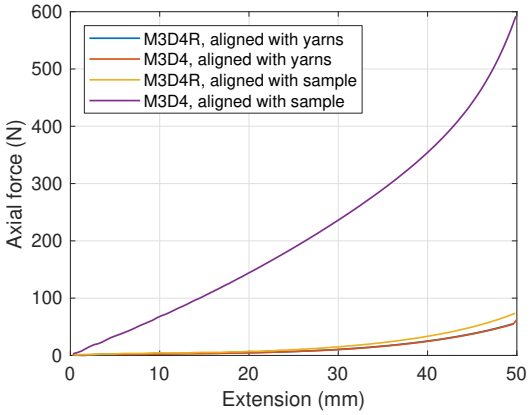

Figure 6.16 – Simulated axial force during bias extension for different mesh and element types

This behaviour is due to spurious extensions in the elements at the interface between the zones (leading in turn to spurious forces as the tensile modulus is much larger than the shear modulus), and described as tension or in-plane shear locking in the literature [Hamila+2013; ten Thije+2008a; Yu+2006]. Aligning the mesh with the yarn directions is sufficient to prevent locking of the elements (regardless of the number of Gauss points).

The use of membrane elements (M3D4R) instead of shells (S4R) is motivated both by the increase in computation speed (as only one Gauss point is evaluated per element, in contrast with a minimum of two in reduced integration shells), and because standard shell elements present a bending behaviour that is too stiff for fabric forming [Hamila+2013; Machado+2016a; Stolarski+1982] as the membrane and bending behaviours are coupled. This would require the development of a custom element [Döbrich+2013; Hamila+2009], as the subroutine allowing for the redefinition of a general shell behaviour in Abaqus/Standard (UGENS) is not available for explicit analyses.

6.4.1.2 Comparison with experimental results

The isothermal experimental tests conducted in chapter 5 have been replicated in Abaqus. The blanks are meshed with M3D4R elements of approximate size 7×7 mm, aligned with the initial yarn directions. The bottom nodes are clamped, and a displacement of 100 mm with constant speed depending of the test is imposed on the top nodes of the sample. The reaction force, and average shear angle in the central region are extracted using a Python script.

Results are presented in Fig. 6.17a and 6.17b, and show a good agreement with the experimental tests. As the material is considered as an homogenized continuum in the simulation, inter-yarn sliding (which is a mesoscale behaviour) cannot be represented, hence the discrepancy between the simulated and measured axial forces at high extension. A softer response is also predicted at low extension/shear angle. The effects of shear rate and temperature are correctly reproduced in all cases tested (a single simulation was run at a test speed of 10 mm min^{-1} because of the extremely high computational time – over 75 h – associated with simulating 10 min of test with an explicit analysis).

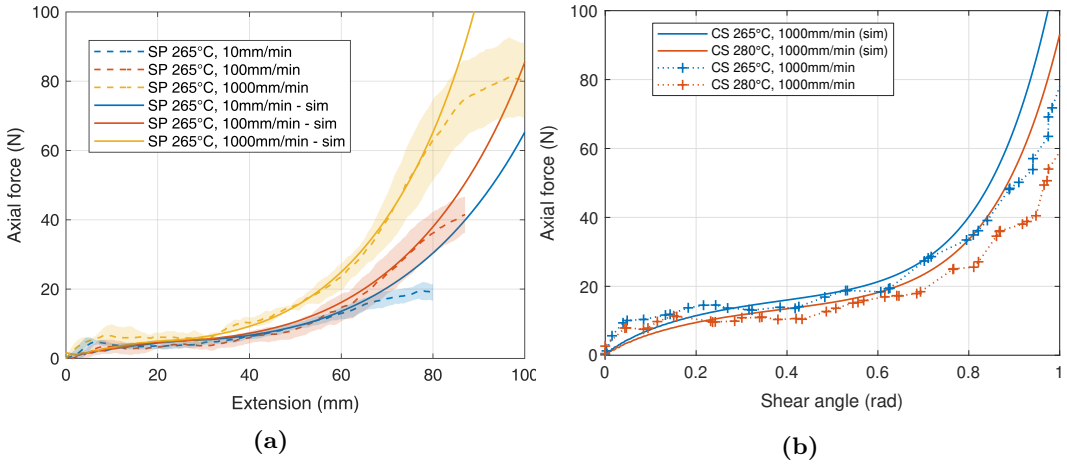

Figure 6.17 – Comparison between experimental and simulated axial force: (a) tests on semipreg sample at 265 °C, (b) tests on consolidated sample at 1000 mm min^{-1}

6.4.2 Finite element model of the forming setup

The finite element model of the experimental forming setup presented in section 6.2.1 is shown in Fig. 6.18.

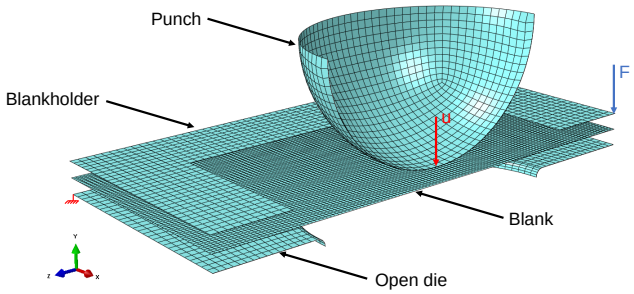

Figure 6.18 – Cut view of the finite element forming model (initial gap between tools is exaggerated)

Given the difference in stiffness between the blank and the stainless steel of the tools, the tooling elements (punch, blankholder and open die) are modelled using 4-nodes rigid elements R3D4 (no deformations are considered) with approximate dimensions of 5×5 mm (refined

in the fillet of the open die). Membrane elements with reduced integration (M3D4R) of approximate dimensions 2.5×2.5 mm are used to model the blank.

The die block is fully constrained. A force of 200 N is applied on the blankholder, with all degrees of freedom constrained except translation in the direction of the force. The vertical displacement of the punch is imposed. A penalty based general contact algorithm is used. The tool/ply friction behaviour of thermoplastic composites has been extensively studied in the literature [Gorczyca+2004; Lebrun+2004; Murtagh+1995; ten Thije+2008b; ten Thije+2011; Vanclooster2010]: the molten matrix is shown to act as a lubricating film between the fibres and the metal tool. As a first approximation, Coulomb friction is considered (i.e., hydrodynamic effects are neglected), as used in [Machado+2016b; Sjölander+2016; Vanclooster2010]: this hypothesis will lead to an underestimation of frictional forces in the model. A friction coefficient of 0.2 is used, based on experimental measurements on unfilled PA66 and PA66/glass composites reported in [Chen+2003]. A sensitivity analysis would allow evaluating the influence of the friction coefficient in the proposed simulation, and help with the selection of a more sophisticated friction model. The simulations are ran on a computer with a 3.5 GHz quad-core Intel Xeon e5 CPU, leading to an approximate runtime of 8 h without mass scaling.

6.4.3 Isothermal forming

Initial simulations are conducted assuming isothermal conditions, i.e. $\partial T/\partial t = 0$. Uniform temperature fields at $T = 265\,°C$ and $T = 300\,°C$, as well as non-uniform temperature fields resulting from the Comsol simulations for lamp configurations LCa and LCopt and mapped on the blank are investigated.

6.4.3.1 Uniform temperature field

The shear angle field resulting from the forming operation is presented in Fig. 6.19 for simulations with (a) zero shear stiffness, (b) $T = 300\,°C$ with a 0° blank and (c) $T = 300\,°C$ with a 45° blank. Maximum shear angle values of 51.2°, 41.2° and 40.3° are observed for simulations on preconsolidated blanks. In all cases, high shear zones are predicted at the base of the hemisphere along the diagonals of the blank.

Wrinkles propagating radially from the high shear zones, not present at zero shear modulus, are observed at both temperatures simulated. In contrast with the experimental parts formed, the wrinkles are limited to the zone bounded by the inner faces of the blankholder. This is due to the bending stiffness being neglected: the wrinkles cannot bear a compressive load and thus cannot propagate under the blankholder.

The reaction force on the punch resulting from shearing of the fabric is presented in Fig. 6.20. The force increases slowly up to an approximate drawing depth of 50 mm; larger forces are observed then, as the shear modulus is increased with higher shear angles. The effect of temperature is clearly visible for simulations using model parameters identified for the

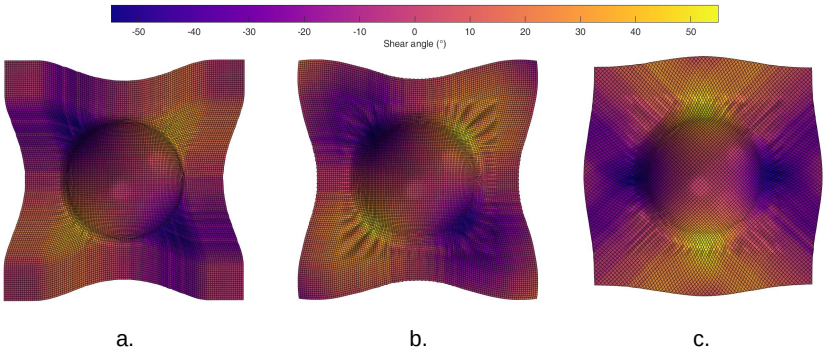

Figure 6.19 – Shear angle field, a. In-plane shear neglected ($G_{12} = 0$), b. $T = 300\,°\mathrm{C}/0°$, c. $T = 300\,°\mathrm{C}/45°$

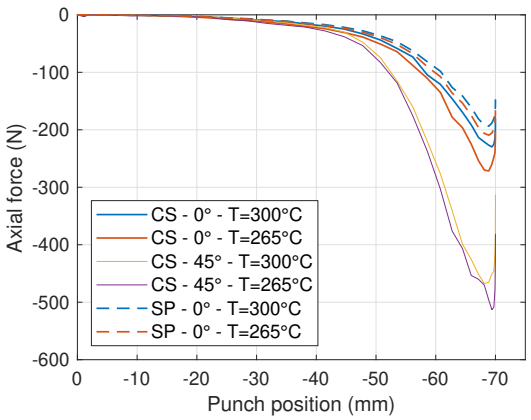

Figure 6.20 – Axial force vs. punch displacement for uniform temperature simulation

preconsolidated material, with larger forces at a lower temperature. The difference is less marked for simulations on semipreg blanks.

The simulations with blanks oriented at ±45° predict reaction forces larger than those for blanks at 0/90° by a factor of 2. This is attributed to the fact that wrinkles originating from high shear zones along the x and y axes propagate on shorter distances compared to those generated in a blank at 0/90°, as the edge of the blankholder is closer to the hemisphere along that direction. The imposed displacement is thus accommodated by further in-plane shear rather than out-of-plane wrinkling.

6.4.3.2 Non-uniform temperature field

Simulations with non-uniform temperature fields have been conducted by mapping the temperature resulting from Comsol simulations as presented in chapter 4 on the mesh of the blank, using a state dependent variable. The shear angle field resulting of simulations with a blank of preconsolidated material is presented in Fig. 6.21 for configurations LCa and LCopt.

Maximum shear angle values of 40.2° and 41.1° are observed respectively for configurations LCa and LCopt. The simulated blanks present an asymmetric deformation coherent with that observed experimentally (although of a much lower magnitude), with deformed corner-to-corner distances of 321 mm and 315 mm in the x and y directions respectively for configuration LCa, and 320 mm and 318 mm in configuration LCopt. A slight difference in the number of wrinkles generated is visible in the zones of high shear: the wrinkles are isolated at various punch depths in Fig. 6.22, using a displacement based criteria. Configuration LCa leads to a higher number of thinner wrinkles compared to configuration LCopt.

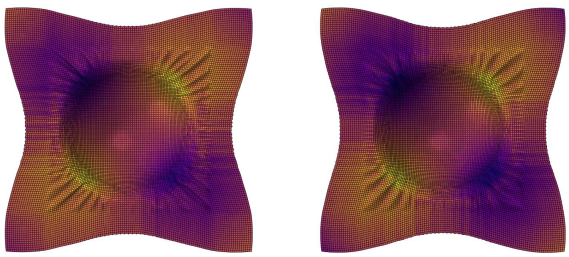

Figure 6.21 – Shear angle map of simulations with non-uniform temperature field. a.: configuration LCa, b.: configuration LCopt

The axial force is plotted as a function of the punch displacement in Fig. 6.23. Both simulations using non-uniform temperature fields predict a lower peak force than the isothermal simulation at $T = 300\,°C$; this result is not surprising as both configurations lead to temperatures higher than 300 °C in the central zone which is under high shear.

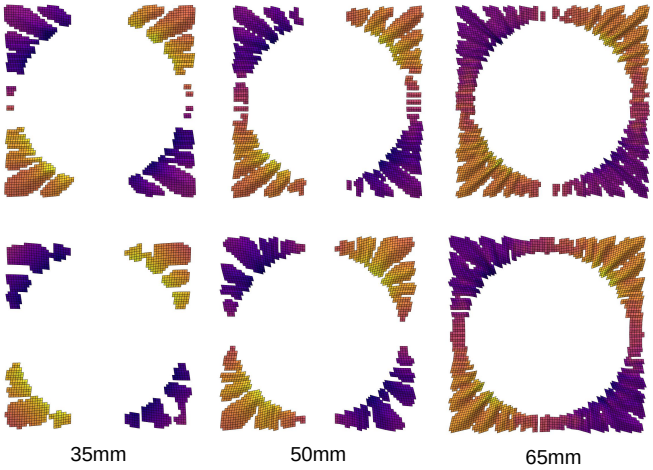

Figure 6.22 – Isolated wrinkles at different punch depths, top: configuration LCa, bottom: configuration LCopt, preconsolidated blank oriented at 0/90°

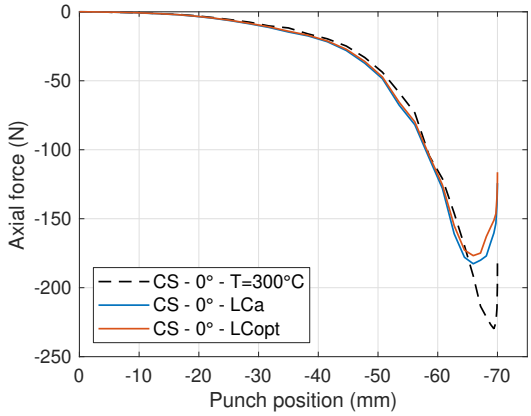

Figure 6.23 – Axial force vs. punch displacement for simulations using configurations LCa and LCopt

6.4.4 Non-isothermal forming

The membrane elements used for the blank do not have a temperature degree of freedom, and a direct coupled thermomechanical analysis procedure cannot be used. Sequential temperature-displacement analysis (in which the stress field and temperature field are updated alternately), as proposed by Guzman-Maldonado et al. [GuzmanMaldonado+2016; GuzmanMaldonado2016], is not directly applicable in Abaqus/Explicit.

Cao et al. and Lee et al. [Cao+2003; Lee+2009] proposed the use of a contact-based criteria to switch between 'high temperature' and 'low temperature' material properties by comparing the distance between integration points in the blank and in the tool to a preset threshold value. This method can lead to numerical instabilities, from the sharp change in modulus imposed by the switch, and is time-independent. A simple approach to take into account and model the temperature evolution in the blank, with low computational cost compared to a coupled mechanical/heat transfer analysis, is proposed here.

A dummy state variable representing the element temperature is initialized based on the results of the Comsol simulation. The elements are considered as independent material points, with a volumetric heat sink of value constant by zone. The heat equation at a material point k defined by its position $\mathbf{x}_k(t)$ is simplified to equation 6.4.1.

$$\rho C_p \frac{\partial T_k}{\partial t} = q_{\text{sink}}(\mathbf{x}_k(t)) \tag{6.4.1}$$

This leads to an evolution of temperature linear by zones. The temperature at the material point can then be expressed incrementally as per equation 6.4.2.

$$T_k^{n+1} = T_k^n + \frac{\partial T}{\partial t}(\mathbf{x}_k)dt \tag{6.4.2}$$

The average cooling rates are identified based on the experimental measurements presented in Fig. 6.14:

$$\frac{\partial T_k}{\partial t} = \begin{cases} -80\,\mathrm{K\,s^{-1}} & \text{for } \mathbf{x}_k \text{ in contact with blankholder} \\ -15\,\mathrm{K\,s^{-1}} & \text{for } \mathbf{x}_k \text{ in contact with punch} \\ -8\,\mathrm{K\,s^{-1}} & \text{for } \mathbf{x}_k \text{ in contact with die block} \\ -4\,\mathrm{K\,s^{-1}} & \text{elsewhere} \end{cases} \tag{6.4.3}$$

The current cooling rate is evaluated in the VUMAT from a distance check based on parametrization of the different surfaces in contact. A modification of the implementation to include a contact pressure-dependent conductance would lead to a much more physical solution, especially in the zones of loss of contact with the tool (wrinkles); this improvement remains as future work. The evolution of temperature during forming of a preconsolidated blank is shown in Fig. 6.24. The simple approach presented is able to reproduce the temperature evolution observed experimentally, with higher cooling rates under the blankholder leading to a significant temperature drop as the material is drawn by the punch.

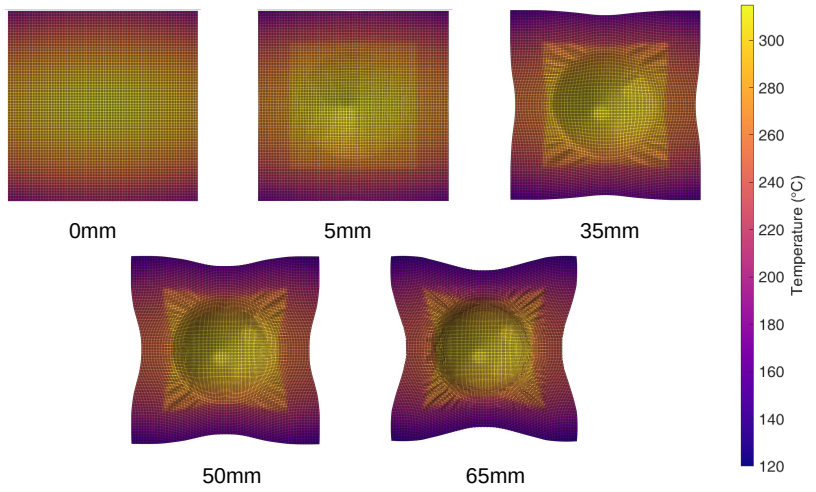

Figure 6.24 – Temperature evolution during forming as predicted by the simulation, preconsolidated blank

The temperature evolution of a profile passing through the center of the blank and aligned along x is presented in Fig. 6.25a. The cooling of the blank from contact with the punch in a progressively larger zone in the center, and from contact with the blankholder in a progressively smaller zones is shown. Additional comparison with experimental measurements on Euler points is presented in Fig. 6.25b; the simulation shows a correct agreement with the experiments in terms of temperature evolution, although a delay is observed; this can be explained either by a slightly different kinematic of the fabric, or by experimental errors associated with difficulties in determining the exact time of initial contact between the punch and the blank.

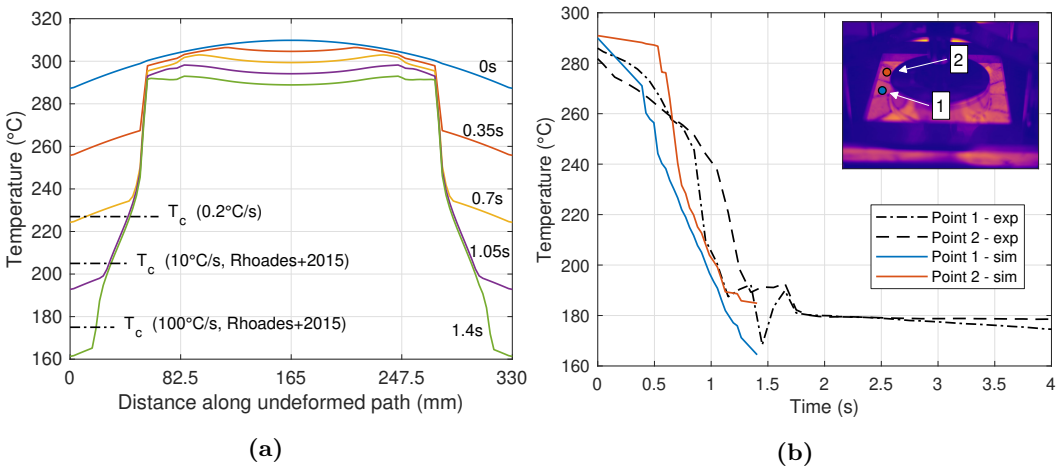

Figure 6.25 – Simulated temperature evolution during forming. a. Temperature along a path through the center of the blank at different times, b. Comparison between experimental and simulated temperature in a point between the punch and the blankholder

The shear angle field for configuration LCa is presented in Fig. 6.26 for both isothermal and non-isothermal analysis. Significant hourglassing is observed in the non-isothermal analysis at large punch depths (towards the end of the simulation). Comparison at lower punch depths show lower shear angle values in the non-isothermal simulations (38.1° vs. 39.7°). The same trend is observed for simulations with the optimized lamp configuration.

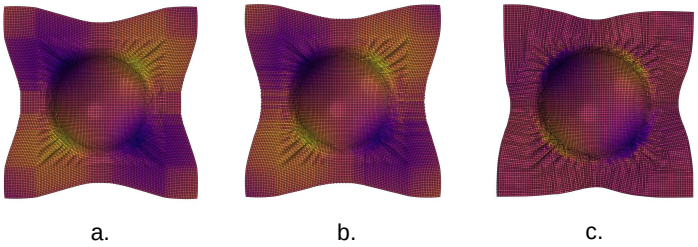

Figure 6.26 – Deformed blanks with configuration LCa, a. Isothermal simulation, punch depth 65 mm, b. Non-isothermal simulation, punch depth 65 mm, c. Non-isothermal simulation, punch depth 70 mm

The axial force as a function of punch displacement is presented in Fig. 6.27 for both configurations. Numerical instabilities resulting from the propagation of hourglass modes are clearly visible after 65 mm.

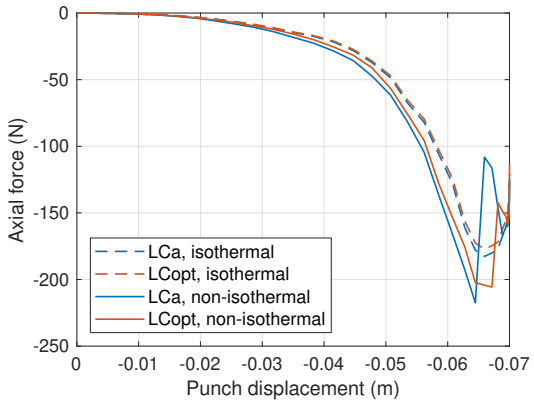

Figure 6.27 – Predicted axial force for isothermal and non-isothermal simulations

The force simulated is higher than that for isothermal simulations, which is expected as the decreasing temperature leads to an increased shear modulus. The forces are however much lower than those measured experimentally (Fig. 6.28): peak forces on simulations with preconsolidated blanks are approximately 5 times lower than the experiments, while peak forces predicted for semipreg blanks are half that measured experimentally.

Various factors, associated with the main limitations of the numerical approach presented in this work, can help explain the differences observed:

- The in-plane shear behaviour was identified in a narrow temperature range compared to the variations observed experimentally, and notably, the characterization was conducted

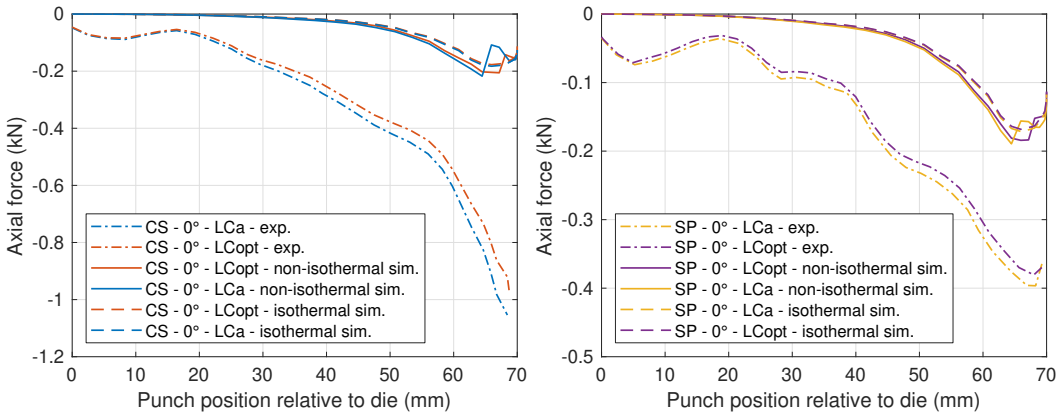

(a) **(b)**

Figure 6.28 – Comparison between experimental axial force and prediction from isothermal and non-isothermal simulations. a. preconsolidated, b. semipreg

at temperatures much larger than the crystallization temperature; additional tests would be required to ensure the validity of the exponential temperature dependence used in the expression of the shear modulus, closer to the crystallization point. Replicating the thermal history and the cooling rates observed during processing in a reproducible manner at the scale of the samples used for bias extension tests might however prove complex.

- Bending stiffness is not considered in the simulations, while its contribution to the axial force is probably not negligible (although studies including bending stiffness in forming simulations report mostly qualitative results on the shape of wrinkles generated, rather than force data [Boisse+2018; Liang+2014; Mathieu+2015]).

- A constant friction coefficient has been considered, while the real behaviour is hydrodynamic and temperature dependent [Gorczyca+2004; Vanclooster2010]: the Coulomb friction approximation underestimates the shear forces generated.

The forming model developed is further used to investigate numerically the interest of local preheating for forming double-curvature parts.

6.4.5 Localized heating of double-curvature parts: preliminary study

A uniform temperature in the blank prior to forming is considered as the ideal case in the vast majority of thermoforming applications [Offringa1996; Throne2008]. This assumption is rarely discussed in the literature; heating the entirety of the blank to a specified forming temperature is energy intensive. Depending on the geometry of the part to be formed, the deformation of certain zones can be negligible: in this case, the interest of uniformly

heating the part appears limited, especially considering that the preheating step can affect considerably the void content [Slange+2016]. Local preheating of blanks prior to forming has been studied by Hwang and Hwang [Hwang+2002] for the manufacturing of single curvature brackets. Results show that mechanical properties equivalent to that of a uniformly heated part can be obtained, with a large reduction in energy consumption. No equivalent studies have been found regarding the forming of locally heated double-curvature parts (which might be due in part to the difficulties associated with designing a suitable oven for complex shapes, although tailor-made, curved tungsten-halogen heaters are commercially available [Ceramicx2015]).

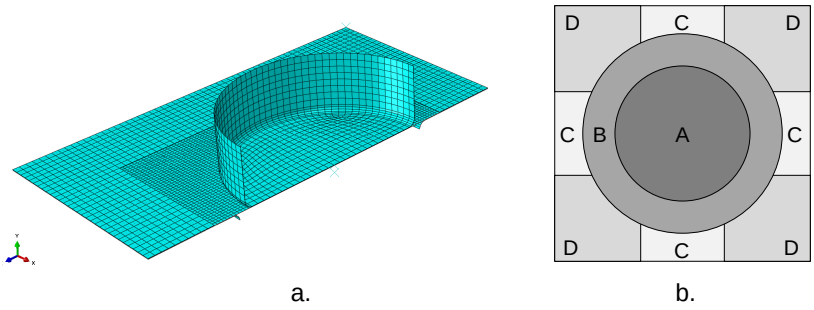

Figure 6.29 – a. Cut view of the cylindrical punch setup, b. partitioning of the blank in zones of constant temperature

A sensitivity study is proposed to evaluate the influence of a highly non-uniform temperature field on forming, based on the simulation tool introduced in section 6.4.2. The finite element model is modified to include a cylindrical punch instead of the hemispherical one used previously (Fig. 6.29a.). This geometry is adopted as the resulting 'top-hat' shape presents a zone under neither shear nor bending [GuzmanMaldonado2016]. The blank is partitioned in four zones (A to D, Fig. 6.29b.) based on the expected location of zones of high shear.

Simulations are conducted using a one-factor-at-a-time (OFAT) approach: the temperature of each zone is varied independently between 300 °C (reference temperature) and 265 °C, for maximal punch displacement of 20 mm. Isothermal simulations are run for efficiency. The resulting shear angle maps are plotted in Fig. 6.30. Maximal shear angles of 32.8°, 32.6°, 30.1°, 32.5° and 32.1° are obtained for the reference simulation and simulations with zone A-D at 265 °C respectively. The localization of the shear zones is not affected by the imposed temperature field, although simulation with zone B at 265 °C leads to a significantly reduced shear angles as well as more marked wrinkles.

Results in terms of axial force, and deviation from the reference configuration, are presented in Fig. 6.31. Configuration with zone B at 265 °C leads to the maximal measured force at approximately 125% of the reference. Configurations with lower temperatures in zones A, C and D lead to forces within 5% of the reference value.

These results indicate that the temperature in zone B has a much higher influence on the shear state of the final part, and reducing the temperature in zones A, C and D has little to

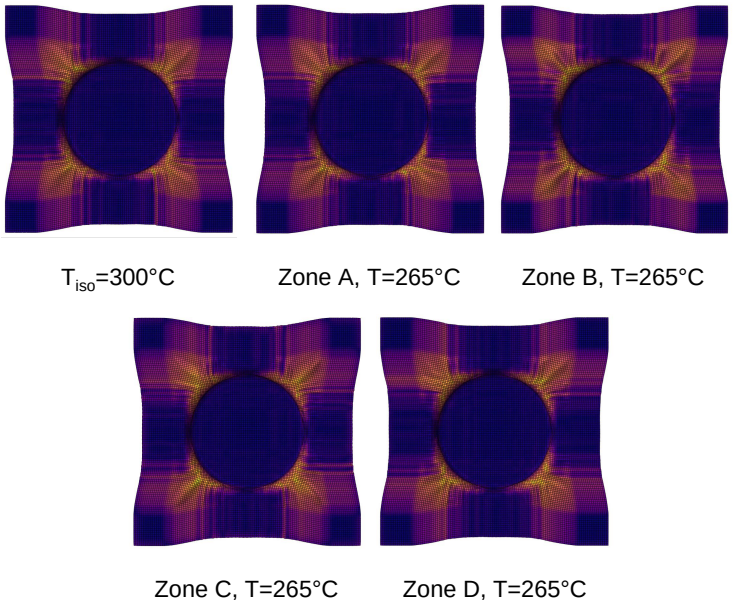

Figure 6.30 – Shear angle map on cylindrical simulations

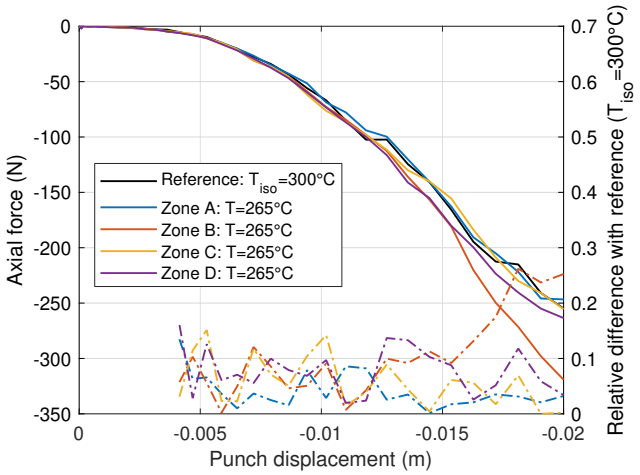

Figure 6.31 – Axial force as a function of punch displacement for different temperature configurations

no effect on the shear angles. This is somewhat expected, considering that zone B includes the regions of the part under high shear. This suggests that a non-uniform temperature distribution is not always detrimental, especially when flat surfaces are considered, and that local heating might prove interesting provided a shear angle distribution can be known a priori.

6.5 Conclusion

The use of a non-orthogonal, hypoelastic model to simulate the forming of thermoplastic composites has been presented in this final chapter. Experimental forming tests have been conducted, using an hemispherical punch design. The influence of the temperature field on wrinkles generated in the parts has been shown experimentally to be non-negligible in preconsolidated blanks, while semipreg blanks are less affected by temperature variations. Quantitative data, in terms of axial force on the punch and shear angle, has been measured on the samples.

The mechanical model has been implemented in finite element software Abaqus through a user subroutine, and validated against the experimental bias extension tests presented in chapter 5. Isothermal forming simulations with uniform and non-uniform temperature fields have been conducted, and the effect of temperature as observed in the experiments has been replicated qualitatively.

A simple approach to consider non-isothermal forming by defining constant cooling rates by zones has been implemented. While the model allows for a correct prediction of the macroscopic defects generated, the limited temperature range in which the in-plane shear behaviour has been characterized appears as one of the main limitations that prevents a good, quantitative agreement with the experimental data.

Finally, the model has been used in a preliminary study to discuss the potential interest of localized preheating for the forming of double-curvature parts. The results suggest that in the case of parts containing flat surfaces with low shear, local heating could be a way to reduce the energy consumption of the process without affecting significantly the shear state. Further developments on this hypothesis remain as future work.

General conclusion and perspectives

Thermoforming of thermoplastic composites is a process well adapted to the production rates required by the automotive industry, with achievable cycle times <1 min. The organosheet blanks used remain however too expensive for high volume production, and limit the possibility of large scale trial-and-error process optimization methods. Consequently, the work presented in this thesis has focused on proposing simulation tools for the numerical optimization of the non-isothermal forming of double curvature woven thermoplastic composite parts, more specifically aiming at understanding the influence of the temperature uniformity in the blank on forming induced defects. In addition, preliminary work has been conducted to evaluate the feasibility of thermoforming parts from non-consolidated blanks, using a PA66/glass powder-impregnated fabric developed by Solvay.

The first part of the study has been dedicated to simulating the preheating step of the thermoforming process, in which the blank is brought to processing temperature in an infrared oven. The interaction between the radiation emitted by the halogen lamps and the powder-impregnated fabric (as a semipreg and following a preconsolidation step) has been characterized experimentally using FTIR. The plies are shown to be opaque to infrared wavelengths, regardless of the consolidation level. The presence of reflecting dry glass fibers on the surface of the semipreg lowers the absorptivity in the near-IR region, which corresponds to the wavelength band of maximum emission for the halogen lamps at 2400 K: 86% of the radiation will be absorbed at the surface, compared to 93% for a preconsolidated blank.

Two approaches have been compared for the determination of the temperature-dependent thermal conductivity tensor of the homogenized orthotropic material. The first one is based on a two-scale homogenization procedure: the thermal conductivity of the constituents has first been obtained from experiments below the melting temperature of the matrix, and from literature data. The yarn conductivity and the macroscale conductivity have then been derived from the Maxwell theory and numerical homogenization respectively, using an approximated fabric architecture based on tomography measurements. A condensed

expression, separating the effect of the temperature dependent matrix conductivity and the mesoscale architecture has been proposed. The second approach is based on inverse analysis, using a non-contact infrared thermography experimental setup. The macroscale thermal conductivity is identified from the transient response of a sample subject to radiative heating on one side, by solving a minimization problem on a finite element model developed in Comsol. The two methods present similar results in terms of temperature dependence; while the homogenization method requires significant work for the characterization of the properties of the constituent and the architecture of the macroscale material compared to the simple experiment in the non-contact approach, the inverse analysis consists in solving an ill-posed problem: the thermal conductivity computed is highly sensitive to measurement errors.

The thermal contact conductance between plies of non-consolidated semipreg has been characterized as a function of pressure. Both the conductance and out-of-plane thermal conductivity increases with pressure, through nesting and increase of the contact point at the interfaces. A finite element model, based on the radiosity method to compute the radiative heat transfer between the halogen lamps (modelled as cylindrical sources) and the blank, has been developed in Comsol Multiphysics® using the properties characterized; the predicted temperature evolution has been validated against experimental results using a lab-scale infrared oven developed in this study, allowing to adjust both the lamp position and temperature. The simulation shows a good quantitative agreement with the experiments in the majority of the test cases considered, but tends to overestimate temperature gradients on the surface of the blank, which could partly be explained by the hypothesis used of perfectly Lambertian surfaces. A numerical sensitivity study on the influence of blank sag has been conducted, showing a significant effect on the temperature distribution with an increase of surface gradients as the curvature of the blank increases. Finally, a procedure to optimize the oven parameters based on a required temperature field has been proposed, using a Monte-Carlo algorithm to explore the research space followed by a refinement of the optima with the simplex method.

The second part of this work has focused on modeling the temperature dependent mechanical behaviour of the woven thermoplastic composite during forming. As shown from the literature review, a large number of models have been proposed to simulate the draping of dry fabrics, although only a few attempt at taking into account temperature effects. A hypoelastic, non-orthogonal approach has been selected based on its ease of implementation in commercial finite element codes. A frame fixed with the yarns is defined and updated using the deformation gradient tensor; this allows for a straightforward expression of the constitutive tensor. The tensile behaviour of the fabric has been characterized from uniaxial tests, and the non-linearity induced by decrimping of the yarn taken into account in a phenomenological expression. In-plane shear, which is the main mode of deformation during forming on double curvature surfaces, has been characterized from bias-extension tests between 265 °C and 280 °C at different shear rates. Both semipreg and preconsolidated fabric present a similar shear behaviour: a first phase in which the yarn are free to rotate around their crossover points, followed by a marked increase of the shear stress as the yarns gradually come in

contact. The semipreg fabric showed a lower sensitivity to both temperature and shear rate compared to the preconsolidated material, which is attributed to the non-uniform repartition of PA66 droplets at the surfaces of the fabric. As the matrix is only present on the surface, intra-ply sliding at high shear angles can also leads locally to an increase of flow distance required for the impregnation of the yarns. The shear modulus has been modelled using a multiplicative decoupling of the effects of temperature and shear rate.

Parts have been formed experimentally using an hemispherical punch and blankholder system, coupled with the infrared oven. Significant asymmetric wrinkling is observed on parts formed from preconsolidated blanks with a highly non-uniform temperature field at the end of the preheating stage; the use of a more uniform temperature leads to reduced wrinkling and a symmetrical shape. In the case of parts formed from non-consolidated fabric, a much lower amount of wrinkling is observed regardless of the temperature field, which is expected from the in-plane shear tests results. A post-processing procedure based on grid strain analysis has been developed to measure shear angle fields on the parts using DIC software Vic-3D, based on a regular grid of circular markers superimposed with a random speckle pattern. A slight increase in maximum shear angle is observed for non-consolidated fabric, and for the more homogeneous temperature field considered. These conditions also lead to a lower axial reaction force measured on the punch.

The temperature dependent material behaviour has been implemented in Abaqus/Explicit using a user material subroutine, and validated through simulation of bias-extension tests. Non-isothermal forming simulations have been conducted, with the blank modelled using membrane elements. The non-uniform temperature field resulting from the preheating simulation has been used as an input, and a simplified approach to consider the temperature evolution due to cooling from contact with the tools has been proposed, assuming a constant cooling rate by zones based on infrared thermography measurements during forming. The regions of high shear are well predicted by the simulation, although both the magnitude of wrinkles and the axial force on the punch are underestimated, which is attributed to the relatively small temperature range on which the in-plane shear behaviour has been identified, and the fact that bending stiffness is neglected. Finally, the use of localized heating for forming parts with double curvatures containing flat surfaces has been investigated numerically: results suggest that reducing the temperature of low shear regions does not significantly affect the resulting shear angle field or axial force required to form the part, while allowing for energy savings.

The simulation tools proposed to model the non-isothermal forming of powder-impregnated thermoplastic composites have shown a good potential for use as part of a process optimization strategy. Various limitations to the approach presented remains, that would need to be addressed in future work.

The non-contact conductivity measurement method presented in Chapter 3 appears as a fast way of evaluating the thermal conductivity tensor of an orthotropic material, however the influence of convective heat transfer on the results computed is significant at the measurement temperatures. A better control of the samples environment would be needed to make it a

robust alternative to contact-based measurement methods, and work has been started in that direction in ICA.

The reflectivity of the materials that make up the oven has been considered as perfectly Lambertian, which is a strong hypothesis especially in the case of the metallic oven panels. Considering a mixed diffuse-specular behaviour could improve the quality of the radiosity prediction at the surface of the blank, although at the expense of computational time since a sufficient number of rays would need to be generated.

Given the influence of blank sag on temperature distribution observed numerically, the inclusion of coupled thermomechanical effects in the analysis, to consider both the progressive deformation of the blank and its effect on incident radiosity, appears as an interesting step to improve the precision of the preheating simulation; another possibility would be the experimental control of the sag via increased membrane tensions triggered for instance with proximity sensors.

The range of temperature in which the in-plane shear behaviour of the material has been characterized is small compared to the temperatures observed during forming, as regions of the blank under the blankholder appear to reach temperatures around the crystallization point of the matrix. A significant change in mechanical behaviour is expected as the matrix crystallizes, which is not reproduced with the current model; additional characterization tests at lower temperature would be valuable to improve the understanding of the shear behaviour and wrinkle formations in non-isothermal forming.

The use of a sequentially coupled thermal/stress analysis would be of great interest to propose a more physical evolution of the temperature in the blank due to contact with the tools during forming; as this analysis procedure is available uniquely in the Abaqus/Standard package, converting the material model implementation from a VUMAT to a UMAT would be required, and stability issues inherent to the implicit formulation would need to be addressed.

Taking into account the bending behaviour of the material will improve the precision of the simulation of wrinkles formation. The membrane elements used in this study have a zero bending stiffness; the use of a classical shell element, in which bending is coupled with the membrane behaviour, is also not adapted to representing the bending of woven fabrics. The implementation of a custom element in which bending and membrane stiffnesses are decoupled would be needed. A test rig based on a cantilever design to evaluate the bending modulus of the materials as a function of temperature has been developed towards the end of this thesis, although only preliminary tests have been conducted so far.

The work presented has focused only on the infrared heating and forming steps in an open mould, and consolidation has not been considered. The prediction of void content or the presence of delaminated zones in the final part is a crucial information given its influence on mechanical properties. This is especially the case when forming parts from non-consolidated semipreg blanks: while it has been shown that parts could be formed, the feasibility of forming and impregnating the yarns in a single step still has to be evaluated.

Finally, the complete simulation process presented requires significant user input for the transfer and processing of the results between the infrared preheating and forming components, and simplification would be required for use in an industrial environment. Currently, different programming languages are used to run and process the heating simulation (Comsol with Matlab) and the forming simulation (Abaqus with Python). Unifying the control scripts would ensure a more user-friendly experience; Python would be the preferred choice, as it is non-proprietary, and accessing the Comsol API using Python is easier than interfacing Abaqus with Matlab.

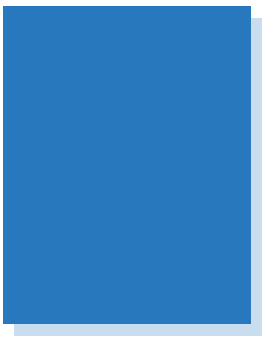

Appendices

Appendix

A

Characterization of the micro and mesoscopic architecture by image analysis

A.1 Fibre volume fraction in the yarns

A.1.1 Sample preparation and observation

Samples for cross-section observation have been cut from two plates of 4 plies of PA66/glass fabric (thermocompressed as per section 3.4.1.2) with a precision saw, before being cold mounted using a low viscosity acrylic resin. Grinding and polishing was conducted on a Buehler AutoMet™ 250, down to a 1 µm grit with a diamond suspension.

A Keyence numerical microscope was used to observe the cross-section of the samples; polarized light was used to ensure a good contrast between the fibres and the matrix. A magnification of ×1000 was sufficient to observe the distribution of fibres in a yarn, with an average fibre diameter measured at 17 µm. Images corresponding to a region of interest of approximate dimensions 400×200 µm were extracted manually from randomly selected yarns for further processing (Fig. A.1).

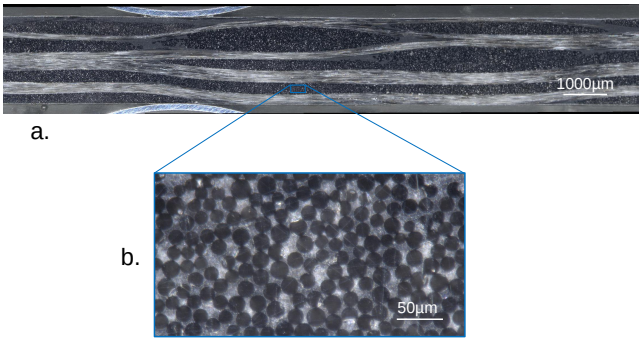

Figure A.1 – Cross-section micrograph of the composite sample. Magnification: x150 (a.), x1000 (b.)

A.1.2 Image analysis

The image analysis was conducted in MATLAB. The micrographs obtained were binarized to separate the 'dark' and 'light' pixels corresponding to the fibre and matrix phase respectively, using an adaptive thresholding algorithm based on local background illumination proposed in [Bradley+2007], implemented in function *adaptthresh*.

Minor artefacts in the resulting black and white images are attributed to polishing lines. This can result in white pixels in regions associated with the fibres, and lead to an artificial reduction of the measured fibre volume fraction. Area opening was applied to the binarized images to mitigate the effect of these artefacts A.2. The quality of the opening was controlled visually. This operation can lead to an *over*estimation of the fibre volume fraction.

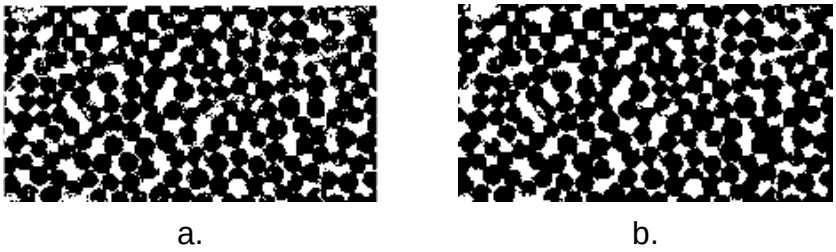

Figure A.2 – a.: binarization, and b.: area opening of the region of interest

The resulting fibre volume fraction, measured on 25 samples, are presented in Fig. A.3. As expected, the area opening operation increases the measured fibre volume fraction; the difference remains however minimal in most cases. The fibre fraction varies between 0.598 and 0.705. The average value is considered as the mean of the measurements with and without area opening, i.e. to a value of $v_f = 0.668 \pm 0.015$.

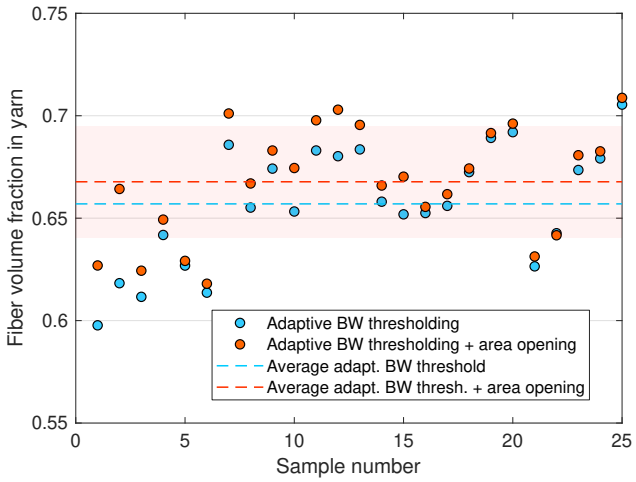

Figure A.3 – Fibre volume fraction per sample

A.2 Fabric architecture from micro-computed tomography

Samples of approximate dimensions $25 \times 25\,\text{mm}$ have been cut out from a preconsolidated plate of four plies. X-ray micro-computed tomography analysis was conducted using a RX Solutions Easytom 130 to observe the architecture of the fabric and undulations of the yarns. A scan resolution of $20\,\mu\text{m}$ has been used for the measurement. A reconstruction of the sample structure from the generated stack of 2D images in ImageJ is presented in Fig. A.4.

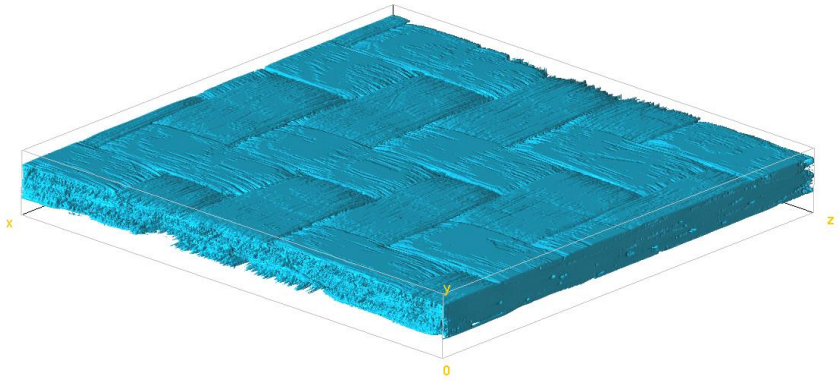

Figure A.4 – μCT reconstruction of the composite sample

Separation of the yarns and matrix phases has been conducted on the stack of images in MATLAB (Fig. A.5); the yarns have been segmented using a watershed algorithm [Meyer1994],

which consists in 'flooding' an image considering light pixels as zones of high elevation, and dark pixels as zones of low elevations (Fig. A.6).

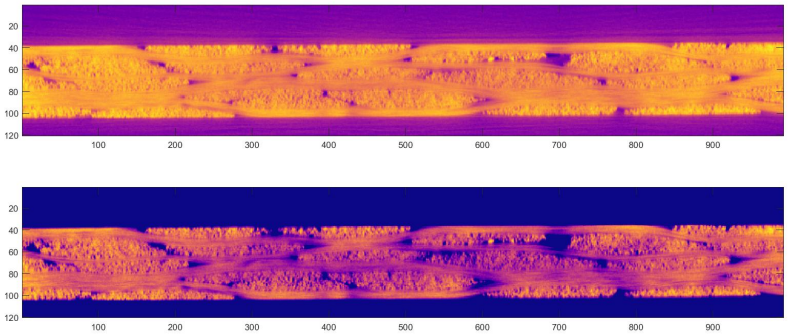

Figure A.5 – Separation of the yarns and matrix phases

Nesting of the yarns in some zones can lead to undersegmentation, i.e. multiple yarns are considered as part of the same region. The resulting clusters are much larger than those corresponding to the section of a single yarn; a size-based criteria was used to discard these regions before further analysis. A potential way of addressing nesting could be to project ellipses fitted on yarns on neighbouring slices where a good segmentation is achieved.

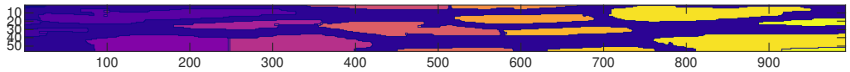

Figure A.6 – Watershed segmentation of the yarns

The centroid of the individual clusters/yarn sections has been computed for all slices, resulting in an array of 3D points. A distance criteria has been used to define the connectivity of the array: as the yarns are continuous, two yarn sections on different slices are considered to be associated with the same yarn if the distance between their respective centroid is smaller than a threshold value, set to 7px.

The resulting reconstructed yarn paths is presented in Fig. A.7 and A.8. While discarding the clusters containing multiple yarns leads to paths showing discontinuities, the pattern and undulation of the yarns is well reproduced. The data computed can be further processed to obtain informations on local yarn curvature, etc.

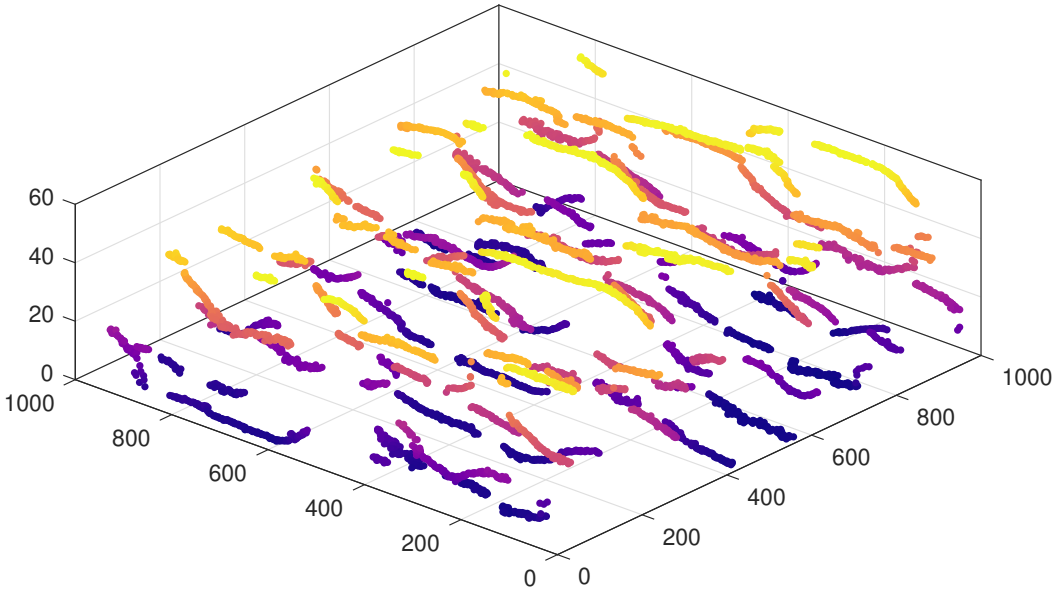

Figure A.7 – Reconstructed yarn paths along direction x in the sample, isometric view

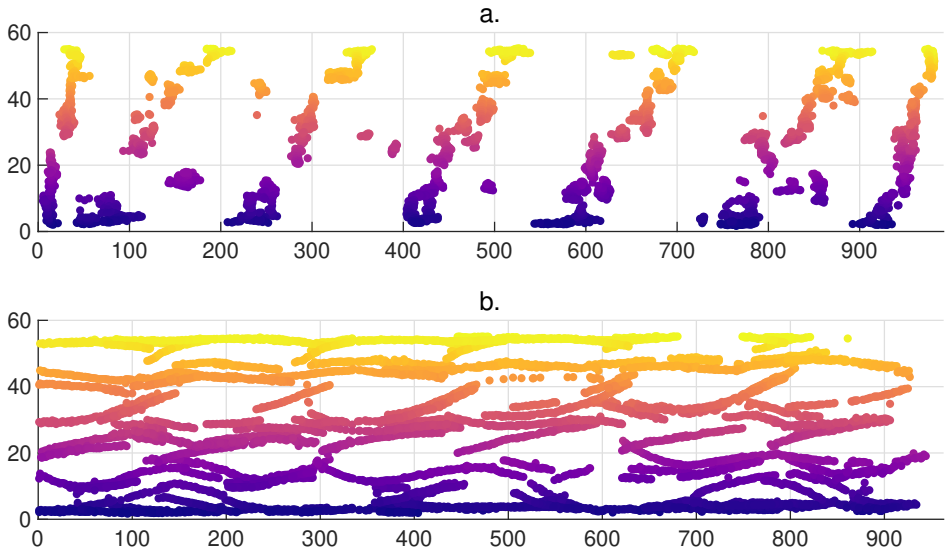

Figure A.8 – Reconstructed yarn paths along direction x in the sample, a. xz projection, b. yz projection

Appendix

B

Implementation of the grid strain analysis procedure

This appendix details the implementation in Matlab of the grid strain algorithm introduced in chapter 6, based on work presented in [Machado+2016b; Shi+2012].

B.1 Reconstruction of the grid nodes

The data obtained from the DIC software Vic-3D corresponds to an array of 3D points corresponding to the surface of the part analyzed, with 'holes' corresponding to the grid nodes with a minimal grey level gradient. The first step in obtaining quantities of interest (strains and shear angle) is the reconstruction of these grid nodes; the procedure is presented here on a simple 3D paraboloid shape.

B.1.1 Definition of boundary points

The array of points exported from Vic-3D is presented in Fig. B.1. Points in this array are assumed to be on a boundary if the distance to the centroid of the associated neighbourhood is larger than a specified tolerance:

$$\left\| \overline{x_i} - \frac{1}{n} \sum_{j=1}^{n} \overline{x_j} \right\| > d_{\text{tol}} \tag{B.1.1}$$

Where $\overline{x_i}$ is the coordinate vector of the current point considered, and $\overline{x_j}$ is the coordinate vector of a point in the n-closest neighbours of $\overline{x_i}$.

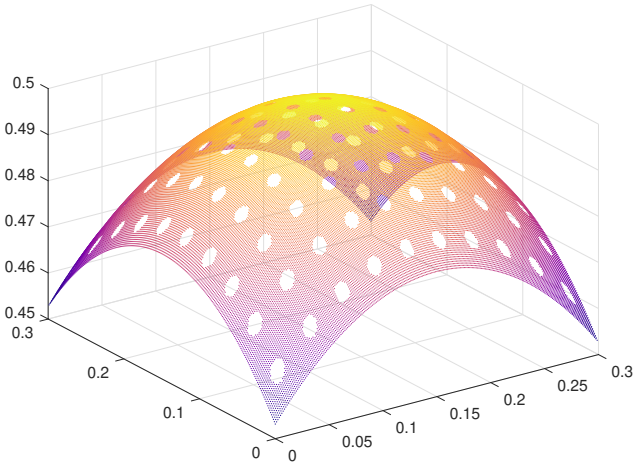

Figure B.1 – 3D point cloud exported from Vic-3D

An example is shown in Fig. B.2 for $n = 4$. The 4 closest neighbours of each points are obtained using function *knnsearch*. As the array of points provided by Vic-3D has an uniform spacing, the current point is coincident with the centroid of its neighbourhood if not on a boundary (which is the case in the lower left).

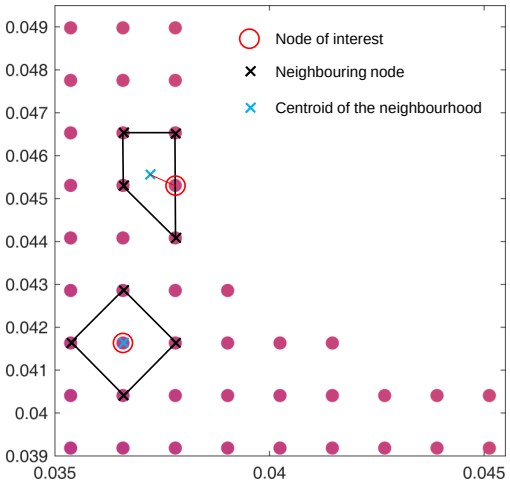

Figure B.2 – Distance-based criterion to determine boundary points

If a point is on the boundary of a node, its neighbourhood will be skewed in one direction and the distance to the centroid will be increased. The numbers of points in the neighbourhood has been set to 8 in practice, and the tolerance d_{tol} defined as the mean distance between the points and their corresponding centroid.

B.1.2 Clustering

The result is an array of points corresponding to the grid nodes boundaries and the edges of the part (shown in Fig. B.3a). An arbitrary polygonal region of interest (ROI) can then be defined interactively. Points in the ROI are partitioned using k-means clustering (function *kmeans*), which aims at minimizing the distance between points within a cluster, and maximizing the distance between the different clusters. The number of clusters expected in the ROI (i.e., the number of grid nodes) must be provided manually. The implementation of k-means clustering in Matlab appears to lead to partitioning errors for when a large number of clusters (>25) is expected; the ROI is selected accordingly to contain a maximum of 25 grid nodes, and the results are concatenated to form larger observation surfaces. The result of the clustering is presented in Fig. B.3b, where the different colors correspond to the partitioned grid nodes, and + is the centroid corresponding to each cluster.

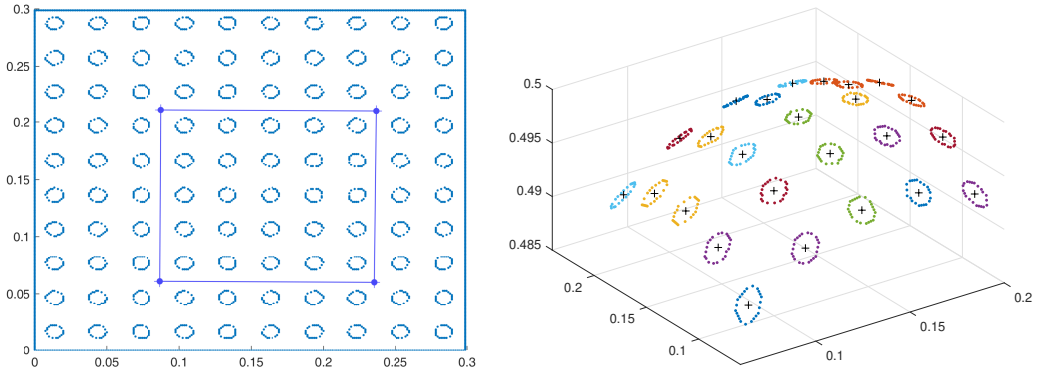

(a) **(b)**

Figure B.3 – a. Definition of a region of interest (ROI), b. Clustering of boundary nodes in ROI

B.2 Meshing of the grid and quantities of interest

The array containing the coordinates of the grid nodes is used to form the nodes of a mesh which is then used to compute strains. A seed element is generated manually, by inputting the indices of the corresponding nodes. The edges of the elements (defined as a couple of node indices) is put in an array that acts as a queue, and the following loop is ran while the queue contains an edge:

- If the edge at the top belongs to more than one element, it is removed from the queue
- Otherwise, the symmetric of the edge about its opposite in the element is generated (Fig. B.4a.)
- The nearest grid point to each extremity of the symmetric edge is computed using *knnsearch*
- If this leads to the creation of a degenerated element (2 or 3 nodes), the edge is removed from the queue

- Otherwise, the element is numbered, its node and edges connectivity defined, and the newly created edges are placed at the bottom of the queue.

The process is repeated iteratively until the mesh is fully generated. In real parts, wrinkles can lead to mesh reconstruction issues; in this case, multiple seed elements are used to reconstruct the majority of the surface.

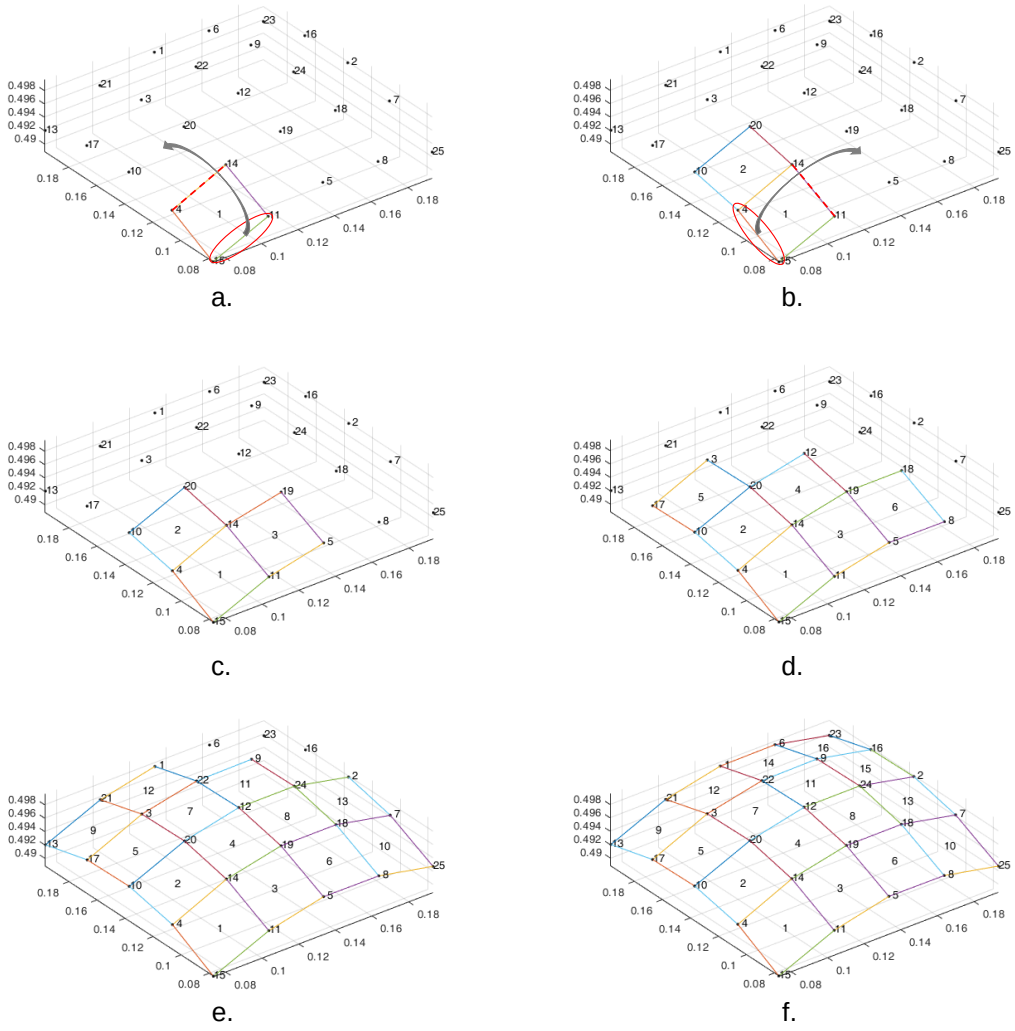

Figure B.4 – Mesh generation from grid nodes

The finite element method is used to compute strains on the resulting mesh; each element is projected on its plane of best fit (i.e., the element is considered 2D). Computing the nodal displacements is straightforward, as the undeformed grid parameter is known. The displacement u in an arbitrary point of the element is computed using bilinear shape functions (with the functionalities available in the Symbolic Math Toolbox™). The deformation gradient tensor is computed as $\mathbf{F} = \mathbf{I} + \mathbf{J}(u)$ where $\mathbf{J}$ is the Jacobian. The right Cauchy-Green tensor is computed as $\mathbf{C} = \mathbf{F}^{\intercal}\mathbf{F}$, from which the desired strain measure can be derived.

Annexe

C

Résumé étendu en français

C.1 Objectifs de la thèse

Les travaux présentés dans ce manuscrit ont été réalisés dans le cadre d'une collaboration entre l'Institut Clément Ader au sein de l'IMT Mines Albi, et de la School of Mechanical and Aerospace Engineering de Queen's University Belfast, avec le support de Solvay. L'objectif principal de la thèse a été le développement d'outils numériques permettant de simuler l'effet de la température d'une préforme composite thermoplastique sur les défauts générés lors de sa mise en forme par thermoformage.

Le procédé de thermoformage/thermoestampage de composites thermoplastiques, décrit en section 1.2.2, consiste au chauffage d'une préforme composite préconsolidée dans un four infrarouge, à une température supérieure à la température de fusion de la matrice thermoplastique semicristalline. La préforme chauffée est ensuite transférée dans une presse et mise en forme (Fig. 1.4). Étant donné la nature séquentielle du procédé, une approche faiblement couplée a été sélectionnée pour la modélisation : un modèle permettant de simuler l'évolution de la température dans la préforme au cours de l'étape de préchauffage infrarouge a été proposé dans un premier temps, cet outil permettant également d'évaluer et d'optimiser l'homogénéité de température dans la pièce pour une configuration de four donnée.

Dans un second temps, le comportement thermomécanique de composites thermoplastiques tissés durant l'étape de mise en forme a été modélisé pour permettre de simuler l'apparition de défauts de type plissements lors de l'étape de mise en forme sous presse. Le champ de température résultant de la simulation du préchauffage est utilisé comme donnée d'entrée de la simulation de formage.

Le matériau utilisé durant ces travaux (voir section 3.4.1) est un tissu de verre sergé 2/2, fourni sous la forme d'un semiproduit poudré PA66. La matrice polyamide utilisée fait partie d'une nouvelle génération de thermoplastiques basse viscosité ($< 50\,\mathrm{Pa\,sec}$) développée par Solvay pour des applications d'injection RTM. Une micrographie du matériau poudré est visible Fig. 3.11 et montre une structure formée par la coalescence de goutelettes de PA66 sur les faces supérieures et inférieures du tissu de verre. Ce type de semiproduit permet de réduire la distance d'imprégnation, tout en limitant les coûts en comparaison aux tissus comélés ou FIT.

La mise en forme de pièces directement à partir de préformes non-consolidées permettrait de réduire les coûts du procédé en supprimant l'étape de préconsolidation ; la nature des préformes conduit cependant à des problématiques spécifiques lors du thermoformage. La caractérisation expérimentale de ces préformes, ainsi que des premières approches de modélisation sont également proposées dans ces travaux.

C.2 Étude bibliographique

Au vu des objectifs proposés, la recherche bibliographique a été orientée suivant trois axes : les outils existants permettant la modélisation numérique du chauffage radiatif, et les problématiques d'identification de propriétés matériaux associées ; la modélisation du comportement mécanique à haute température de composites thermoplastiques tissés ; enfin, la mise en forme de préformes non-consolidées.

C.2.1 Modélisation numérique du chauffage radiatif

Les approches de modélisations développées pour l'étape de chauffage infrarouge (voir section 2.2.3.2) ont pour but de simuler l'évolution de température dans la préforme par la résolution de l'équation de la chaleur ; les transferts radiatifs sont considérés soit par un terme source volumique (en considérant une absorption partielle du flux, de type Beer-Lambert par exemple), soit en exprimant le flux radiatif comme une condition aux limites surfacique (adaptée dans le cas d'un matériau opaque).

Etant donné la complexité de la résolution dans un cas général ou des facteurs de forme analytiques ne sont pas disponibles, de nombreux codes de calculs commerciaux ou académiques sont utilisés dans la littérature (COMSOL ou Ray-Heat à l'Institut Clément Ader).

Le calcul de facteurs de forme (équation 2.2.9) apparaît comme la méthode la plus utilisée pour déterminer le flux radiatif incident sur la préforme ; les approches basées sur le lancer de rayons, si elles permettent une prise en compte physique des phénomènes d'absorption et de réflection spéculaire, présentent des coûts de calculs plus élevés.

La fidélité de la simulation est tributaire de la bonne caractérisation des propriétés du matériau. Si les méthodes de mesure des propriétés optiques (réflectivité, absorbtivité, transmissivité) dans la gamme de longueur d'onde d'intérêt du procédé sont standardisées, la mesure du tenseur de conductivité thermique est plus complexe de par la nature hétérogène du matériau, et diverses approches sont employées dans la littérature (homogénéisation, méthodes inverses, ...). Une caractérisation et une modélisation adéquate des sources radiatives (lampes infrarouges du four) est également importante.

C.2.2 Modélisation du comportement mécanique des composites tissés et méthodes de caractérisation expérimentales associées

La modélisation du comportement mécanique des composites tissés est un problème pouvant être considéré à plusieurs échelles : microscopique (l'échelle des fibres), mésoscopique (celle des mèches) et macroscopique (l'échelle du tissu). Le choix de l'échelle influe sur la complexité et les temps de calculs de l'approche de modélisation, ainsi que sur la caractérisation matériau

nécessaire. Au vu des applications souhaitées, la revue de littérature s'est concentrée principalement sur l'échelle macroscopique (des travaux aux échelles inférieures étant également présentées aux sections 2.3.2.1-2).

A cette échelle, les principaux modes de déformation des composites tissés durant le drapage de formes non-dévelopables sont la tension, le cisaillement plan et la flexion. Les interactions entre les directions principales du tissu entrainent des non-linéarités fortes, et les méthodes de caractérisation expérimentales associées ne sont pas standardisées.

Deux tests principaux sont proposés dans la littérature pour la caractérisation du cisaillement plan : le bias extension test (traction de biais) et le picture frame test (essai de cadre), les deux tests visant à générer une sollicitation en cisaillement pur dans tout ou partie de l'échantillon. Des méthodes de mesures ponctuelles ou de champs sont nécessaires pour déterminer l'évolution de l'angle de cisaillement durant l'essai, afin de limiter l'impact de potentiels glissement de mèches sur le résultat.

Dans le cas des composites thermoplastiques, l'influence de la viscosité de la matrice sur le comportement en cisaillement et flexion est important ; la prise en compte de cet effet nécessite une caractérisation du comportement du matériau dans la gamme de températures du procédé. Des couplages entre les modes de déformations sont observés, de par les interactions entre les mèches à l'échelle mésoscopique. La détermination expérimentale des facteurs de couplage nécessite cependant le développement de montages complexes, et les couplages tension-cisaillement sont souvent négligés dans la littérature.

Bien que des lois de comportement mécaniques aient été développées à différentes échelles, les approches macroscopiques apparaissent comme les plus adaptées à la simulation du drapage de pièces de taille industrielles. Le matériau est dans ce cas approximé par un matériau homogène et continu. Des approches hyperélastiques (basées sur la définition de potentiels) ou hypoélastiques (exprimées en taux) ont été proposées dans la littérature (section 2.3.2.3) ; dans le cas des modèles hypoélastiques, la représentation du changement d'orientation des sens mèche et trame du tissu nécessite une implémentation particulière pour assurer le caractère objectif de la loi de comportement mécanique.

Ces modèles mécaniques ayant été développés à l'origine pour le drapage de tissus secs, l'influence de la température n'a que récemment été considérée dans les outils de simulation de mise en forme. De plus, les modèles proposés dans la littérature supposent une température homogène dans la préforme au début de l'étape de formage, et l'influence de l'étape de préchauffage sur le formage n'est que rarement considérée.

C.2.3 Thermoformage de préformes non-consolidées

La mise en forme de pièces directement à partir de préformes constituées de plis non-consolidées apparaît comme une alternative économique au thermoformage d'*organosheets* pour des volumes de production élevée, la qualité de la consolidation des pièces finales étant le principal verrou technologique. Les travaux expérimentaux présentés dans la littérature sont consacrés principalement à la mise en forme de tissus comélés (voir section 2.4.1), pour

lesquels des modèles de consolidation ont été proposés et validés pour la mise en forme de plaques planes ; la drapabilité de ces matériaux a également été étudiée, sans que l'influence du niveau de consolidation sur le comportement en cisaillement (dans le cas de la mise en forme de pièces complexes) soit évaluée. Par comparaison, peu de travaux portent sur les tissus poudrés, et notamment aucune étude n'a été réalisée sur l'influence de la consolidation sur la drapabilité.

C.3 Modélisation du chauffage radiatif dans le procédé de thermoformage

La première étape de la mise en forme d'une pièce composite par thermoformage correspond à une étape de chauffage afin d'amener la préforme à une température supérieure à la température de fusion de la matrice semicristalline pour permettre la mise en forme. Industriellement, cette étape est généralement réalisée dans un four infrarouge à lampes halogènes.

Le problème thermique considéré est schématisé Fig. 3.1 ; la simulation du champ de température durant cette étape nécessite la caractérisation de l'interaction entre le rayonnement émis par les lampes infrarouge et la préforme, ainsi que les propriétés contrôlant les transferts thermiques au sein de la pièce.

Dans le cas d'une préforme non-consolidée, le contact imparfait entre plis ainsi que la présence d'air limite le transfert de chaleur à travers l'épaisseur ; la résistance thermique de contact doit donc être prise en compte lors de l'étape de modélisation.

Les transferts radiatifs sont traités en utilisant une méthode de facteurs de formes permettant un traitement rapide au vu de la géométrie du four, les lampes étant assimilées à des cylindres isothermes, avec la température du filament caractérisée expérimentalement en fonction de la puissance électrique fournie.

C.3.1 Caractérisation des propriétés optiques et thermiques

Les propriétés optiques du semiproduit poudré et du matériau consolidé ont été caractérisées par spectroscopie infrarouge, dans la gamme de longueur d'onde correspondant à une lampe émettant à 2400 K. La transmittivité du matériau est négligeable dans cette gamme quelle que soit le niveau de consolidation, et le matériau peut donc être considéré comme opaque à l'échelle d'un pli.

L'étude de la réflectivité spectrale diffuse (directement corrélée à l'émissivité étant donné le caractère opaque du matériau) montre une forte absorption du rayonnement pour le matériau préconsolidé, ce qui était attendu de par l'utilisation de noir de carbone comme charge dans la matrice PA66. Dans le cas du semiproduit poudré, les mèches de verres apparentes à la surface du semiproduit poudré tend à diminuer l'absorption du rayonnement aux faibles longueurs d'ondes ($<6\,\mu m$) comparé au matériau préconsolidé.

Les propriétés thermophysiques du matériau ont également été caractérisées expérimentalement, et deux approches ont été proposées pour déterminer le tenseur de conductivité thermique : la première basée sur une stratégie d'homogénéisation à deux échelles à partir de la caractérisation de la conductivité thermique des constituants et de l'analyse de la morphologie du composite, et la seconde sur une méthode d'analyse inverse couplée à un montage expérimental permettant des mesures de température sans contact. L'approche par homogénéisation requiert une caractérisation et une modélisation fine de la micro- et mésostructure du composite tissé, mais permet une prise en compte aisée de la dépendance en température de la conductivité thermique effective à partir de la connaissance de celle des constituants. La seconde méthode est basée sur un essai expérimental rapide ; les variations de températures non-négligeables pendant le test nécéssitent cependant de poser des hypothèses sur la dépendance en température des propriétés.

C.3.2 Caractérisation de la conductance de contact

La conductivité thermique effective, ainsi que la conductance de contact dans un empilement de plis non-consolidés a été caractérisée sous presse chauffante instrumentée. Une dépendance non-linéaire à la pression, cohérente avec la réponse en compression des tissus, est observée. La compression affecte à la fois la conductivité thermique effective du pli (en augmentant le nombre de contacts fibre/fibre), et la conductance thermique de contact entre plis par la déformation des points de contacts. Des tests effectués à pression réduite montrent l'influence non négligeable des transferts par conduction gazeuse au sein de la préforme non consolidée.

Le comportement du matériau modélisé a été implémenté dans le logiciel élément finis Comsol et validé sur un cas test de chauffage par une lampe, en modifiant le montage expérimental utilisé pour la détermination par analyse inverse de la conductivité thermique. Une préforme non-consolidée sous bâche à vide est utilisée comme échantillon. Un bon accord entre les données expérimentales et la simulation est observée, à l'exception du panache convectif qui n'est pas reproduit par le modèle.

C.4 Étude expérimentale et numérique du préchauffage de préformes composites dans un four infrarouge

C.4.1 Travail expérimental

Pour valider ce modèle dans des conditions se rapprochant de l'environnement industriel, un four infrarouge instrumenté permettant la modification de la configuration spatiale des lampes ainsi que de leur température a été développé. Ce four est composé d'un banc de 10 lampes d'entraxe fixe, et de trois positions possibles par lampe. Ce banc est situé à une distance réglable sous la préforme à chauffer. La température de la préforme est monitorée

par une caméra infrarouge mesurant le champ de température sur la surface supérieure, ainsi que par deux thermocouples infrarouges pour des mesures ponctuelles sur la surface inférieure.

Quatre configurations de lampes distinctes ont été testées (voir Fig. 4.5) ; des différences significatives dans les distributions spatiales de températures sont observées, avec des isocontours elliptiques ou plus complexes selon les cas, et une différence de température maximale allant jusqu'à 60 °C.

C.4.2 Simulations thermiques et optimisation

Les simulations réalisées à partir du modèle élément finis du four montrent un bon accord avec les résultats expérimentaux en termes de prédiction du champ de température , l'erreur induite par la simulation augmentant avec la distance à la normale des lampes ; les gradients de température tendent à être surestimés à la surface de la préforme.

Un affaissement des préformes a été observé avec l'élévation de la température au delà du point de fusion de la matrice polyamide. L'effet de cet affaissement sur la distribution de température dans la préforme a été évalué numériquement, en supposant une courbure uniforme, les résultats montrant des variations de température jusqu'à 20%, les positions des points chauds et froids sur la surface n'étant pas affectés dans la gamme de courbure évaluée. Cet effet n'a pas été considéré dans la suite des simulations, à cause du manque de données expérimentales.

Une stratégie d'optimisation permettant de définir la température des lampes à partir d'un champ de température désiré dans la préforme a été proposée. Dans le cas ou les seules variables d'optimisation considérées sont la puissance des lampes, une méthode de résolution basée sur l'algorithme GCMMA est employée. Dans le cas plus complexe ou la géométrie du four est également considérée comme une variable d'optimisation, une première passe est réalisée à l'aide d'une méthode d'échantillonage type Monte-Carlo, les meilleures solutions étant raffinées à l'aide de l'algorithme du simplexe.

C.5 Caractérisation expérimentale et modélisation des propriétés mécaniques des composites thermoplastiques tissés à haute température

Le comportement thermomécanique des composites thermoplastiques tissés durant l'étape de formage a été modélisé à l'échelle macroscopique à l'aide d'un modèle non-orthogonal, dans lequel la loi de comportement hypoélastique (en taux) est exprimée dans deux repères fixes par rapport aux directions principales du tissu. Seuls les termes en tension et cisaillement sont considérés, les interactions tension/tension et tension/cisaillement étant négligés.

Cette loi est implémentée dans une sous-routine Abaqus (VUMAT). Les dérivées de Green-Naghdi utilisées dans Abaqus/Explicit ne sont pas objectives dans le cas considéré, étant

basées sur la rotation moyenne du milieu ; la sous-routine effectue donc la rotation des quantités d'intérêt (déformations et taux de déformations) du repère de Green-Naghdi aux deux repères liés aux directions principales ; la loi de comportement est appliquée dans ce repère objectif, et les contraintes calculées sont converties par rotation inverse dans le repère de Green-Naghdi avant l'incrément suivant.

C.5.1 Comportement en tension

Le comportement en tension du matériau non-consolidé et consolidé a été caractérisé à température ambiante (seul le cisaillement étant considéré thermodépendant) par des essais de traction quasistatique. Un comportement non linéaire est observé : une première phase à module apparent faible correspondant au désembuvage du tissu dans la direction sollicitée, et une deuxième phase linéaire correspondant à la traction sur le tissu tendu. La comparaison des résultats pour le tissu poudré et le matériau consolidé montre que l'influence de la consolidation est limitée à la phase initiale de désembuvage du tissu (qui correspond à la mise en tension des mèches directement sollicitées). Aux plus grandes déformations, le module d'élasticité apparent est identique dans les deux cas.

Un modèle phénoménologique avec un nombre de paramètres réduit, composé d'un terme linéaire et d'un terme logistique représentant le comportement non linéaire a été proposé (eq. 5.3.1), et montre un bon accord avec les données expérimentales.

C.5.2 Comportement en cisaillement

Le comportement en cisaillement plan du matériau a été caractérisé à hautes températures et pour différentes vitesses de déformations à l'aides d'essais de traction de biais (*bias-extension test*). Cet essai correspond à un essai de traction sur un échantillon de rapport longueur/largeur supérieur à 2, dans lequel les directions principales du tissu sont orientées initialement à $\pm 45°$ par rapport à la direction de sollicitation. La partie centrale de l'échantillon est alors sollicitée en cisaillement pur ; la cinématique de l'essai est représentée Fig. 5.7. Un suivi par caméra est réalisé pour permettre de mesurer l'évolution de l'angle de cisaillement au cours de l'essai, à l'aide de marqueurs sur les échantillons.

Un comportement non-linéaire typique des matériaux tissés est observé, une première phase correspondant à la rotation des mèches (conduisant à une déformation de type treillis du tissu) associée à un faible module de cisaillement ; passé un angle de cisaillement limite, les mèches rentrent en contact et les efforts de compaction transverse conduisent à une augmentation du module.

Une élévation de la rigidité en cisaillement est observée avec la diminution de la température/l'augmentation de la vitesse de sollicitation pour le matériau consolidé, ce qui est cohérent avec les résultats reportés dans la littérature pour d'autres matériaux. L'influence de la température et de la vitesse apparaissent moins marqués pour le semiproduit poudré.

La distribution non uniforme de résine à la surface des mèches du tissu poudré conduit en outre à un motif de zones riches en résine et de mèches de verre apparentes «en accordéon» ;

ce motif est dû au glissement intra-pli pour des angles de cisaillement élevés, ce qui a pour effet de rendre visible des parties des mèches non poudrées, en plus d'une accrétion de la résine dans les zones de glissement. Ce phénomène pourrait notamment conduire à des zones sèches dans la pièce finale, de par l'augmentation de la distance d'imprégnation de la résine.

Un modèle basé sur un découplage multiplicatif des effets de la température et de la vitesse de cisaillement est proposé pour modéliser le comportement observé expérimentalement (eq. 5.4.3).

C.6 Mise en forme de pièces hémisphériques PA66/verre : étude expérimentale et numérique

C.6.1 Travail expérimental

Des essais de formage ont été réalisés à l'aide d'un pilote de thermoformage associant le four infrarouge présenté précedemment et une presse équipée d'un poinçon hémisphérique. L'influence du champ de température sur les plissements générés sur les pièces formées est non-négligeable pour les préformes préconsolidées, les préformes consistant en un empilement de plis non-consolidés étant moins affectées par les variations de température.

Etant donné l'encombrement de la presse, le suivi de la déformation pendant l'essai n'a pas pu être réalisé. En l'absence d'un système disponible à QUB, une procédure de traitement d'image, permettant l'utilisation d'une méthode de grille à l'aide d'un système d'acquisition type corrélation d'image, a été développée pour obtenir des données quantitatives sur les angles de cisaillement générés par la mise en forme (section 6.2.2) : une grille de marqueurs circulaires uniformes, superposée à un motif speckle aléatoire, est peinte sur la préforme avant mise en forme. VIC-3D est utilisé pour l'acquisition des coordonnées de la surface hors marqueurs après la mise en forme ; ce nuage de points, qui forme donc un *négatif* de la position des marqueurs, est exporté dans MATLAB pour la suite du prost-traitement. Après obtention des coordonnées spatiales des marqueurs, les déplacements et déformations sont calculées à partir d'un maillage élément finis, permettant d'obtenir un champ de déformation sur la pièce.

C.6.2 Simulation numérique de la mise en forme

Le modèle non-orthogonal présenté a été implémenté dans Abaqus/Explicit à l'aide d'une sous-routine utilisateur (VUMAT) et validé à partir des résultats des essais de traction de biais à haute température. Des simulation de formage isotherme avec un champ de température uniforme et non-uniforme ont été réalisées, montrant un accord qualitatif correct avec les pièces expérimentales.

Une approche simplifiée pour pour la prise en compte du formage non-isotherme a été employée. La surface de la préforme a été partitionnée en zones distinctes en fonction de la position par rapport à l'outillage de la presse (i.e., en contact avec le poinçon, le serre-flanc, etc.) ; des vitesses de refroidissement constantes, identifiées à partir de mesures par caméra infrarouge, ont été considérées sur ces zones distinctes. Bien que le modèle permette de prédire correctement les défauts macroscopiques engendrés, la plage de température restreinte sur laquelle le comportement en cisaillement du matériau a été caractérisée limite la précision de la simulation, les essais expérimentaux montrant que la préforme peut atteindre par endroit des températures largement inférieures à 265 °C.

Dans une dernière partie des travaux, les outils de simulations développés ont été utilisés dans une étude préliminaire pour évaluer l'intérêt du chauffage localisé pour le formage de pièces à double courbure ; les résultats suggèrent que dans le cas de pièces dont la géométrie contient des zones plates et peu sollicitées en cisaillement, le chauffage localisé pourrait permettre de réduire la consommation d'énergie du procédé ainsi que limiter la déconsolidation thermique de la préforme, sans conduire à des défauts de forme plus important.

C.7 Conclusion et perspectives des travaux

Les outils de simulation développés pour la modélisation du formage non-isotherme de composites thermoplastiques poudrés montrent un bon potentiel pour être utilisés dans le cadre d'une stratégie d'optimisation de type *virtual manufacturing*, en permettant l'analyse de l'étape de préchauffage infrarouge d'une préforme composite, consolidée ou non, et d'étudier son influence sur les défauts macroscopiques apparaissant lors de la mise en forme. L'approche mise en oeuvre et les outils numériques développés durant cette thèse permettent notamment, à partir de la caractérisation des propriétés matériaux d'une préforme, d'optimiser les paramètres de chauffage infrarouge en fonction d'un champ de température désiré, ou de simuler l'évolution de la température à partir d'une configuration de four donnée, en considérant si besoin des résistances thermiques de contact dans une préforme non-consolidée, et de simuler le comportement mécanique à haute température d'un composite thermoplastique tissé, en considérant un champ de température initial réaliste et non-homogène, et en prenant en compte de manière simple le formage non-isotherme.

Certains points de l'approche proposée restent cependant à améliorer :

- L'influence des transferts convectifs sur la méthode de mesure de conductivité thermique présentée au chapitre 3 nécessite d'être traitée plus finement soit du point de vue numérique soit par un meilleur contrôle de l'environnement expérimental.
- Le calcul des transferts radiatifs au sein du four infrarouge pourrait être amélioré par la prise en compte de la nature non-Lambertienne de la réflectivité des matériaux de l'enceinte et de la préforme, ainsi qu'en considérant l'affaissement progressif de la préforme au cours du chauffage.

- La plage de température dans laquelle le comportement en cisaillement plan du tissu a été caractérisé est limitée comparée aux températures observées expérimentalement lors du formage ; par conséquent, la cristallisation de la matrice et son effet sur les propriétés mécaniques n'est pas correctement prise en compte dans la simulation actuelle. Le comportement en flexion a été négligé durant ces travaux ; l'utilisation d'éléments coques non-standard découplant le comportement membrane et flexion permettrait d'améliorer la fidélité de la simulation des plissements.

- L'utilisation d'une analyse séquentielle couplée thermique/mécanique permettrait une meilleure représentation de l'évolution de la température de la préforme après contact avec les outils.

- Enfin, l'étape de reconsolidation n'a pas été étudiée durant ces travaux : la prédiction du taux de vide, ou d'éventuelles zones de délamination serait une information intéressante étant donné son influence sur les propriétés mécaniques de la pièce finie, et ce particulièrement dans le cas de pièces formées à partir de préformes non-consolidées, la faisabilité de former et d'imprégner les mèches en une seule étape restant à être évaluée.

Bibliography

[Abbassi+2011] F. Abbassi, I. Elfaleh, S. Mistou, A. Zghal, M. Fazzini, and T. Djilali. "Experimental and numerical investigations of a thermoplastic composite (carbon/PPS) thermoforming". In: *Structural Control and Health Monitoring* 18.7 (Sept. 2011), pp. 769–780 (cit. on p. 26).

[Akkerman2018] R. Akkerman. "Processing and properties of thermoplastic composite materials". In: *Proceedings of SIP-IMASM2018*. 2018 (cit. on p. 5).

[Akué Asséko+2015] A. C. Akué Asséko, B. Cosson, F. Schmidt, Y. Le Maoult, and E. Lafranche. "Laser transmission welding of composites-Part A: Thermo-physical and optical characterization of materials". In: *Infrared Physics & Technology* 72 (Sept. 2015), pp. 293–299 (cit. on p. 74).

[Amiot2014] M. Amiot. "L'auto cherche son régime minceur". In: *Les Echos* (Nov. 2014) (cit. on p. 2).

[Andrieu+2004] S. Andrieu, F. Schmidt, and Y. Le Maoult. "Experimental and numerical infrared heating of thermoplastic sheet during thermoforming process". In: *Proceedings of the 20th Polymer Processing Society annual meeting PPS2004*. 2004 (cit. on p. 23).

[Andrieu2005] S. Andrieu. "Étude expérimentale et numérique du chauffage infrarouge de plaques thermoplastiques pour le thermoformage". PhD thesis. École des Mines de Paris, 2005 (cit. on pp. 23, 53, 88).

[Ashby1992] M. F. Ashby. *Materials selection in mechanical design*. Ed. by Butterworth-Heinemann. Pergamon, 1992 (cit. on p. 10).

[ASTM2007] ASTM. *ASTM D1777-96: Standard Test Method for Thickness of Textile Materials*. American Society for Testing and Materials (ASTM), 2007 (cit. on p. 65).

[ASTM2015] ASTM. *ASTM D5035-11: Standard Test Method for Breaking Force and Elongation of Textile Fabrics (Strip Method)*. American Society for Testing and Materials (ASTM), 2015 (cit. on p. 118).

[Badel+2008a] P. Badel, E. Vidal-Sallé, and P. Boisse. “Large deformation analysis of fibrous materials using rate constitutive equations”. In: *Computers & Structures* 86.11-12 (June 2008), pp. 1164–1175 (cit. on pp. 36, 38).

[Badel+2008b] P. Badel, E. Vidal-Sallé, E. Maire, and P. Boisse. “Simulation and tomography analysis of textile composite reinforcement deformation at the mesoscopic scale”. In: *Composites Science and Technology* 68.12 (Sept. 2008), pp. 2433–2440 (cit. on pp. 35, 149).

[Baek+2013] H. M. Baek, A. J. Giacomin, and M. J. Wurz. “Sag in commercial thermoforming”. In: *AIChE Journal* 60.4 (Nov. 2013), pp. 1529–1535 (cit. on p. 106).

[Barbagallo+2016] Gabriele Barbagallo, Angela Madeo, Ismael Azehaf, Ivan Giorgio, Fabrice Morestin, and Philippe Boisse. “Bias extension test on an unbalanced woven composite reinforcement: Experiments and modeling via a second-gradient continuum approach”. In: *Journal of Composite Materials* 51.2 (July 2016), pp. 153–170 (cit. on p. 25).

[Beardmore+1986] P. Beardmore and C. F. Johnson. “The potential for composites in structural automotive applications”. In: *Composites Science and Technology* 26.4 (Jan. 1986), pp. 251–281 (cit. on p. 3).

[Bédard+1996] N. Bédard and S. Brunet. “Evaluation d’émetteurs infrarouges électriques et de radiants à gaz”. In: *Proc. 13th Int. Congr. on Electricity Applications*. 1996 (cit. on p. 12).

[Bédard1998] N. Bédard. “Laboratory testing of radiant gas burners and electric infrared emitters”. In: *Experimental Heat Transfer* 11.3 (July 1998), pp. 255–279 (cit. on p. 12).

[Bento+2015] A. M. Bento, K. D. Roth, and Y. Wang. “The Impact of CAFE Standards on Innovation in the US Automobile Industry”. In: *Proceedings of the 2015 AAEA & WAEA Joint Annual Meeting*. 2015 (cit. on p. 2).

[Benveniste1987] Y. Benveniste. “Effective thermal conductivity of composites with a thermal contact resistance between the constituents: Nondilute case”. In: *Journal of Applied Physics* 61.8 (Apr. 1987), pp. 2840–2843 (cit. on p. 67).

[Bernet+1999] N. Bernet, V. Michaud, P. E. Bourban, and J. A.E. Manson. “An Impregnation Model for the Consolidation of Thermoplastic Composites Made from Commingled Yarns”. In: *Journal of Composite Materials* 33.8 (Apr. 1999), pp. 751–772 (cit. on p. 41).

[Bernet+2001] N. Bernet, V. Michaud, P.-E. Bourban, and J.-A.E. Månson. “Commingled yarn composites for rapid processing of complex shapes”. In: *Composites Part A: Applied Science and Manufacturing* 32.11 (Nov. 2001), pp. 1613–1626 (cit. on pp. 40, 41).

[Bersee+1991] H.E.N. Bersee and L.M.J. Robroek. “The role of the thermoplastic matrix in forming processes of composite materials”. In: *Composites Manufacturing* 2.3-4 (Jan. 1991), pp. 217–222 (cit. on p. 13).

[Bessard2012] É. Bessard. “Matériaux composites structuraux à base PEEK élaborés par thermocompression dynamique: relation procédé-propriétés”. PhD thesis. Université de Toulouse, 2012 (cit. on p. 59).

[Bhattacharyya+2003] D. Bhattacharyya, M. Bowis, and K. Jayaraman. “Thermoforming woodfibre–polypropylene composite sheets”. In: *Composites Science and Technology* 63.3-4 (Feb. 2003), pp. 353–365 (cit. on pp. 13, 14).

[Bian+2013] X. X. Bian, Y. Z. Gu, J. Sun, M. Li, W. P. Liu, and Z. G. Zhang. “Effects of processing parameters on the forming quality of C-shaped thermosetting composite laminates in hot diaphragm forming process”. In: *Applied Composite Materials* 20.5 (Jan. 2013), pp. 927–945 (cit. on p. 14).

[Bian+2015] D. Bian, G. Satoh, and Y. L. Yao. “The Laser Interlaminar Reinforcement of Continuous Glass Fiber Composites”. In: *Journal of Manufacturing Science and Engineering* 137.6 (Sept. 2015), p. 061001 (cit. on p. 62).

[Biron2007] M. Biron. *Thermoplastics and Thermoplastic Composites: Technical Information for Plastics Users*. Elsevier Science, 2007 (cit. on p. 43).

[Boisse+2005] P Boisse, B Zouari, and A Gasser. “A mesoscopic approach for the simulation of woven fibre composite forming”. In: *Composites Science and Technology* 65.3-4 (Mar. 2005), pp. 429–436 (cit. on p. 25).

[Boisse+2011] P. Boisse, N. Hamila, E. Vidal-Sallé, and F. Dumont. “Simulation of wrinkling during textile composite reinforcement forming. Influence of tensile, in-plane shear and bending stiffnesses”. In: *Composites Science and Technology* 71.5 (Mar. 2011), pp. 683–692 (cit. on pp. 26, 32, 136).

[Boisse+2016] P. Boisse, N. Hamila, E. Guzman-Maldonado, A. Madeo, G. Hivet, and F. dell’Isola. “The bias-extension test for the analysis of in-plane shear properties of textile composite reinforcements and prepregs: a review”. In: *International Journal of Material Forming* 10.4 (Apr. 2016), pp. 473–492 (cit. on pp. 30, 125, 129).

[Boisse+2018] P. Boisse, J. Colmars, N. Hamila, N. Naouar, and Q. Steer. “Bending and wrinkling of composite fiber preforms and prepregs. A review and new developments in the draping simulations”. In: *Composites Part B: Engineering* 141 (May 2018), pp. 234–249 (cit. on pp. 31, 143, 159).

[Bonnaire+2017] R. Bonnaire, J. Patou, E. De Luycker, T. Cutard, and G. Bernhart. “Utilisation de la corrélation d’images pour le suivi de la mise en forme de renfort textile dans le cadre de la fabrication de pièces composites pour l’aéronautique”. In: *23ème Congrès Français de Mécanique*. 2017 (cit. on p. 137).

[Bordival+2010] M. Bordival, F. M. Schmidt, Y. Le Maoult, B. Cosson, and B. Plantamura. “A ray tracing method to simulate the infrared heating of semi-transparent thermoplastics”. In: *International Journal of Material Forming* 3.S1 (Apr. 2010), pp. 809–812 (cit. on p. 24).

[Bourban+2001] P.-E. Bourban, N. Bernet, J.-E. Zanetto, and J.-A. E. Månson. “Material phenomena controlling rapid processing of thermoplastic composites”. In: *Composites Part A: Applied Science and Manufacturing* 32.8 (Aug. 2001), pp. 1045–1057 (cit. on pp. 4, 40).

[Bouwman+2016] M. M. Bouwman, T. G. Donderwinkel, and S. Wijskamp. “Overmoulding – An Integrated Design Approach for Dimensional Accuracy and Strength of structural Parts”. In: *Proceedings of the 3rd International Conference on Thermoplastic Composites (ITHEC)*. 2016 (cit. on p. 3).

[Bradley+2007] D. Bradley and G. Roth. “Adaptive Thresholding using the Integral Image”. In: *Journal of Graphics Tools* 12.2 (Jan. 2007), pp. 13–21 (cit. on p. 172).

[Brandrup+1998] J. Brandrup, E.H. Immergut, and E.A. Grulke. *Polymer Handbook*. Wiley & Sons, 1998 (cit. on pp. 68, 69).

[Brinken+1980] F. Brinken and H. Potente. “Some considerations of heat-transfer problems in thermoforming”. In: *Polymer Engineering and Science* 20.15 (Oct. 1980), pp. 1009–1014 (cit. on p. 20).

[BRITEEURAM1992] BRITE-EURAM. *Industrial press forming of continuous fibre reinforced thermoplastic sheets and the development of numerical simulation tools*. BE 5092. 1992 (cit. on p. 21).

[Brodu+2015] E. Brodu, M. Balat-Pichelin, J.-L. Sans, and J.C. Kasper. “Evolution of the emissivity of tungsten at high temperature with and without proton bombardment”. In: *Acta Materialia* 84 (Feb. 2015), pp. 305–316 (cit. on p. 51).

[Brogan+1996] M.T. Brogan and P.F. Monaghan. “Thermal simulation of quartz tube infrared heaters used in the processing of thermoplastic composites”. In: *Composites Part A: Applied Science and Manufacturing* 27.4 (Jan. 1996), pp. 301–306 (cit. on p. 21).

[Brooks2007] R. Brooks. “Forming technology for thermoplastic composites”. In: *Composites Forming Technologies*. Elsevier, 2007, pp. 256–276 (cit. on pp. 4, 5, 11).

[BuetGautier+2001] K. Buet-Gautier and P. Boisse. “Experimental analysis and modeling of biaxial mechanical behavior of woven composite reinforcements”. In: *Experimental Mechanics* 41.3 (Sept. 2001), pp. 260–269 (cit. on pp. 26, 27).

[Bunsell2011] A.R. Bunsell. “Fibres for composite reinforcement: properties and microstructures”. In: *Composite Reinforcements for Optimum Performance*. Elsevier, 2011, pp. 3–31 (cit. on p. 25).

[Bussetta+2018] P. Bussetta and N. Correia. “Numerical forming of continuous fibre reinforced composite material: A review”. In: *Composites Part A: Applied Science and Manufacturing* 113 (Oct. 2018), pp. 12–31 (cit. on p. 33).

[Cai1992] W. Cai. “Développement et applications de modèles d’échanges radiatifs par suivi de rayons”. PhD thesis. École des Mines de Paris, 1992 (cit. on p. 23).

[Cakmak+1991] M. Cakmak and A. Dutta. “Instrumented thermoforming of advanced thermoplastic composites. II: Dynamics of double curvature part formation and structure development from PEEK/carbon fiber prepreg tapes”. In: *Polymer Composites* 12.5 (Oct. 1991), pp. 338–353 (cit. on pp. 13, 40).

[Calex2015] Calex. *PyroMini - Technical datasheet*. 2015 (cit. on p. 91).

[Cao+2003] J. Cao, P. Xue, X. Peng, and N. Krishnan. “An approach in modeling the temperature effect in thermo-stamping of woven composites”. In: *Composite Structures* 61.4 (Sept. 2003), pp. 413–420 (cit. on pp. 38, 136, 156).

[Cao+2008] J. Cao et al. “Characterization of mechanical behavior of woven fabrics: Experimental methods and benchmark results”. In: *Composites Part A: Applied Science and Manufacturing* 39.6 (June 2008), pp. 1037–1053 (cit. on pp. 29, 30, 43, 123).

[Capelle+2014] E. Capelle, P. Ouagne, D. Soulat, and D. Duriatti. “Complex shape forming of flax woven fabrics: Design of specific blank-holder shapes to prevent defects”. In: *Composites Part B: Engineering* 62 (June 2014), pp. 29–36 (cit. on p. 137).

[Carminati2006] R. Carminati. *Transports en milieux dilués*. 2006 (cit. on p. 83).

[Cassel+2010] B. Cassel and R. Packer. *Modulated temperature DSC and the DSC 8500: a step up in performance*. Tech. rep. PerkinElmer, 2010 (cit. on p. 66).

[Cassidy+1994] S. F. Cassidy and P. F. Monaghan. “Effect of contact resistances on the thermal conductivity of an unconsolidated fibre-reinforced thermoplastic prepreg stack”. In: *Composites Manufacturing* 5.4 (Dec. 1994), pp. 225–230 (cit. on p. 79).

[Cavallaro+2007] P. V. Cavallaro, A. M. Sadegh, and C. J. Quigley. “Decrimping Behavior of Uncoated Plain-woven Fabrics Subjected to Combined Biaxial Tension and Shear Stresses”. In: *Textile Research Journal* 77.6 (June 2007), pp. 403–416 (cit. on p. 26).

[Cazaux2016] G. Cazaux. “Faisabilité des procédés LCM pour l’élaboration de composites renfort continu à matrice thermoplastique polyamide”. PhD thesis. Université du Havre, 2016 (cit. on p. 4).

[Ceramicx2015] Ceramicx. *HeatWorks 14*. May 2015 (cit. on pp. 12, 160).

[Chalmovianský+2003] P. Chalmovianský and B. Jüttler. “Filling Holes in Point Clouds”. In: *Lecture Notes in Computer Science*. Springer Berlin Heidelberg, 2003, pp. 196–212 (cit. on p. 138).

[Champin2007] C. Champin. “Modélisation 3D du chauffage par rayonnement infrarouge et de l’étirage-soufflage de corps creux en PET”. PhD thesis. École des Mines de Paris, 2007 (cit. on p. 24).

[Chang+2003] S. Chang, S.B Charma, and M.P.F. Sutcliffe. “Microscopic investigation of tow geometry of a dry satin weave fabric during deformation”. In: *Composites Science and Technology* 63.1 (Jan. 2003), pp. 99–111 (cit. on p. 29).

[Charmetant+2011] A. Charmetant, E. Vidal-Sallé, and P. Boisse. “Hyperelastic modelling for mesoscopic analyses of composite reinforcements”. In: *Composites Science and Technology* 71.14 (Sept. 2011), pp. 1623–1631 (cit. on pp. 36, 37).

[Cheah2010] L. W. Cheah. “Cars on a diet: the material and energy impacts of passenger vehicle weight reduction in the US”. PhD thesis. Massachussets Institute of Technology, 2010 (cit. on p. 2).

[Chen+2000] J. Chen, J. A. Sherwood, P. Buso, S. Chow, and D. Lussier. “Stamping of continuous fiber thermoplastic composites”. In: *Polymer Composites* 21.4 (Aug. 2000), pp. 539–547 (cit. on p. 15).

[Chen+2003] Y.K. Chen, O.P. Modi, A.S. Mhay, A. Chrysanthou, and J.M. O'Sullivan. "The effect of different metallic counterface materials and different surface treatments on the wear and friction of polyamide 66 and its composite in rolling–sliding contact". In: *Wear* 255.1-6 (Aug. 2003), pp. 714–721 (cit. on p. 152).

[Chen+2006a] Z.-R. Chen and L. Ye. "A micromechanical compaction model for woven fabric preforms. Part II: Multilayer". In: *Composites Science and Technology* 66.16 (Dec. 2006), pp. 3263–3272 (cit. on p. 83).

[Chen+2006b] Z.-R. Chen, L. Ye, and T. Kruckenberg. "A micromechanical compaction model for woven fabric preforms. Part I: Single layer". In: *Composites Science and Technology* 66.16 (Dec. 2006), pp. 3254–3262 (cit. on p. 120).

[Chen+2011] M. Chen, G. Zak, and P. J. Bates. "Effect of carbon black on light transmission in laser welding of thermoplastics". In: *Journal of Materials Processing Technology* 211.1 (Jan. 2011), pp. 43–47 (cit. on p. 62).

[Chen+2015] S. Chen, L.T. Harper, A. Endruweit, and N.A. Warrior. "Formability optimisation of fabric preforms by controlling material draw-in through in-plane constraints". In: *Composites Part A: Applied Science and Manufacturing* 76 (Sept. 2015), pp. 10–19 (cit. on p. 31).

[Choy1977] C.L. Choy. "Thermal conductivity of polymers". In: *Polymer* 18.10 (Oct. 1977), pp. 984–1004 (cit. on p. 67).

[Chung+1989] B. T. F. Chung and M. M. Kermani. "Radiation View Factors From a Finite Rectangular Plate". In: *Journal of Heat Transfer* 111.4 (1989), p. 1115 (cit. on p. 49).

[Churchill+1973] S. W. Churchill and H. Ozoe. "A Correlation for Laminar Free Convection From a Vertical Plate". In: *Journal of Heat Transfer* 95.4 (1973), p. 540 (cit. on pp. 54, 76).

[Cohen+1985] M. F. Cohen and D. P. Greenberg. "The hemi-cube: a radiosity solution for complex environments". In: *Proceedings of the 12th annual conference on Computer graphics and interactive techniques - SIGGRAPH '85*. ACM Press, 1985 (cit. on p. 19).

[COMSOL2013a] COMSOL. *COMSOL Multiphysics Reference Manual, version 4.4*. COMSOL, Inc. 2013 (cit. on p. 49).

[COMSOL2013b] COMSOL. *Heat Transfer Module User's Guide, version 4.4*. COMSOL, Inc. 2013 (cit. on p. 49).

[COMSOL2018] COMSOL. *Heat Transfer Module User's Guide, version 5.4*. COMSOL, Inc. 2018 (cit. on p. 106).

[Connor+1995] M. Connor, S. Toll, J. -A. E. Månson, and A. G. Gibson. "A Model for the Consolidation of Aligned Thermoplastic Powder Impregnated Composites". In: *Journal of Thermoplastic Composite Materials* 8.2 (1995), pp. 138–162 (cit. on p. 43).

[Connor1995] M. Connor. "Consolidation mechanisms and interfacial phenomena in thermoplastic powder impregnated composites". PhD thesis. Ecole Polytechnique Fédérale de Lausanne, 1995 (cit. on p. 43).

[Correlated Solutions] Correlated Solutions. *Vic-3D v7 - Reference manual*. Correlated Solutions (cit. on p. 137).

[Cosson+2010] B. Cosson, F. Schmidt, Y. Le Maoult, and M. Bordival. "Infrared heating stage simulation of semi-transparent media (PET) using ray tracing method". In: *International Journal of Material Forming* 4.1 (May 2010), pp. 1–10 (cit. on p. 24).

[Cowper+1957] G. Cowper and P. Symonds. *Strain hardening and strain-rate effects in the impact loading of cantilever beams*. Tech. rep. Brown University, 1957 (cit. on p. 131).

[Creech+2006] G. Creech and A. K. Pickett. "Meso-modelling of Non-Crimp Fabric composites for coupled drape and failure analysis". In: *Journal of Materials Science* 41.20 (Aug. 2006), pp. 6725–6736 (cit. on p. 36).

[Cunningham+1997] J.E. Cunningham, P.F. Monaghan, M.T. Brogan, and S.F. Cassidy. "Modelling of pre-heating of flat panels prior to press forming". In: *Composites Part A: Applied Science and Manufacturing* 28.1 (Jan. 1997), pp. 17–24 (cit. on p. 21).

[Cunningham+1998] J.E. Cunningham, P.F. Monaghan, and M.T. Brogan. "Predictions of the temperature profile within composite sheets during pre-heating". In: *Composites Part A: Applied Science and Manufacturing* 29.1-2 (Jan. 1998), pp. 51–61 (cit. on pp. 21, 22).

[Cutolo+1992] D. Cutolo, P. Canonico, M. Marchetti, and A.M. Porcari. "Analysis of diaphragm forming of powder impregnated thermoplastic composites". In: *Composites Manufacturing* 3.1 (Jan. 1992), pp. 20–24 (cit. on p. 44).

[Daelemans+2016] L. Daelemans, J. Faes, S. Allaoui, G. Hivet, M. Dierick, L. Van Hoorebeke, and W. Van Paepegem. "Finite element simulation of the woven geometry and mechanical behaviour of a 3D woven dry fabric under tensile and shear loading using the digital element method". In: *Composites Science and Technology* 137 (Dec. 2016), pp. 177–187 (cit. on p. 34).

[Dangora+2015] L. M. Dangora, C. J. Hansen, C. J. Mitchell, J. A. Sherwood, and J. C. Parker. "Challenges associated with shear characterization of a cross-ply thermoplastic lamina using picture frame tests". In: *Composites Part A: Applied Science and Manufacturing* 78 (Nov. 2015), pp. 181–190 (cit. on pp. 29, 129).

[Dasgupta+1992] A. Dasgupta and R.K. Agarwal. "Orthotropic Thermal Conductivity of Plain-Weave Fabric Composites Using a Homogenization Technique". In: *Journal of Composite Materials* 26.18 (Dec. 1992), pp. 2736–2758 (cit. on p. 67).

[Dasgupta+1996] A. Dasgupta, R.K. Agarwal, and S.M. Bhandarkar. "Three-dimensional modeling of woven-fabric composites for effective thermo-mechanical and thermal properties". In: *Composites Science and Technology* 56.3 (Jan. 1996), pp. 209–223 (cit. on pp. 34, 67).

[Dauphin+2012] M. Dauphin, S. Albin, M. El Hafi, Y. Le Maoult, and F.M. Schmidt. "Towards thermal model of automotive lamps". In: *Proceedings of the 2012 International Conference on Quantitative InfraRed Thermography*. QIRT Council, 2012 (cit. on p. 74).

[De Almeida+2012] O. De Almeida, E. Bessard, and G. Bernhart. “Influence of processing parameters and semi-finished product on consolidation of carbon/peek laminates”. In: *Proceedings of the 15th European Conference on Composite Materials – ECCM15*. 2012 (cit. on p. 44).

[Desvignes1997] F. Desvignes. *Rayonnements optiques: radiometrie, photometrie*. Ed. by Masson. 1997 (cit. on p. 51).

[Döbrich+2013] O. Döbrich, T. Gereke, O. Diestel, S. Krzywinski, and C. Cherif. “Decoupling the bending behavior and the membrane properties of finite shell elements for a correct description of the mechanical behavior of textiles with a laminate formulation”. In: *Journal of Industrial Textiles* 44.1 (Feb. 2013), pp. 70–84 (cit. on p. 150).

[Donadei+2018] V. Donadei, F. Lionetto, M. Wielandt, A. Offringa, and A. Maffezzoli. “Effects of Blank Quality on Press-Formed PEKK/Carbon Composite Parts”. In: *Materials* 11.7 (June 2018), p. 1063 (cit. on p. 40).

[Donaldson+2005] K. Y. Donaldson, B. D. Trandell, Y. Lu, D. P. H. Hasselman, and N. Maurer. “Effect of Delamination on the Transverse Thermal Conductivity of a SiC-Fiber-Reinforced SiC-Matrix Composite”. In: *Journal of the American Ceramic Society* 81.6 (Jan. 2005), pp. 1583–1588 (cit. on p. 83).

[Dong+2009] Z. Dong and C. T. Sun. “Testing and modeling of yarn pull-out in plain woven Kevlar fabrics”. In: *Composites Part A: Applied Science and Manufacturing* 40.12 (Dec. 2009), pp. 1863–1869 (cit. on p. 127).

[Duan+2006] Y. Duan, M. Keefe, T.A. Bogetti, and B. Powers. “Finite element modeling of transverse impact on a ballistic fabric”. In: *International Journal of Mechanical Sciences* 48.1 (Jan. 2006), pp. 33–43 (cit. on p. 36).

[Dumont2003] F. Dumont. “Mesures de champs pour des essais de cisaillement sur des renforts tissésField measurements for shear tests on woven reinforcements”. In: *Mécanique & Industries* 4.6 (Dec. 2003), pp. 627–635 (cit. on pp. 28, 127).

[Durville+2018] D. Durville, I. Baydoun, H. Moustacas, G. Périé, and Y. Wielhorski. “Determining the initial configuration and characterizing the mechanical properties of 3D angle-interlock fabrics using finite element simulation”. In: *International Journal of Solids and Structures* 154 (Dec. 2018), pp. 97–103 (cit. on p. 34).

[Durville2002] D. Durville. “Modélisation par éléments finis du comportement mécanique de structures textiles : de la fibre au tissu”. In: *Revue Européenne des Éléments Finis* 11.2-4 (Jan. 2002), pp. 463–477 (cit. on p. 34).

[Durville2009] D. Durville. “A Finite Element Approach of the Behaviour of Woven Materials at Microscopic Scale”. In: *Mechanics of Microstructured Solids*. Springer Berlin Heidelberg, 2009, pp. 39–46 (cit. on p. 34).

[Durville2010] D. Durville. “Simulation of the mechanical behaviour of woven fabrics at the scale of fibers”. In: *International Journal of Material Forming* 3.S2 (Jan. 2010), pp. 1241–1251 (cit. on p. 34).

[El Bakali+2013] A. El Bakali, O. de Almeida, J. Bikard, M. Villière, F. Schmidt, Y. Le Maoult, and M. Dauphin. “Simulation of IR Heating for Composite Stamping”. In: *Key Engineering Materials* 554-557 (June 2013), pp. 1523–1529 (cit. on pp. 24, 49, 74).

[El Rassy+2019] E. El Rassy, Y. Billaud, and D. Saury. “Simultaneous and direct identification of thermophysical properties for orthotropic materials”. In: *Measurement* 135 (Mar. 2019), pp. 199–212 (cit. on p. 79).

[ElHage+2018] Y. El-Hage, S. Hind, and F. Robitaille. “Thermal conductivity of textile reinforcements for composites”. In: *Journal of Textiles and Fibrous Materials* 1 (Jan. 2018), p. 251522111775115 (cit. on p. 79).

[ElMazry+2013] C. El-Mazry, M. Ben Hassine, O. Correc, and X. Colin. “Thermal oxidation kinetics of additive free polyamide 6-6”. In: *Polymer Degradation and Stability* 98.1 (Jan. 2013), pp. 22–36 (cit. on p. 29).

[Faraj+2016] J. Faraj, N. Boyard, B. Pignon, J.-L. Bailleul, D. Delaunay, and G. Orange. “Crystallization kinetics of new low viscosity polyamides 66 for thermoplastic composites processing”. In: *Thermochimica Acta* 624 (Jan. 2016), pp. 27–34 (cit. on pp. 4, 56).

[Faraj2016] J. Faraj. “Analyse thermocinétique de la cristallisation en milieu confiné d’un composite à base d’une résine thermoplastique (Polyamide 66)”. PhD thesis. Université de Nantes, 2016 (cit. on pp. 67, 69).

[Fink+1978] D. G. Fink and H. W. Beaty. *Standard Handbook for Electrical Engineers*. McGraw-Hill, 1978 (cit. on p. 52).

[FLIR2010] FLIR. *FLIR SC640 - Technical specifications*. 2010 (cit. on p. 91).

[Friedrich+1997] K. Friedrich, M. Hou, and J. Krebs. “Thermoforming of continuous fibre/thermoplastic composite sheets”. In: *Composite Sheet Forming*. Elsevier, 1997, pp. 91–162 (cit. on p. 11).

[Friedrich+1998] K. Friedrich and M. Hou. “On stamp forming of curved and flexible geometry components from continuous glass fiber/polypropylene composites”. In: *Composites Part A: Applied Science and Manufacturing* 29.3 (Jan. 1998), pp. 217–226 (cit. on p. 14).

[Friedrich+2012] K. Friedrich and A. A. Almajid. “Manufacturing Aspects of Advanced Polymer Composites for Automotive Applications”. In: *Applied Composite Materials* 20.2 (Feb. 2012), pp. 107–128 (cit. on p. 3).

[Gasser+2000] A. Gasser, P. Boisse, and S. Hanklar. “Mechanical behaviour of dry fabric reinforcements. 3D simulations versus biaxial tests”. In: *Computational Materials Science* 17.1 (Jan. 2000), pp. 7–20 (cit. on pp. 26, 36).

[Gassoumi+2017] M. Gassoumi, S. Rolland du Roscoat, P. Casari, P. J. J. Dumont, L. Orgéas, and F. Jacquemin. “Shear behavior of thermoformed woven-textile thermoplastic prepregs: An analysis combining bias-extension test and X-ray microtomography”. In: *AIP Conference Proceedings*. Vol. 1896. Author(s), 2017 (cit. on p. 35).

[Gatouillat+2013] S. Gatouillat, A. Bareggi, E. Vidal-Sallé, and P. Boisse. "Meso modelling for composite preform shaping – Simulation of the loss of cohesion of the woven fibre network". In: *Composites Part A: Applied Science and Manufacturing* 54 (Nov. 2013), pp. 135–144 (cit. on p. 36).

[Gereke+2013] T. Gereke, O. Döbrich, M. Hübner, and C. Cherif. "Experimental and computational composite textile reinforcement forming: A review". In: *Composites Part A: Applied Science and Manufacturing* 46 (Mar. 2013), pp. 1–10 (cit. on p. 33).

[Giacomin+2010] A. J. Giacomin, A. W. Mix, and O. Mahmood. "Sag in thermoforming". In: *Polymer Engineering & Science* 50.10 (Sept. 2010), pp. 2060–2068 (cit. on p. 106).

[Gorczyca+2004] J. L. Gorczyca, J. A. Sherwood, L. Liu, and J. Chen. "Modeling of Friction and Shear in Thermostamping of Composites - Part I". In: *Journal of Composite Materials* 38.21 (Nov. 2004), pp. 1911–1929 (cit. on pp. 152, 159).

[GorczycaCole+2007] J. L. Gorczyca-Cole, J. A. Sherwood, and J. Chen. "A friction model for thermostamping commingled glass–polypropylene woven fabrics". In: *Composites Part A: Applied Science and Manufacturing* 38.2 (Feb. 2007), pp. 393–406 (cit. on p. 143).

[Grédiac+2016] M. Grédiac, F. Sur, and B. Blaysat. "The Grid Method for In-plane Displacement and Strain Measurement: A Review and Analysis". In: *Strain* 52.3 (May 2016), pp. 205–243 (cit. on p. 137).

[Gröschel+2017] C. Gröschel and D. Drummer. "Forming of thermoplastic matrix composites with gas pressure – the influence of blank holder and sheet temperature on the forming pressure and drawing ratio". In: *International Polymer Processing* 32.2 (May 2017), pp. 194–202 (cit. on p. 14).

[Grouve2012] W. Grouve. "Weld strength of laser-assisted tape-placed thermoplastic composites". PhD thesis. University of Twente, 2012 (cit. on pp. 64, 106).

[Gustafsson1991] S. E. Gustafsson. "Transient plane source techniques for thermal conductivity and thermal diffusivity measurements of solid materials". In: *Review of Scientific Instruments* 62.3 (Mar. 1991), pp. 797–804 (cit. on p. 68).

[GuzmanMaldonado+2015] E. Guzman-Maldonado, N. Hamila, P. Boisse, and J. Bikard. "Thermomechanical analysis, modelling and simulation of the forming of preimpregnated thermoplastics composites". In: *Composites Part A: Applied Science and Manufacturing* 78 (Nov. 2015), pp. 211–222 (cit. on pp. 14, 31, 37, 38).

[GuzmanMaldonado+2016] E. Guzman-Maldonado, N. Hamila, N. Naouar, G. Moulin, and P. Boisse. "Simulation of thermoplastic prepreg thermoforming based on a visco-hyperelastic model and a thermal homogenization". In: *Materials & Design* 93 (Mar. 2016), pp. 431–442 (cit. on pp. 31, 32, 38, 39, 118, 129, 156).

[GuzmanMaldonado2016] E. Guzman-Maldonado. "Modélisation et simulation de la mise en forme des composites préimprégnés à matrice thermoplastiques et fibres continues". PhD thesis. Institut National des Sciences Appliquées de Lyon, 2016 (cit. on pp. 29, 121, 156, 160).

[Haanappel+2012] S. P. Haanappel, U. Sachs, R. H.W. ten Thije, B. Rietman, and R. Akkerman. “Forming of thermoplastic composites”. In: *Key Engineering Materials* 504-506 (Feb. 2012), pp. 237–242 (cit. on p. 94).

[Haanappel+2014] S.P. Haanappel, R.H.W. ten Thije, U. Sachs, B. Rietman, and R. Akkerman. “Formability analyses of uni-directional and textile reinforced thermoplastics”. In: *Composites Part A: Applied Science and Manufacturing* 56 (Jan. 2014), pp. 80–92 (cit. on pp. 14, 31, 38, 94, 129).

[Hamila+2009] N. Hamila, P. Boisse, F. Sabourin, and M. Brunet. “A semi-discrete shell finite element for textile composite reinforcement forming simulation”. In: *International Journal for Numerical Methods in Engineering* 79.12 (Sept. 2009), pp. 1443–1466 (cit. on p. 150).

[Hamila+2013] N. Hamila and P. Boisse. “Locking in simulation of composite reinforcement deformations. Analysis and treatment”. In: *Composites Part A: Applied Science and Manufacturing* 53 (Oct. 2013), pp. 109–117 (cit. on p. 150).

[Harrison+2004] P. Harrison, M.J. Clifford, and A.C. Long. “Shear characterisation of viscous woven textile composites: a comparison between picture frame and bias extension experiments”. In: *Composites Science and Technology* 64.10-11 (Aug. 2004), pp. 1453–1465 (cit. on pp. 14, 29, 31, 127).

[Harrison+2012] P. Harrison, F. Abdiwi, Z. Guo, P. Potluri, and W.R. Yu. “Characterising the shear–tension coupling and wrinkling behaviour of woven engineering fabrics”. In: *Composites Part A: Applied Science and Manufacturing* 43.6 (June 2012), pp. 903–914 (cit. on p. 33).

[Harrison+2013] P. Harrison, R. Gomes, and N. Curado-Correia. “Press forming a 0/90 cross-ply advanced thermoplastic composite using the double-dome benchmark geometry”. In: *Composites Part A: Applied Science and Manufacturing* 54 (Nov. 2013), pp. 56–69 (cit. on pp. 38, 94, 136).

[Härtel+2014] F. Härtel and P. Harrison. “Evaluation of normalisation methods for uniaxial bias extension tests on engineering fabrics”. In: *Composites Part A: Applied Science and Manufacturing* 67 (Dec. 2014), pp. 61–69 (cit. on pp. 31, 126).

[Hartigan+1979] J. A. Hartigan and M. A. Wong. “Algorithm AS 136: A K-Means Clustering Algorithm”. In: *Applied Statistics* 28.1 (1979), p. 100 (cit. on p. 70).

[Hasselman+1987] D. P. H. Hasselman and L. F. Johnson. “Effective Thermal Conductivity of Composites with Interfacial Thermal Barrier Resistance”. In: *Journal of Composite Materials* 21.6 (June 1987), pp. 508–515 (cit. on pp. 67, 70).

[Hay+2004] B. Hay, J.-R. Filtz, and J.-C. Batsale. “Mesure de la diffusivité thermique par la méthode flash”. In: *Techniques de l’Ingénieur* (2004) (cit. on p. 67).

[Heardman+2001] E. Heardman, C. Lekakou, and M. G. Bader. “In-plane permeability of sheared fabrics”. In: *Composites Part A: Applied Science and Manufacturing* 32.7 (July 2001), pp. 933–940 (cit. on p. 130).

[Heisey+1988] F. L. Heisey and K. D. Haller. “Fitting Woven Fabric to Surfaces in Three Dimensions”. In: *Journal of the Textile Institute* 79.2 (Jan. 1988), pp. 250–263 (cit. on p. 37).

[Hoff+1989] S. J. Hoff and K. A. Janni. “Monte-Carlo technique for the determination of thermal radiation shape factors”. In: *Journal of the American Society of Agricultural Engineering* 32.3 (1989) (cit. on p. 20).

[Holmes2017] M. Holmes. “High volume composites for the automotive challenge”. In: *Reinforced Plastics* 61.5 (Sept. 2017), pp. 294–298 (cit. on p. 3).

[Hou+1991] M. Hou and K. Friedrich. “Stamp forming of continuous carbon fibre/polypropylene composites”. In: *Composites Manufacturing* 2.1 (Mar. 1991), pp. 3–9 (cit. on p. 11).

[Hou1996] M. Hou. “Stamp forming of fabric-reinforced thermoplastic composites”. In: *Polymer Composites* 17.4 (Aug. 1996), pp. 596–603 (cit. on p. 11).

[Howell+2011] J. R. Howell and M. Pinar Mengüç. “Radiative transfer configuration factor catalog: a listing of relations for common geometries”. In: *Journal of Quantitative Spectroscopy and Radiative Transfer* 112.5 (Mar. 2011), pp. 910–912 (cit. on p. 19).

[Hwang+2002] S.-F. Hwang and K.-J. Hwang. “Stamp forming of locally heated thermoplastic composites”. In: *Composites Part A: Applied Science and Manufacturing* 33.5 (May 2002), pp. 669–676 (cit. on pp. 15, 109, 160).

[Ibos+2016] L. Ibos, J.-P. Monchau, V. Feuillet, J. Dumoulin, P. Ausset, J. Hameury, and B. Hay. “Investigation of the directional emissivity of materials using infrared thermography coupled with a periodic excitation”. In: *Proceedings of the 2016 International Conference on Quantitative InfraRed Thermography*. QIRT Council, 2016 (cit. on p. 106).

[Incropera+2006] F. P. Incropera, D. P. DeWitt, T. L. Bergman, and A. S. Lavine. *Fundamentals of heat and mass transfer*. John Wiley and Sons, 2006 (cit. on pp. 99, 100).

[Ishikawa+2018] T. Ishikawa, K. Amaoka, Y. Masubuchi, T. Yamamoto, A. Yamanaka, M. Arai, and J. Takahashi. “Overview of automotive structural composites technology developments in Japan”. In: *Composites Science and Technology* 155 (Feb. 2018), pp. 221–246 (cit. on p. 3).

[ISO2012] ISO. *ISO 1183-1: Plastics – Methods for determining the density of non-cellular plastics*. International Organization for Standardization (ISO), 2012 (cit. on p. 65).

[Jannot+2010] Y Jannot, V Felix, and A Degiovanni. “A centered hot plate method for measurement of thermal properties of thin insulating materials”. In: *Measurement Science and Technology* 21.3 (Feb. 2010), p. 035106 (cit. on p. 67).

[Jauffrès+2009] D. Jauffrès, J. A. Sherwood, C. D. Morris, and J. Chen. “Discrete mesoscopic modeling for the simulation of woven-fabric reinforcement forming”. In: *International Journal of Material Forming* 3.S2 (Nov. 2009), pp. 1205–1216 (cit. on pp. 34, 43).

[Kadoya+1985] K. Kadoya, N. Matsunaga, and A. Nagashima. “Viscosity and Thermal Conductivity of Dry Air in the Gaseous Phase”. In: *Journal of Physical and Chemical Reference Data* 14.4 (Oct. 1985), pp. 947–970 (cit. on p. 81).

[Kalaprasad+2000] G. Kalaprasad, P. Pradeep, George Mathew, C. Pavithran, and Sabu Thomas. “Thermal conductivity and thermal diffusivity analyses of low-density polyethylene composites reinforced with sisal, glass and intimately mixed sisal/glass fibres”. In: *Composites Science and Technology* 60.16 (Dec. 2000), pp. 2967–2977 (cit. on p. 70).

[Kashani+2016] M. Haghi Kashani, A. Rashidi, B.J. Crawford, and A.S. Milani. “Analysis of a two-way tension-shear coupling in woven fabrics under combined loading tests: global to local transformation of non-orthogonal normalized forces and displacements”. In: *Composites Part A: Applied Science and Manufacturing* 88 (Sept. 2016), pp. 272–285 (cit. on p. 33).

[Kashani+2017] M. Haghi Kashani, A. Hosseini, F. Sassani, F.K. Ko, and A.S. Milani. “Understanding different types of coupling in mechanical behavior of woven fabric reinforcements: a critical review and analysis”. In: *Composite Structures* 179 (Nov. 2017), pp. 558–567 (cit. on p. 33).

[Kawabata+1973] S. Kawabata, Masako Niwa, and H. Kawai. “The finite-deformation theory of plain weave fabrics—Part I: The biaxial deformation theory”. In: *The Journal of The Textile Institute* 64.1 (Jan. 1973), pp. 21–46 (cit. on pp. 26, 34, 35).

[Kawabata+2002] S. Kawabata and R.S. Rengasamy. “Thermal conductivity of unidirectional fibre composites made from yarns and computation of thermal conductivity of yarns”. In: *Indian Journal of Fibre & Textile Research* 27.3 (2002), pp. 217–223 (cit. on p. 70).

[Keeler1968] S. P. Keeler. “Circular Grid System — A Valuable Aid for Evaluating Sheet Metal Formability”. In: *SAE Transactions* 77 (1968), pp. 371–379 (cit. on p. 137).

[Khan+2010] M.A. Khan, T. Mabrouki, E. Vidal-Sallé, and P. Boisse. “Numerical and experimental analyses of woven composite reinforcement forming using a hypoelastic behaviour. Application to the double dome benchmark”. In: *Journal of Materials Processing Technology* 210.2 (Jan. 2010), pp. 378–388 (cit. on pp. 37, 38, 116, 118, 121, 136).

[Knights1996] M. Knights. “The truth about heaters”. In: *Plastics Technology* 42.5 (1996), pp. 38–46 (cit. on p. 11).

[Labanieh+2018] A. R. Labanieh, C. Garnier, P. Ouagne, O. Dalverny, and D. Soulat. “Intra-ply yarn sliding defect in hemisphere preforming of a woven preform”. In: *Composites Part A: Applied Science and Manufacturing* 107 (Apr. 2018), pp. 432–446 (cit. on pp. 143, 144).

[Labeas+2008] G.N. Labeas, V.B. Watiti, and C. V. Katsiropoulos. “Thermomechanical simulation of infrared heating diaphragm forming process for thermoplastic parts”. In: *Journal of Thermoplastic Composite Materials* 21.4 (July 2008), pp. 353–370 (cit. on p. 22).

[Land+2015] P. Land, R. Crossley, D. Branson, and S. Ratchev. "Technology Review of Thermal Forming Techniques for use in Composite Component Manufacture". In: *SAE International Journal of Materials and Manufacturing* 9.1 (Sept. 2015), pp. 81–89 (cit. on p. 5).

[Latil+2011] P. Latil, L. Orgéas, C. Geindreau, P.J.J. Dumont, and S. Rolland du Roscoat. "Towards the 3D in situ characterisation of deformation micro-mechanisms within a compressed bundle of fibres". In: *Composites Science and Technology* 71.4 (Feb. 2011), pp. 480–488 (cit. on p. 35).

[Launay+2008] J. Launay, G. Hivet, A. V. Duong, and P. Boisse. "Experimental analysis of the influence of tensions on in plane shear behaviour of woven composite reinforcements". In: *Composites Science and Technology* 68.2 (Feb. 2008), pp. 506–515 (cit. on pp. 31, 126).

[Le Louët+2017] V. Le Louët, B. Rousseau, S. Le Corre, N. Boyard, X. Tardif, J. Delmas, and D. Delaunay. "Directional spectral reflectivity measurements of a carbon fibre reinforced composite up to 450 °C". In: *International Journal of Heat and Mass Transfer* 112 (Sept. 2017), pp. 882–890 (cit. on pp. 64, 106).

[Lebrun+2003] G. Lebrun, M. N. Bureau, and J. Denault. "Evaluation of bias-extension and picture-frame test methods for the measurement of intraply shear properties of PP/glass commingled fabrics". In: *Composite Structures* 61.4 (Sept. 2003), pp. 341–352 (cit. on pp. 14, 29, 31, 43).

[Lebrun+2004] G. Lebrun, M. N. Bureau, and J. Denault. "Thermoforming-Stamping of Continuous Glass Fiber/Polypropylene Composites: Interlaminar and Tool–Laminate Shear Properties". In: *Journal of Thermoplastic Composite Materials* 17.2 (Mar. 2004), pp. 137–165 (cit. on pp. 143, 152).

[Lee+2001] W. B. Lee, C. F. Cheung, and J. G. Li. "Applications of virtual manufacturing in materials processing". In: *Journal of Materials Processing Technology* 113.1-3 (June 2001), pp. 416–423 (cit. on p. 5).

[Lee+2009] W. Lee, M.-K. Um, J.-H. Byun, P. Boisse, and J. Cao. "Numerical study on thermo-stamping of woven fabric composites based on double-dome stretch forming". In: *International Journal of Material Forming* 3.S2 (Dec. 2009), pp. 1217–1227 (cit. on p. 156).

[Lee+2017] J.-M. Lee, B.-M. Kim, C.-J. Lee, and D.-C. Ko. "A characterisation of tool-ply friction behaviors in thermoplastic composite". In: *Procedia Engineering* 207 (2017), pp. 90–94 (cit. on p. 143).

[Leuenberger+1956] H. Leuenberger and R.A. Person. "Compilation of radiation shape factors for cylindrical assemblies". In: *American Society of Mechanical Engineers* 56-A-144 (1956) (cit. on p. 49).

[Li+2011] H. Li, S. Li, and Y. Wang. "Prediction of effective thermal conductivities of woven fabric composites using unit cells at multiple length scales". In: *Journal of Materials Research* 26.03 (Feb. 2011), pp. 384–394 (cit. on p. 34).

[Liang+2014] B. Liang, N. Hamila, M. Peillon, and P. Boisse. “Analysis of thermoplastic prepreg bending stiffness during manufacturing and of its influence on wrinkling simulations”. In: *Composites Part A: Applied Science and Manufacturing* 67 (Dec. 2014), pp. 111–122 (cit. on pp. 14, 32, 38, 141, 143, 159).

[Lin+2007] H. Lin, J. Wang, A. C. Long, M. J. Clifford, and P. Harrison. “Predictive modelling for optimization of textile composite forming”. In: *Composites Science and Technology* 67.15-16 (Dec. 2007), pp. 3242–3252 (cit. on p. 31).

[Lin+2011] H. Lin, L. P. Brown, and A. C. Long. “Modelling and Simulating Textile Structures Using TexGen”. In: *Advanced Materials Research* 331 (Sept. 2011), pp. 44–47 (cit. on p. 35).

[Liraut+2015] G. Liraut and K. Bender. *Practical application of thermoplastic composites for body-in-white application development: A collaborative approach between DuPont and Renault*. Tech. rep. DuPont, 2015 (cit. on p. 3).

[Log+1995] T. Log and S. E. Gustafsson. “Transient plane source (TPS) technique for measuring thermal transport properties of building materials”. In: *Fire and Materials* 19.1 (Jan. 1995), pp. 43–49 (cit. on p. 68).

[Loix+2008] F. Loix, P. Badel, L. Orgéas, C. Geindreau, and P. Boisse. “Woven fabric permeability: From textile deformation to fluid flow mesoscale simulations”. In: *Composites Science and Technology* 68.7-8 (June 2008), pp. 1624–1630 (cit. on p. 34).

[Lomov+2000] S.V. Lomov, A.V. Gusakov, G. Huysmans, A. Prodromou, and I. Verpoest. “Textile geometry preprocessor for meso-mechanical models of woven composites”. In: *Composites Science and Technology* 60.11 (Aug. 2000), pp. 2083–2095 (cit. on p. 35).

[Long+2001] A. C. Long, M. J. Clifford, P. Harrison, and C. D. Rudd. “Modelling of draping and deformation for textile composites.” In: *ICMAC–international conference for manufacturing of advanced composites. Belfast: IOM Communications*. 2001 (cit. on p. 28).

[Machado+2016a] M. Machado, M. Fischlschweiger, and Z. Major. “A rate-dependent non-orthogonal constitutive model for describing shear behaviour of woven reinforced thermoplastic composites”. In: *Composites Part A: Applied Science and Manufacturing* 80 (Jan. 2016), pp. 194–203 (cit. on pp. 31, 37, 38, 116, 118, 136, 137, 150).

[Machado+2016b] M. Machado, L. Murenu, M. Fischlschweiger, and Z. Major. “Analysis of the thermomechanical shear behaviour of woven-reinforced thermoplastic-matrix composites during forming”. In: *Composites Part A: Applied Science and Manufacturing* 86 (July 2016), pp. 39–48 (cit. on pp. 14, 31, 38, 39, 129, 131, 152, 177).

[Mack+1956] C. Mack and H. M. Taylor. “The Fitting of Woven Cloth to Surfaces”. In: *Journal of the Textile Institute Transactions* 47.9 (Sept. 1956), T477–T488 (cit. on p. 36).

[Mahlke+1989] M. Mahlke, G. Menges, and W. Michaeli. “New strategies to preheat glass mat reinforced thermoplastics (GMT)”. In: *Proceedings of ANTEC1989*. Ed. by Society of Plastics Engineers. 1989, pp. 873–875 (cit. on p. 13).

[Mainguy+1991] S. Mainguy, M. Olivier, M. A. Josse, and M. Guidon. “Description and calibration of a fully automated infrared scatterometer”. In: *Optical Scatter: Applications, Measurement, and Theory*. Ed. by John C. Stover. SPIE, Dec. 1991 (cit. on p. 106).

[Maire+2001] E. Maire, J. Y. Buffière, L. Salvo, J. J. Blandin, W. Ludwig, and J. M. Létang. “On the Application of X-ray Microtomography in the Field of Materials Science”. In: *Advanced Engineering Materials* 3.8 (Aug. 2001), p. 539 (cit. on p. 35).

[Martin+1997] T. A. Martin, G. R. Christie, and D. Bhattacharyya. “Grid strain analysis and its application in composite sheet forming”. In: *Composite Materials Series*. Elsevier, 1997, pp. 217–245 (cit. on p. 137).

[Mathieu+2015] S. Mathieu, N. Hamila, F. Bouillon, and P. Boisse. “Enhanced modeling of 3D composite preform deformations taking into account local fiber bending stiffness”. In: *Composites Science and Technology* 117 (Sept. 2015), pp. 322–333 (cit. on p. 159).

[Mathijsen2016] D. Mathijsen. “Thermoplastic composites keep gaining momentum in the automotive industry”. In: *Reinforced Plastics* 60.6 (Nov. 2016), pp. 408–412 (cit. on p. 3).

[Matsumoto+1999] T. Matsumoto, A. Cezairliyan, and D. Basak. “Hemispherical total emissivity of Niobium, Molybdenum, and Tungsten at high temperatures using a combined transient and brief steady-state technique”. In: *International Journal of Thermophysics* 20.3 (1999), pp. 943–952 (cit. on p. 51).

[Maxwell+1986] G. M. Maxwell, M. J. Bailey, and V. W. Goldschmidt. “Calculations of the radiation configuration factor using ray casting”. In: *Computer-Aided Design* 18.7 (Sept. 1986), pp. 371–379 (cit. on p. 23).

[Mazumder+2000] S. Mazumder and A. Kersch. “A fast Monte Carlo scheme for thermal radiation in semiconductor applications”. In: *Numerical Heat Transfer, Part B: Fundamentals* 37.2 (Mar. 2000), pp. 185–199 (cit. on p. 24).

[McGuinness+1998] G. B. McGuinness and C. M. Ó Brádaigh. “Characterisation of thermoplastic composite melts in rhombus-shear: the picture-frame experiment”. In: *Composites Part A: Applied Science and Manufacturing* 29.1-2 (Jan. 1998), pp. 115–132 (cit. on p. 29).

[Meyer+2009] B. C. Meyer, C. V. Katsiropoulos, and S. G. Pantelakis. “Hot forming behavior of non-crimp fabric peek/c thermoplastic composites”. In: *Composite Structures* 90.2 (Sept. 2009), pp. 225–232 (cit. on p. 44).

[Meyer1994] F. Meyer. “Topographic distance and watershed lines”. In: *Signal Processing* 38.1 (July 1994), pp. 113–125 (cit. on p. 173).

[Michaud+2011] R. A. Michaud and A. J. Giacomin. “Sheet temperature in thermoforming”. In: *Journal of Plastic Film & Sheeting* 27.4 (Oct. 2011), pp. 293–330 (cit. on p. 106).

[Milani+2007] A.S. Milani, J.A. Nemes, R.C. Abeyaratne, and G.A. Holzapfel. “A method for the approximation of non-uniform fiber misalignment in textile composites using picture frame test”. In: *Composites Part A: Applied Science and Manufacturing* 38.6 (June 2007), pp. 1493–1501 (cit. on p. 29).

[Minissale+2017] M. Minissale, C. Pardanaud, R. Bisson, and L. Gallais. “The temperature dependence of optical properties of tungsten in the visible and near-infrared domains: an experimental and theoretical study”. In: *Journal of Physics D: Applied Physics* 50.45 (Oct. 2017), p. 455601 (cit. on p. 51).

[Mishra+2016] R. R. Mishra and A. K. Sharma. “Microwave–material interaction phenomena: Heating mechanisms, challenges and opportunities in material processing”. In: *Composites Part A: Applied Science and Manufacturing* 81 (Feb. 2016), pp. 78–97 (cit. on p. 11).

[Mock2019] P. Mock. *CO_2 emission standards for passenger cars and light-commercial vehicles in the European Union*. Tech. rep. The International Council on Clean Transportation, 2019 (cit. on p. 2).

[Modest2013] M. F. Modest. *Radiative Heat Transfer*. Elsevier LTD, Oxford, Apr. 19, 2013 (cit. on p. 19).

[Monaghan+1991] P. F. Monaghan, M. T. Brogan, and P. H. Oosthuizen. “Heat transfer in an autoclave for processing thermoplastic composites”. In: *Composites Manufacturing* 2.3-4 (Jan. 1991), pp. 233–242 (cit. on p. 21).

[Monteix2001] S. Monteix. “Modélisation du chauffage convecto-radiatif de préformes en PET pour la réalisation de corps creux”. PhD thesis. École des Mines de Paris, 2001 (cit. on pp. 22, 23, 51).

[Muhlbauer+2007] A. Muhlbauer, A. Von Starck, and C. Kramer. *Handbook of Thermoprocessing Technologies: Fundamentals - Processes - Components - Safety*. Vulkan-Verlag GmbH, 2007 (cit. on p. 11).

[Murtagh+1995] A. M. Murtagh, J. J. Lennon, and P. J. Mallon. “Surface friction effects related to pressforming of continuous fibre thermoplastic composites”. In: *Composites Manufacturing* 6.3-4 (Jan. 1995), pp. 169–175 (cit. on pp. 143, 152).

[Najjar+2013] W. Najjar, X. Legrand, P. Dal Santo, D. Soulat, and S. Boude. “Analysis of the Blank Holder Force Effect on the Preforming Process Using a Simple Discrete Approach”. In: *Key Engineering Materials* 554-557 (June 2013), pp. 441–446 (cit. on p. 139).

[Nakouzi+2011] S. Nakouzi, J. Pancrace, F. Schmidt, Y. Le Maoult, and F. Berthet. “Simulations of an Infrared Composite Curing Process”. In: *Advanced Engineering Materials* 13.7 (May 2011), pp. 604–608 (cit. on pp. 24, 50).

[Nakouzi+2012] S. Nakouzi, F. Berthet, D. Delaunay, Y. Le Maoult, Fabrice Schmidt, and Vincent Sobotka. “Optimization of the Incident IR Heat Flux upon a 3D Geometry Composite Part (Carbon/Epoxy)”. In: *Key Engineering Materials* 504-506 (Feb. 2012), pp. 1085–1090 (cit. on pp. 24, 110).

[Nakouzi2012] S. Nakouzi. “Modélisation du procédé de cuisson de composites infusés par chauffage infrarouge”. PhD thesis. Université de Toulouse, 2012 (cit. on pp. 49, 84).

[Naouar+2014] N. Naouar, E. Vidal-Sallé, J. Schneider, E. Maire, and P. Boisse. "Meso-scale FE analyses of textile composite reinforcement deformation based on X-ray computed tomography". In: *Composite Structures* 116 (Sept. 2014), pp. 165–176 (cit. on p. 35).

[Nawrocki+2000] A. Nawrocki and M. Labrosse. "A finite element model for simple straight wire rope strands". In: *Computers & Structures* 77.4 (July 2000), pp. 345–359 (cit. on p. 34).

[Nilakantan+2010] G. Nilakantan, M. Keefe, T. A. Bogetti, R. Adkinson, and J. W. Gillespie. "On the finite element analysis of woven fabric impact using multiscale modeling techniques". In: *International Journal of Solids and Structures* 47.17 (Aug. 2010), pp. 2300–2315 (cit. on p. 36).

[NosratNezami+2014] F. Nosrat-Nezami, T. Gereke, C. Eberdt, and C. Cherif. "Characterisation of the shear–tension coupling of carbon-fibre fabric under controlled membrane tensions for precise simulative predictions of industrial preforming processes". In: *Composites Part A: Applied Science and Manufacturing* 67 (Dec. 2014), pp. 131–139 (cit. on p. 33).

[Offringa1996] A. R. Offringa. "Thermoplastic composites—rapid processing applications". In: *Composites Part A: Applied Science and Manufacturing* 27.4 (Jan. 1996), pp. 329–336 (cit. on p. 159).

[Orange+2014] G. Orange, E. Bessard, J. Bréard, L. Bizet, J.L. Bailleul, S. Comas-Cardona, C. Binetruy, P. Boisse, and M. Gomina. "Development of composite parts with RTM process based on new high fluidity thermoplastic polymers". In: *Proceedings of the 12th conference on Flow Processes in Composite Materials*. 2014 (cit. on p. 57).

[Otsu1979] N. Otsu. "A Threshold Selection Method from Gray-Level Histograms". In: *IEEE Transactions on Systems, Man, and Cybernetics* 9.1 (Jan. 1979), pp. 62–66 (cit. on p. 61).

[Ouagne+2013] P. Ouagne, D. Soulat, J. Moothoo, E. Capelle, and S. Gueret. "Complex shape forming of a flax woven fabric, analysis of the tow buckling and misalignment defect". In: *Composites Part A: Applied Science and Manufacturing* 51 (Aug. 2013), pp. 1–10 (cit. on p. 144).

[Patou+2018] J. Patou, R. Bonnaire, E. De Luycker, and G. Bernhart. "Influence of consolidation process on voids and mechanical properties of powdered and commingled carbon/PPS laminates". In: *Composites Part A: Applied Science and Manufacturing* (Nov. 2018) (cit. on pp. 41, 44).

[Patou2018] J. Patou. "Elaboration de pièces composites complexes par consolidation autoclave à partir de préformes textiles thermoplastiques renforcées fibres de carbone". PhD thesis. IMT Mines Albi, 2018 (cit. on p. 137).

[PechMay+2016] N. W. Pech-May, A. Mendioroz, and A. Salazar. "Simultaneous measurement of the in-plane and in-depth thermal diffusivity of solids using pulsed infrared thermography with focused illumination". In: *NDT & E International* 77 (Jan. 2016), pp. 28–34 (cit. on p. 67).

[Peeters+2016] J. Peeters, B. Ribbens, J.J.J. Dirckx, and G. Steenackers. “Determining directional emissivity: Numerical estimation and experimental validation by using infrared thermography”. In: *Infrared Physics & Technology* 77 (July 2016), pp. 344–350 (cit. on p. 106).

[Peng+2002] X. Peng and J. Cao. “A dual homogenization and finite element approach for material characterization of textile composites”. In: *Composites Part B: Engineering* 33.1 (Jan. 2002), pp. 45–56 (cit. on p. 121).

[Peng+2003] X. Peng and J. Cao. *Bias extension test standard*. Tech. rep. Northwestern University, 2003 (cit. on p. 125).

[Peng+2005] X. Peng and J. Cao. “A continuum mechanics-based non-orthogonal constitutive model for woven composite fabrics”. In: *Composites Part A: Applied Science and Manufacturing* 36.6 (June 2005), pp. 859–874 (cit. on pp. 37, 38, 116, 121).

[Peng+2011] X. Peng and Z. U. Rehman. “Textile composite double dome stamping simulation using a non-orthogonal constitutive model”. In: *Composites Science and Technology* 71.8 (May 2011), pp. 1075–1081 (cit. on p. 116).

[Peng+2013] X. Peng, Z. Guo, T. Du, and W.-R. Yu. “A simple anisotropic hyperelastic constitutive model for textile fabrics with application to forming simulation”. In: *Composites Part B: Engineering* 52 (Sept. 2013), pp. 275–281 (cit. on p. 118).

[Pettersson+2000] M. Pettersson and S. Stenström. “Modelling of an electric IR heater at transient and steady state conditions”. In: *International Journal of Heat and Mass Transfer* 43.7 (Apr. 2000), pp. 1209–1222 (cit. on p. 22).

[Pierce+2014] R. Pierce, B. Falzon, M. Thompson, and R. Boman. “Implementation of a Non-Orthogonal Constitutive Model for the Finite Element Simulation of Textile Composite Draping”. In: *Applied Mechanics and Materials* 553 (May 2014), pp. 76–81 (cit. on pp. 38, 116, 121).

[Porcher Industries2017] Porcher Industries. *Selector Guide – Composites*. 2017 (cit. on p. 43).

[Prodromou+1997] A. G. Prodromou and J. Chen. “On the relationship between shear angle and wrinkling of textile composite preforms”. In: *Composites Part A: Applied Science and Manufacturing* 28.5 (Jan. 1997), pp. 491–503 (cit. on p. 28).

[Quaglini+2008] V. Quaglini, C. Corazza, and C. Poggi. “Experimental characterization of orthotropic technical textiles under uniaxial and biaxial loading”. In: *Composites Part A: Applied Science and Manufacturing* 39.8 (Aug. 2008), pp. 1331–1342 (cit. on p. 118).

[Rao+1996] V. R. Rao and V. M. K. Sastri. “Efficient evaluation of diffuse view factors for radiation”. In: *International Journal of Heat and Mass Transfer* 39.6 (Apr. 1996), pp. 1281–1286 (cit. on p. 23).

[Rayleigh1892] Lord Rayleigh. “LVI. On the influence of obstacles arranged in rectangular order upon the properties of a medium”. In: *The London, Edinburgh, and Dublin Philosophical Magazine and Journal of Science* 34.211 (Dec. 1892), pp. 481–502 (cit. on p. 67).

[Redelbach+2012] M. Redelbach, M. Klötzke, and H. E. Friedrich. “Impact of lightweight design on energy consumption and cost effectiveness of alternative powertrain concepts”. In: *Proceedings of the European Electric Vehicle Conference (EEVC)*. 2012 (cit. on p. 2).

[Renault2001] T. Renault. “Les matériaux composites dans l’automobile”. In: *Mécanique & Industries* 2.3 (June 2001), pp. 211–218 (cit. on p. 3).

[Renault2015] T. Renault. “Developments in thermoplastic composites for automotive applications”. In: *Franco-British Symposium on Composite Materials*. 2015 (cit. on pp. 4, 40).

[Reynolds1961] P. M. Reynolds. “Spectral emissivity of 99.7% aluminium between 200 and 540 C”. In: *British Journal of Applied Physics* 12.3 (Mar. 1961), pp. 111–114 (cit. on p. 100).

[Rhoades+2015] A. M. Rhoades, J. L. Williams, and R. Androsch. “Crystallization kinetics of polyamide 66 at processing-relevant cooling conditions and high supercooling”. In: *Thermochimica Acta* 603 (Mar. 2015), pp. 103–109 (cit. on p. 148).

[Ropers+2016] S. Ropers, M. Kardos, and T. A. Osswald. “A thermo-viscoelastic approach for the characterization and modeling of the bending behavior of thermoplastic composites”. In: *Composites Part A: Applied Science and Manufacturing* 90 (Nov. 2016), pp. 22–32 (cit. on pp. 14, 32).

[Ropers+2017] S. Ropers, U. Sachs, M. Kardos, and T. A. Osswald. “A thermo-viscoelastic approach for the characterization and modeling of the bending behavior of thermoplastic composites – Part II”. In: *Composites Part A: Applied Science and Manufacturing* 96 (May 2017), pp. 67–76 (cit. on p. 32).

[Rudkin+1962] R. L. Rudkin, W. J. Parker, and R. J. Jenkins. “Measurements of the Thermal Properties of Metals at Elevated Temperatures”. In: *Temperature; Its Measurement and Control in Science and Industry*. Reinhold Publishing Corp, 1962 (cit. on p. 51).

[Sachs+2014] U. Sachs, R. Akkerman, and S. P. Haanappel. “Bending Characterization of UD Composites”. In: *Key Engineering Materials* 611-612 (May 2014), pp. 399–406 (cit. on p. 32).

[Schindelin+2012] J. Schindelin, I. Arganda-Carreras, E. Frise, V. Kaynig, M. Longair, T. Pietzsch, S. Preibisch, C. Rueden, S. Saalfeld, B. Schmid, J.-Y. Tinevez, D. J. White, V. Hartenstein, K. Eliceiri, P. Tomancak, and A. Cardona. “Fiji: an open-source platform for biological-image analysis”. In: *Nature Methods* 9.7 (July 2012), pp. 676–682 (cit. on p. 126).

[Schmidt+2003] F. Schmidt, Y. Le Maoult, and S. Monteix. “Modelling of infrared heating of thermoplastic sheet used in thermoforming process”. In: *Journal of Materials Processing Technology* 143-144 (Dec. 2003), pp. 225–231 (cit. on p. 23).

[Sharma+2003] S. B. Sharma, M. P. F. Sutcliffe, and S. H. Chang. “Characterisation of material properties for draping of dry woven composite material”. In: *Composites Part A: Applied Science and Manufacturing* 34.12 (Dec. 2003), pp. 1167–1175 (cit. on pp. 28, 33).

[Sherburn2007] M. Sherburn. “Geometric and mechanical modelling of textiles”. PhD thesis. University of Nottingham, 2007 (cit. on p. 35).

[Sherwood+2012] J. A. Sherwood, K. A. Fetfatsidis, and J. L. Gorczyca andd L. Berger. “Fabric thermostamping in polymer matrix composites”. In: *Manufacturing Techniques for Polymer Matrix Composites*. Elsevier, 2012, pp. 139–181 (cit. on p. 28).

[Shi+2012] B.-Q. Shi and J. Liang. “Circular grid pattern based surface strain measurement system for sheet metal forming”. In: *Optics and Lasers in Engineering* 50.9 (Sept. 2012), pp. 1186–1195 (cit. on pp. 137, 139, 177).

[Siegel+1992] R. Siegel and J. R. Howell. *Thermal Radiation Heat Transfer*. Third. Taylor & Francis, 1992 (cit. on p. 51).

[Silvestri+2019] S. Silvestri and R. Pecnik. “A fast GPU Monte Carlo radiative heat transfer implementation for coupling with direct numerical simulation”. In: *Journal of Computational Physics: X* 3 (June 2019), p. 100032 (cit. on p. 24).

[Sjölander+2016] J. Sjölander, P. Hallander, and M. Åkermo. “Forming induced wrinkling of composite laminates: A numerical study on wrinkling mechanisms”. In: *Composites Part A: Applied Science and Manufacturing* 81 (Feb. 2016), pp. 41–51 (cit. on p. 152).

[Skelton1976] J. Skelton. “Fundamentals of Fabric Shear”. In: *Textile Research Journal* 46.12 (Dec. 1976), pp. 862–869 (cit. on p. 28).

[Skordos+2007] A. A. Skordos, C. Monroy Aceves, and M. P. F. Sutcliffe. “A simplified rate dependent model of forming and wrinkling of pre-impregnated woven composites”. In: *Composites Part A: Applied Science and Manufacturing* 38.5 (May 2007), pp. 1318–1330 (cit. on p. 139).

[Slange+2016] T. K. Slange, L. Warnet, W. J. B. Grouve, and R. Akkerman. “Influence of preconsolidation on consolidation quality after stamp forming of C/PEEK composites”. In: *AIP Conference Proceedings 1769*. 2016 (cit. on pp. 40, 160).

[Slange+2018] T.K. Slange, L.L. Warnet, W.J.B. Grouve, and R. Akkerman. “Deconsolidation of C/PEEK blanks: on the role of prepreg, blank manufacturing method and conditioning”. In: *Composites Part A: Applied Science and Manufacturing* 113 (Oct. 2018), pp. 189–199 (cit. on p. 40).

[Smith+2013] J. R. Smith and U. K. Vaidya. “Processing Optimization of Deformed Plain Woven Thermoplastic Composites”. In: *Applied Composite Materials* 20.6 (July 2013), pp. 1265–1272 (cit. on p. 136).

[Solvay2012] Solvay. *Evolite XA1481 technical data sheet*. Solvay. 2012 (cit. on p. 66).

[Spagnol+2009] S. Spagnol, B. Lartigue, A. Trombe, and F. Despetis. “Experimental Investigations on the Thermal Conductivity of Silica Aerogels by a Guarded Thin-Film-Heater Method”. In: *Journal of Heat Transfer* 131.7 (2009), p. 074501 (cit. on p. 83).

[Sparrow+1978] E. M. Sparrow and R. D. Cess. *Radiation Heat Transfer, Augmented Edition*. CRC PR INC, June 11, 1978. 382 pp. (cit. on p. 19).

[Starke2016] J. Starke. “Carbon composites in automotive structural applications”. In: *Proceedings of EuCIA: Composites and Sustainability*. 2016 (cit. on p. 3).

[SteggallMurphy+2010] C. Steggall-Murphy, P. Simacek, S. G. Advani, S. Yarlagadda, and S. Walsh. “A model for thermoplastic melt impregnation of fiber bundles during consolidation of powder-impregnated continuous fiber composites”. In: *Composites Part A: Applied Science and Manufacturing* 41.1 (Jan. 2010), pp. 93–100 (cit. on p. 44).

[StokesGriffin+2015] C.M. Stokes-Griffin and P. Compston. “A combined optical-thermal model for near-infrared laser heating of thermoplastic composites in an automated tape placement process”. In: *Composites Part A: Applied Science and Manufacturing* 75 (Aug. 2015), pp. 104–115 (cit. on p. 11).

[Stolarski+1982] H. Stolarski and T. Belytschko. “Membrane Locking and Reduced Integration for Curved Elements”. In: *Journal of Applied Mechanics* 49.1 (1982), p. 172 (cit. on p. 150).

[Suemasu+1994] H. Suemasu, K. Friedrich, and M. Hou. “On deformation of woven fabric-reinforced thermoplastic composites during stamp-forming”. In: *Composites Manufacturing* 5.1 (Mar. 1994), pp. 31–39 (cit. on p. 27).

[Svanberg2002] K. Svanberg. “A Class of Globally Convergent Optimization Methods Based on Conservative Convex Separable Approximations”. In: *SIAM Journal on Optimization* 12.2 (Jan. 2002), pp. 555–573 (cit. on p. 110).

[Svensson+1998] N. Svensson, R. Shishoo, and M. Gilchrist. “Manufacturing of Thermoplastic Composites from Commingled Yarns-A Review”. In: *Journal of Thermoplastic Composite Materials* 11.1 (Jan. 1998), pp. 22–56 (cit. on p. 40).

[Sweeney+1995] G.J. Sweeney, P.F. Monaghan, M.T. Brogan, and S.F. Cassidy. “Reduction of infra-red heating cycle time in processing of thermoplastic composites using computer modelling”. In: *Composites Manufacturing* 6.3-4 (Jan. 1995), pp. 255–262 (cit. on pp. 11, 21).

[Taggart+1987] D. G. Taggart and F. J. Schwan. “Evaluation of woven fabric composites for automotive applications”. In: *Journal of Materials Shaping Technology* 5.1 (Mar. 1987), pp. 41–51 (cit. on p. 3).

[Tanaka+2015] S. Tanaka, K. Yoshikawa, T. Okamoto, and K. Hasegawa. “A new ray-tracing scheme for 3D diffuse radiation transfer on highly parallel architectures”. In: *Publications of the Astronomical Society of Japan* 67.4 (May 2015), p. 62 (cit. on p. 24).

[Tavana+2012] R. Tavana, S. Shaikhzadeh Najar, M. Tahaye Abadi, and M. Sedighi. “Meso/-macroscale finite element model for forming process of woven fabric reinforcements”. In: *Journal of Composite Materials* 47.17 (July 2012), pp. 2075–2085 (cit. on p. 36).

[ten Thije+2007] R.H.W. ten Thije, R. Akkerman, and J. Huétink. “Large deformation simulation of anisotropic material using an updated Lagrangian finite element method”. In: *Computer Methods in Applied Mechanics and Engineering* 196.33-34 (July 2007), pp. 3141–3150 (cit. on p. 31).

[ten Thije+2008a] R. H. W. ten Thije and R. Akkerman. “Solutions to intra-ply shear locking in finite element analyses of fibre reinforced materials”. In: *Composites Part A: Applied Science and Manufacturing* 39.7 (July 2008), pp. 1167–1176 (cit. on p. 150).

[ten Thije+2008b] R. H. W. ten Thije, R. Akkerman, L. van der Meer, and M. P. Ubbink. "Tool-ply friction in thermoplastic composite forming". In: *International Journal of Material Forming* 1.S1 (Apr. 2008), pp. 953–956 (cit. on pp. 143, 152).

[ten Thije+2011] R. H. W. ten Thije, R. Akkerman, M. Ubbink, and L. van der Meer. "A lubrication approach to friction in thermoplastic composites forming processes". In: *Composites Part A: Applied Science and Manufacturing* 42.8 (Aug. 2011), pp. 950–960 (cit. on p. 152).

[Tephany+2016] C. Tephany, J. Gillibert, P. Ouagne, G. Hivet, S. Allaoui, and D. Soulat. "Development of an experimental bench to reproduce the tow buckling defect appearing during the complex shape forming of structural flax based woven composite reinforcements". In: *Composites Part A: Applied Science and Manufacturing* 81 (Feb. 2016), pp. 22–33 (cit. on p. 144).

[Thomann+2004] U. Thomann, M. Sauter, and P. Ermanni. "A combined impregnation and heat transfer model for stamp forming of unconsolidated commingled yarn preforms". In: *Composites Science and Technology* 64.10-11 (Aug. 2004), pp. 1637–1651 (cit. on p. 41).

[Thomann2003] U. Thomann. "Direct stamp forming of non-consolidated carbon/thermoplastic fibre commingled yarns". PhD thesis. ETH Zürich, 2003 (cit. on pp. 41, 68).

[Thomas+2010] M. Thomas, N. Boyard, N. Lefèvre, Y. Jarny, and D. Delaunay. "An experimental device for the simultaneous estimation of the thermal conductivity 3-D tensor and the specific heat of orthotropic composite materials". In: *International Journal of Heat and Mass Transfer* 53.23-24 (Nov. 2010), pp. 5487–5498 (cit. on p. 67).

[Thomas+2012] S. Thomas, K. Joseph, S. K. Malhotra, K. Goda, and M. S. Sreekala. *Polymer Composites – Macro- and microcomposites*. Wiley VCH Verlag GmbH, Mar. 27, 2012 (cit. on p. 70).

[Thompson+2018a] A. J. Thompson, B. El Said, D. Ivanov, J. P-H. Belnoue, and S. R. Hallett. "High fidelity modelling of the compression behaviour of 2D woven fabrics". In: *International Journal of Solids and Structures* 154 (Dec. 2018), pp. 104–113 (cit. on p. 120).

[Thompson+2018b] A. J. Thompson, B. El Said, J. P-H. Belnoue, and S. R. Hallett. "Modelling process induced deformations in 0/90 non-crimp fabrics at the meso-scale". In: *Composites Science and Technology* 168 (Nov. 2018), pp. 104–110 (cit. on p. 36).

[Throne2008] J. L. Throne. *Understanding Thermoforming*. Hanser, May 11, 2008. 266 pp. (cit. on pp. 10, 159).

[TrudelBoucher+2006] D. Trudel-Boucher, B. Fisa, J. Denault, and P. Gagnon. "Experimental investigation of stamp forming of unconsolidated commingled E-glass/polypropylene fabrics". In: *Composites Science and Technology* 66.3-4 (Mar. 2006), pp. 555–570 (cit. on pp. 11, 42).

[Vaidya+2008] U. K. Vaidya and K. K. Chawla. "Processing of fibre reinforced thermoplastic composites". In: *International Materials Reviews* 53.4 (July 2008), pp. 185–218 (cit. on p. 4).

[Van West+1991] B. P. Van West, R. Byron Pipes, and S. G. Advani. “The consolidation of commingled thermoplastic fabrics”. In: *Polymer Composites* 12.6 (Dec. 1991), pp. 417–427 (cit. on p. 41).

[Vanclooster+2010] K. Vanclooster, S. V. Lomov, and I. Verpoest. “Simulation of Multilayered Composites Forming”. In: *International Journal of Material Forming* 3.S1 (Apr. 2010), pp. 695–698 (cit. on p. 143).

[Vanclooster2010] K. Vanclooster. “Forming of multilayered fabric reinforced thermoplastic composites”. PhD thesis. Katholieke Universiteit Leuven, 2010 (cit. on pp. 94, 152, 159).

[Verleye+2008] B. Verleye, R. Croce, M. Griebel, M. Klitz, S.V. Lomov, G. Morren, H. Sol, I. Verpoest, and D. Roose. “Permeability of textile reinforcements: Simulation, influence of shear and validation”. In: *Composites Science and Technology* 68.13 (Oct. 2008), pp. 2804–2810 (cit. on p. 130).

[Verpoest+2005] I. Verpoest and S. Lomov. “Virtual textile composites software : Integration with micro-mechanical, permeability and structural analysis”. In: *Composites Science and Technology* 65.15-16 (Dec. 2005), pp. 2563–2574 (cit. on p. 35).

[Vicard+2017] C. Vicard, O. De Almeida, A. Cantarel, and G. Bernhart. “Experimental study of polymerization and crystallization kinetics of polyamide 6 obtained by anionic ring opening polymerization of ε-caprolactam”. In: *Polymer* 132 (Dec. 2017), pp. 88–97 (cit. on p. 4).

[Vodak+2011] P.B. Vodak, A.W. Mix, and A.J. Giacomin. “Sheet bowing in thermoforming”. In: *Polymer Engineering & Science* 51.12 (Oct. 2011), pp. 2571–2577 (cit. on p. 106).

[Vu+2015] T.D. Vu, D. Durville, and P. Davies. “Finite element simulation of the mechanical behavior of synthetic braided ropes and validation on a tensile test”. In: *International Journal of Solids and Structures* 58 (Apr. 2015), pp. 106–116 (cit. on p. 34).

[Vueghs+2006] P. Vueghs and P. Beckers. “Presentation of the hemisphere method”. In: *Advanced Computational Methods in Heat Transfer IX*. WIT Press, June 2006 (cit. on p. 19).

[Wakeman+1998] M.D. Wakeman, T.A. Cain, C.D. Rudd, R. Brooks, and A.C. Long. “Compression moulding of glass and polypropylene composites for optimised macro- and micro- mechanical properties—1 commingled glass and polypropylene”. In: *Composites Science and Technology* 58.12 (Dec. 1998), pp. 1879–1898 (cit. on p. 41).

[Wakeman+2006] M.D. Wakeman, L. Zingraff, P.-E. Bourban, J.-A.E. Månson, and P. Blanchard. “Stamp forming of carbon fibre/PA12 composites – A comparison of a reactive impregnation process and a commingled yarn system”. In: *Composites Science and Technology* 66.1 (Jan. 2006), pp. 19–35 (cit. on pp. 4, 42).

[Waltz+2005] R.A. Waltz, J.L. Morales, J. Nocedal, and D. Orban. “An interior algorithm for nonlinear optimization that combines line search and trust region steps”. In: *Mathematical Programming* 107.3 (Nov. 2005), pp. 391–408 (cit. on p. 131).

[Wang+1995] J.-S. Wang and R. S. Porter. “On the viscosity-temperature behavior of polymer melts”. In: *Rheologica Acta* 34.5 (1995), pp. 496–503 (cit. on p. 13).

[Wang+1998] J. Wang, J.R. Page, and R. Paton. “Experimental investigation of the draping properties of reinforcement fabrics”. In: *Composites Science and Technology* 58.2 (Jan. 1998), pp. 229–237 (cit. on p. 28).

[Wang+2012] P. Wang, N. Hamila, P. Pineau, and P. Boisse. “Thermomechanical analysis of thermoplastic composite prepregs using bias-extension test”. In: *Journal of Thermoplastic Composite Materials* 27.5 (Aug. 2012), pp. 679–698 (cit. on pp. 38, 44).

[Wang+2014] P. Wang, N. Hamila, P. Boisse, P. Chaudet, and D. Lesueur. “Thermomechanical behavior of stretch-broken carbon fiber and thermoplastic resin composites during manufacturing”. In: *Polymer Composites* 36.4 (Mar. 2014), pp. 694–703 (cit. on pp. 27, 118, 121).

[Wedhorn+2017] L. Wedhorn and R. Ebeling. “Quilted Stratum Process for High-performance CFRP Production”. In: *Lightweight Design worldwide* 10.1 (Mar. 2017), pp. 50–55 (cit. on p. 12).

[Weeën1991] F. van der Weeën. “Algorithms for draping fabrics on doubly-curved surfaces”. In: *International Journal for Numerical Methods in Engineering* 31.7 (May 1991), pp. 1415–1426 (cit. on p. 37).

[Willems+2006] A. Willems, S. V. Lomov, D.. Vandepitte, and I. Verpoest. “Double dome forming simulation of woven textile composites”. In: *Proceedings of the 7th international ESAFORM conference*. 2006, pp. 26–28 (cit. on p. 139).

[Willems+2008] A. Willems, S.V. Lomov, I. Verpoest, and D. Vandepitte. “Optical strain fields in shear and tensile testing of textile reinforcements”. In: *Composites Science and Technology* 68.3-4 (Mar. 2008), pp. 807–819 (cit. on pp. 26, 33).

[Williams+2016] M. Williams and R. Minjares. *A technical summary of Euro 6/VI vehicle emission standards*. Tech. rep. The International Council on Clean Transportation, 2016 (cit. on p. 2).

[Wilson2017] A. Wilson. “Vehicle weight is the key driver for automotive composites”. In: *Reinforced Plastics* 61.2 (Mar. 2017), pp. 100–102 (cit. on p. 2).

[Xiao+2014] X. Xiao, A. Long, and X. Zeng. “Through-thickness permeability modelling of woven fabric under out-of-plane deformation”. In: *Journal of Materials Science* 49.21 (July 2014), pp. 7563–7574 (cit. on p. 130).

[Yang+2012] Y. Yang, R. Boom, B. Irion, D.-J. van Heerden, P. Kuiper, and H. de Wit. “Recycling of composite materials”. In: *Chemical Engineering and Processing: Process Intensification* 51 (Jan. 2012), pp. 53–68 (cit. on p. 3).

[Yang+2014] B. Yang, T. Jin, F. Bi, and J. Li. “A Geometry Information Based Fishnet Algorithm for Woven Fabric Draping in Liquid Composite Molding”. In: *Materials Science* 20.4 (Dec. 2014) (cit. on p. 37).

[Ye+1995] L. Ye, K. Friedrich, J. Kästel, and Y.-W. Mai. “Consolidation of unidirectional CF/PEEK composites from commingled yarn prepreg”. In: *Composites Science and Technology* 54.4 (Jan. 1995), pp. 349–358 (cit. on p. 41).

[Ye+2005] L. Ye, Z.-R. Chen, M. Lu, and M. Hou. “De-consolidation and re-consolidation in CF/PPS thermoplastic matrix composites”. In: *Composites Part A: Applied Science and Manufacturing* 36.7 (July 2005), pp. 915–922 (cit. on p. 40).

[Yu+2006] X. Yu, B. Cartwright, D. McGuckin, L. Ye, and Y.-W. Mai. “Intra-ply shear locking in finite element analyses of woven fabric forming processes”. In: *Composites Part A: Applied Science and Manufacturing* 37.5 (May 2006), pp. 790–803 (cit. on p. 150).

[Zeng+2014] X. Zeng, L. P. Brown, A. Endruweit, M. Matveev, and A. C. Long. “Geometrical modelling of 3D woven reinforcements for polymer composites: Prediction of fabric permeability and composite mechanical properties”. In: *Composites Part A: Applied Science and Manufacturing* 56 (Jan. 2014), pp. 150–160 (cit. on p. 34).

[Zhou+2004] G. Zhou, X. Sun, and Y. Wang. “Multi-chain digital element analysis in textile mechanics”. In: *Composites Science and Technology* 64.2 (Feb. 2004), pp. 239–244 (cit. on p. 34).

[Zhu+2007] B. Zhu, T.X. Yu, and X.M. Tao. “Large deformation and slippage mechanism of plain woven composite in bias extension”. In: *Composites Part A: Applied Science and Manufacturing* 38.8 (Aug. 2007), pp. 1821–1828 (cit. on pp. 30, 31, 43).

Publications and presentations resulting from this study

T. Baumard, G. Menary, O. De Almeida, P. Martin, F. Schmidt, J. Bikard. "Experimental characterization and modeling of the temperature and rate-dependent shear behaviour of powder-impregnated glass fiber/PA66 woven semipregs". *Composites Science and Technology* 180 (August 2019), pp. 23–32.

T. Baumard, G. Menary, O. De Almeida, F. Schmidt, J. Bikard. "Characterization and modelling of the temperature and rate dependent shear behaviour of a non-consolidated powder impregnated fabric". In: *Proceedings of the 18th European Conference on Composite Materials (ECCM18)*, June 2018, Athens, Greece.

T. Baumard, G. Menary, O. De Almeida, P. Martin, F. Schmidt. "Direct forming of powder-impregnated thermoplastic composites: experimental characterization and modelling of the shear behaviour". In: *Proceedings of the KTN conference on Out-of-Autoclave Processing of Composites*, Mar. 2018, Belfast, United Kingdom.

T. Baumard, G. Menary, O. De Almeida, P. Martin, F. Schmidt, J. Bikard. "Towards a coupled heating-forming simulation of the thermoforming of thermoplastic composites". In: *AIP – Proceedings of the 20th International ESAFORM Conference on Material Forming* 1896.1, Apr. 2017, Dublin, Ireland.

T. Baumard, G. Menary, O. De Almeida, P. Martin, F. Schmidt, J. Bikard. "Towards a coupled heating-forming simulation of the thermoforming of thermoplastic composites". In: *20th Sir Bernard Crossland Symposium and Postgraduate Research Workshop*, Apr. 2017, Dublin, Ireland.

T. Baumard, G. Menary, O. De Almeida, F. Schmidt, J. Bikard. "Simulation de la mise en forme de tissus préimprégnés par thermoformage". In: *JST AMAC – Mise en Oeuvre des Composites à Matrice Thermoplastique*, Jan. 2017, Toulouse, France.

T. Baumard, O. De Almeida, G. Menary, P. Martin, F. Schmidt, J. Bikard. “Coupled heating-forming simulation of the thermoforming of thermoplastic composites”. In: *Proceedings of the 3rd International Conference on Thermoplastic Composites (ITHEC)*, Oct. 2016, Bremen, Germany.

T. Baumard, O. De Almeida, G. Menary, Y. Le Maoult, F. Schmidt, J. Bikard. “Determination of thermal contact conductance in vacuum-bagged thermoplastic prepreg stacks using infrared thermography”. In: *AIP – Proceedings of the 19th International ESAFORM Conference on Material Forming* 1769.1, Apr. 2016, Nantes, France.

Résumé

Modélisation du thermoformage de composites thermoplastiques poudrés : influence de l'étape de préchauffage infrarouge sur la mise en forme

Le thermoformage non-isotherme de composites thermoplastiques, qui consiste à chauffer une préforme consolidée à une température supérieure à la fusion de la matrice avant de la transférer dans une presse d'estampage, est un procédé bien adapté à la production grande série de pièces structurelles pour l'industrie automobile (avec des temps de cycle <1 min). L'utilisation d'outils numériques pour prédire l'apparition de défauts en fonction des paramètres procédés utilisés est d'un grand intérêt pour éviter l'emploi de procédures d'optimisation expérimentales couteuses de type essais/erreur.

Ces travaux de thèse ont porté sur le développement d'une simulation de la mise en forme de composites poudrés PA66/verre, incluant la modélisation explicite de l'étape de préchauffage infrarouge, afin d'étudier l'effet de l'homogénéité du champ de température sur la présence de défauts de forme. Les propriétés thermophysiques et optiques du matériau ont été caractérisées expérimentalement à deux niveaux de consolidation. La structure du matériau non consolidé conduit à un chauffage moins uniforme, comparé à une préforme préconsolidée. Un modèle éléments finis, basé sur la méthode des radiosités pour la prise en compte des transferts radiatifs a été utilisé pour simuler l'étape de préchauffage ; la démarche a été validée par comparaison avec des essais menés sur un pilote de four infrarouge. L'effet de l'affaissement de la préforme sur la distribution de température a été évalué numériquement, et une procédure d'optimisation pour déterminer les paramètres du four en fonction d'un champ de température requis a été présentée.

Le comportement mécanique du composite tissé a été modélisé à l'échelle macroscopique par une loi hypoélastique, implémentée dans Abaqus/Explicit. Les paramètres du modèle ont été déterminés à l'aide d'essais en traction et cisaillement en fonction de la température et de la vitesse de sollicitation. Des simulations non-isothermes de la mise en forme de pièces hémisphériques ont été réalisées, et montrent un bon accord avec les données expérimentales obtenues à l'aide d'un pilote de formage à l'échelle laboratoire.

Mots-clés : Thermoformage, Composites thermoplastiques, Transferts thermiques, Simulation thermomécanique

---

Abstract

Modelling the influence of infrared preheating and temperature uniformity in forming of powder-impregnated thermoplastic composites

Non-isothermal thermoforming of thermoplastic composites, in which a preconsolidated blank is heated above the melting temperature of the matrix before being formed in a press, is a process well adapted to the high production rates of automotive structural parts, allowing for cycle times <1 min. Numerical tools to predict the apparition of manufacturing-induced defects based on the process parameters used are of an obvious industrial interest to avoid relying on a cost and time intensive trial-and-error approach.

This thesis focused on the development of a comprehensive simulation of the forming of powder-impregnated PA66/glass composites, modelling explicitly the infrared preheating step to investigate the effect of temperature homogeneity on shape defects. The thermophysical and optical properties of the material were characterized experimentally at two levels of consolidation, and as a function of temperature when relevant. The structure of the non-consolidated material leads to a less uniform heating, compared to preconsolidated blanks. A finite element model based on the radiosity method to compute the radiative heat transfer was used to simulate the preheating step; this approach was validated against experimental results from a custom-built infrared oven. The model has been used to investigate the effect of blank sag on temperature distribution, and an optimization method to determine the oven parameters based on a desired temperature field has been presented.

The mechanical behaviour of the woven composite during forming was modelled with a hypoelastic continuum approach, implemented in Abaqus/Explicit. The model parameters were determined from experimental tensile tests and in-plane shear tests at various temperatures and shear rates. Non-isothermal simulations of the forming of hemispherical parts were conducted, using the temperature field predicted from the preheating simulation as an input, and showed good agreement with that observed on parts formed on a lab-scale thermoforming setup.

Keywords: Thermoforming, Thermoplastic composites, Heat transfer, Thermomechanical simulation